UNIVERSITY OF SOUTHAMPTON

FACULTY OF PHYSICAL AND APPLIED SCIENCES

Optoelectronics Research Centre

Laser-Induced Forward Transfer Techniques for Printing Functional Materials and Photonic Devices

by

Kamalpreet Kaur

Thesis for the degree of Doctor of Philosophy

June 2011

UNIVERSITY OF SOUTHAMPTON

ABSTRACT

FACULTY OF PHYSICAL AND APPLIED SCIENCES
OPTOELECTRONICS RESEARCH CENTRE

Doctor of Philosophy

by Kamalpreet Kaur

The subject of this thesis is to study the Laser-Induced Forward Transfer (LIFT) technique using a time-resolved method in order to gain a better insight into the dynamics of the transfer process and to use the technique for rapid prototyping of photonic devices and printing piezoelectric materials for energy harvesting applications.

A nanosecond shadowgraphy technique was used to study the triazene polymer (TP)-dynamic release layer (DRL) assisted LIFT technique for solid-phase ceramic materials namely gadolinium gallium oxide (Gd-Ga-O)and ytterbium doped yttrium aluminium oxide (Yb:YAG). The dependence of the distance travelled by the shockwave and the ejected donor material, their velocities and the quality of the ejected donor pixel on the laser fluence, the thickness of the TP-DRL and donor film thickness was studied and is discussed.

Segmented channel waveguides, X-couplers and mode-filters based on titanium (Ti) in-diffused lithium niobate (LN) have been fabricated using the LIFT technique. The segment separation was found to be the key factor in determining mode profiles of waveguides. The corrugations due to the segmented nature of the deposits was observed to introduce non-adiabatic behavior in the mode filters which was further confirmed by theoretical modeling.

Forward transfer of donor films with patterns to be transferred machined into them prior to LIFT have been investigated. This technique allows debris-free printing of thicker and fragile donors films with extremely smooth and uniform edges in intact and solid-phase without the need of any sacrificial layer. Results of debris-free printing of micro-pellets of zinc oxide (ZnO) with extremely good quality edges from donor films pre-machined using focused ion beam (FIB) are presented.

Printing and post-transfer characterization of both lead zirconate titanate (PZT) and non-lead based ZnO piezoelectric materials for energy harvesting applications using the LIFT and TP-DRL assisted LIFT techniques have been studied and discussed.

Contents

List of Figures

List of Tables

Declaration Of Authorship

I, Kamalpreet Kaur declare that the thesis entitled "Laser-Induced Forward Transfer Techniques for Printing Functional Materials and Photonic Devices" and the work presented in it are my own. I confirm that

1. This work was done wholly or mainly while in candidature for a research degree at this University;
2. Where any part of this thesis has previously been submitted for a degree or any other qualification at this University or any other institution, this has been clearly stated;
3. Where I have consulted the published work of others, this is always clearly attributed;
4. Where I have quoted from the work of others, the source is always given. With the exception of such quotations, this thesis is entirely my own work;
5. I have acknowledged all main sources of help;
6. Where the thesis is based on work done by myself jointly with others, I have made clear exactly what was done by others and what I have contributed myself;
7. Either none of this work has been published before submission, or parts of this work have been published as [please see List of Publications]:

Signed: .....

Date: .....

Acknowledgement

I would like to express my deepest gratitude for Rob for his invaluable help and support throughout the PhD. Without his suggestions, feedback and guidance this thesis would have not been possible. He tried to help in every possible way to make my stay at the ORC and Southampton comfortable. I won't be wrong in saying that he is the best supervisor a student can ask for. Thanks for everything.

I would like extend my special thanks to Dave for teaching me all the stuff and the 'secret' tricks about LIFT in the FASTlab and for patiently listening and answering to all my questions/doubts. I learnt a lot from you Dave. Thanks to Matthias for the help with the experiments and discussions that helped in understanding things better. Vielen Dank. I would like to thank Tim, Rossana, Kate, Alberto and Fabio for providing the donor substrates. Thanks to Tim for showing me how to work in the mechanical workshop and helping me build the excimer set-up. Thanks to Tom, Romain and Jamie for providing the TP substrates and for hosting me and for their help in their labs at PSI.

Many thanks to Sak for his help with the work on LIFTing of photonic devices and for the useful discussions and helping me learn the topic. Thanks to Charlie and Pranabendu for their help with the simulations. Thanks to Collin for help in characterisation and polishing of waveguides. Thanks to Bruce for the help with FIBbing of substrates. Thanks to Russel and Neil White for letting me use their equipments for PZT characterisation experiments. I would like to thank Ben Mills for the help with the LabView codes and help in sorting things in the FASTlab. Thanks to Neil and Dave for their help in clean room. Thanks to Simon for patiently going through my bad drawings and magically turning them into holders and other experimental set-up bits.

I would like to thank Eve for helping me with all the student formalities and providing me all those countless visa letters with a smiling face. Many thanks to all my friends at ORC for all the fun times that made my PhD journey an enjoyable and memorable one.

I would like to thank my loving husband for his constant motivation and support throughout my PhD work. He believed in me more than I did myself and it is his unconditional love and support that kept me going even during the rough phases of my PhD. Love you loads. Finally, many thanks to my parents for their blessings, love and constant support.

Nomenclature

a:Si:H	Hydrogenated amorphous silicon
AFA	Absorbing film assisted
AFM	Atomic force microscopy
BLAST	Ballistic Laser-Assisted Solid Tranfer
BPM	Beam propagation method
CMOS	Complementary metal-oxide semiconductor
CW	Continuous wave
DMD	Digital micro mirror device
DRL	Dynamic Release Layer
DW	Direct-write
FIB	Focussed ion beam
FP	Fabry-Perot
fs	Femtosecond
FWHM	Full width at half maximum
Gd-Ga-O	Gadolinium gallium oxide
IR	Infrared
kHz	Kilohertz
LDW	Laser Direct Write
LIBT	Laser induced backward transfer

LIFT	Laser-Induced Forward Transfer
LIMIT	Laser Induced Molecular Implantation technique
LISE	Laser-Induced Solid Etching
LITI	Laser Induced Thermal Imaging
LMI	Laser Molecular Implantation
LN	Lithium niobate
LTHC	Light-to-heat conversion
MAPLE-DW	Matrix-Assisted Pulsed Laser Evaporation Direct-Write
MEMS	Microelectromechanical systems
MFD	Mode field diameter
MMF	Multimode fibre
NELT	Nanoparticle enabled laser transfer
ns	Nanosecond
OLED	Organic light-emitting diode
PFM	Piezoelectric force microscopy
PLD	Pulsed laser deposition
PZT	Lead zirconate titanate
RT	Room temperature
SEM	Scanning electron microscope
SGL	Shock generation layer
SLM	Spatial light modulator
SMF	Single mode fibre
Ti	Titanium
TM	Transverse magnetic
TP	Triazene polymer

Yb:YAG	Ytterbium doped yttrium aluminium oxide
ZnO	Zinc oxide
ZnTPP	Zinc tetraphenyl porphine

Dedicated to my parents and husband

Chapter 1

Introduction

1.1 Motivation

The deposition and controlled patterning (from meso - to nanoscale) of thin film materials is an inherent requirement to a vast range of fields extending from microelectromechanical systems (MEMS) to biological sensors and optoelectronics. The most established technique for material processing and large-scale production of micron and sub-micron size devices is photolithography. For cases where rapid prototyping of devices is required and patterning and transfer of materials is desired onto non-planar substrates photolithography offers limited flexibility and increased complexity, time and cost. Laser Direct Write (LDW) techniques are ideal candidates for such cases (Chrisey, 2000), as they offer significant advantages in terms of simplicity, cost effectiveness, flexibility, fast processing speeds for rapid prototyping and also eliminate the need for a clean room environment, which is a must for photolithography. A family of LDW techniques that has emerged quite rapidly in the past few years is the Laser-Induced Forward Transfer (LIFT) (Bohandy et al., 1986) method which uses a laser for selective ablation of materials from thin film targets coated onto transparent carrier substrates and forward transfers them onto receiver substrates placed in closed proximity. Figure 1.1 depicts the general principle of the LIFT technique.

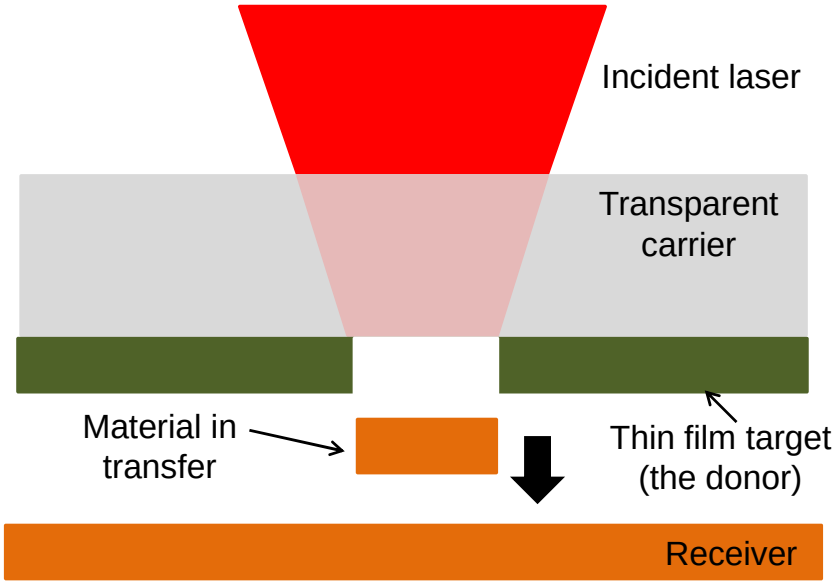

FIGURE 1.1: Illustration of the general principle of the LIFT technique.

The LIFT process was first demonstrated by Bohandy et al. (Bohandy et al., 1986) for depositing metals to repair damaged photomasks. Due to its simplicity and flexibility its use was quickly extended to print a variety of metals (Bohandy et al., 1986; Zergioti et al., 1998a), semiconductors (Toet et al., 1999), superconductors (Fogarassy et al., 1990), oxides (Mailis et al., 1999; Zergioti et al., 1998b), and biomaterials (Barron et al., 2004). As LIFT is a laser-based direct-writing method the focused laser beam can be used for in-situ micromachining, annealing and feature-trimming applications by simply removing the target from the laser beam path. Hence LIFT is both an additive and subtractive direct-write (DW) process but it will be referred to, and was used as an additive LDW process in the remainder of this thesis report.

In the conventional LIFT process the material to be transferred (the donor) acts as its own propellant which leads to its unavoidable damage. To prevent this damage of the donor material due to the direct exposure to the laser many complementary LIFT techniques have been introduced and developed in the past years such as Matrix-Assisted Pulsed Laser Evaporation Direct-Write (MAPLE-DW)) (Pique et al., 1999), Dynamic Release Layer (DRL)-LIFT (Tolbert et al., 1993), Laser Induced Thermal Imaging (LITI) (Blanchet et al., 2003), Ballistic Laser-Assisted Solid Transfer (BLAST) (Banks et al., 2008), Laser-Induced Solid Etching (LISE) (Banks et al., 2009) and Laser Molecular

Implantation (LMI) (Fukumura et al., 1994). A detailed overview of the conventional LIFT technique and all these complementary LIFT techniques is presented in chapter 2.

The main aim of this thesis was to use the LIFT technique for printing functional materials and fabricating devices for photonics and energy harvesting applications. In particular, fabrication of channel waveguides and index-tapered mode filters based on titanium (Ti) in-diffused lithium niobate (LN), and printing of lead zirconate titanate (PZT) and zinc oxide (ZnO) for micro-energy harvesters were the main focus for the thesis work. In addition to that, some work dedicated to understand the dynamics of the transfer process itself using a time-resolved technique was also done as part of the thesis.

1.2 Achievements

The main achievements of the thesis can be summarized as below:

1.2.1 Time-Resolved Study of the LIFT Technique

In chapter 3, the laser-induced forward transfer process was studied using triazene polymer (TP) as a sacrificial layer by means of a conventional time-resolved ns-shadowgraphy imaging technique for the first time for solid-phase ceramic donor materials such as gadolinium gallium oxide (Gd-Ga-O) and ytterbium doped yttrium aluminium oxide (Yb:YAG). The time evolution of the process, dependence of the ablation dynamics and quality of the ejected donor material disc (flyer) on the various key operating parameters such as laser fluence and thickness of the TP-DRL and donor layers were investigated and results are discussed in this chapter. Elements of the work presented in chapter 3 have been published in (Kaur et al., 2009).

1.2.2 Fabrication of Photonic devices using LIFT

Rapid prototyping of Ti in-diffused channel waveguides, X-couplers and mode-filters using the LIFT technique followed by thermal treatment is reported for the first time in chapters 4 and 5. Optical propagation losses as low as 0.8 dB/cm were measured from channel waveguides showing great potential of this very simple yet powerful technique.

The Ti segment separation was observed as the key factor in determining the waveguide mode profiles. This dependence on the segment separation was employed as the basic principle for preparing index-tapered waveguide mode filters, which were fabricated by varying the segment separation along the length of the waveguide. The corrugations in the refractive index profile due to the segmented geometry of the deposits was identified as introducing non-adiabatic behavior in the mode-filters and this was confirmed by theoretical modelling results. This work has been published in (Sones et al., 2010; Kaur et al., 2011b).

1.2.3 LIFTing of Pre-Machined Donor Films

In chapter 6, femtosecond (fs) LIFT of pre-machined donor films is studied for the first time. 1 μm thick ZnO films were first machined using the focused ion beam (FIB) technique up to a depth of 0.8 μm. Debris-free micro-pellets of ZnO with extremely smooth edges and surface uniformity were subsequently printed from these pre-machined donors using LIFT. Printing results of non-machined ZnO donor films and films deposited on top of a polymer DRL are also presented in this chapter for comparison, indicating the superior quality of transfer achievable and utility of this pre-machining technique. The initial results obtained show great potential for printing thick and fragile donors in solid and intact format without any DRL layer. Results of this work have been published in (Kaur et al., 2011a).

1.2.4 Printing Piezoelectric Donor Materials

In chapter 7, printing and post-transfer characterization of both lead based (PZT) and non-lead based (ZnO) piezoelectric donor materials for energy harvesting applications is reported. Micron-sized PZT deposits were transferred using fs-TP-DRL LIFT but due to the small size of the features, reliable d_{33} measurements were not possible. PZT deposits with mm^2 size were then printed using nanosecond (ns)-TP-DRL LIFT and d_{33} coefficients with small values of $\sim$ 19 - 20 pC/N were measured making it the first time for printing of PZT deposits using LIFT that show piezoelectric behavior post-printing. ZnO printed pellets showed poor adhesion onto the receiver substrates so couldn't be characterized. Work is being pursued to print piezoelectric deposits with electrodes on top in one shot and to improve the adhesion using chemical treatment

or an adhesion promoter layer. These issues once resolved would make possible the realization of a micro-energy harvester printed using LIFT, something which has not been achieved/reported before.

1.3 Thesis Structure

A brief outline of each chapter of the thesis is presented below:

Chapter 2 begins by giving an overview of the LIFT technique, its historical origin, the success it has achieved in the past years and its current state-of-the-art. In addition to LIFT some complementary LIFT techniques such as MAPLE-DW, DRL-LIFT, LITI, BLAST, LISE and LMI introduced to overcome some of the challenges faced by the conventional LIFT technique are also presented in this chapter.

The experimental results obtained during the thesis work are presented in chapters 3-7. Study of the dynamics of the TP-DRL assisted LIFT process using ns-shadowgraphy technique for Gd-Ga-O and Yb:YAG ceramics and the effect of various operating parameters such as laser fluence, donor and DRL thickness on the quality of the ejected donor are discussed in chapter 3.

Chapter 4 and 5 discuss the rapid prototyping of Ti:LN segmented channel waveguides, X-couplers and index-tapered mode filters respectively, using LIFT with post-transfer thermal diffusion. The details of experimental set-up used, fabrication and optical characterization of the prepared devices are presented in this chapter. Theoretical models developed to show the variation of the effective refractive index with segment separation and the non-adiabatic nature of the mode filters attributed to the segmented nature of the deposits is also presented in chapters 4 and 5 respectively. It should be mentioned that these models were developed in assistance with Dr. Pranabendu Gangopadhyay from the Indian Institute of Kharagpur, India and Dr. Ying from the Optoelectronics Research Centre (ORC), University of Southampton.

Initial results of printing ZnO donor films pre-machined up to a depth of 0.8 μm using the FIB technique prior to transfer are described in chapter 6. A comparison with the deposits printed using non-machined ZnO films employing the conventional LIFT and TP-DRL assisted LIFT techniques is also presented in this chapter.

Various attempts to print piezoelectric materials (PZT and ZnO) using ns/fs-LIFT and TP-DRL assisted LIFT techniques and to measure the their piezoelectric coefficients post-transfer are described in chapter 7. The problems faced such as poor donor quality, Pb deficiency and adhesion of the printed features onto receiver substrates that hampered the characterization of the deposits are also discussed in this chapter.

Finally, in chapter 8 conclusions and suggestions for future work based on the results obtained in this thesis are presented.

Bibliography

D. P. Banks, C. Grivas, I. Zergioti, and R. W. Eason. "Ballistic laser-assisted solid transfer (BLAST) from a thin film precursor". *Optics Express*, **16**:3249, 2008.

D. P. Banks, K. S. Kaur, and R. W. Eason. "Etching and forward transfer of fused silica in solid-phase by femtosecond laser-induced solid etching (LISE)". *Applied Surface Science*, **255**:8343, 2009.

J. A. Barron, P. Wu, H. D. Ladouceur, and B. R. Ringeisen. "Biological laser printing: A novel technique for creating heterogeneous 3-dimensional cell patterns". *Biomedical Microdevices*, **6**:139, 2004.

G. B. Blanchet, Y. L. Loo, J. A. Rogers, F. Gao, and C. R. Fincher. "Large area, high resolution, dry printing of conducting polymers for organic electronics". *Applied Physics Letters*, **82**:463, 2003.

J. Bohandy, B. F. Kim, and F. J. Adrian. "Metal-Deposition from a Supported Metal-Film Using an Excimer Laser". *Journal of Applied Physics*, **60**:1538, 1986.

D. B. Chrisey. "Materials processing - The power of direct writing". *Science*, **289**:879, 2000.

E. Fogarassy, C. Fuchs, and J. Perriere. "Deposition of High-Tc Superconductor Films Using Laser-Induced Transfer". *Vide-Science Technique Et Applications*, **45**:166, 1990.

H. Fukumura, Y. Kohji, K. Nagasawa, and H. Masuhara. "Laser Implantation of Pyrene Molecules into Poly(Methyl Methacrylate) Films". *Journal of the American Chemical Society*, **116**:10304, 1994.

K. S. Kaur, R. Fardel, T. C. May-Smith, M. Nagel, D. P. Banks, C. Grivas, T. Lippert, and R. W. Eason. "Shadowgraphic studies of triazene assisted laser-induced forward transfer of ceramic thin films". *Journal of Applied Physics*, **105**:113119, 2009.

K.S. Kaur, M. Feinaeugle, D. P. Banks, J.Y. Ou, F.Di Pietrantonio, E. Verona, C. L. Sones, and R. W. Eason. "Laser-induced forward transfer of focussed ion beam pre-machined donors". *Applied Surface Science*, **257**:6650, 2011a.

K.S. Kaur, A.Z. Subramanian, Y.J. Ying, D.P Banks, M. Feinaeugle, P. Horak, V. Apostolopoulos, C.L. Sones, S. Mailis, and R.W. Eason. "Waveguide mode filters fabricated using laserinduced forward transfer ". *Optics Express*, **19**, 2011b.

S. Mailis, I. Zergioti, G. Koundourakis, A. Ikiades, A. Patentalaki, P. Papakonstantinou, N. A. Vainos, and C. Fotakis. "Etching and printing of diffractive optical microstructures by a femtosecond excimer laser". *Applied Optics*, **38**:2301, 1999.

A. Pique, D. B. Chrisey, R. C. Y. Auyeung, J. Fitz-Gerald, H. D. Wu, R. A. McGill, S. Lakeou, P. K. Wu, V. Nguyen, and M. Duignan. "A novel laser transfer process for direct writing of electronic and sensor materials". *Applied Physics a-Materials Science & Processing*, **69**:S279, 1999.

C. L. Sones, K. S. Kaur, P. Ganguly, D. P. Banks, Y. J. Ying, R. W. Eason, and S. Mailis. "Laser-induced-forward-transfer: a rapid prototyping tool for fabrication of photonic devices". *Applied Physics a-Materials Science & Processing*, **101**:333, 2010.

D. Toet, M. O. Thompson, P. M. Smith, and T. W. Sigmon. "Laser-assisted transfer of silicon by explosive hydrogen release". *Applied Physics Letters*, **74**:2170, 1999.

W. A. Tolbert, I. Y. S. Lee, M. M. Doxtader, E. W. Ellis, and D. D. Dlott. "High-Speed Color Imaging by Laser-Ablation Transfer with a Dynamic Release Layer - Fundamental Mechanisms". *Journal of Imaging Science and Technology*, **37**:411, 1993.

I. Zergioti, S. Mailis, N. A. Vainos, C. Fotakis, S. Chen, and C. P. Grigoropoulos. "Microdeposition of metals by femtosecond excimer laser". *Applied Surface Science*, **127**:601, 1998a.

I. Zergioti, S. Mailis, N. A. Vainos, P. Papakonstantinou, C. Kalpouzos, C. P. Grigoropoulos, and C. Fotakis. "Microdeposition of metal and oxide structures using ultrashort laser pulses". *Applied Physics a-Materials Science & Processing*, **66**:579, 1998b.

Chapter 2

Overview of laser-induced forward transfer (LIFT) technique

In this chapter a general overview of the LIFT technique is presented and will include its historical origin, the success it has achieved to date, some variations of LIFT that have been developed and reported in the literature with the intent to overcome some of the basic limitations of the technique. Section 2.1 describes the basic LIFT technique, suggested physical mechanisms responsible for the forward transfer and the fundamental difference between the ns and fs LIFT methods. Section 2.3 is focused on the various complementary LIFT techniques and the transfer results achieved using them. Finally the significant works reported in the literature using LIFT and LIFT-related techniques are listed in chronological order in Table 2.1.

2.1 Laser-Induced Forward Transfer (LIFT)

LIFT is an additive laser based direct-write (DW) technique for spatially-selective printing of materials from thin film precursors. In LIFT, a thin film of the material to be transferred (the donor) is coated onto a laser-transparent substrate (the carrier) and is placed in close proximity to another substrate (the receiver) as depicted in fig. 2.1. A laser pulse is then focused or imaged onto the carrier-donor interface which induces the necessary impulsive force to push the donor onto the receiver substrate placed below. The physical mechanism responsible for LIFT was suggested to be the thermal ablation

of the donor film (Bohandy et al., 1986). It was believed that the laser pulse was absorbed by the metal donor film causing its vaporization at the carrier–donor interface (fig. 2.1 (a)). The hot metal vapour trapped between the carrier and the donor film provided the required driving force for forward transfer of donor material to the receiver substrate (fig. 2.1 (b)). This hypothesis was supported by the theoretical models proposed by Adrian et al. (Adrian et al., 1987) and Baseman et al. (Baseman et al., 1990).

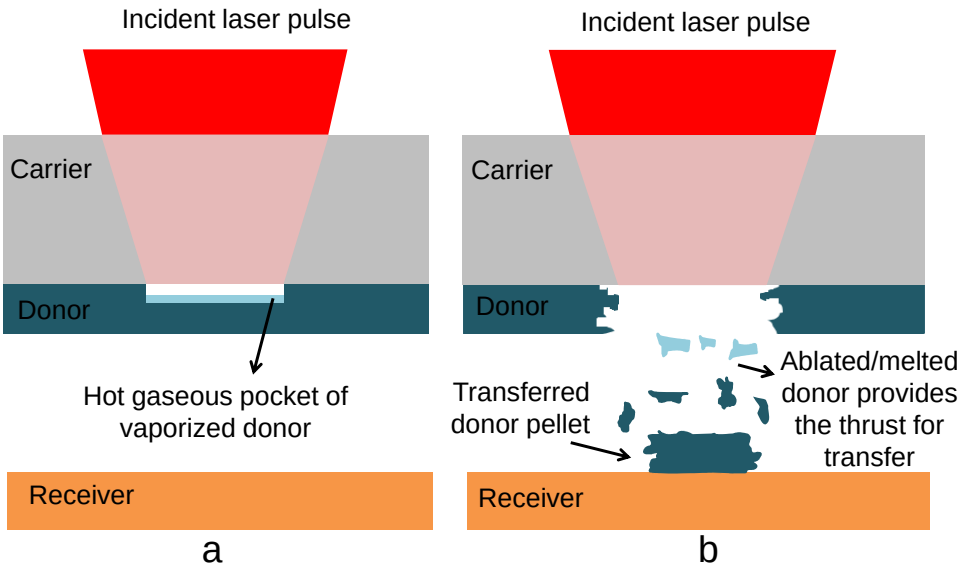

FIGURE 2.1: Schematic of LIFT technique.

The LIFT technique was first demonstrated for the deposition of copper metal lines onto a silicon receiver, using ns pulses from an excimer laser (193 nm, 15 ns) by Bohandy et al. in 1986 (Bohandy et al., 1986). In this work, it was observed that the quality of the transferred material depended strongly on the laser fluence and an optimum fluence value was required to transfer uniform and clean deposits of the donor to the receiver. The transferred material splattered away from the irradiated area at higher fluences and material transfer was incomplete at lower fluences. Although LIFT was originally developed to repair damaged photomasks, its use was quickly extended to deposit a variety of metals (Ag (Bohandy et al., 1988), Pd (Esrom et al., 1995), W (Kantor et al., 1995), Cr (Zergioti et al., 1998, 2003a,b), Ni (Yamada et al., 2002), Pt (Papakonstantinou et al., 1999), Au/Sn (Bahnisch et al., 2000)), metal oxides (Mailis et al., 1999), (Koundourakis

et al., 2001), (Zergioti et al., 2002)), semiconductors (Mogyorosi et al., 1989), superconductors (Fogarassy et al., 1989b), quantum dots (Xu et al., 2007), carbon nanotubes (Chang-Jian et al., 2006), polymers (Lee and Lee, 2004) and biomaterials (Serra et al., 2004a; Dinca et al., 2007).

Typically feature sizes of the LIFT-transferred structures are of the order of the laser spot size (Zergioti et al., 1998; Papakonstantinou et al., 1999; Yamada et al., 2002). Recently, the printing of donor material with features size significantly smaller than the laser spot size has been reported (Willis and Grosu, 2005; Banks et al., 2006; Narazaki et al., 2008; Kuznetsov et al., 2009b). All these studies used the standard LIFT experimental set-up of fig. 2.1 except for the work reported by Chichkov et al. (Kuznetsov et al., 2009a,b) where the transfer was performed in the backward direction to the laser incidence direction and the technique was termed as laser induced backward transfer (LIBT). Nanodroplet transfer using LIFT and LIBT technique is depicted in fig. 2.2 (a-c) and 2.3 (a-c) respectively.

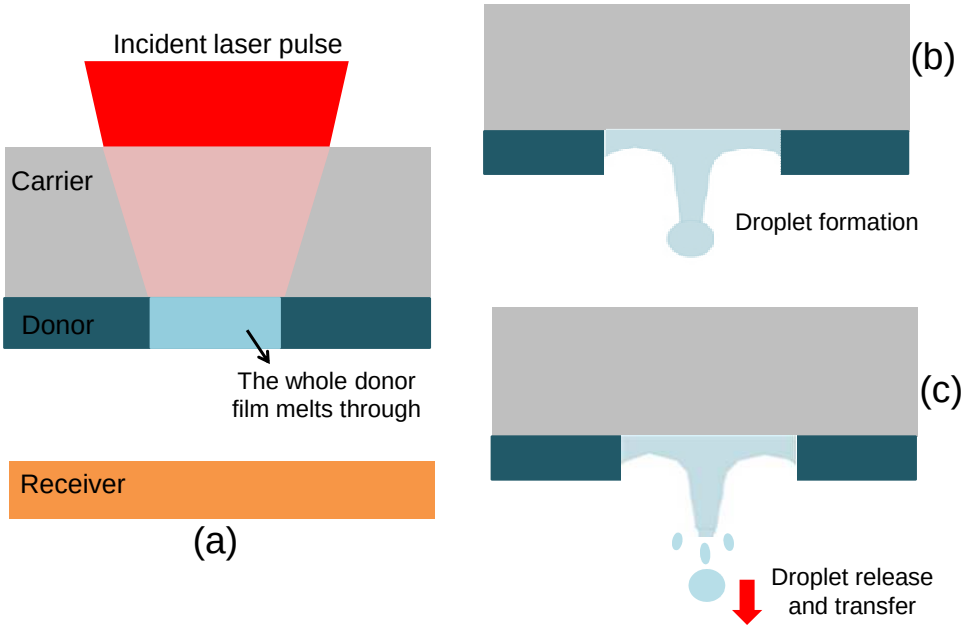

FIGURE 2.2: Illustration of nanodroplet growth and transfer using the LIFT technique.

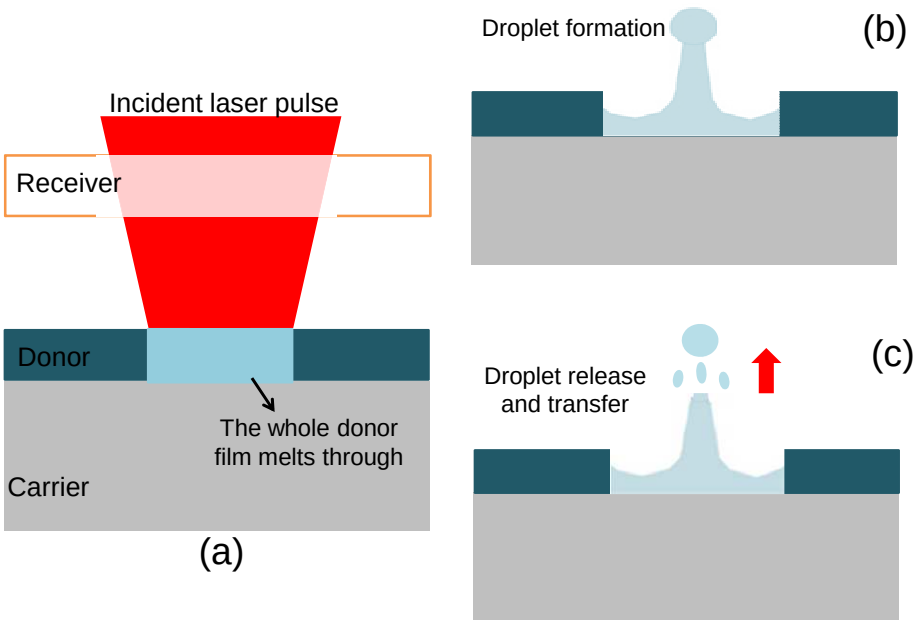

FIGURE 2.3: Illustration of nanodroplet growth and transfer using the LIBT technique [Kuznetsov2009a].

In the case of nanodroplet transfer using LIFT it was suggested that a laser pulse with a fluence just above the transfer threshold melts the donor film at the carrier-donor interface over the irradiated region. With an accurate control of the laser fluence the melt can be made to reach the free surface i.e. the donor film over the irradiated area fully melts through, thereby allowing sub-spot size depositions. For the LIBT case the laser pulse first melts the donor material on the free surface before the whole donor film completely melts through over the irradiated area. The expansion of the melted donor is confined by the surrounding solid film leading to build up of pressure that pushes the melted donor material out of the film towards the receiver (Kuznetsov et al., 2009b). Two obvious advantages offered by these nanodroplet printing methods are the sub-spot size printing and less splattering due to the surface tension of the molten donor material. The smallest features of ∼500 nm (Willis and Grosu, 2005; Narazaki et al., 2008)and ∼300 nm ((Banks et al., 2006); the smallest transferred to date) have been transferred using LIFT process with ns pulses and fs duration pulses respectively, and feature sizes of ∼ 220 nm have been deposited using the LIBT technique (Kuznetsov et al., 2009b).

Although we have reported fs LIFT in previous paragraph, in fact $>$ 90 % of the published work has used ns laser pulses except for the work by Kantor et al. in which they used μs pulses to transfer tungsten segments (Kantor et al., 1995, 1994). The use of

ultrashort pulses for ablation applications has resulted in features with high precision and significantly reduced collateral damage (Dausinger, 2003; Dausinger et al., 2004; Misawa and Juodkazis, 2006). As LIFT is also an ablation-based process these results inspired the idea of using fs pulses for LIFT. In the past few years, fs-LIFT has gained much attention and the transfer of metals (Zergioti et al., 1998; Banks et al., 2006; Germain et al., 2007), oxides (Zergioti et al., 2002; Mailis et al., 1999; Papazoglou et al., 2002b) and biomaterials (Zergioti et al., 2005a; Serra et al., 2004a), ceramics (Banks et al., 2008b) using fs-LIFT has been reported. The difference between ns and fs-LIFT is attributed to the fundamentally different laser-material interactions involved in these two pulse regimes as discussed below.

When a laser pulse interacts with a material, energy is first absorbed by the electrons and then subsequently transferred to the lattice by electron-phonon collisions, in a time scale of picoseconds, typically 1- 10 ps (Elsayedali et al., 1987; Gamaly et al., 2002a,b; Schoenlein et al., 1987) for most of the materials. In the case of fs pulses, there is not enough time for the electrons to transfer the heat to the lattice during the pulse, resulting in a reduced heat-affected zone, while conversely for ns pulses there is a significant energy transfer from the electrons to the lattice during the pulse, leading to a relatively larger heat-affected zone. The thermal diffusion length can be estimated by using equation 2.1

$$l_d = \frac{1}{2}\sqrt{\pi D t_p} \tag{2.1}$$

where l_d, D and t_p are thermal diffusion length, heat diffusion coefficient and laser pulse duration respectively (Papakonstantinou et al., 1999). For the fs regime $l_d < l_s$ (optical skin depth of the donor material), so the heat diffusion is limited to the skin depth, while for the ns regime $l_d > l_s$ implying a greater heat-affected area (Yao et al., 2005). The restriction of the heat diffusion to the skin depth only due to the extremely short energy deposition time in the case of ultrashort pulses gives the possibility of localized laser-material interaction resulting in improved quality deposits with reduced thermal damage to the donor and higher spatial resolution as has been reported in the literature (Mailis et al., 1999; Papazoglou et al., 2002a; Zergioti et al., 2005b; Banks et al., 2006; Bera et al., 2007; Germain et al., 2007).

In the conventional LIFT process (using ns or fs duration pulses) the donor material is directly exposed to the laser radiation leading to its ablation, melting or evaporation. The donor forward transfer is achieved either through the propulsion of the material by the ablated/evaporated film at the interface (Bohandy et al., 1986) or by melting of the entire donor film (Willis and Grosu, 2005; Banks et al., 2006; Narazaki et al., 2008). The phase transformations involved in the transfer are not a problem for materials like metals or those insensitive to light and heat. However, photo/thermal sensitive donors such as biological cells/tissues are quite susceptible to damage by the incident laser pulse. Also the conventional LIFT process is not suitable when an intact transfer of a donor material in solid phase is desired. To surmount these problems various complementary LIFT techniques have been introduced and developed in the past years and are discussed in the next section.

2.2 Complementary LIFT techniques

2.2.1 Matrix-Assisted Pulsed Laser Evaporation-Direct Write (MAPLE-DW)

The MAPLE-DW technique is based on the LIFT and the MAPLE (Pique et al., 1999a) processes. This technique therefore takes advantage of the technical approaches of both the LIFT and MAPLE techniques. In MAPLE-DW the target is prepared by making a solution of the material to be deposited with a volatile laser absorbing solvent matrix. The matrix helps in avoiding the laser degradation of the material to be deposited. A uniform coating of this solution is then applied onto a transparent carrier and upon irradiation with a focused laser pulse, the solvent evaporates and propels the donor material to the receiver (Pique et al., 1999b). A schematic of the MAPLE-DW process is shown in fig. 2.4.

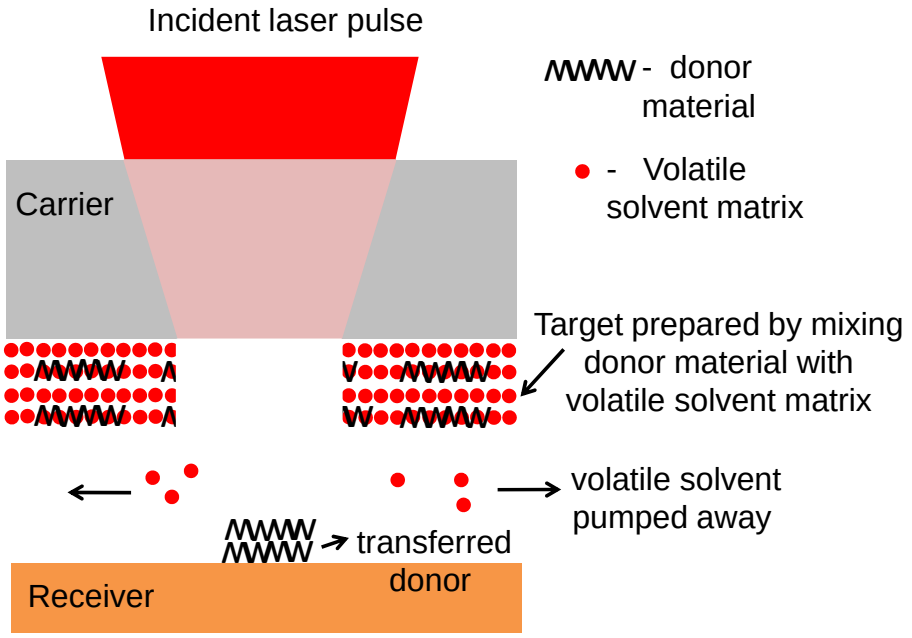

FIGURE 2.4: Illustration of MAPLE-DW technique.

High-resolution displays (Fitz-Gerald et al., 2000), thick film resistors (Modi et al., 2001), ferroelectric capacitors (Modi et al., 2002; Arnold et al., 2002a), micro-batteries (Pique et al., 2004; Wartena et al., 2004), chemical sensors (Pique et al., 2003b) and solar cells (Kim et al., 2004a) have been realized using this technique. The preferential vaporization of the matrix solvent makes possible the deposition of the delicate biomaterials which otherwise is not possible by the conventional LIFT process (Pique et al., 2002; Wu et al., 2001; Ringeisen et al., 2002). However, an inherent disadvantage of the MAPLE-DW is that the donor material has to be used in a particulate form so that an ink, fluid or paste of it with the volatile matrix solvent can be deposited onto the carrier before printing. This limits the choice of materials to only those that can be obtained in powder or particulate form which obviously is not suitable when printing of solid donor materials is desired. In addition, evaporation of the matrix solvent leaves high porosity in the printed materials/devices resulting in a significant difference in the properties of the transferred materials with respect to the original source film (Pique et al., 1999b).

2.2.2 Dynamic Release Layer (DRL)-LIFT

In the DRL-LIFT technique, also known as absorbing film assisted (AFA)-LIFT (Hopp et al., 2004, 2005b), a sacrificial layer referred to as DRL is sandwiched between the

carrier and the donor. This sacrificial layer absorbs the incident laser energy and ablates/evaporates thereby providing the thrust required for transferring the donor to the receiver as shown in fig. 2.5.

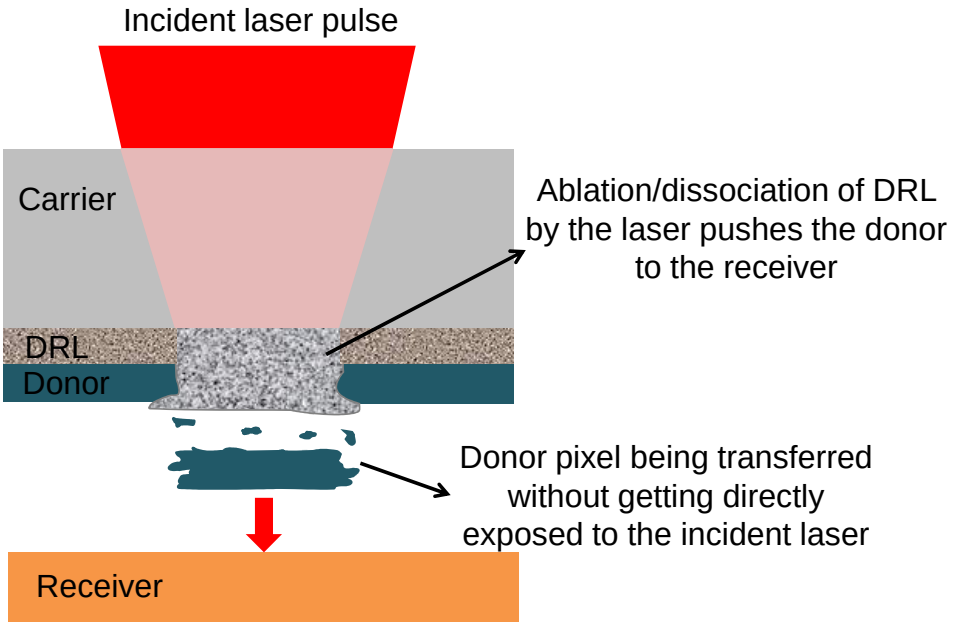

FIGURE 2.5: Illustration of the DRL-LIFT technique.

The DRL technique helps to transfer materials without directly exposing them to the incident laser energy thereby printing them without damage. It can also be used for materials having weak absorption at the incident laser wavelength without the need of producing them in a powder form as in the case of MAPLE-DW. The use of Al as an absorbing layer for producing high-resolution colour images demonstrated the first implementation of DRL-LIFT in 1993 by Tolbert et al. (Tolbert et al., 1993a,b). Most commonly thin metal and metal oxide layers are used as DRLs (Barron et al., 2004a; Hopp et al., 2004; Serra et al., 2004a). Functional DNA and bio-molecule microarrays have been realized using liquid targets with Ti metal and titanium oxide (TiO_2) as the sacrificial layer materials respectively (Barron et al., 2004a; Serra et al., 2004a; Colina et al., 2006; Fernandez-Pradas et al., 2004). Living fungi have also been transferred using silver as a DRL (Hopp et al., 2004).

However, contamination of the deposits with metallic residual DRL post-transfer is a matter of concern with the DRL-LIFT technique as was reported by Smausz et al. using

Ag as DRL (Smausz et al., 2006). A specially designed nitrogen (N_2) releasing UV-absorbing TP has shown great potential as a DRL material in the past few years (Nagel et al., 2007; Lippert and Dickinson, 2003). The TP decomposes upon irradiation to release N_2 gas and other gaseous molecular fragments (Nagel et al., 2007) which provide the push required for forward transfer. Mammalian cells (Doraiswamy et al., 2006), quantum dot emitters (Xu et al., 2007), organic light-emitting diode () pixels (Fardel et al., 2007a)and ceramic materials (Banks et al., 2008b) have been deposited using the triazene-assisted LIFT technique. Due to its decomposition into gaseous fragments the TP shows very little or no contamination of the transferred deposits (Fardel et al., 2007a; Banks et al., 2008b). However the TP decomposes at $\sim$ 250 ^{0}C (Lippert and Dickinson, 2003) so it is not compatible with donor deposition processes that involve high temperatures e.g. thermal evaporation (Banks et al., 2008b). The TP is also sensitive to solvents such as chloroform, chlorobenzene and toluene. This heat and solvent chemical sensitivity of the TP puts a limit on the range of donor materials that can be deposited using TP as a DRL. Thick layer of polymers used as radiation absorbers for the DRL-LIFT technique have also been proposed for contamination-free printing of delicate biological materials that are highly sensitive to thermal and mechanical shocks. Living mammalian embryonic stem cells have been transferred using a thick polyimide ($\sim$ 4 μm) layer as DRL by Arnold et al. (Arnold et al., 2007a).

2.2.3 Hydrogen assisted LIFT

In this technique, developed by Toet et al., the donor film consists of a hydrogenated amorphous silicon (a:Si:H) thin layer (Toet et al., 1999) (fig. 2.6 (a)). The mechanism for transfer involves melting of the a:Si:H layer at the interface by the incident laser pulse which leads to an explosive effusion of hydrogen thereby providing the required thrust for transfer. The Si film melts and breaks down into droplets during ejection (fig. 2.6 (b)) and condenses on the receiver substrate as polycrystalline silicon (poly-Si) (fig. 2.6 (c)). Other materials such as Al have also been transferred using this technique employing the a:Si:H as the propellant layer (Toet et al., 2000a,b). However only hydrogen gets ejected by the incident laser pulse and the rest of the film melts completely leading to contamination of the resultant deposit with poly-Si.

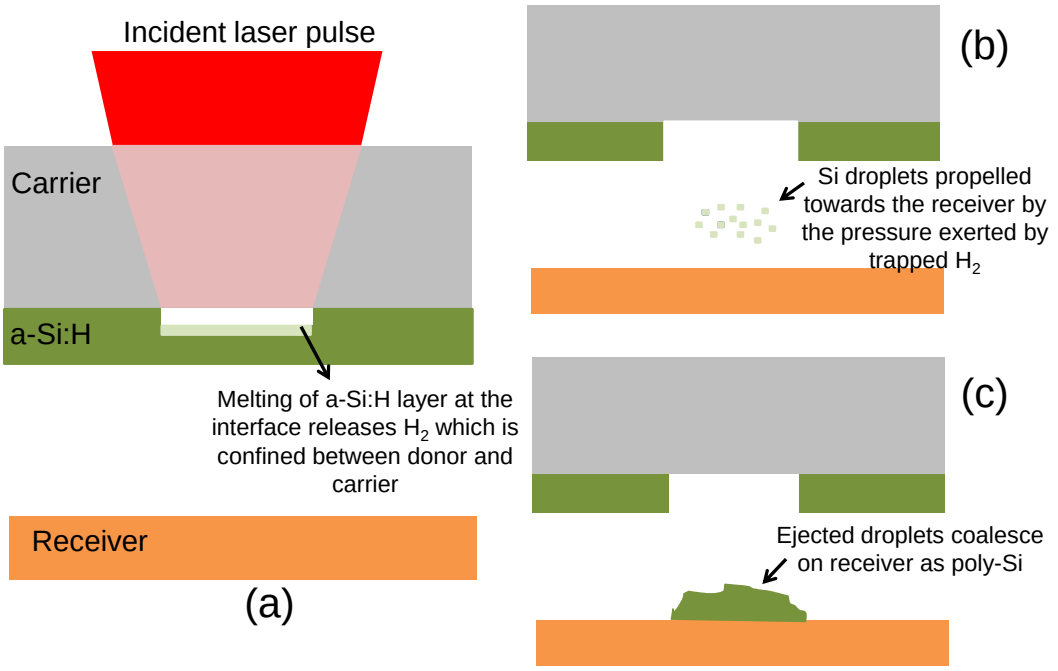

FIGURE 2.6: Illustration of the hydrogen assisted LIFT technique.

2.2.4 Laser-Induced Thermal Imaging (LITI)

In LITI an additional layer is introduced between the carrier and the donor (Blanchet et al., 2003; Lee and Lee, 2004) that absorbs the energy of the incident laser pulse (fig. 2.7 (a)), gets heated up and evaporates the surrounding organics at the interface. The expansion of the gaseous decomposition products provides the push necessary to propel the donor onto the receiver (fig. 2.7 (b)) (Blanchet et al., 2003). The additional layer between the carrier and the donor is referred to as a light-to-heat conversion (LTHC) layer in the literature. The LITI technique is usually used for transferring organic materials such as conducting light emitting polymers (Lee and Lee, 2004) and a thin metal film is generally used as the LTHC layer. The pixelated transfer is achieved by splitting a continuous wave (CW) laser diode into individually addressable laser spots. The use of metallic nanoparticles as the LTHC layer has also been reported for transferring OLEDS with the technique termed as nanoparticle enabled laser transfer (NELT) (Ko et al., 2008).

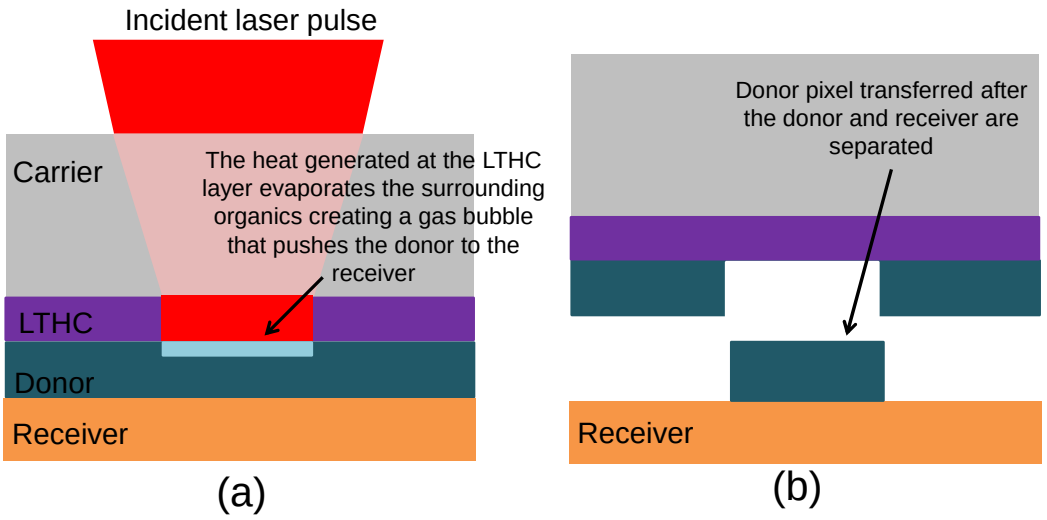

FIGURE 2.7: Illustration of the LITI technique.

2.2.5 Ballistic Laser-Assisted Solid Transfer (BLAST)

Another complementary LIFT technique called BLAST was reported recently mainly for transferring materials in intact and solid phase (Banks et al., 2008a). The principle of BLAST relies on using multiple spatially-shaped pulses with fluence well below the transfer threshold (Banks, 2008). The basic idea of BLAST is to delaminate the donor film over the irradiated region first by weakening the carrier–donor adhesion with the initial sub-threshold pulses (fig. 2.8 (a)) and then to achieve the transfer gently with the subsequent pulses as shown in fig. 2.8 (b). The spatial shaping of pulses in the BLAST work reported was achieved using the Fresnel (near-field) diffraction pattern of a circular aperture (Banks et al., 2008a). The BLAST technique does offer advantages in terms of having the transfers achieved without the need for a DRL material and thus widening the range of materials that can be transferred. Also the use of sub-threshold pulses reduces the damage to the donor as compared to the conventional LIFT technique and makes the transfer process relatively gentler as the donor is delaminated prior to LIFT. However, the exposure of the whole donor region to be deposited to the multiple pulses lead to significant damage especially in the centre of the printed pellets and a better pulse-to-pulse control is required to prevent this damage.

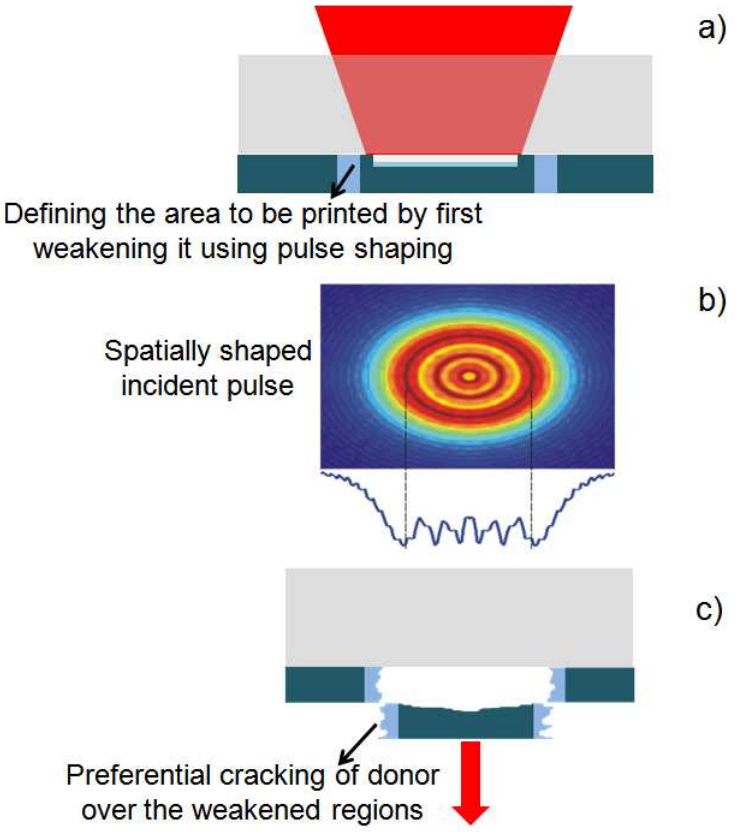

FIGURE 2.8: Illustration of the BLAST technique [Banks2008].

2.2.6 Laser Molecular Implantation (LMI)

The LMI technique also known as Laser Induced Molecular Implantation technique (LIMIT) is a laser based method for doping polymer films by implanting functional molecules from a doped polymer film (known as the source film) to an undoped polymer film (known as the target film) (Fukumura et al., 1994; Okada et al., 1998; Goto et al., 1999). The source and the target film are placed in tight contact with each other and irradiated with a laser pulse at the interface of source and target film (fig. 2.9). The suggested transfer mechanism involves absorption of many photons by one dopant molecule in the polymer matrix that heats up the surrounding polymer network, and gets ejected with a high kinetic energy from the expanded doped polymer network into the undoped polymer (fig. 2.9). The laser intensity is not enough to decompose the polymer or the dopant molecules so this process does not involve either polymer ablation or transfer and only the dopant molecules are transferred from one polymer host/source film to the target film. The transfer of dopant molecules has been reported both in forward

(Karnakis et al., 1998a) and backward directions (Fukumura et al., 1996) implying that the source and target films are interchangeable. The LMI technique is different from LIFT is the sense that no ablation-driven transfer of donor films occur but it involves the implantation of dopant molecules by a thermally activated diffusion process. It has been successfully employed for spatially-selective doping of polymer films with fluorescent dye molecules (Fukumura et al., 1996), zinc tetraphenyl porphine (ZnTPP) (Goto et al., 2004) and dicyanoanthracene DCNA (Goto et al., 2000).

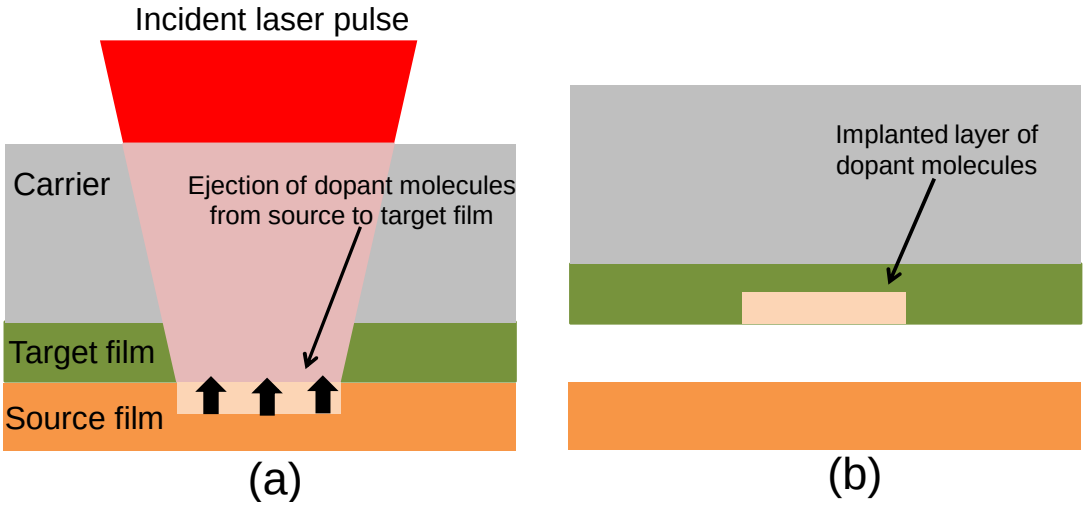

FIGURE 2.9: Illustration of the LMI technique.

2.2.7 Laser Induced Solid Etching (LISE)

The LISE technique, although it doesn't fit exactly into the category of complementary LIFT techniques, is being mentioned here as it uses the same set-up as the conventional LIFT method and has recently reported etching of solid brittle materials (Banks et al., 2009b). In principle, a thin shock generation layer (SGL) is sandwiched between the transparent carrier and the brittle solid material to be etched using the LISE technique as shown in the schematic in fig. 2.10. The SGL and the brittle solid material are placed in tight contact with each other (fig. (2.10 (a))). A huge pressure is generated in the SGL by the incident fs pulses which in turn generate shockwaves (fig. 2.10 (c)). Multiple cracks can be generated in the substrate by controlling the spatial profile of the incident laser pulse (fig. 2.10 (d)). These shockwaves then travel through the underlying solid layer thereby cracking and etching it (fig. 2.10 (e,f)). The etched material can then be

transferred on a nearby receiver substrate and the solid state of the material is preserved throughout the transfer process. In the initial LISE experiments a thin Cr film ($\sim$ 80 nm) was used as the SGL and the transparent quartz carrier and/or the Si receiver were etched (Banks et al., 2009b). Although the initial results of LISE are promising this technique is still at an early stage of development and requires further investigations to entirely understand the phenomena and the effect of experimental parameters on it.

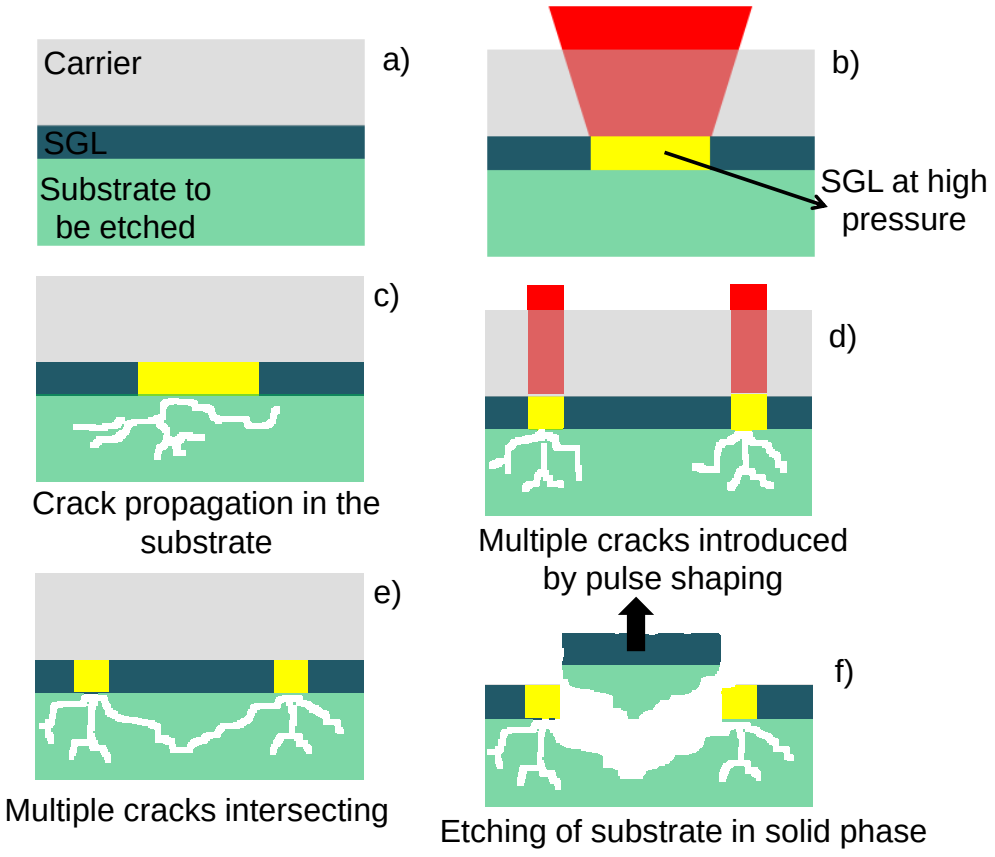

FIGURE 2.10: Illustration of the LISE technique [Banks2009a].

2.3 Summary of the significant works

In this section significant works representing the state of the art of LIFT and its complementary techniques is presented in a chronological order and in tabular form:

TABLE 2.1: Overview of laser-induced forward transfer work

Technique	Transferred material	Sacrificial layer	Feature size (μm)	Laser type (λ(nm))	Reference
LIFT	Cu	-	50-70	ArF (193)	(Bohandy et al., 1986)
LIFT	Cu, Ag	-	15-50	2ω-Nd:YAG (532)	(Bohandy et al., 1988)
LIFT	YBaCuO and BiSrCaCuO	-	100	Nd:YAG (1064)	(Fogarassy et al., 1989b,a)
LIFT	V,Cr,Ti,Ge,Sn	-	100	Ruby (694), XeCl (308)	(Mogyorosi et al., 1989)
LIFT	Ti, Cr, Ge/Se	-	10	Ruby (694), Ar^{+}(514)	(Toth et al., 1990)
LIFT	Al	-	200	Nd:YAG (1064)	(Schultze and Wagner, 1991)
DRL-LIFT	PMMA/colored dyes	Al		Nd:YAG (1064)	(Tolbert et al., 1993a)
LIFT	W	-	5-10	Nd:YAG (1064)	(Kantor et al., 1994, 1995)
LIFT	Au, Al	-	7-10	ArF (193)	(Latsch et al., 1994)
LIFT	Pd	-	150	ArF (193), KrCl (222), KrF (248), XeCl (308), XeF (351)	(Esrom et al., 1995; Zhang et al., 1998)
LIFT	Diamond	-	10	KrF (248), Cu (510)	(Pimenov et al., 1995)
LIFT	Cu, Ag	-	15-20	2ω-Nd:YAG (532)	(Tatah and Fukumoto, 1995)

Overview of laser-induced forward transfer work-continued

Technique	Transferred material	Sacrificial layer	Feature size (μm)	Laser type (λ(nm))	Reference
LMI	diphenyl anthracene doped PMMA, pyrene doped PMMA	-	200	KrF (248) , 3ω-Nd:YAG (351)	(Fukumura et al., 1998; Karnakis et al., 1998b,a; Fukumura et al., 1996)
LIFT	Al	-		Ti:sapph (1053)	(Bullock et al., 1997; Bullock and Bolton, 1999)
LMI	Zinc tetraphenyl porphyrin (ZnTPP)	-	2-100	KrF (248)	(Goto et al., 1999, 2004)
LIFT	Cr, In_2O_3, Pt	-	0.7-5	KrF (248)	(Zergioti et al., 1998; Mailis et al., 1999; Papakonstantinou et al., 1999; Koundourakis et al., 2001)
LIFT	Au	-		dye laser (440), Nd:YAG (532), KrF (248)	(Baseman et al., 1990)(Nakata and Okada, 1999)
MAPLE-DW	Ab, Au, NiCr, $BaTiO_3$, $SrTiO_3$, Y_3FeO_{12}	PBMA	20-25	KrF (248)	(Pique et al., 1999a, 2000)
a-Si:H	Si, Al	H_2	5-10	XeCl (308)	(Toet et al., 1999, 2000a,b)

Technique	Transferred material	Sacrificial layer	Feature size (μm)	Laser type (λ(nm))	Reference
LMI	pyrene	TP	200	3ω-Nd:YAG (355)	(Karnakis et al., 1998b)
LIFT	Au/Sn	-	30	Ti:sapph (775)	(Bahnisch et al., 2000)
LIMIT	Dicyanoanthracene, Coumarin (C6,C545), Zinc tetraphenyl porphyrin (ZnTPP)	-	1-40	Nd:YAG (355), dye laser (440)	(Goto et al., 2000), (Pihosh et al., 2005)(Kishimoto et al., 2001)
MAPLE-DW	Phosphor powders of Y_2O_3:Eu and Zn_2SiO_4:Mn	glycerin, isopropanol, $LaNO_2$, and $Mg_2(NO_3)_2$	100	KrF (248)	(Fitz-Gerald et al., 2000)
MAPLE-DW	PTF resistors, lead magnesium niobate (PMN) based inks IP9331.5 and IP9333	Epoxy resin, Glass frit binder	10-50	3ω-Nd:YAG (355)	(Modi et al., 2001), (Modi et al., 2002)
MAPLE-DW	PEG, Eukaryotic cells	Volatile solvent	10	ArF (193)	(Wu et al., 2001, 2003)
DRL-LIFT	pyrene doped PMMA	Triazeno polymer		KrF (248)	(Mito et al., 2001)

Overview of laser-induced forward transfer work-continued

Overview of laser-induced forward transfer work-continued

Technique	Transferred material	Sacrificial layer	Feature size (μm)	Laser type (λ(nm))	Reference
LIFT	Al	-	0.8-2	Nd:glass (1.06)	(Tien et al., 2001)
LIFT	Ni	-	200	KrF (248)	(Yamada et al., 2002, 2003)
MAPLE-DW	E-coli, Biotinylated bovine serum albumin (BSA), anti- BSA	Luria–Bertani (LB) broth, 40 vol % glycerol/60 vol % phosphate buffer solution (PBS)	50-100	ArF (193)	(Ringeisen et al., 2002) (Ringeisen et al., 2004)
LIFT	In_2O_3	-	200 x 300	dye laser/KrF (248)	(Papazoglou et al., 2002a,b)
LIFT/DRL-LIFT	Rhodamine 610 laser dye, TiO_2	Au	300	2ω-Nd:YAG (532)	(Nakata et al., 2002a,b)
LIFT	Au, Ni	-	150	KrF (248)	(Sano et al., 2002)
MAPLE-DW	RuO_2. 0.5 H_2O	ethylene glycol, glycerol/ sulfuric acid		3ω-Nd:YAG (355)	(Arnold et al., 2002b, 2003)

Technique	Transferred material	Sacrificial layer	Feature size (μm)	Laser type (λ(nm))	Reference
MAPLE-DW	Ag, MnO_2, Ag_2O, PECH/graphite, $LiCoO_2$, $LiMn_2O_4$	KOH and glycerol, propylene carbonate or dibasic ester and PVDF-HFP		Nd:YAG (355)	(Pique et al., 2003b,a, 2004)
LIFT	Cr	-	200 x 300	dye/KrF, KrF (248)	(Zergioti et al., 2003a,b)
LIFT	Au	-	2.5-3.3	Ti:sapph (400)	(Tan et al., 2003)
LITI	DNSS-PANI, SWNT	-	2.7-5	Infrared diode laser (780, CW)	(Blanchet et al., 2003)
LIFT	Lambda phage DNA	-	100	dye laser/KrF (248)	(Karaiskou et al., 2003)
LIFT	Sn	-	200	KrF (248)	(Komorita et al., 2003)
LIFT	Au	-	2-15	Ti:sapph (800)	(Germain and Tsui, 2003)
LIFT	Au, Al, Ni, Fe	-	2-6	KrF (248)	(Landstrom et al., 2004)
MAPLE-DW	C, $LiCoO_2$	binder	40-60	3ω-Nd:YAG (355)	(Wartena et al., 2004)(Arnold et al., 2004)
LIFT	TiO_2 nano-powder	-	250	3ω-Nd:YVO_4	(Kim et al., 2004a,b)

Overview of laser-induced forward transfer work-continued

Overview of laser-induced forward transfer work-continued

Technique	Transferred material	Sacrificial layer	Feature size (μm)	Laser type (λ(nm))	Reference
MAPLE-DW, DRL-LIFT	Mammalian cells	Glycerol/ DMEM, Ti	80-100	ArF (193), 4ω-Nd:YAG (266)	(Barron et al., 2004a,b, 2005)
DRL-LIFT	fungus (trichoderma conidia)	AgKrF (248)	800	KrF (248)	(Hopp et al., 2004, 2005a)
LITI	Light emitting and inert polymers	-	50	Nd:YAG (CW)	(Lee and Lee, 2004; Lee et al., 2004)
DRL-LIFT	DNA, proteins	Ti	40-80	Nd:YAG (355)	(Serra et al., 2004a,b)
DRL-LIFT	DNA, water and glycerol	Ti	30-100	3ω-Nd:YAG (355)	(Fernandez-Pradas et al., 2004; Colina et al., 2006, 2005)
LIFT	Al, Ni	-	1-3	Nd:YAG (1064)	(Willis and Grosu, 2004, 2005)
LIFT	lambda bacteriophage DNA, bovine serum albumin and glutathione S–Transferase, horseradish peroxidase enzyme	-	50	KrF (248)	(Zergioti et al., 2005a,b)

Technique	Transferred material	Sacrificial layer	Feature size (μm)	Laser type (λ(nm))	Reference
DRL-LIFT	Mammalian cells	TP		ArF (193)	(Doraiswamy et al., 2006)
LIFT	Cu	-	2-3	Ti:sapph (775)	(Li et al., 2006)
LIFT	Cr	-	0.3	Ti:sapph (800)	(Banks et al., 2006)
LIFT	Al	-	5	Ti:sapph (785)	(Bera et al., 2007)
LIFT	V_2O_5	-	290	2ω-Nd:YAG (532)	(Wakaki et al., 2007)
LIFT	Au	-	3	Ti:sapph (800)	(Germain et al., 2007)
DRL-LIFT	Quantum dot emitters	TP	800	ArF (193)	(Xu et al., 2007)
DRL-LIFT	embryonic stem cells	polyimide	5-20	3ω- Nd:YVO_4 (355)	(Arnold et al., 2007a,b)
LIFT	Cr	-		4ω-Nd:YAG (266)	(Le Drogoff et al., 2006)
LIFT	Luciferase enzyme	-	100-300	Nd:YAG (355, 266)	(Tsuboi et al., 2007)
LIFT	PEDOT-PSS (poly(3,4-ethylenedioxythiophene)-poly(styrenesulfonate))	-	100-250	KrF(248), Nd:YAG (532,1064), Yb:YKW (1025)	(Alloncle et al., 2007)

Overview of laser-induced forward transfer work-continued

Overview of laser-induced forward transfer work-continued

Technique	Transferred material	Sacrificial layer	Feature size (μm)	Laser type (λ(nm))	Reference
DRL-LIFT	peptides	Au	20-150	KrF (248)	(Dinca et al., 2007, 2008)
DRL-LIFT	OLEDs	TP	500	XeCl (308)	(Fardel et al., 2007a,b)
BLAST	Cr	-	10-12	Ti:sapph (800)	(Banks et al., 2008a)
LIFT	ZnO, TiO_2	-	5-30	dye laser (248), Ti:sapph (800)	(Klini et al., 2007; Loukakos et al., 2010)
NELT	OLEDs	Ag NPs	3-900	Nd:YAG (532)	(Ko et al., 2008, 2010)
LIFT	$FeSi_2$	-	0.5	KrF (248)	(Narazaki et al., 2008, 2009)
DRL-LIFT	GGG	TP	10-12	Ti:sapph (800)	(Banks et al., 2008b, 2009a)
LIFT	silver nanoparticle ink, CuPc	-	500	3ω-Nd:YAG (355)	(Rapp et al., 2008, 2009, 2011a,b)
LIBT	Au	-	220	Ti:sapph (800)	(Kuznetsov et al., 2009a,b)
LISE	Si, Silica	Cr	10-12	Ti:sapph (800)	(Banks et al., 2009b)
DRL-LIFT	GGG, YAG	TP	500	XeCl (308)	(Kaur et al., 2009)
LIFT	-	Ti	10-12	Ti:sapph (800)	(Mailis et al., 2010)
LIFT	PHEMA, P4VP, PVP, PMMA	-	20-250	Nd:YAG (266)	(Tsouti et al., 2010)

Technique	Transferred material	Sacrificial layer	Feature size (μm)	Laser type (λ(nm))	Reference
LIFT	SiO_x	-	5	KrF (248)	(Ihlemann and Weichenhain-Schriever, 2010)
LIFT	PAA/CNT, PVP/CNT	-	70	Nd:YAG (266)	(Boutopoulos et al., 2010)
DRL-LIFT	HT-29 cells	cyanoacrylate /brass foil		ArF (193)	(Huang et al., 2011)
DRL-LIFT	PS-μbeads, Liposome/water/glycerol	TP	40-200	XeCl (308), ArF (193)	(Palla-Papavlu et al., 2010a,b, 2011)
DRL-LIFT	MEH-PPV	TP	600	XeCl (308)	(Lippert et al., 2011)
DRL-LIFT	Poly- 3-hexylthiophene (P3HT)	Ti	60-130	Nd:YAG (266)	(Zergioti et al., 2011)
LIFT	Immunoglobulin G (IgG)/PBS, water/glycerol	-	20	Nd:YAG (532), Yb:YKW (1027)	(Patrascioiu et al., 2011)(Dinca et al., 2010)

Overview of laser-induced forward transfer work-continued

Bibliography

F. J. Adrian, J. Bohandy, B. F. Kim, A. N. Jette, and P. Thompson. "A Study of the Mechanism of Metal-Deposition by the Laser-Induced Forward Transfer Process". *Journal of Vacuum Science & Technology B*, **5**:1490, 1987.

A. P. Alloncle, B. Thomas, P. Delaporte, M. Sentis, S. Sanaur, M. Barret, and P. Collot. "Experimental investigations of laser-induced forward transfer process of organic thin films". *Applied Surface Science*, **254**:1206, 2007.

C. B. Arnold, R. C. Wartena, B. Pratap, K. E. Swider-Lyons, and A. Pique. "Direct writing of planar ultracapacitors by laser forward transfer processing". *Photon Processing in Microelectronics and Photonics*, **4637**:353, 2002a.

C. B. Arnold, R. C. Wartena, B. Pratap, K. E. Swider-Lyons, and A. Pique. "Laser direct writing of hydrous ruthenium dioxide micro-pseudocapacitors". *Electroactive Polymers and Rapid Prototyping*, **698**:275, 2002b.

C. B. Arnold, R. C. Wartena, K. E. Swider-Lyons, and A. Piquea. "Direct-write planar microultracapacitors by laser engineering". *Journal of the Electrochemical Society*, **150**:A571, 2003.

C. B. Arnold, H. Kim, and A. Pique. "Laser direct write of planar alkaline microbatteries". *Applied Physics a-Materials Science & Processing*, **79**:417, 2004.

C. B. Arnold, N. T. Kattamis, P. E. Purnick, and R. Weiss. "Thick film laser induced forward transfer for deposition of thermally and mechanically sensitive materials". *Applied Physics Letters*, **91**:171120, 2007a.

C. B. Arnold, P. Serra, and A. Pique. "Laser direct-write techniques for printing of complex materials". *MRS Bulletin*, **32**:23, 2007b.

R. Bahnisch, W. Gross, and A. Menschig. "Single-shot, high repetition rate metallic pattern transfer". *Microelectronic Engineering*, **50**:541, 2000.

D. P. Banks, C. Grivas, J. D. Mills, R. W. Eason, and I. Zergioti. "Nanodroplets deposited in microarrays by femtosecond Ti : sapphire laser-induced forward transfer". *Applied Physics Letters*, **89**:193107, 2006.

D. P. Banks, C. Grivas, I. Zergioti, and R. W. Eason. "Ballistic laser-assisted solid transfer (BLAST) from a thin film precursor". *Optics Express*, **16**:3249, 2008a.

D. P. Banks, K. Kaur, R. Gazia, R. Fardel, M. Nagel, T. Lippert, and R. W. Eason. "Triazene photopolymer dynamic release layer-assisted femtosecond laser-induced forward transfer with an active carrier substrate". *Europeon Physics Letters*, **83**:38003, 2008b.

D. P. Banks, K. Kaur, and R. W. Eason. "Influence of optical standing waves on the femtosecond laser-induced forward transfer of transparent thin films". *Applied Optics*, **48**:2058, 2009a.

D. P. Banks, K. S. Kaur, and R. W. Eason. "Etching and forward transfer of fused silica in solid-phase by femtosecond laser-induced solid etching (LISE)". *Applied Surface Science*, **255**:8343, 2009b.

J. A. Barron, B. R. Ringeisen, H. S. Kim, B. J. Spargo, and D. B. Chrisey. "Application of laser printing to mammalian cells". *Thin Solid Films*, **453**:383, 2004a.

J. A. Barron, B. J. Spargo, and B. R. Ringeisen. "Biological laser printing of three dimensional cellular structures". *Applied Physics a-Materials Science & Processing*, **79**:1027, 2004b.

J. A. Barron, D. B. Krizman, and B. R. Ringeisen. "Laser printing of single cells: Statistical analysis, cell viability, and stress". *Annals of Biomedical Engineering*, **33**: 121, 2005.

R. J. Baseman, N. M. Froberg, J. C. Andreshak, and Z. Schlesinger. "Minimum Fluence for Laser Blow-Off of Thin Gold-Films at 248 nm and 532 nm". *Applied Physics Letters*, **56**:1412, 1990.

S. Bera, A. J. Sabbah, J. M. Yarbrough, C. G. Allen, B. Winters, C. G. Durfee, and J. A. Squier. "Optimization study of the femtosecond laser-induced forward-transfer process with thin aluminum films". *Applied Optics*, **46**:4650, 2007.

G. B. Blanchet, Y. L. Loo, J. A. Rogers, F. Gao, and C. R. Fincher. "Large area, high resolution, dry printing of conducting polymers for organic electronics". *Applied Physics Letters*, **82**:463, 2003.

J. Bohandy, B. F. Kim, and F. J. Adrian. "Metal-Deposition from a Supported Metal-Film Using an Excimer Laser". *Journal of Applied Physics*, **60**:1538, 1986.

J. Bohandy, B. F. Kim, F. J. Adrian, and A. N. Jette. "Metal-Deposition at 532-nm Using a Laser Transfer Technique". *Journal of Applied Physics*, **63**:1158, 1988.

C. Boutopoulos, C. Pandis, K. Giannakopoulos, P. Pissis, and I. Zergioti. "Polymer/carbon nanotube composite patterns via laser induced forward transfer". *Applied Physics Letters*, **96**:041104, 2010.

A. B. Bullock and P. R. Bolton. "Laser-induced back ablation of aluminum thin films using picosecond laser pulses". *Journal of Applied Physics*, **85**:460, 1999.

A. B. Bullock, P. R. Bolton, and F. J. Mayer. "Time-integrated reflectivity of laser-induced back-ablated aluminum thin film targets". *Journal of Applied Physics*, **82**: 1828, 1997.

S. K. Chang-Jian, J. R. Ho, J. W. J. Cheng, and C. K. Sung. "Fabrication of carbon nanotube field emission cathodes in patterns by a laser transfer method". *Nanotechnology*, **17**:1184, 2006.

M. Colina, P. Serra, J. M. Fernandez-Pradas, L. Sevilla, and J. L. Morenza. "DNA deposition through laser induced forward transfer". *Biosensors & Bioelectronics*, **20**: 1638, 2005.

M. Colina, M. Duocastella, J. M. Fernandez-Pradas, P. Serra, and J. L. Morenza. "Laser-induced forward transfer of liquids: Study of the droplet ejection process". *Journal of Applied Physics*, **99**:084909, 2006.

F. Dausinger. "Femtosecond technology for precision manufacturing: Fundamental and technical aspects". *Third International Symposium on Laser Precision Microfabrication*, **4830**:471, 2003.

F. Dausinger, F. Lichtner, and H. Lubatschowki. *"Femtosecond Technology for Technical and Medical applications"*. Springer, New York, USA, 2004.

V. Dinca, E. Kasotakis, J. Catherine, A. Mourka, A. Mitraki, A. Popescu, M. Dinescu, M. Farsari, and C. Fotakis. "Development of peptide-based patterns by laser transfer". *Applied Surface Science*, **254**:1160, 2007.

V. Dinca, M. Farsari, D. Kafetzopoulos, A. Popescu, M. Dinescu, and C. Fotakis. Patterning parameters for biomolecules microarrays constructed with nanosecond and femtosecond UV lasers". *Thin Solid Films*, **516**:6504, 2008.

V. Dinca, A. Palla-Papavlu, M. Dinescu, J. S. Stewart, T. K. Lippert, F. Di Pietrantonio, D. Cannata, M. Benetti, and E. Verona. "Polymer pixel enhancement by laser-induced forward transfer for sensor applications". *Applied Physics a-Materials Science & Processing*, **101**:559, 2010.

A. Doraiswamy, R. J. Narayan, T. Lippert, L. Urech, A. Wokaun, M. Nagel, B. Hopp, M. Dinescu, R. Modi, R. C. Y. Auyeung, and D. B. Chrisey. "Excimer laser forward transfer of mammalian cells using a novel triazene absorbing layer". *Applied Surface Science*, **252**:4743, 2006.

H. E. Elsayedali, T. B. Norris, M. A. Pessot, and G. A. Mourou. "Time-Resolved Observation of Electron-Phonon Relaxation in Copper". *Physical Review Letters*, **58**: 1212, 1987.

H. Esrom, J. Y. Zhang, U. Kogelschatz, and A. J. Pedraza. "New Approach of a Laser-Induced Forward Transfer for Deposition of Patterned Thin Metal-Films". *Applied Surface Science*, **86**:202, 1995.

R. Fardel, M. Nagel, F. Nuesch, T. Lippert, and A. Wokaun. "Fabrication of organic light-emitting diode pixels by laser-assisted forward transfer". *Applied Physics Letters*, **91**:061103, 2007a.

R. Fardel, M. Nagel, F. Nusch, T. Lippert, and A. Wokaun. "Laser forward transfer using a sacrificial layer: Influence of the material properties". *Applied Surface Science*, **254**: 1322, 2007b.

J. M. Fernandez-Pradas, M. Colina, P. Serra, J. Dominguez, and J. L. Morenza. "Laser-induced forward transfer of biomolecules". *Thin Solid Films*, **453**:27, 2004.

J. M. Fitz-Gerald, A. Pique, D. B. Chrisey, P. D. Rack, M. Zeleznik, R. C. Y. Auyeung, and S. Lakeou. "Laser direct writing of phosphor screens for high-definition displays". *Applied Physics Letters*, **76**:1386, 2000.

E. Fogarassy, C. Fuchs, F. Kerherve, G. Hauchecorne, and J. Perriere. "Laser-Induced Forward Transfer - a New Approach for the Deposition of High-Tc Superconducting Thin-Films". *Journal of Materials Research*, **4**:1082, 1989a.

E. Fogarassy, C. Fuchs, F. Kerherve, G. Hauchecorne, and J. Perriere. "Laser-Induced Forward Transfer of High-Tc YbaCuO and BiSrCaCuO Superconducting Thin-Films". *Journal of Applied Physics*, **66**:457, 1989b.

H. Fukumura, Y. Kohji, K. Nagasawa, and H. Masuhara. "Laser Implantation of Pyrene Molecules into Poly(Methyl Methacrylate) Films". *Journal of the American Chemical Society*, **116**:10304, 1994.

H. Fukumura, Y. Kohji, and H. Masuhara. "Laser implantation of fluorescent molecules into polymer films". *Applied Surface Science*, **96-8**:569, 1996.

H. Fukumura, H. Uji-i, H. Banjo, H. Masuhara, D. M. Karnakis, N. Ichinose, S. Kawanishi, K. Uchida, and M. Irie. "Laser implantation of photochromic molecules into polymer films: a new approach towards molecular device fabrication". *Applied Surface Science*, **127**:761, 1998.

E. G. Gamaly, A. V. Rode, B. Luther-Davies, and V. T. Tikhonchuk. "Ablation of solids by femtosecond lasers: Ablation mechanism and ablation thresholds for metals and dielectrics". *Physics of Plasmas*, **9**:949, 2002a.

E. G. Gamaly, A. V. Rode, V. T. Tikhonchuk, and B. Luther-Davies. "Electrostatic mechanism of ablation by femtosecond lasers". *Applied Surface Science*, **197**:699, 2002b.

C. Germain and Y. Y. Tsui. "Femtosecond laser induced forward transfer of materials". *International Conference on Mems, Nano and Smart Systems, Proceedings*, page 44, 2003.

C. Germain, L. Charron, L. Lilge, and Y. Y. Tsui. "Electrodes for microfluidic devices produced by laser induced forward transfer". *Applied Surface Science*, **253**:8328, 2007.

M. Goto, N. Ichinose, S. Kawanishi, and H. Fukumura. "Implantation of organic molecules into biotissue by pulsed laser irradiation". *Japanese Journal of Applied Physics Part 2-Letters*, **38**:L87, 1999.

M. Goto, S. Kawanishi, and H. Fukumura. "Laser implantation of dicyanoanthracene in poly(methyl methacrylate) from a 100-nm aperture micropipette". *Applied Surface Science*, **154**:701, 2000.

M. Goto, J. Hobley, T. Oishi, A. Kasahara, M. Tosa, K. Yoshihara, M. Kishimoto, and H. Fukumura. "Micro-patterning of multiple organic molecules by laser implantation". *Applied Physics a-Materials Science & Processing*, **79**:157, 2004.

B. Hopp, T. Smausz, Z. Antal, N. Kresz, Z. Bor, and D. Chrisey. "Absorbing film assisted laser induced forward transfer of fungi (Trichoderma conidia)". *Journal of Applied Physics*, **96**:3478, 2004.

B. Hopp, T. Smausz, N. Barna, C. Vass, Z. Antal, L. Kredics, and D. Chrisey. "Time-resolved study of absorbing film assisted laser induced forward transfer of Trichoderma longibrachiatum conidia". *Journal of Physics D-Applied Physics*, **38**:833, 2005a.

B. Hopp, T. Smausz, N. Kresz, N. Barna, Z. Bor, L. Kolozsvari, D. B. Chrisey, A. Szabo, and A. Nogradi. "Survival and proliferative ability of various living cell types after laser-induced forward transfer". *Tissue Engineering*, **11**:1817, 2005b.

Y. Huang, Y. F. Lin, and D. B. Chrisey. "Metallic Foil-Assisted Laser Cell Printing". *Journal of Biomechanical Engineering-Transactions of the Asme*, **133**, 2011.

J. Ihlemann and R. Weichenhain-Schriever. "Laser-induced congruent forward transfer of SiO_x-layers". *Applied Physics a-Materials Science & Processing*, **101**:483, 2010.

Z. Kantor, Z. Toth, and T. Szorenyi. "Deposition of micrometer-sized tungsten patterns by laser transfer technique ". *Applied Physics Letters*, **64**:3506, 1994.

Z. Kantor, Z. Toth, and T. Szorenyi. "Metal Pattern Deposition by Laser-Induced Forward Transfer". *Applied Surface Science*, **86**:196, 1995.

A. Karaiskou, I. Zergioti, C. Fotakis, M. Kapsetaki, and D. Kafetzopoulos. "Microfabrication of biomaterials by the sub-ps laser-induced forward transfer process". *Applied Surface Science*, **208**:245, 2003.

D. M. Karnakis, M. Goto, N. Ichinose, S. Kawanishi, and H. Fukumura. "Forward-transfer laser implantation of pyrene molecules in a solid polymer". *Applied Physics Letters*, **73**:1439, 1998a.

D. M. Karnakis, T. Lippert, N. Ichinose, S. Kawanishi, and H. Fukumura. "Laser induced molecular transfer using ablation of a triazeno-polymer". *Applied Surface Science*, **127**: 781, 1998b.

K. S. Kaur, R. Fardel, T. C. May-Smith, M. Nagel, D. P. Banks, C. Grivas, T. Lippert, and R. W. Eason. "Shadowgraphic studies of triazene assisted laser-induced forward transfer of ceramic thin films". *Journal of Applied Physics*, **105**:113119, 2009.

H. Kim, G. P. Kushto, C. B. Arnold, Z. H. Kafafi, and A. Pique. "Laser processing of nanocrystalline TiO_2 films for dye-sensitized solar cells". *Applied Physics Letters*, **85**: 464, 2004a.

H. Kim, A. Pique, G. P. Kushto, R. C. Y. Auyeung, S. H. Lee, C. B. Arnold, and Z. H. Kafafi. "Dye-sensitized solar cells using laser processing techniques". *Photon Processing in Microelectronics and Photonics Iii*, **5339**:348, 2004b.

M. Kishimoto, J. Hobley, M. Goto, and H. Fukumura. "Microscopic laser patterning of functional organic molecules". *Advanced Materials*, **13**:1155, 2001.

A. Klini, F. Claeyssens, A. Mourka, and C. Fotakis. "Laser patterning of Zn for ZnO nanostructure growth: Comparison between laser induced forward transfer in air and in vacuum". *Thin Solid Films*, **515**:8529, 2007.

S. H. Ko, H. Pan, S. G. Ryu, N. Misra, C. P. Grigoropoulos, and H. K. Park. "Nanomaterial enabled laser transfer for organic light emitting material direct writing". *Applied Physics Letters*, **93**:151110, 2008.

S. H. Ko, H. Pan, D. Lee, C. P. Grigoropoulos, and H. K. Park. "Nanoparticle Selective Laser Processing for a Flexible Display Fabrication". *Japanese Journal of Applied Physics*, **49**:05EC03, 2010.

K. Komorita, T. Sano, H. Yamada, and I. Miyamoto. "Oxidation state control of micro metal oxide patterns produced by using laser-induced forward transfer technique". *Third International Symposium on Laser Precision Microfabrication*, **4830**:20, 2003.

G. Koundourakis, C. Rockstuhl, D. Papazoglou, A. Klini, I. Zergioti, N. A. Vainos, and C. Fotakis. "Laser printing of active optical microstructures". *Applied Physics Letters*, **78**:868, 2001.

A. I. Kuznetsov, A. B. Evlyukhin, C. Reinhardt, A. Seidel, R. Kiyan, W. Cheng, A. Ovsianikov, and B. N. Chichkov. "Laser-induced transfer of metallic nanodroplets for plasmonics and metamaterial applications". *Journal of the Optical Society of America B-Optical Physics*, **26**:B130, 2009a.

A. I. Kuznetsov, J. Koch, and B. N. Chichkov. "Laser-induced backward transfer of gold nanodroplets". *Optics Express*, **17**:18820, 2009b.

L. Landstrom, J. Klimstein, G. Schrems, K. Piglmayer, and D. Bauerle. "Single-step patterning and the fabrication of contact masks by laser-induced forward transfer". *Applied Physics a-Materials Science & Processing*, **78**:537, 2004.

S. Latsch, H. Hiraoka, W. Nieveen, and J. Bargon. "Interface study on laser-induced material transfer from polymer and quartz surfaces". *Applied Surface Science*, **81**:183, 1994.

B. Le Drogoff, B. Cui, and T. Veres. "Fast three-dimensional nanostructure fabrication by laser-assisted nanotransfer printing". *Applied Physics Letters*, **89**:113103, 2006.

J. Y. Lee and S. T. Lee. "Laser-induced thermal imaging of polymer light-emitting materials on poly(3,4-ethylenedioxythiophene): Silane hole-transport layer". *Advanced Materials*, **16**:51, 2004.

S. T. Lee, M. C. Suh, M. H. Kim, B. D. Chin, T. M. Kang, N. C. Yang, M. W. Song, J. H. Lee, H. K. Chung, M. B. Wolk, E. Bellmann, J. P. Baetzold, V. Savvateev, T. R. Hoffend, H. T. Le, K. T. Huynh, and L. A. Kreilich. "High resolution OLED patterning using laser transfer technology". *ASID'04: Proceedings of the 8th Asian Symposium on Information Display*, page 296, 2004.

Y. Li, C. Y. Wang, X. C. Ni, Z. J. Wang, W. Jia, and L. Chai. "Microdroplet deposition of copper film by femtosecond laser-induced forward transfer". *Applied Physics Letters*, **89**:161110, 2006.

T. Lippert and J. T. Dickinson. "Chemical and spectroscopic aspects of polymer ablation: Special features and novel directions". *Chemical Reviews*, **103**:453, 2003.

T. Lippert, J. Shaw-Stewart, M. Nagel, F. Nuesch, and A. Wokaun. "Laser-Induced Forward Transfer of Polymer Light-Emitting Diode Pixels with Increased Charge Injection". *Acs Applied Materials & Interfaces*, **3**:309, 2011.

P. A. Loukakos, E. L. Papadopoulou, E. Axente, E. Magoulakis, and C. Fotakis. "Laser induced forward transfer of metal oxides using femtosecond double pulses". *Applied Surface Science*, **257**:508, 2010.

S. Mailis, I. Zergioti, G. Koundourakis, A. Ikiades, A. Patentalaki, P. Papakonstantinou, N. A. Vainos, and C. Fotakis. "Etching and printing of diffractive optical microstructures by a femtosecond excimer laser". *Applied Optics*, **38**:2301, 1999.

S. Mailis, C. L. Sones, K. S. Kaur, P. Ganguly, D. P. Banks, Y. J. Ying, and R. W. Eason. "Laser-induced-forward-transfer: a rapid prototyping tool for fabrication of photonic devices". *Applied Physics a-Materials Science & Processing*, **101**:333, 2010.

H. Misawa and S. Juodkazis. *"3D Laser Microfabrication, principles and Applications"*. Wiley-VCH, Weinhein, Germany, 2006.

T. Mito, T. Tsujita, H. Masuhara, N. Hayashi, and K. Suzuki. "Hollowing and transfer of polymethyl methacrylate film propelled by laser ablation of triazeno polymer film". *Japanese Journal of Applied Physics Part 2-Letters*, **40**:L805, 2001.

R. Modi, H. D. Wu, R. C. Y. Auyeung, C. M. Gilmore, and D. B. Chrisey. "Direct writing of polymer thick film resistors using a novel laser transfer technique". *Journal of Materials Research*, **16**:3214, 2001.

R. Modi, H.D. Wu, R.C.Y. Auyeung, J.E.S. Vollmers, and D.B. Chrisey. "Ferroelectric capacitors made by a laser forward transfer technique", 2002.

R. Mogyorosi, T. Szorenyi, K. Ball, Z. Toth, and I. Hevesi. "Pulsed laser ablative deposition of thin metal films". *Applied Surface Science*, **36**:157, 1989.

M. Nagel, R. Fardel, P. Feurer, T. Lippert, F. A. Nusch, and A. Wokaun. "Laser ablation of aryltriazene photopolymer films: Effects of polymer structure on ablation properties". *Applied Surface Science*, **254**:1332, 2007.

Y. Nakata and T. Okada. "Time-resolved microscopic imaging of the laser-induced forward transfer process". *Applied Physics a-Materials Science & Processing*, **69**: S275, 1999.

Y. Nakata, T. Okada, and M. Maeda. "Application and observation of laser-induced forward Transfer process". *Photon Processing in Microelectronics and Photonics*, **4637**: 435, 2002a.

Y. Nakata, T. Okada, and M. Maeda. "Transfer of laser dye by laser-induced forward transfer". *Japanese Journal of Applied Physics Part 2-Letters*, **41**:L839, 2002b.

A. Narazaki, T. Sato, R. Kurosaki, Y. Kawaguchi, and H. Niino. "Nano- and microdot array formation of $FeSi_2$ by nanosecond excimer laser-induced forward transfer". *Applied Physics Express*, **1**:057001, 2008.

A. Narazaki, T. Sato, R. Kurosaki, Y. Kawaguchi, and H. Niino. "Nano- and microdot array formation by laser-induced dot transfer". *Applied Surface Science*, **255**:9703, 2009.

T. Okada, Y. Nakata, J. Muramoto, and M. Maeda. "New developments of pulsed-laser deposition process". *Laser Applications in Microelectronic and Optoelectronic Manufacturing III*, **3274**:246, 1998.

A. Palla-Papavlu, V. Dinca, C. Luculescu, J. Shaw-Stewart, M. Nagel, T. Lippert, and M. Dinescu. "Laser induced forward transfer of soft materials". *Journal of Optics*, **12**: 124014, 2010a.

A. Palla-Papavlu, V. Dinca, I. Paraico, A. Moldovan, J. Shaw-Stewart, C. W. Schneider, E. Kovacs, T. Lippert, and M. Dinescu. "Microfabrication of polystyrene microbead arrays by laser induced forward transfer". *Journal of Applied Physics*, **108**:033111, 2010b.

A. Palla-Papavlu, I. Paraico, J. Shaw-Stewart, V. Dinca, T. Savopol, E. Kovacs, T. Lippert, A. Wokaun, and M. Dinescu. "Liposome micropatterning based on laser-induced forward transfer". *Applied Physics a-Materials Science & Processing*, **102**:651, 2011.

P. Papakonstantinou, N. A. Vainos, and C. Fotakis. "Microfabrication by UV femtosecond laser ablation of Pt, Cr and indium oxide thin films". *Applied Surface Science*, **151**:159, 1999.

D. G. Papazoglou, A. Karaiskou, I. Zergioti, and C. Fotakis. "Shadowgraphic imaging of the sub-ps laser-induced forward transfer process". *Applied Physics Letters*, **81**:1594, 2002a.

D. G. Papazoglou, I. Zergioti, N. A. Vainos, and C. Fotakis. "Microfabrication of optically active InO_x microstructures by ultrashort laser pulses". *Journal of Optoelectronics and Advanced Materials*, **4**:809, 2002b.

A. Patrascioiu, M. Duocastella, J. M. Fernandez-Pradas, J. L. Morenza, and P. Serra. "Liquids microprinting through a novel film-free femtosecond laser based technique". *Applied Surface Science*, **257**:5190, 2011.

Y. Pihosh, T. Oishi, M. Goto, A. Kasahara, and M. Tosa. "Preparation of Coumarin 6 and ZnTPP micro dots on PBMA films by laser molecular implantation". *Applied Surface Science*, **241**:205, 2005.

S. M. Pimenov, G. A. Shafeev, A. A. Smolin, V. I. Konov, and B. K. Vodolaga. "Laser-Induced Forward Transfer of Ultra-Fine Diamond Particles for Selective Deposition of Diamond Films". *Applied Surface Science*, **86**:208, 1995.

A. Pique, D. B. Chrisey, R. C. Y. Auyeung, J. Fitz-Gerald, H. D. Wu, R. A. McGill, S. Lakeou, P. K. Wu, V. Nguyen, and M. Duignan. "A novel laser transfer process for direct writing of electronic and sensor materials". *Applied Physics a-Materials Science & Processing*, **69**:S279, 1999a.

A. Pique, D. B. Chrisey, R. C. Y. Auyeung, S. Lakeou, R. Chung, R. A. McGill, P. K. Wu, M. Duignan, J. Fitz-Gerald, and H. D. Wu. "Laser Direct Writing of circuit elements and sensors". *Laser Applications in Microelectronic and Optoelectronic Manufacturing Iv*, **3618**:330, 1999b.

A. Pique, D. B. Chrisey, J. M. Fitz-Gerald, R. A. McGill, R. C. Y. Auyeung, H. D. Wu, S. Lakeou, V. Nguyen, R. Chung, and M. Duignan. "Direct writing of electronic and sensor materials using a laser transfer technique". *Journal of Materials Research*, **15**: 1872, 2000.

A. Pique, D. W. Weir, P. K. Wu, B. Pratap, C. B. Arnold, B. R. Ringeisen, R. A. McGill, R. C. Y. Auyeung, R. A. Kant, and D. B. Chrisey. "Direct-write of sensor devices by a laser forward transfer technique". *Photon Processing in Microelectronics and Photonics*, **4637**:361, 2002.

A. Pique, C. B. Arnold, R. C. Wartena, D. W. Weir, B. Pratap, K. E. Swider-Lyons, R. A. Kant, and D. B. Chrisey. "Laser-induced forward transfer direct-write of miniature sensor and microbattery systems". *Third International Symposium on Laser Precision Microfabrication*, **4830**:182, 2003a.

A. Pique, R. C. Y. Auyeung, J. L. Stepnowski, D. W. Weir, C. B. Arnold, R. A. McGill, and D. B. Chrisey. "Laser processing of polymer thin films for chemical sensor applications". *Surface & Coatings Technology*, **163**:293, 2003b.

A. Pique, C. B. Arnold, H. Kim, M. Ollinger, and T. E. Sutto. "Rapid prototyping of micropower sources by laser direct-write". *Applied Physics a-Materials Science & Processing*, **79**:783, 2004.

L. Rapp, C. Cibert, A. P. Alloncle, and P. Delaporte. "Study on the transfer induced by laser of organic conducting thin films". *Uvx 2008: 9e Colloque Sur Les Sources Coherentes Et Incoherentes Uv, Vuv Et X; Applications Et Developpements Recents*, page 173, 2008.

L. Rapp, C. Cibert, A. P. Alloncle, P. Delaporte, S. Nenon, C. Videlot-Ackermann, and F. Fages. "Comparative time resolved shadowgraphic imaging studies of nanosecond and picosecond laser transfer of organic materials". *XVII International Symposium on Gas Flow, Chemical Lasers, and High-Power Lasers*, **7131**, 2009.

L. Rapp, C. Cibert, S. Nenon, A. P. Alloncle, M. Nagel, T. Lippert, C. Videlot-Ackermann, F. Fages, and P. Delaporte. "Improvement in semiconductor laser printing using a sacrificial protecting layer for organic thin-film transistors fabrication". *Applied Surface Science*, **257**:5245, 2011a.

L. Rapp, S. Nenon, A. P. Alloncle, C. Videlot-Ackermann, F. Fages, and P. Delaporte. "Multilayer laser printing for Organic Thin Film Transistors". *Applied Surface Science*, **257**:5152, 2011b.

B. R. Ringeisen, D. B. Chrisey, A. Pique, H. D. Young, R. Modi, M. Bucaro, J. Jones-Meehan, and B. J. Spargo. "Generation of mesoscopic patterns of viable Escherichia coli by ambient laser transfer". *Biomaterials*, **23**:161, 2002.

B. R. Ringeisen, J. A. Barron, and B. J. Spargo. "Novel seeding mechanisms to form multilayer heterogeneous cell constructs". *Architecture and Application of Biomaterials and Biomolecular Materials*, **1**:105, 2004.

T. Sano, H. Yamada, T. Nakayama, and I. Miyamoto. "Experimental investigation of laser induced forward transfer process of metal thin films". *Applied Surface Science*, **186**:221, 2002.

R. W. Schoenlein, W. Z. Lin, J. G. Fujimoto, and G. L. Eesley. "Femtosecond Studies of Nonequilibrium Electronic Processes in Metals". *Physical Review Letters*, **58**:1680, 1987.

V. Schultze and M. Wagner. "Laser-Induced Forward Transfer of Aluminum". *Applied Surface Science*, **52**:303, 1991.

P. Serra, M. Colina, J. M. Fernandez-Pradas, L. Sevilla, and J. L. Morenza. "Preparation of functional DNA microarrays through laser-induced forward transfer". *Applied Physics Letters*, **85**:1639, 2004a.

P. Serra, J. M. Fernandez-Pradas, F. X. Berthet, M. Colina, J. Elvira, and J. L. Morenza. "Laser direct writing of biomolecule microarrays". *Applied Physics a-Materials Science & Processing*, **79**:949, 2004b.

T. Smausz, B. Hopp, G. Kecskemeti, and Z. Bor. "Study on metal microparticle content of the material transferred with Absorbing Film Assisted Laser Induced Forward Transfer when using silver absorbing layer". *Applied Surface Science*, **252**:4738, 2006.

B. Tan, K. Venkatakrishnan, and K. G. Tok. "Selective surface texturing using femtosecond pulsed laser induced forward transfer". *Applied Surface Science*, **207**:365, 2003.

K. Tatah and A. Fukumoto. "Laser ablation forward deposition of metal lines for electrical interconnect repair". In *Int. Electronics Manufacturing Technology Symposium*, page 176, 1995.

A. C. Tien, Z. S. Sacks, and F. J. Mayer. "Precision laser metallization". *Microelectronic Engineering*, **56**:273, 2001.

D. Toet, M. O. Thompson, P. M. Smith, and T. W. Sigmon. "Laser-assisted transfer of silicon by explosive hydrogen release". *Applied Physics Letters*, **74**:2170, 1999.

D. Toet, P. M. Smith, T. W. Sigmon, and M. O. Thompson. "A new laser printing technique for the fabrication of thin film transistors". *Flat-Panel Displays and Sensors: Principles, Materials and Processes*, **558**:213, 2000a.

D. Toet, P. M. Smith, T. W. Sigmon, and M. O. Thompson. "Spatially selective materials deposition by hydrogen-assisted laser-induced transfer". *Applied Physics Letters*, **77**: 307, 2000b.

W. A. Tolbert, I. Y. S. Lee, M. M. Doxtader, E. W. Ellis, and D. D. Dlott. "High-Speed Color Imaging by Laser-Ablation Transfer with a Dynamic Release Layer - Fundamental Mechanisms". *Journal of Imaging Science and Technology*, **37**:411, 1993a.

W. A. Tolbert, I. Y. S. Lee, X. N. Wen, D. D. Dlott, M. M. Doxtader, and E. W. Ellis. "Laser-Ablation Transfer Imaging Using Picosecond Optical Pulses - Ultra-High-Speed, Lower Threshold and High-Resolution". *Journal of Imaging Science and Technology*, **37**:485, 1993b.

Z. Toth, Z. Kantor, P. Mogyorosi, and T. Szorenyi. "Surface Patterning by Pulsed Laser-Induced Transfer of Metals and Compounds". *Laser-Assisted Processing Ii*, **1279**:150, 1990.

V. Tsouti, C. Boutopoulos, D. Goustouridis, I. Zergioti, P. Normand, D. Tsoukalas, and S. Chatzandroulis. "A chemical sensor microarray realized by laser printing of polymers". *Sensors and Actuators B-Chemical*, **150**:148, 2010.

Y. Tsuboi, Y. Furuhata, and N. Kitamura. "A sensor for adenosine triphosphate fabricated by laser-induced forward transfer of luciferase onto a poly (dimethylsiloxane) microchip". *Applied Surface Science*, **253**:8422, 2007.

M. Wakaki, S. Chakraborty, H. Sakata, E. Yokoyama, and D. Chakravorty. "Laser-induced forward transfer technique for maskless patterning of amorphous V_2O_5 thin film". *Applied Surface Science*, **254**:638, 2007.

R. Wartena, A. E. Curtright, C. B. Arnold, A. Pique, and K. E. Swider-Lyons. "Li-ion microbatteries generated by a laser direct-write method". *Journal of Power Sources*, **126**:193, 2004.

D. A. Willis and V. Grosu. "Evaporation and phase explosion during Laser-Induced Forward Transfer of aluminum". *Photon Processing in Microelectronics and Photonics Iii*, **5339**:304, 2004.

D. A. Willis and V. Grosu. "Microdroplet deposition by laser-induced forward transfer". *Applied Physics Letters*, **86**:244103, 2005.

P. K. Wu, B. R. Ringeisen, J. Callahan, M. Brooks, D. M. Bubb, H. D. Wu, A. Pique, B. Spargo, R. A. McGill, and D. B. Chrisey. "The deposition, structure, pattern deposition, and activity of biomaterial thin-films by matrix-assisted pulsed-laser evaporation (MAPLE) and MAPLE direct write". *Thin Solid Films*, **398**:607, 2001.

P. K. Wu, B. R. Ringeisen, D. B. Krizman, C. G. Frondoza, M. Brooks, D. M. Bubb, R. C. Y. Auyeung, A. Pique, B. Spargo, R. A. McGill, and D. B. Chrisey. "Laser transfer of biomaterials: Matrix-assisted pulsed laser evaporation (MAPLE) and MAPLE Direct Write". *Review of Scientific Instruments*, **74**:2546, 2003.

J. Xu, J. Liu, D. H. Cui, M. Gerhold, A. Y. Wang, M. Nagel, and T. K. Lippert. "Laser-assisted forward transfer of multi-spectral nanocrystal quantum dot emitters". *Nanotechnology*, **18**:025403, 2007.

H. Yamada, T. Sano, T. Nakayama, and I. Miyamoto. "Optimization of laser-induced forward transfer process of metal thin films". *Applied Surface Science*, **197**:411, 2002.

H. Yamada, T. Sano, E. Ohmura, and I. Miyamoto. "Excimer and femtosecond pulsed laser induced forward transfer process of metal thin film". *Photon Processing in Microelectronics and Photonics Ii*, **4977**:426, 2003.

Y. L. Yao, H. Q. Chen, and W. W. Zhang. "Time scale effects in laser material removal: a review". *International Journal of Advanced Manufacturing Technology*, **26**:598, 2005.

I. Zergioti, S. Mailis, N. A. Vainos, C. Fotakis, S. Chen, and C. P. Grigoropoulos. "Microdeposition of metals by femtosecond excimer laser". *Applied Surface Science*, **127**:601, 1998.

I. Zergioti, D. G. Papazoglou, A. Karaiskou, N. A. Vainos, and C. Fotakis. "Laser microprinting of InOx active optical structures and time resolved imaging of the transfer process". *Applied Surface Science*, **197**:868, 2002.

I. Zergioti, D. G. Papazoglou, E. Gamaly, A. Rode, and C. Fotakis. "Studies on ultrashort laser micro structuring". *Advanced Optical Processing of Materials*, **780**:143, 2003a.

I. Zergioti, D. G. Papazoglou, A. Karaiskou, C. Fotakis, E. Gamaly, and A. Rode. "A comparative schlieren imaging study between ns and sub-ps laser forward transfer of Cr". *Applied Surface Science*, **208**:177, 2003b.

I. Zergioti, A. Karaiskou, D. G. Papazoglou, C. Fotakis, M. Kapsetaki, and D. Kafetzopoulos. "Femtosecond laser microprinting of biomaterials". *Applied Physics Letters*, **86**:163902, 2005a.

I. Zergioti, A. Karaiskou, D. G. Papazoglou, C. Fotakis, M. Kapsetaki, and D. Kafetzopoulos. "Time resolved schlieren study of sub-pecosecond and nanosecond laser transfer of biomaterials". *Applied Surface Science*, **247**:584, 2005b.

I. Zergioti, M. Makrygianni, P. Dimitrakis, P. Normand, and S. Chatzandroulis. "Laser printing of polythiophene for organic electronics". *Applied Surface Science*, **257**:5148, 2011.

J. Y. Zhang, I. W. Boyd, and H. Esrom. "Lamp-induced forward transfer: a new approach for deposition of metal films". *Journal of Materials Science Letters*, **17**:2037, 1998.

Chapter 3

Time resolved study of the LIFT process using ns-shadowgraphy

3.1 Introduction

The basic principle of the LIFT technique involves pulsed irradiation of a donor material to achieve transfer from the carrier substrate to a nearby placed receiver substrate (Bohandy et al., 1986). As discussed in the previous chapter to avoid the direct exposure of the donor (especially thermally and photosensitive materials) to the incoming laser, a sacrificial layer commonly known as the dynamic release layer (DRL) is introduced between the donor and the carrier (Tolbert et al., 1993). Good quality transfer depends on optimisation of various operating parameters such as the fluence, donor and DRL thicknesses, pulse shape and duration.

To understand the dynamics of the LIFT process and to study the influence of key parameters such as laser fluence, DRL and donor thicknesses on the transfer dynamics and the quality of the ejected donor material we studied the DRL-assisted LIFT process in real time using a time-resolved technique called shadowgraphy (Settles, 2001). A specially designed polymer called a triazene polymer (TP) (Lippert, 2004) was used as the DRL material in all these experiments (for more details please refer to section 2.2.2). This shadowgraphy technique has been used to study the ablation of biomaterials (Zergioti et al., 1998), polymers (Hauer et al., 2005), metals (Zhang et al., 2007), for imaging the ejection process during LIFT and to compare the ns and sub ps LIFT process (Zergioti et al., 2005). The basic working principle of shadowgraphy includes illuminating the object of interest by a light source and the shadows are cast on a screen.

In our set-up (explained below) the screen was replaced by a camera and the objects of interest were the opaque transferred discs of donor (from now on referred to as the "flyer") and the transparent shockwave induced by the huge pressure jump at the ablation site. An opaque flyer obviously will cast shadows on the screen but when the refractive index gradients ($\frac{\partial^2 n}{\partial^2 x}, \frac{\partial^2 n}{\partial^2 y}$) are non-zero, transparent media such as shockwaves can also form shadows. The inhomogeneous zone deviates the previous linear propagation of rays in an inhomogeneous manner, thereby producing a variation of intensity and hence casting a shadow on the screen.

The chapter begins with a description of the pump-probe set-up used for studying the time evolution of the TP-DRL assisted LIFT process for solid phase ceramic materials gadolinium gallium oxide (Gd-Ga-O) and ytterbium-yttrium aluminium garnet (Yb:YAG). It is followed by the discussion of the results obtained by varying the operating parameters and their influence on the quality of the flyer.

3.2 Experimental set-up[1]

The samples for the the ns-shadowgraphic studies were prepared by depositing the films of donor materials of Gd-Ga-O and Yb:YAG on top of previously TP coated fused silica substrates (25 x 25 x 1 mm^3). The TP was synthesized by the method described in (Nagel et al., 2007) and spin-coated on the silica substrates from solutions of the polymer in chlorobenzene and cyclohexanone (1:1w/w). Samples with polymer thicknesses of 50 nm, 150 nm and 350 nm were prepared by varying the viscosity of the solution and the spin speed. The donor material layer was then deposited on top by employing the pulsed laser deposition (PLD) technique (Eason, 2007). The target used was a single crystal gagolinium gallium garnet ($Gd_3Ga_5O_{12}$). In the PLD technique the target material is ablated in partial vacuum and the resultant laser-plasma is incident on a target substrate located nearby. A thin film progressively grows on this substrate at a rate of some few μm per hour. All the donor films were prepared under room temperature conditions and in an oxygen atmosphere (7x 10^{-2} mbar for GdGaO and 2x 10^{-3} mbar for Yb:YAG). Several samples with different donor thicknesses (200 nm and 1000 nm) on top of different thicknesses of TP were prepared to study the effect of the relative thicknesses of the DRL

[1]This work was done at General Energy Research department, Paul Scherrer Institut, Villigen, Switzerland

and donor material on the quality of the ablated flyer. The reason for choosing Gd-Ga-O and Yb:YAG as donor materials is the temperature sensitivity of the TP (it decomposes at 250 ^{0}C (Nagel et al., 2007) as these materials can be deposited at room temperature.

The pump-probe set-up used for the experiments is shown in fig. 3.1. A XeCl excimer laser (Compex, Lambda Physik, λ = 308 nm, τ = 30 ns) was used as the pump source. The reason for choosing this laser was the strong absorption of the TP at this wavelength (Lippert, 2004). The second harmonic of the Nd:YAG laser (λ= 532 nm, τ = 6 ns) was used as the probe beam. The pump pulses were centrally incident on a square mask with an aperture of 2 mm, resulting in an effectively spatially homogeneous beam. This uniform beam was then imaged by a lens (f = 250 mm) onto the sample with a demagnification of x 4, yielding a spot size of 500 μm x 500 μm. The pump laser energy incident on the target was controlled by a variable attenuator plate. The pulse energy was measured by a pyroelectric energy meter (Molectron J4-09 or Gentec QE 50) placed at the end of the beam line. The sample was placed on a motorized 3D translation stage, with the film facing away from the laser beam. The probe beam generated fluorescence in a dye (Rhodamine 6G) in a quartz cuvette placed on the camera axis on the opposite side of the sample, which in turn illuminated the ejected flyer and the released shockwave. The dye was used to remove the coherence of the probe laser and hence laser speckle effects thereby providing better quality illumination. The fluorescence decay time for the dye was $\sim$ 6-10 ns that determined the temporal resolution of the experiment. Visualization of the process was achieved by a complementary metal-oxide semiconductor (CMOS) camera with a microscope objective placed perpendicular to the laser beam (i.e. parallel to the sample surface) with the focus at the point of ablation, as shown in fig. 3.1. The delay between the pump and the probe beam was achieved using a digital pulse/delay generator (Stanford Research Systems DG535). A computer-controlled system allowed variation of the fluence, exposed position of the sample, the delay time between the pump and probe beam, and capture of a sequence of frames showing the generated shockwave and the ejected flyer. Each picture was recorded using a different pulse and corresponded to a new position on the sample.

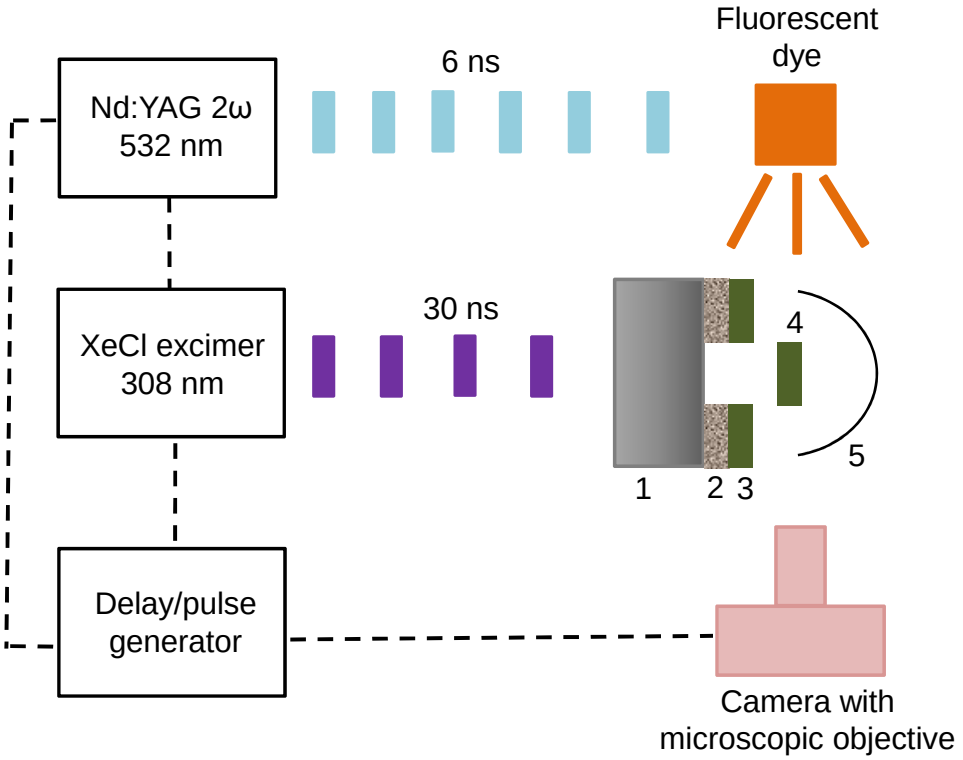

FIGURE 3.1: Schematic of the ns-shadowgraphy set-up.

3.3 Results

The results corresponding to the study of the effect of the laser fluence, TP-DRL and donor thicknesses on the flyer dynamics are discussed in the sub-sections 3.3.1, 3.3.2 and 3.3.3, respectively.

3.3.1 Laser fluence dependence

To study the influence of laser fluence on the dynamics of the transfer process and the quality of the ejected flyer the pump laser pulse was raster scanned across the samples to selectively ablate an array of square holes with each row corresponding to a different laser fluence value. Figure 3.2 shows the schematic of the corresponding ablated matrix generated on the samples and the inset to the figure shows one of the ablated square patterns (500 μm x 500 μm) observed under an optical microscope. The laser fluence value was varied from $\sim$ 60 mJ/cm^2 to $\sim$ 700 mJ/cm^2 and for each fluence value the camera recorded a sequence of pictures at different delay times between the pump and the probe pulses.

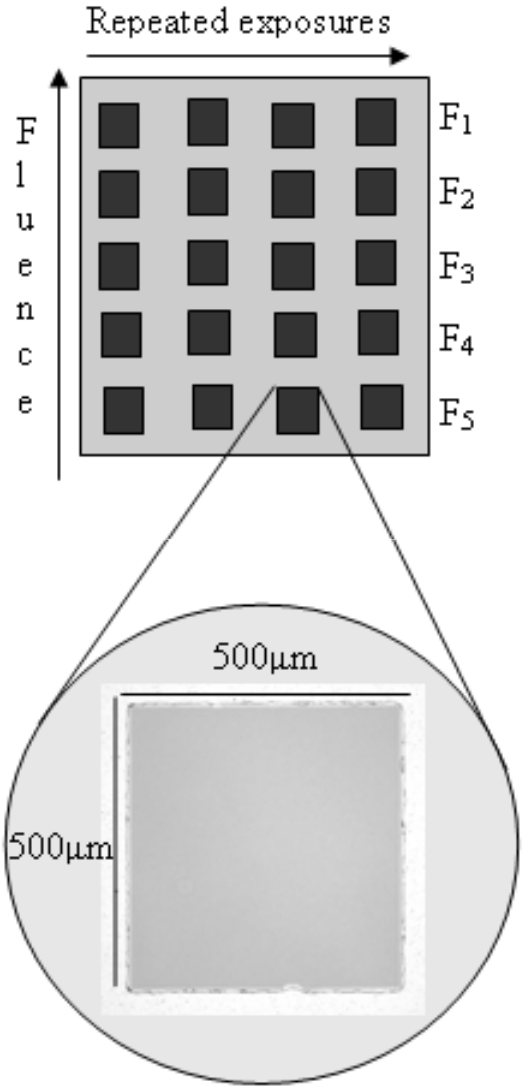

FIGURE 3.2: Schematic of the donor sample ablated using different fluence values (from $F_1$to F_5) for each row. The inset shows the optical microscope image of an ablated region on the donor.

Figure 3.3 shows time-resolved shadowgraphs of the target (carrier-donor unit) having a 1 μm thick Gd-Ga-O film deposited on top of a 350 nm thick TP at fluence values of $\sim$ 60 mJ/cm^2(i) and $\sim$ 600 mJ/cm^2(ii). The time delay between the pump and the probe pulses was varied from 400 to 2400 ns with a delay step of 400 ns.

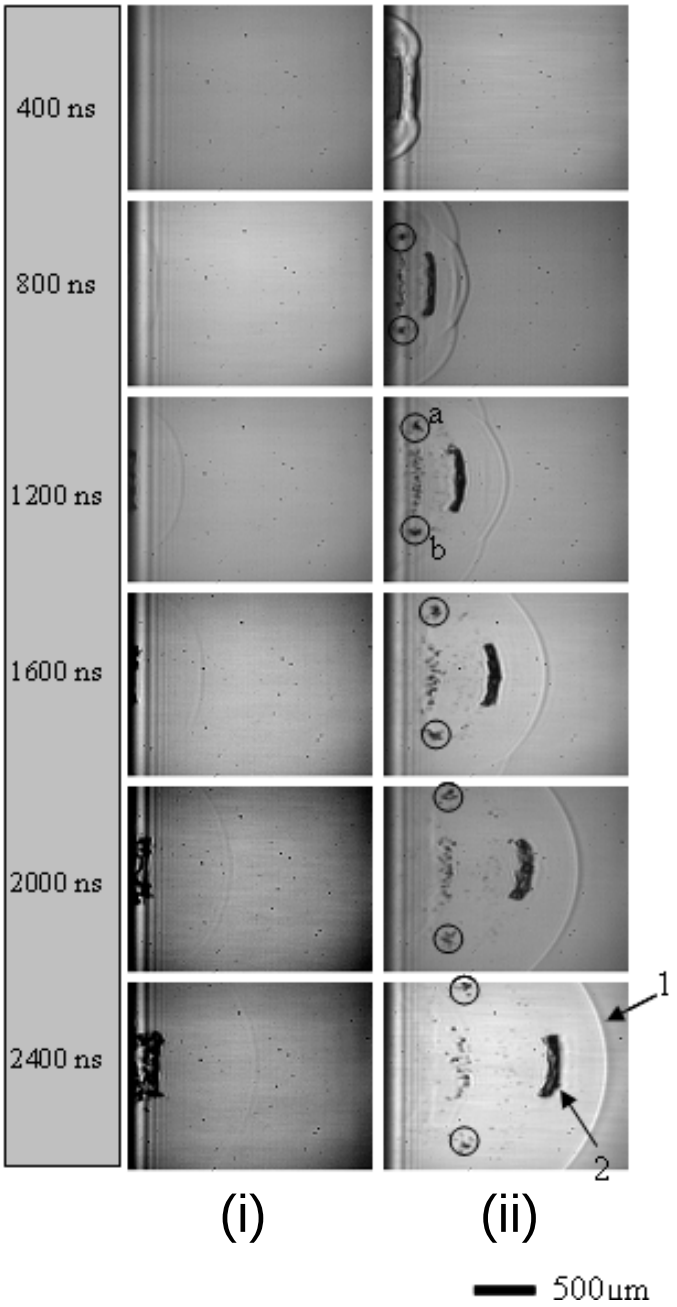

FIGURE 3.3: Shadowgraphs recorded for 1 μm thick Gd-Ga-O target with 350 nm TP for fluence values of (i) 60 mJ/cm^2 and (ii) 600 mJ/cm^2. The shockwave front and the flyer have been marked as 1 and 2, respectively as an example in (ii). Also the solid chunks of the Gd-Ga-O layer from the shattered edges of its flyer are circled and marked as (a) and (b).

Figure 3.4 (i, ii) show the images for the second donor material Yb:YAG (1 μm thick) with all other conditions kept the same. The shockwave released by the huge pressure jump at the ablation site and the opaque flyer ejected from the target surface are clearly

visible in all these pictures. It is clear from these images that the higher the fluence, the farther the shockwave and flyer propagate away from the target surface. In figs. 3.3 (i) and 3.4 (i), for a delay time of 1200 ns, while the flyer had just started to delaminate from the surface at an irradiance of $\sim$ 60 mJ/cm^2 pulse, it had already moved a substantial distance from the target surface for a $\sim$ 10 x higher fluence ($\sim$ 600 mJ/cm^2) (see 3.3 (ii) and 3.4 (ii)). This can be attributed to the fact that at low fluence the pressure generated by the decomposed polymer was not sufficient to expel the flyer far from the surface. However, as the fluence was increased, the ablation depth also increased, which in turn decomposed a larger fraction of the TP film, and this released more gaseous fragments and hence an increased pressure was exerted on the top donor layer. A distorted shockwave front was also observed at the higher fluence value ($\sim$ 600 mJ/cm^2) for both the materials. The reason for this is believed to be the decomposed TP escaping out from the sides of the flyer at the time of ejection due to an extremely high pressure present at the ablation spot which led to the overlapping side shockwaves. After time delays of around 1600 ns the shockwave appeared to regain the hemispherical shape (refer to fig. 3.3 (ii)).

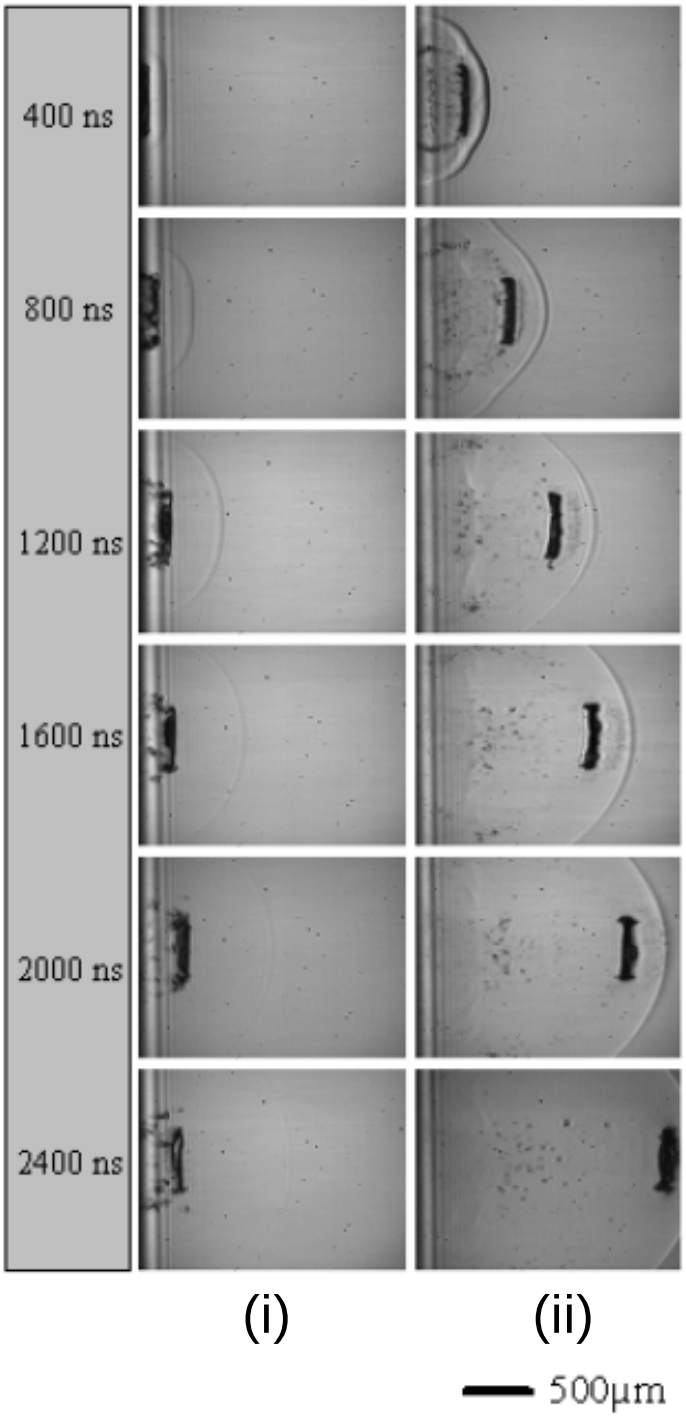

FIGURE 3.4: Images for the 1 μm thick Yb:YAG target with 350 nm TP for fluence values of (i) 60 mJ/cm^2 and (ii) 600 mJ/cm^2 at delay times of 400-2400 ns between the pump and the probe.

On comparing the shadowgraphs of the two ceramic materials it is evident that the Yb:YAG flyer was travelling farther than that of the Gd-Ga-O flyer at all delay times,

for both fluences. Two additional much smaller flyers were also observed in the case of the Gd-Ga-O donor layer (circled and marked as (a) and (b) in Fig. 3.3 (ii)). These observations can be attributed to the difference in the quality of the two donor films as analysed by a scanning electron microscope (SEM) shown in fig. 3.5 (a,b). The Yb:YAG film was somewhat porous and had substantial surface texturing while the Gd-Ga-O was a much smoother and flatter film. The solid Gd-Ga-O film is likely to offer more resistance to shearing than the porous Yb:YAG layer, which was relatively easily detached resulting in a cleaner and less violent detachment process. Comparatively less force was therefore required to forward-transfer the Yb:YAG layer and hence the greater distance of travel observed by the flyer from this film for the same fluence. The solid material which resulted from the comparatively violent shearing of the flyer from the non-porous solid Gd-Ga-O film which in turn may have disrupted the edges of the flyer during its detachment from the donor surface. These shattered edges appear as the two smaller flyers when captured by the camera mounted perpendicular to the target surface as depicted in fig. 3.6. However only fragments are observed for the case of Yb:YAG due to the relatively less violent shearing process and difference in the surface quality. This clearly explains the lesser amount of debris seen in the case of the flyer from the Yb:YAG film.

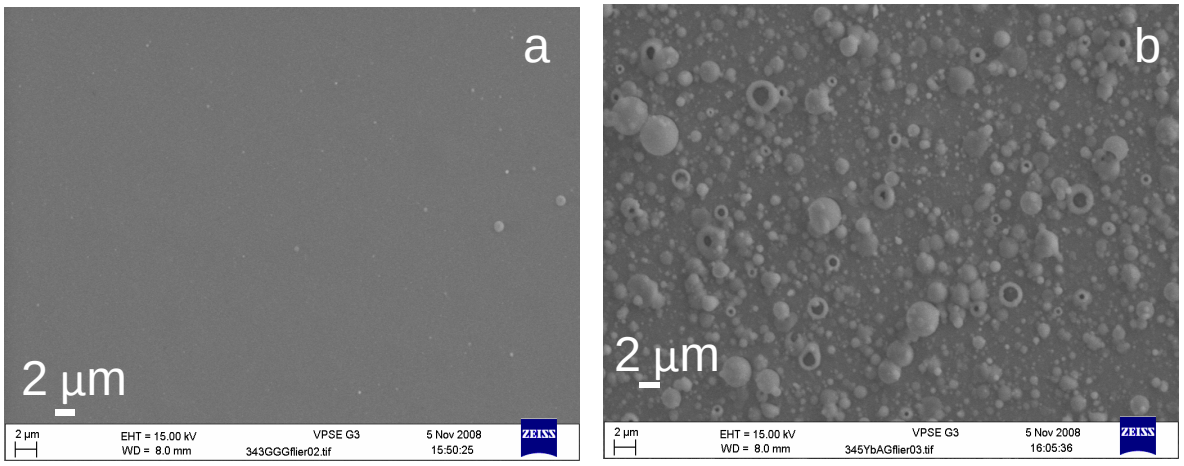

FIGURE 3.5: SEM images displaying the difference in the surface quality of (a) the Gd-Ga-O and (b) Yb:YAG donor films respectively.

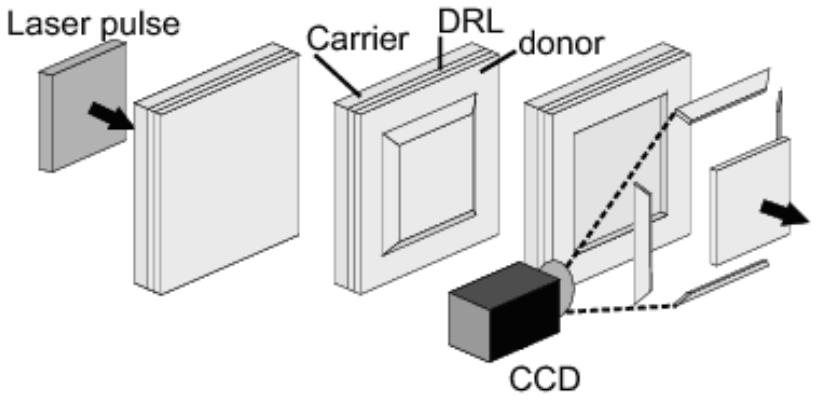

FIGURE 3.6: The 3D schematic of the Gd-Ga-O shearing process.

The graphs shown in fig. 3.7 (a, b) show the distance propagated by the shockwave and the flyer respectively as a function of delay time for a range of pump laser fluence values for the 1 μm thick Yb:YAG on top of 350 nm TP-DRL target sample. The solid lines in fig. 3.7 (a,b) are simple guides to the eye. The experimental data for the shockwave propagation follows the similar qualitative trend (shown in fig. 3.8) as predicted by the theoretical model (Freiwald, 1972; Bennett et al., 1996) which is based on Eq. (3.1).

$$R = \left\{ \left[1.5 C_5 \left(E_o \right)^{1/2} t + C_4^{3/2} \right]^{2/3} - C_4 \right\} / C_5 \tag{3.1}$$

where

$$C_4 = \frac{A\delta}{8} \left(\frac{2}{\gamma + 1} \right)^2 \rho_s \tag{3.2}$$

$$C_5 = \frac{\rho_o A}{\gamma + 1} \left(\frac{1}{\gamma - 1} + \frac{4}{\gamma + 1} \right) \tag{3.3}$$

Here R is the propagation distance, E_o is the laser energy, γ is the specific heat ratio of the atmosphere, A is the laser-ablated area, ϱ_s is the TP density, δ is the ablation depth ρ_o is the atmospheric density and t is the delay time. However, quantitatively the experimental and theoretical values differ by $\sim 60\%$ as shown in fig. 3.8. The reason for this discrepancy is the overlying donor layer in the present case, while the theoretical model takes the TP layer into account only. The generated shockwave has to travel through the donor layer which results in the lower values of distance propagated. For the case of the flyer, the range of incident energy densities spans more than one order of magnitude, and while a straight-line fit appears to be appropriate for the lowest incident

energy density results ($\sim$ 60 mJ/cm^2), the data points for the $\sim$ 680 mJ/cm^{2}are seen to depart from a simple straight line fit, as shown in fig. 3.7 (b). Given that the flyer will experience a frictional damping force from the surrounding air, it is to be expected that some slowing down will occur, particularly for the higher velocities recorded, as the drag experienced by an object is proportional to (velocity)^2. For this reason, the fits (which remain as guides to the eye) are not shown as straight lines.

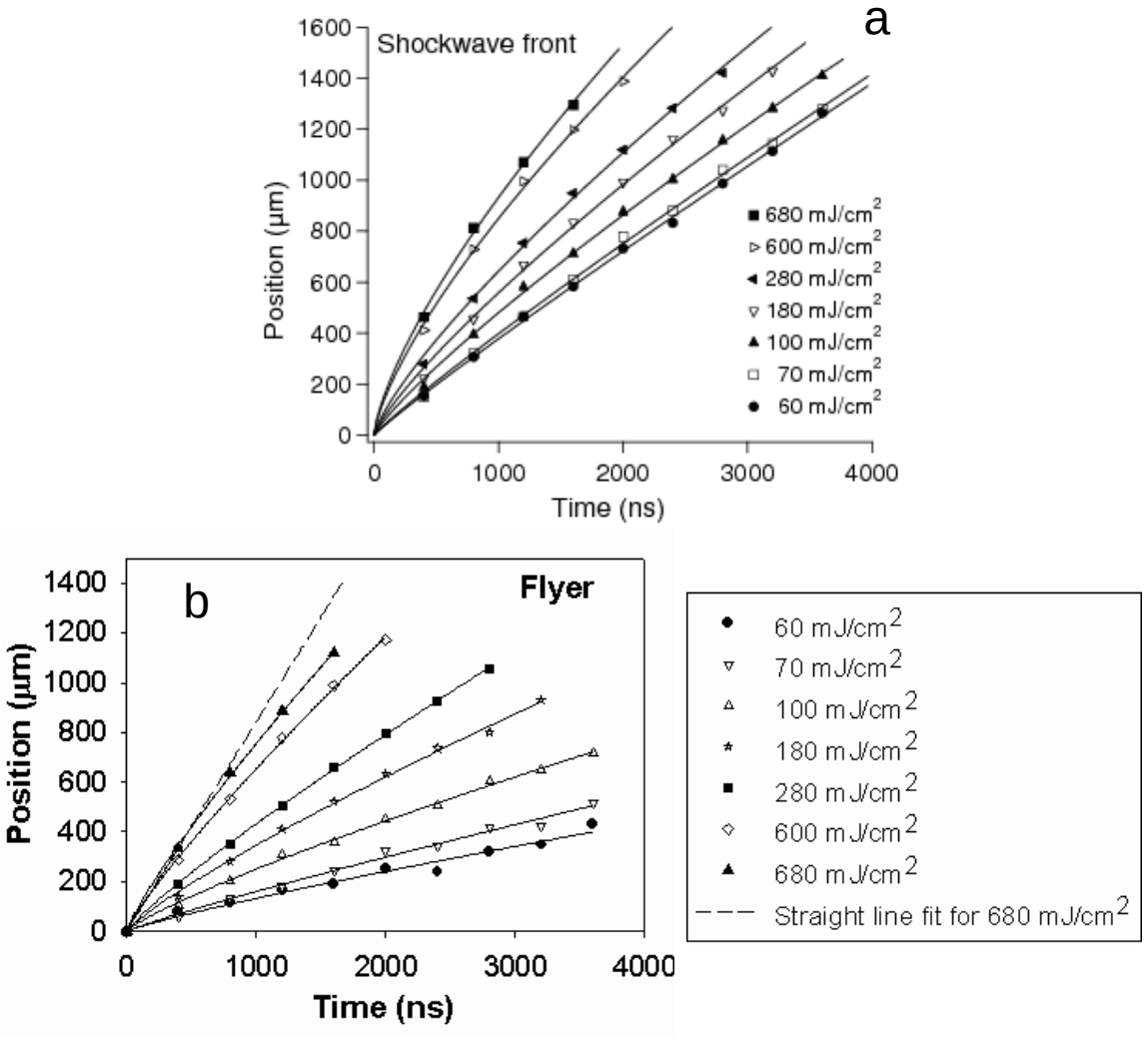

FIGURE 3.7: Variation in the position of (a) the shockwave and (b) the flyer as functions of the pump fluence at different delay times with 1 μm thick Yb:YAG on top of 350 nm TP. The flyer is shown to slow down and depart from a constant velocity straight line fit for a fluence of 680 mJ/cm^2 in (b).

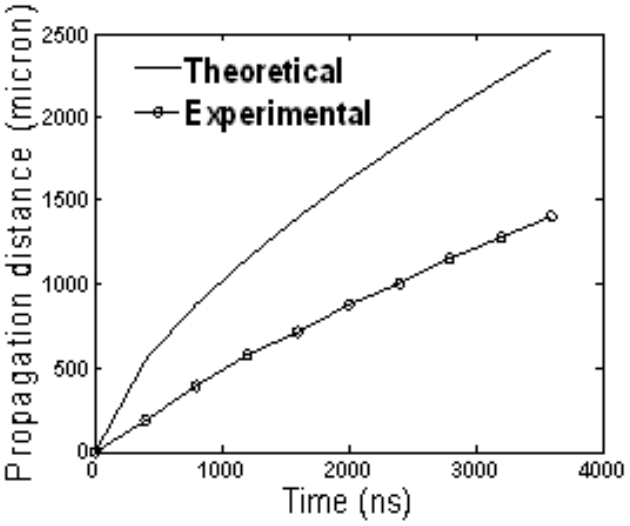

FIGURE 3.8: Plot showing the variation in the propagation distance of the shockwave as a function of delay time as predicted by the theory and that given by experimental values for 1 μm thick Yb:YAG on top of a 350 nm TP at a fluence of 100 mJ/cm^2.

The variation of the propagation velocity, for both the shockwave and the flyer, as a function of the fluence at a delay time of 800 ns is also shown in fig. 3.9 (a) and (b) respectively for 1 μm thick Gd-Ga-O donor film on top of a 350 nm TP-DRL. The velocity for both the shockwave and the flyer increase monotonically with the laser fluence. The solid line drawn through the experimental data points for the shockwave is a guide to the eye (fig. 3.9 (a)). However the dashed curve drawn along the flyer data points in the log-log plot of fig. 3.9 (b) is a theoretical fit based on the following model: The energy density of the incident laser pulse was used to decompose the TP-DRL layer into gaseous fragments which in turn pushed the irradiated donor film forward. Assuming that the incident absorbed energy of the laser pulse was proportional to the kinetic energy of the ejected flyer i.e.

$$E_{pulse} \propto \frac{1}{2}mv^2 \tag{3.4}$$

where E_{pulse}, m and v are energy of the laser pulse, mass and velocity of the ejected flyer respectively. For fixed values of m

$$E_{pulse} \propto v^2 \tag{3.5}$$

$$\therefore v = K\sqrt{E_{pulse}} \tag{3.6}$$

where K is a proportionality constant. Eq. (3.6) represents the analytical dashed plot of fig. 3.9 (b) and it is consistent with the experimental data. However it should be mentioned that the experimental data points corresponding to low fluences depart from the theoretical straight line fit based on the above model. This is due to the fact that at these fluence values the laser energy is not sufficient to completely decompose the TP layer hence a lesser forward push acts on the flyer leading to a lower value of the flyer velocity (Fardel et al., 2008, 2009). A similar trend in the variation of propagation distance and velocity with laser fluence was observed for all the other samples irrespective of the TP-DRL and donor material (Gd-Ga-O or Yb:YAG) and their thicknesses. As an example plots for the variation of propagation velocity of both the shockwave and flyer as a function of laser fluence, for a sample with 200 nm thick Yb:YAG on top of 350 nm thick TP is shown in fig. 3.10 (a) and (b) respectively.

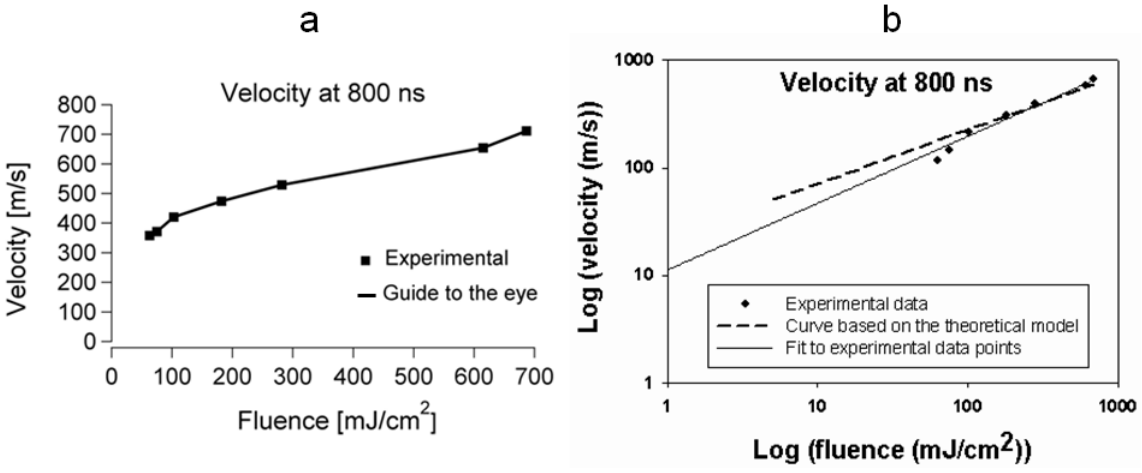

FIGURE 3.9: Variation in the propagation velocity of (a) the shockwave and (b) the flyer as a function of the pump fluence at a delay time of 800 ns for a sample with 1 μm thick Gd-Ga-O donor film on top of a 350 nm TP-DRL.

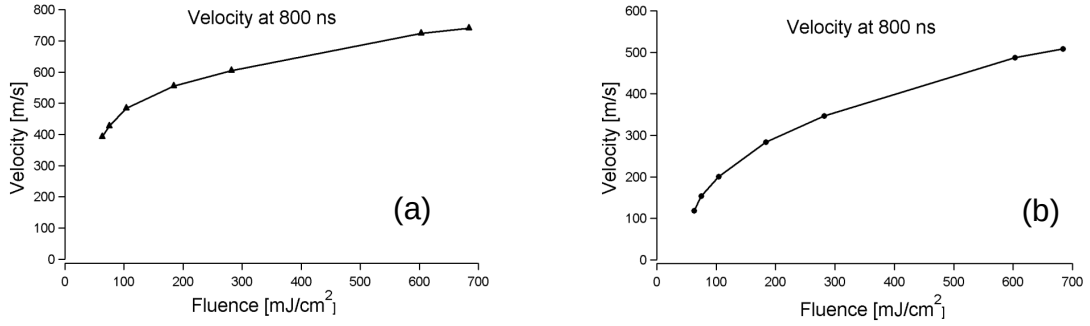

FIGURE 3.10: Variation in the propagation velocity of (a) the shockwave and (b) the flyer as a function of the pump fluence at a delay time of 800 ns for a sampe with 200 nm thick Yb:YAG donor film on top of a 350 nm TP-DRL.

To better understand the relative pathways for conversion of the incident absorbed laser energy into the kinetic energy of the flyer, the shockwave, the physical processes behind the DRL decomposition and rupture of the donor film, we considered the overall energy budget for the entire LIFT process based on the above analysis. The efficiency of energy conversion from incident pulse energy to kinetic energy of the flyer was directly inferred from the fit to the experimental data points in fig. 3.9 (b) for a 1 μm thick Gd-Ga-O donor film on top of a 350 nm TP-DRL. The kinetic energy of the flyer resulted in $\sim$ 20% of the pulse energy using the slope of the fit ($\sim$ 0.62) and the y-intercept ($\sim$ 11.2). What remains therefore is the energy required to rupture or shear the donor film, and the residual energy contained within the multiple shockwaves generated. The TP decomposition process is exothermic and the amount of energy released is 6.97 x 10^5 J/kg. The thermal energy released by the decomposition of a 500 μm x 500 μm region of a 350 nm thick TP film is therefore $\sim$68 μJ (density of triazene = 1.12 x 10^3 kg/m3). This is only 4% of the incident laser energy (for a fluence of 600 mJ/cm^2) so the energy released during TP decomposition can be considered to contribute little to the energy balance equation.

Apart from the laser fluence, the thickness of the donor and the underlying TP layer should also play an important role in determining the dynamics of the flyer. For example if the ablation depth exceeded the TP layer thickness, then the donor would be damaged and the basic idea of achieving an intact transfer using a DRL is defeated. Also for a thicker donor film the flyer would travel a smaller distance as compared to the flyer from a sample with a thinner donor film due to the greater force required to shear a

thicker film. The study of the effect of these parameters is discussed in the next two sub-sections.

3.3.2 Donor thickness dependence

The influence of the donor thickness on the quality of the ejected flyer was studied by performing pump-probe experiments with the delay time between the pump and the probe pulses set at a constant value of 1600 ns. Pump pulses with a constant energy density were raster-scanned across the sample and the shadowgraphs of the ejected flyer and the shockwave were recorded. For the case of a constant donor thickness the distance propagated by the shockwave or the flyer as a function of the position on the donor should also be constant, provided the DRL film had a uniform thickness. In the present case, a very homogeneous layer of TP-DRL on the silica substrate was obtained by spin-coating. However, the donor layer deposited by PLD had a radial thickness variation. Any deviation from the straight line behavior can thus be attributed to the thickness variation of the donor film and not the TP.

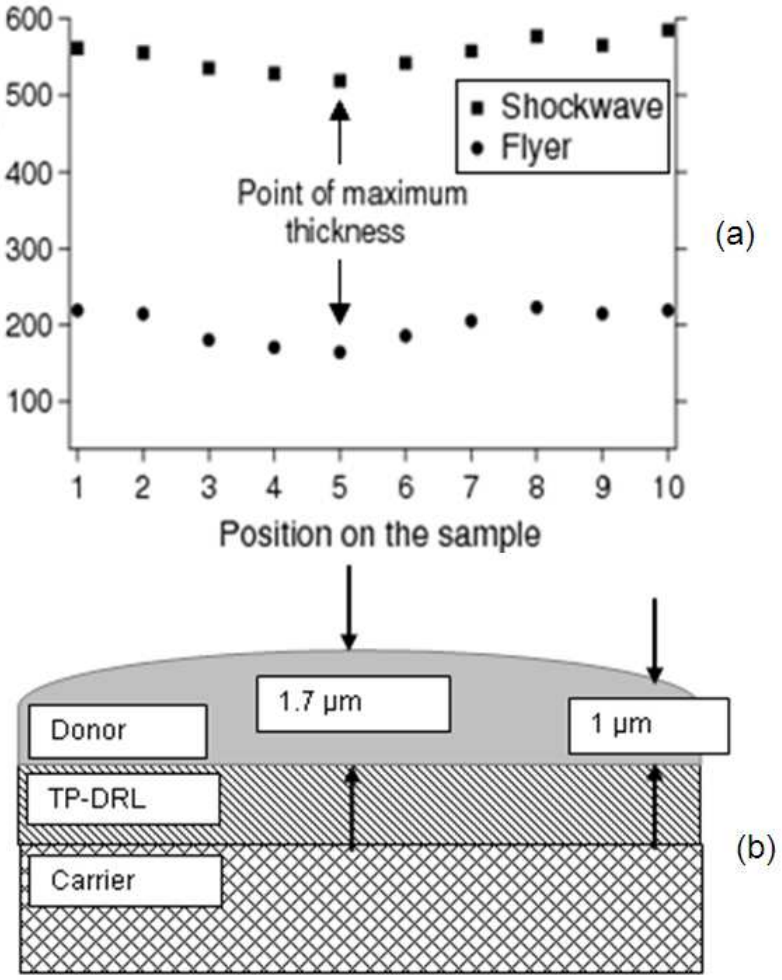

FIGURE 3.11: (a) Plot showing the dependence of the position of the shockwave and the flyer on the donor thickness for fixed values of TP thickness (350 nm) and delay time (1600 ns) for a Gd-Gd-O sample having a maximum thickness ($\sim 1.7\ \mu m$) at the centre and a minimum thickness ($\sim 1\ \mu m$) around the edges. The x-axis corresponds to the position on the sample with varying thickness as shown in (b).

Figure 3.11 (a) shows such a plot for a Gd-Ga-O sample having a maximum thickness ($\sim 1.7\ \mu$m) at the centre and a minimum thickness ($\sim 1\ \mu$m) around the edges and fig. 3.11 (b) shows the schematic of the target with varying donor thickness. The TP thickness was 350 nm and the fluence was ~ 100 mJ/cm^2. The layer thicknesses were measured using a stylus profiler. The dip at the centre of the plot (arrowed) coincides with the point of maximum thickness on the target which suggests a clear dependence of the transfer mechanism on the donor thickness.

The graph depicting the decrement of the distance travelled by the flyer with the donor thickness, for the above discussed sample, is shown in fig. 3.12. The dashed line represents the analytical fit to the experimental data points. It was obtained using the following simple model: As mentioned in the previous section, the energy of the laser pulse is proportional the kinetic energy of the flyer (Eq. (3.4)), so for different donor film thicknesses X_1 and X_2

$$E_{pulse} \propto \frac{1}{2} m_1 v_1^2 = \frac{1}{2} m_2 v_2^2 \tag{3.7}$$

$$\therefore \frac{m_1}{m_2} = \frac{v_2^2}{v_1^2} \tag{3.8}$$

where m_1 and m_2 are the masses of the ejected flyer corresponding to the thicknesses X_1 and X_2 respectively and v_1 and v_2 are the corresponding velocities. For a given distance d travelled by the flyer and at a given time t,

$$d = vt \tag{3.9}$$

$$\therefore v^2 = \frac{d^2}{t^2} \tag{3.10}$$

$$\Rightarrow v^2 \propto d^2 \tag{3.11}$$

From Eq. (3.8) and Eq. (3.11) we obtain

$$\frac{m_1}{m_2} = \frac{d_2^2}{d_1^2} \tag{3.12}$$

$$\Rightarrow \frac{d_2}{d_1} = \sqrt{\frac{m_1}{m_2}} = \sqrt{\frac{X_1}{X_2}} \tag{3.13}$$

Here d_1 and d_2 represent the distances travelled by the flyer corresponding to thicknesses X_1 and X_2 respectively. Eq. (3.13) represents the theoretical curve plotted in fig. 3.12 and is consistent with the experimental data. Similar dependence of the flyer propagation distance was observed for all the other samples with different thickness of donor (Gd-Ga-O and Yb:YAG) and TP-DRL.

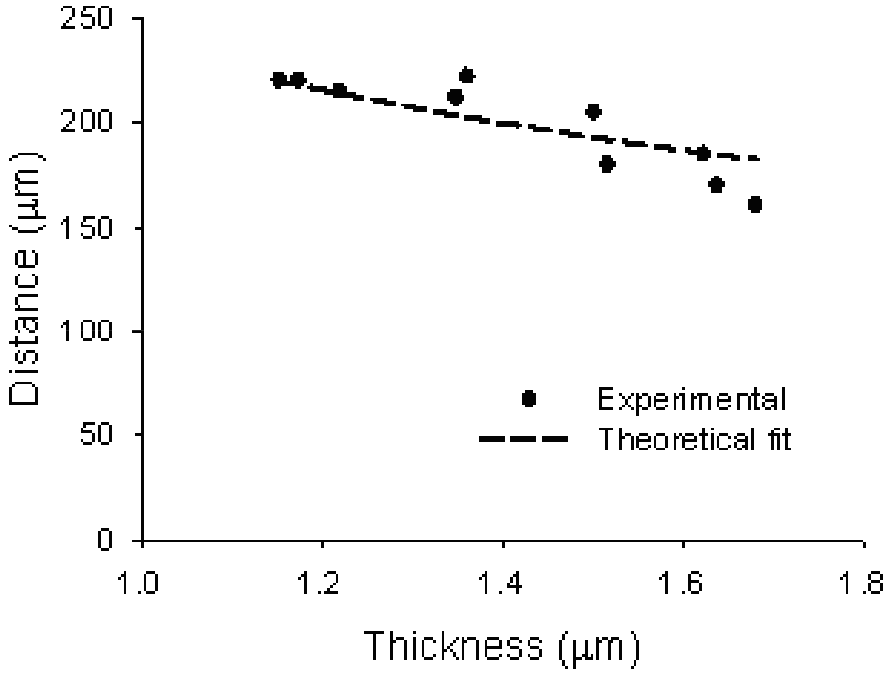

FIGURE 3.12: The propagation distance of the flyer plotted against the thickness of the donor film of Gd-Ga-O for the fixed values of TP (350 nm) and the delay time (1600 ns). The curve clearly shows that thicker films have slower velocities, as expected.

3.3.3 TP thickness dependence

To examine the effect of the DRL layer thickness on the transfer process, shadowgraphy experiments were performed for target samples with different thickness values of TP while keeping the central thickness of the donor material approximately constant. Figures 3.13 (a, b) show the recorded time-resolved images of the 1 μm thick Yb:YAG flyers with pulses of $\sim$ 100 mJ/cm^2 and at delay times of 0-3600 ns between the pump and the probe for 50 nm and 350 nm thick TP respectively.

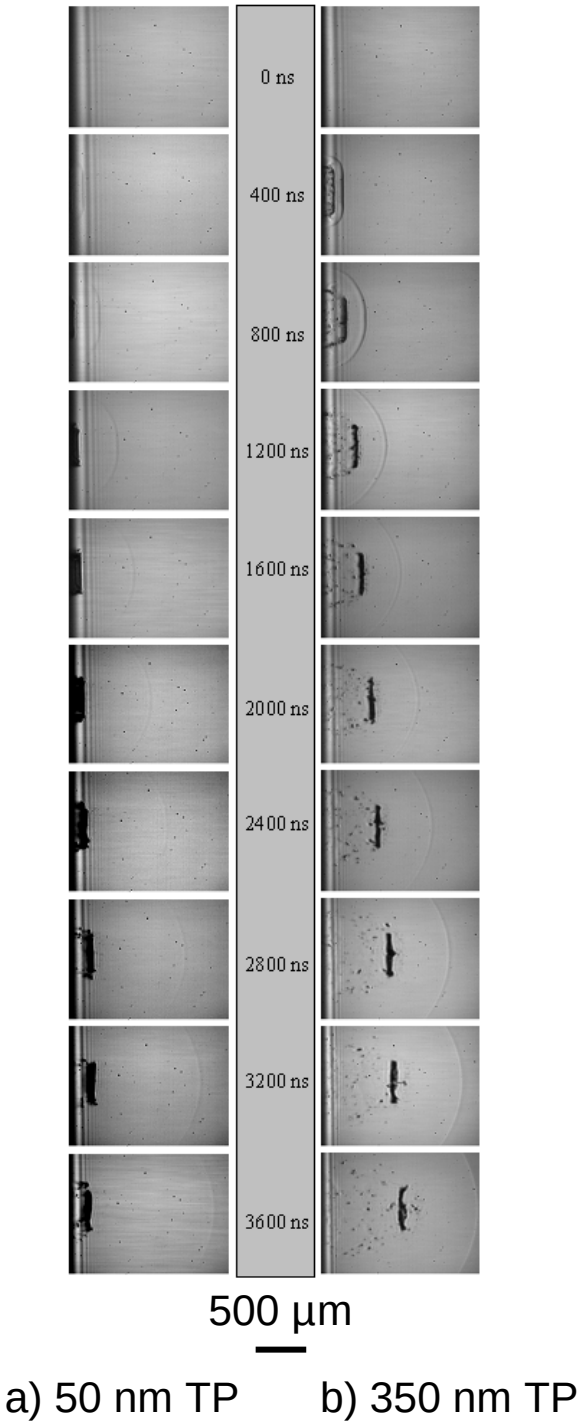

FIGURE 3.13: Shadowgraphs recorded for targets with (a) 50 and (b) 350 nm TP-DRL while keeping the donor (Yb:YAG) thickness constant ($\sim$ 1 μm) at the delay times of 0-3600 ns between the pump and the probe and a fluence of 100 mJ/cm^2.

The key observations and the qualitative conclusions from the shadowgraphs obtained from the 1μm Yb:YAG samples with two different values of TP (50 nm and 350 nm) are stated below:

a) It appears that the delamination of the donor material started earlier for samples with a thicker TP layer (350 nm) as compared to those with thinner TP layer (50 nm). For example even after 400 ns only a weak shockwave was visible for the sample with a 50 nm TP-DRL, while the flyer and shockwave were both clearly visible for the 350 nm TP sample.

b) The ejected flyer travelled a significantly greater distance for the sample with the thicker TP-DRL film (350 nm) than for the one with the thinner TP layer (50 nm). For example after 1600 ns the flyer from the former sample was already hundreds of microns away from the donor surface while the flyer from the latter target was barely detached from the surface of the donor.

c) The flyer from the sample with the thicker TP appears to be associated with noticeably more debris than the one from the thinner TP.

d) The flyer started to disintegrate and deform in shape with increasing distance. This effect was more prominent for targets with thicker TP layers.

The explanation for these observations is based on the decomposition of the DRL layer beneath the donor film into gaseous fragments by the pump pulse which then exerted a forward push on the donor material. The thicker TP layer applied a greater force on the ejected flyer causing its early delamination and providing it with a greater kinetic energy to propagate farther from the sample surface. This long distance travel of the flyer is useful for any practical industrial applications that require large donor-receiver separations e.g. for transferring multi-layers of dissimilar materials sequentially. In contrast, the lesser pressure exerted on the flyer for the sample with thinner TP layer explains the smaller distance travelled by the flyer and its delayed delamination. The pump pulse decomposed the TP-DRL layer over the irradiated region thereby shearing the flyer apart from the donor surface by the exerted pressure. For the thicker TP-DRL sample the huge pressure exerted on the flyer made this shearing a violent process and shattered the edges of the flyer during its detachment from the surface, and this may well explain the debris seen in the images for the thicker TP samples.

It should be mentioned that the ablation depth depends not only on the fluence but on TP-DRL thickness as well (Fardel et al., 2008). For a given fluence the absolute amount of ablated TP increases with increasing film thickness, thereby providing more thrust for flyer ejection with thicker DRLs, however beyond a certain value of thickness (beyond the ablation depth) the relative percentage of undecomposed TP increases (Fardel et al., 2009). For example at 100 mJ/cm^2 a 50 nm TP film is completely dissociated while $\sim$ 30 % of the TP remains undecomposed for the sample with a 350 nm TP-DRL layer (data interpolated from that presented in (Bennett et al., 1996). So the flyer from this sample was bilayered i.e. consists of both the ceramic material (Yb:YAG or Gd-Ga-O) and the remaining TP. This undissociated TP could also be a possible cause of the debris seen in the shadowgraphs apart from the shattered edges of the flyer. The actual reason behind this debris is not known for the present case due to the absence of a receiver to collect the transferred flyers, however this can be very well investigated using an experimental set-up including a receiver substrate to collect the flyer along-with the debris.

Also the quality of the flyer deteriorated as it moved away from the target surface. Therefore, for an intact long distance transfer of the flyer, an optimal thickness of the sacrificial layer has to be chosen taking into account the fluence, donor material and thickness. It should me mentioned here that these experiments were only performed for two different TP thicknesses, and hence for definitive and fully quantitative conclusions a much more systematic study of what is actually a complex and coupled problem should be done.

3.4 Conclusions

In this chapter the results of the study of the dependence of the TP-DRL assisted LIFT process on laser fluence and thickness of the donor and the TP-DRL using a time-resolved ns-shadowgraphy technique, for solid phase ceramic Gd-Ga-O and Yb:YAG materials were presented and discussed. The results showed that the propagation distance and velocity for both the shockwave and the flyer increase with the laser fluence. Also the distance travelled by the ejected flyer decreases with increasing donor film thickness. Finally, the investigation of the effect of the thickness of the TP layer on the process revealed that an optimal value of the TP-DRL thickness is required and that the optimal thickness varied with donor material, donor thickness and the laser energy.

Bibliography

L. S. Bennett, T. Lippert, H. Furutani, H. Fukumura, and H. Masuhara. "Laser induced microexplosions of a photosensitive polymer". *Applied Physics a-Materials Science & Processing*, **63**:327, 1996.

J. Bohandy, B. F. Kim, and F. J. Adrian. "Metal-Deposition from a Supported Metal-Film Using an Excimer Laser". *Journal of Applied Physics*, **60**:1538, 1986.

R. Eason, editor. *"Pulsed Laser Deposition of Thin Films"*. John Wiley and Sons, Inc., 2007.

R. Fardel, M. Nagel, T. Lippert, F. Nuesch, A. Wokaun, and B. S. Luk'yanchuk. "Influence of thermal diffusion on the laser ablation of thin polymer films". *Applied Physics a-Materials Science & Processing*, **90**:661, 2008.

R. Fardel, M. Nagel, F. Nuesch, T. Lippert, and A. Wokaun. "Shadowgraphy investigation of laser-induced forward transfer: Front side and back side ablation of the triazene polymer sacrificial layer". *Applied Surface Science*, **255**:5430, 2009.

D. A. Freiwald. "Approximate Blast Wave Theory and Experimental-Data for Shock Trajectories in Linear Explosive-Driven Shock-Tubes". *Journal of Applied Physics*, **43**:2224, 1972.

M. Hauer, D. J. Funk, T. Lippert, and A. Wokaun. "Time-resolved techniques as probes for the laser ablation process". *Optics and Lasers in Engineering*, **43**:545, 2005.

T. Lippert. "Laser Applications of Polymers". *Advanced Polymer Science*, **168**:51, 2004.

M. Nagel, R. Hany, T. Lippert, M. Molberg, F. A. Nuesch, and D. Rentsch. "Aryltriazene photopolymers for UV-laser applications: Improved synthesis and photodecomposition study". *Macromolecular Chemistry and Physics*, **208**:277, 2007.

G.S. Settles. *"Schlieren and shadowgraph techniques: visualising phenomena in transparent media"*. Springer-Verlang, Berlin, 2001.

W. A. Tolbert, I. Y. S. Lee, M. M. Doxtader, E. W. Ellis, and D. D. Dlott. "High-Speed Color Imaging by Laser-Ablation Transfer with a Dynamic Release Layer - Fundamental Mechanisms". *Journal of Imaging Science and Technology*, **37**:411, 1993.

I. Zergioti, S. Mailis, N. A. Vainos, C. Fotakis, S. Chen, and C. P. Grigoropoulos. "Microdeposition of metals by femtosecond excimer laser". *Applied Surface Science*, **127**:601, 1998.

I. Zergioti, A. Karaiskou, D. G. Papazoglou, C. Fotakis, M. Kapsetaki, and D. Kafetzopoulos. "Time resolved schlieren study of sub-pecosecond and nanosecond laser transfer of biomaterials". *Applied Surface Science*, **247**:584, 2005.

N. Zhang, X. N. Zhu, J. J. Yang, X. L. Wang, and M. W. Wang. "Time-resolved shadowgraphs of material ejection in intense femtosecond laser ablation of aluminum". *Physical Review Letters*, **99**:167602, 2007.

Chapter 4

Rapid prototyping of photonic devices using LIFT

4.1 Introduction

Channel waveguides are at the heart of a large number of photonic devices/circuits and are most commonly fabricated using photolithography. Photolithography is a well established technique used for mass production of photonic devices and is compatible with the current wafer-scale parallel techniques used in the microelectronics industry. However, for cases that require rapid prototyping of devices, e.g. at the device development stage in any industry, more flexible and faster techniques are needed that allow quick fabrication of good quality devices particularly at the experimental level. Flexibility (essential for rapid prototyping) is one of the key advantages offered by the LIFT technique along with simplicity, less stringent experimental conditions, patterning and transfer in a single step and the ability to transfer on non-planar receiver substrates (Bohandy et al., 1986). We employed LIFT followed by thermal post-processing (Alferness and Buhl, 1980; Hofmann et al., 1999) for the fabrication of channel waveguides and other complex photonic structures in lithium niobate (LN). LN is one of the best dielectric materials in the optoelectronics industry due to its excellent electro/acousto-optical properties. It has been used in a diverse range of applications and has been the work-horse of the optoelectronics industry for switching applications and nonlinear frequency generation (Weis and Gaylord, 1985).

This new method offers both the flexibility of the established non-contact LIFT technique, and the large refractive index change, low optical loss and stability associated with the thermal diffusion method. Additionally, printing of multiple diffusion sources in a single shot, post processing (e.g. repairing or trimming, local addition of secondary in-diffusants) of existing waveguides, local tailoring of the refractive index profile and deposition on pre-patterned non-planar structures, which is challenging for conventional photolithographic methods, are the other advantages offered by this technique.

The chapter begins by describing in section 4.2 the experimental set-up used for fabricating the titanium (Ti) in-diffused channel waveguides and X-couplers in LN using the above mentioned approach. The characterization results are presented in section 4.3 with the loss measurements, optical mode profile characterisation of the devices and the discussion of the results obtained discussed in sub-sections 4.3.1 and 4.3.2, respectively.

4.2 Fabrication

The fabrication of devices was a two step process. First segmented lines of Ti metal were printed on top of LN substrates using the LIFT technique as shown in fig. 4.1. The donor samples were prepared by depositing thin films ($\sim$ 150 nm) of Ti on top of transparent borosilicate glass substrates (50 x 50 x 1 mm) by e-beam evaporation. In the e-beam evaporation technique the target is bombarded with an electron beam that transforms the atoms from the target onto gaseous phase which then precipitate into solid form over the substrate thereby, depositing a thin film of the target material (Singh et al.).

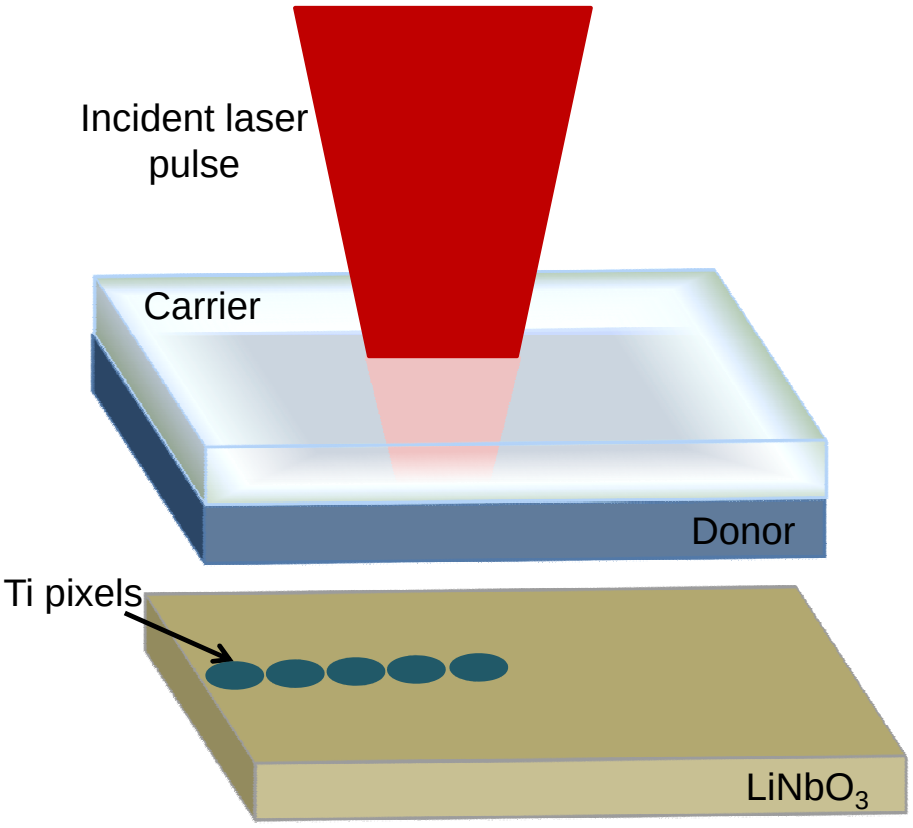

FIGURE 4.1: Schematic showing the LIFTing of segmented Ti lines onto LN substrate.

For all the experiments a commercial Ti:sapphire femtosecond (fs) laser system based around an oscillator (Coherent MIRA 900) and a regenerative amplifier (Coherent Legend-F) was used. The laser system delivered $\approx$ 130 fs pulses with a Gaussian spatial profile having full width at half maximum (FWHM) $\approx$ 10 mm with an average power of 2.5 W at 800 nm. The repetition rate of the laser could be tuned from single shot up to 1 kilo-hertz (kHz). It is the high repetition rate of the laser that made it suitable for this rapid prototyping method. These fs pulses were then demagnified and relayed to the donor-receiver assembly using a commercial micromachining workstation (New Wave UP-266, USA). The micromachiner contained an aperture wheel with aperture diameters varying from $\backsim$ 120 μm to $\gtrsim$ 2 mm. Laser pulses from the amplifier were first reduced using a telescope to $\sim$ 4 mm diameter (FWHM) and then centrally incident on a 450 μm diam-eter aperture of the aperture wheel, resulting in a homogeneous circular beam. A highly demagnified image of the aperture was then relayed to the target using an intermediate relaying lens (f $\sim$ 400 mm) and an objective lens (5 x with $\sim$ 35 mm working distance) resulting in a $\sim$ 10-12 μm diameter spot at the carrier-film interface (as measured by

the laser damaged area). For real time observation of the deposition process a white light source and a CCD camera were used and the image plane of the CCD was adjusted using a lens to coincide with the best image plane of the laser. Figure 4.2 shows the schematic of how the incident laser pulses are relayed to the carrier-donor interface using the micromachining workstation. The donor-receiver assembly was mounted on a highly precise (10 nm resolution), fast (max velocity $\sim$ 100 mm/s), computer-controlled 3D translation stage to achieve relative movement with respect to the incoming laser pulses. It should be noted that as the writing velocity approach the maximum available velocity the resolution decreases. All experiments were performed under a background pressure of 10^{-1} mbar.

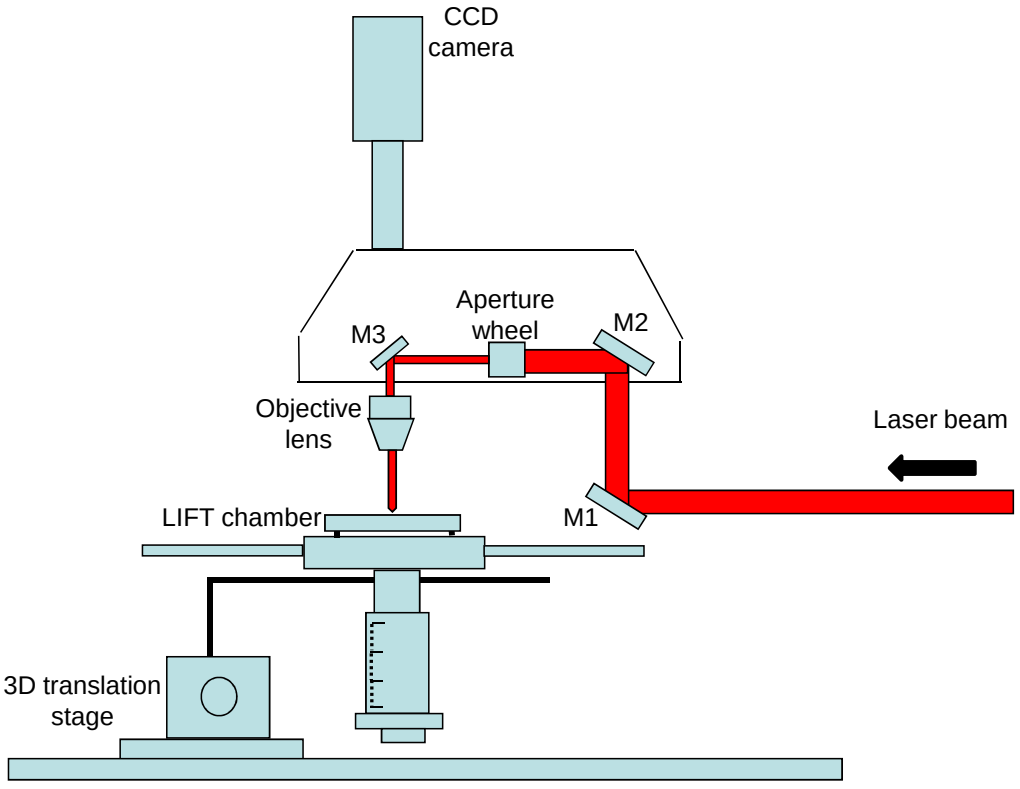

FIGURE 4.2: Show the front view of the micromachiner used for the LIFT experiments. The incident laser pulse is directed to the computer-controlled aperture wheel by the mirrors M1 and M2. The spatial extent of the pulse is controlled by the aperture and the pulse is then directed to an objective lens by the mirror M3. The objective lens then focuses the pulse onto the carrier-donor interface.

Ti metal pixels approximately circular in shape with diameter $\sim$ 10-12 μm (comparable to the incident laser spot size) were printed onto a nearby placed congruent undoped

z-cut LN substrate (18 x 18 mm; the receiver) on –z face along the crystallographic y-direction with the separation between donor and receiver maintained at 1 μm using Mylar spacer. The holes created in the donor substrate after the transfer matched the size of the deposited metal dots. To identify the optimum conditions for LIFT several Ti lines were written with different writing parameters such as fluence values and segment separations. The separation between adjacent Ti dots could be controlled either by adjusting the laser repetition rate or the stage scan speed. The optimum value of laser threshold fluence for Ti metal transfer was found to be ϕ_{th}~0.4 J/cm^2. The effect of laser fluence on the quality of printed dots/lines is shown in fig. 4.3. The best deposits were obtained at ϕ_{th} (4.3 b), below which the transfer was not complete (4.3 a), and on increasing the fluence values the deposits got quite splashy with lot of debris around them (4.3 c). When the laser fluence was further increased etching of the LN substrate was observed (4.3 d) rather than the Ti metal deposition. The reason for this was believed to be the LISE effect (Banks et al., 2009) where the Ti metal layer acted as a shock generation layer for etching the LN substrate in solid phase by the incoming laser pulses. The effect was seen to be more pronounced at slower scan speeds and when the donor and the receiver substrates were kept in tight contact with each other as shown in fig. 4.4 for a scan speed of 0.5 mm/s at a fluence value of $\sim$ 2 J/cm^2.

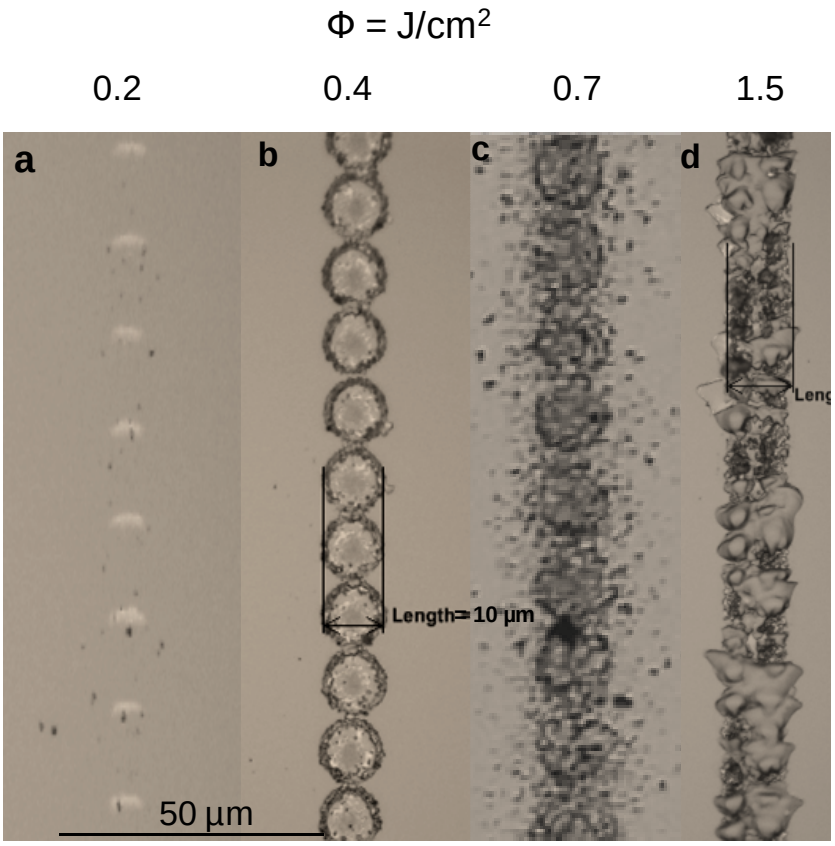

FIGURE 4.3: Optical microscope images of segmented Ti lines deposited at different values of laser fluence.

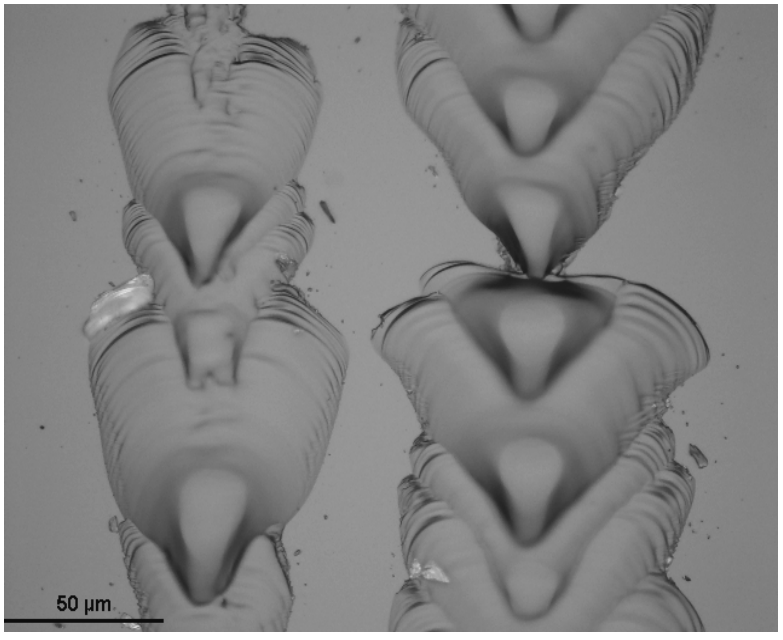

FIGURE 4.4: Etching of LN substrate observed at high fluence values and slow scan speeds due to the LISE effect.

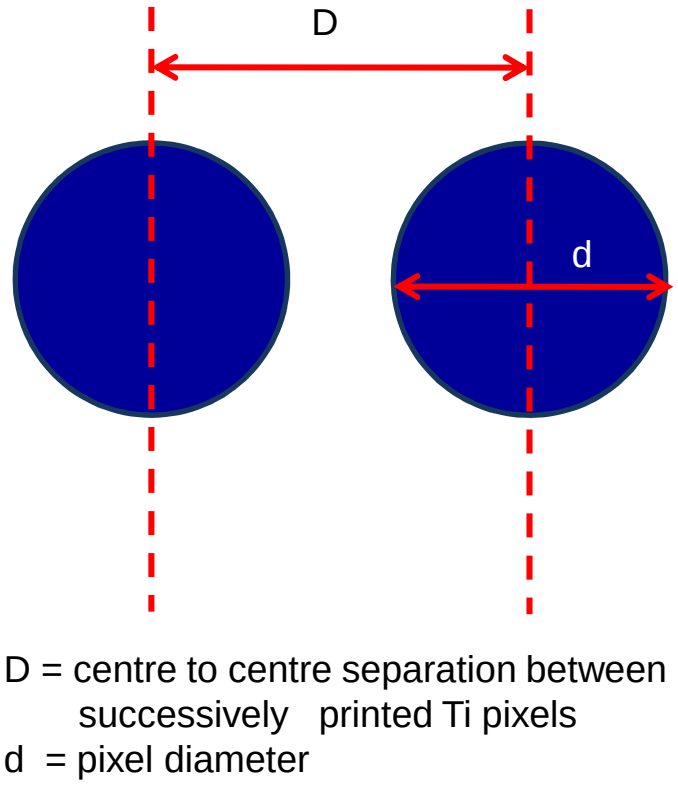

FIGURE 4.5: Schematic illustrating the segment separation.

Figure 4.6 shows optical microscope images of segmented Ti lines printed using LIFT at scan speeds varying from 3 mm/s to 25 mm/s at a laser repetition rate of 1 kHz and a fluence value of $\sim$ 0.4 J/cm^2. The Ti segment centre to centre separation (fig. 4.5) varied from 3 μm (more than 50 % overlapping) to 25 μm (completely separated) corresponding to these scan speeds. Stylus profiling results for the Ti deposits are shown in fig. 4.7. The deposits were of $\sim$ 150 nm thickness (same as the donor thickness) and did not have very smooth surface. The rough surface and edges can lead to a lossy waveguide however, in the case of diffusion the deposited metal is distributed over an area which is roughly 10 % (for Ti on LN) larger than the deposited pixel area. This process will then smooth out any sharp features contained in the original metal dot and as a result the diffusion profile is much smoother than the deposited pattern which is beneficial for the waveguide performance.

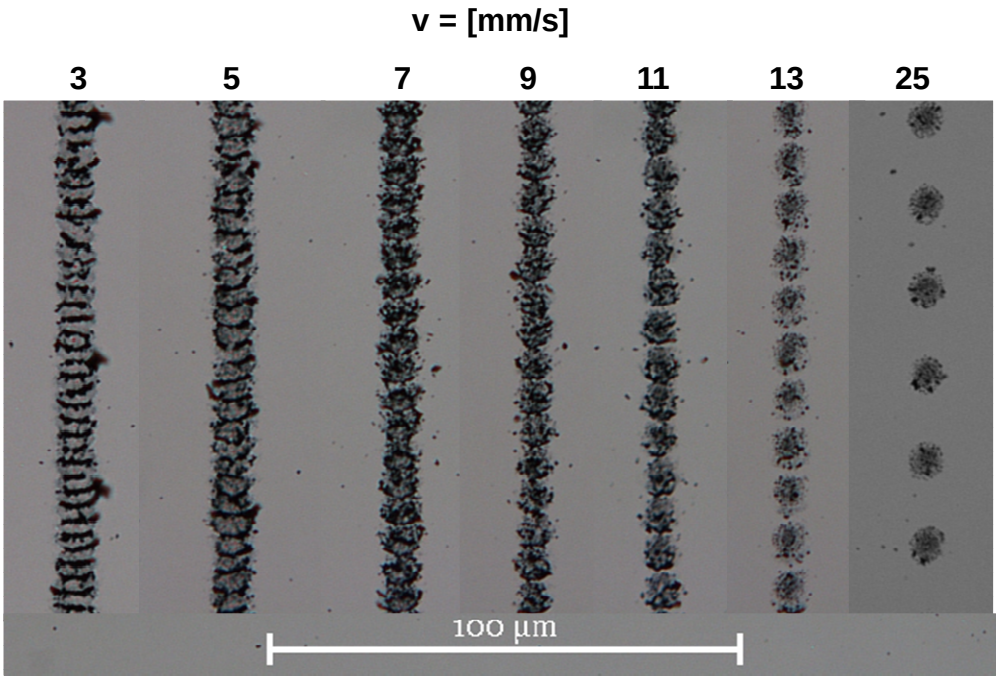

FIGURE 4.6: Optical microscope images of Ti lines printed at different scan speeds. The segment separation increased from 3 μm to 25 μm with increasing the scan speed from 3 mm/s to 25 mm/s at a laser repetition rate of 1 kHz.

After printing, the metal line patterns were successively in-diffused into the LN substrates by placing the samples into a furnace at 1050^{o}C in an oxygen atmosphere for 10 hours. The schematic of the cross-section of Ti in-diffused LN waveguides is shown in fig. 4.8. Figure 4.9 (a) and 4.9 (b) show the optical microscope images of typical deposited linear arrays of Ti pixels at different scan speeds and the corresponding sample area after diffusion respectively. The outline of the deposited metal is still visible after diffusion due to the presence of TiO_2 residue on the surface of the sample. However the TiO_2 residue was not the same for all the deposited lines. The top line with slight overlap of the adjacent Ti dots showed significantly less residue than the bottom line with completely separated Ti dots. This reason for this was believed to be the overlap between adjacent deposited metal pixels that resulted in a partial re-ablation process for each subsequent laser pulse which removed metal from the sample surface thus reducing the available diffusion source for the case of overlapping pixels.

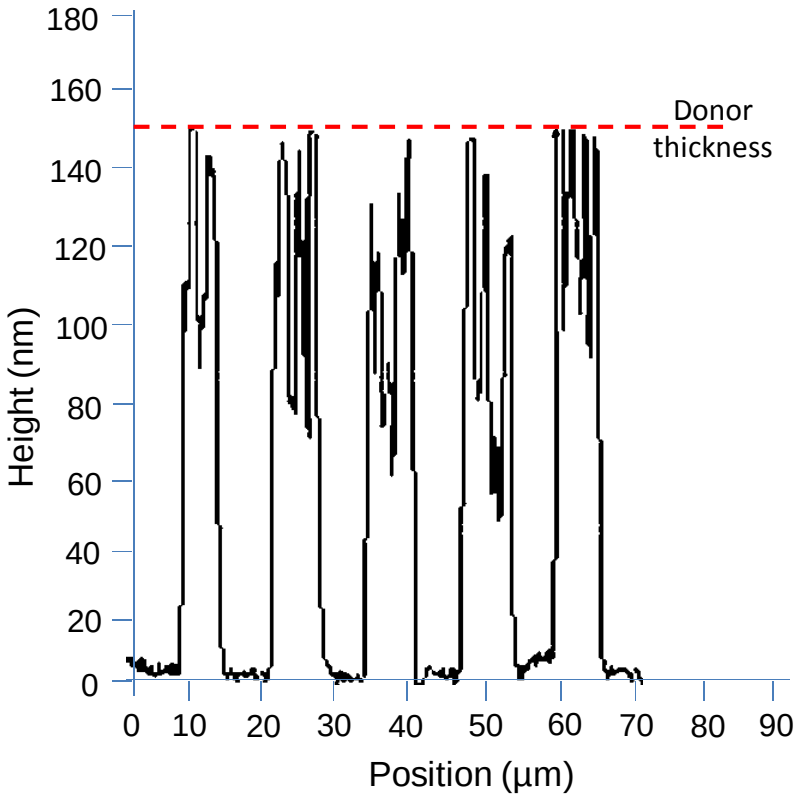

FIGURE 4.7: Stylus profiling measurement of Ti pixelated lines printed using LIFT.

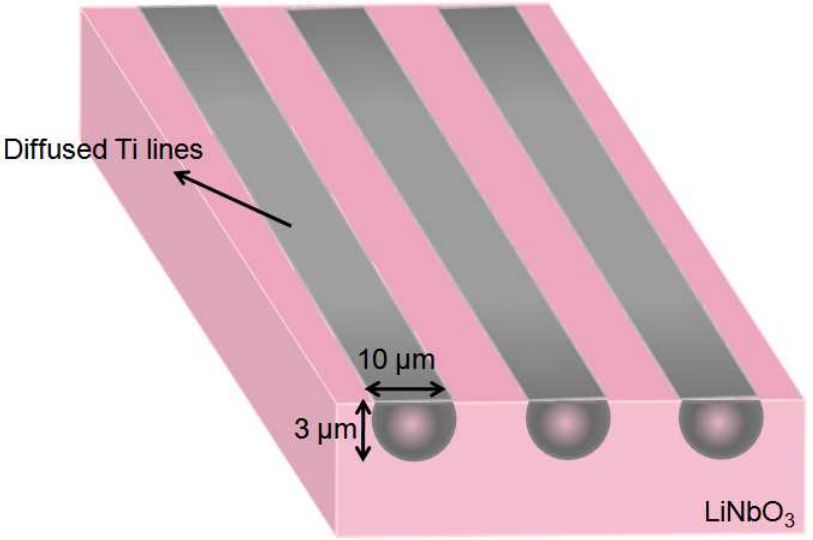

FIGURE 4.8: Schematic of the cross-section of waveguides prepared by thermal in-diffusion of Ti into LN substrate.

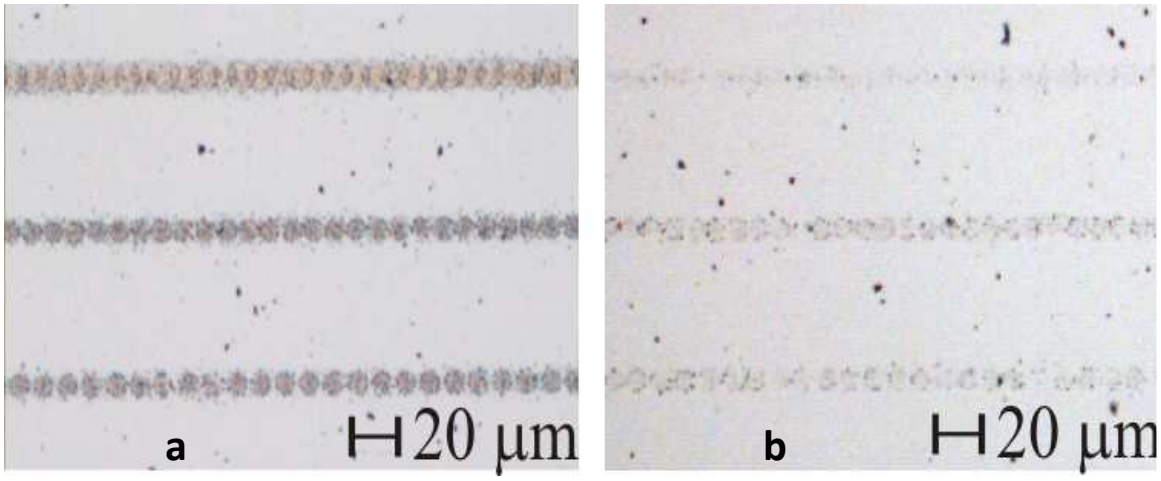

FIGURE 4.9: a) Optical microscope images of linear pixelated Ti LIFTed lines at different separations. b) The same surface of the sample after diffusion has taken place.

4.3 Characterisation

4.3.1 Loss measurements of the waveguides

The in-diffused LN substrates were subsequently edge-polished perpendicular to the Ti lines for characterizing the fabricated optical waveguides. The optical loss of the waveguides was estimated by two different methods: cut-back (Hunsperger, 1982) and Fabry-Perot (FP) (Regener and Sohler, 1985). The set-up used for measuring the losses of the waveguides is shown in fig. 4.10. Light from a tunable fiberised laser was coupled into the waveguides using an objective lens (40 x) and the output was collected using another objective lens (40 x) and the throughput was measured using a power meter. Cut-back method involved repetitive measurement of throughput for progressively shorter channel lengths. First the losses were measured for $\sim$ 17 mm long samples which were then cut into two shorter length samples ($\sim$ 8.8 mm and $\sim$ 5.2 mm) and these samples were then again edge polished for throughput measurements. Cut-back was clearly a destructive and time-consuming method and is therefore of limited utility for measurement of waveguide loss. The second method relied on formation of a low finesse Fabry-Perot cavity between the two end faces of the waveguide. In this method the light was launched into the waveguide using a single mode fibre and the coupled light formed

a standing wave pattern within the waveguide. The contrast of these fringes (standing wave pattern) of the optical cavity gave an estimate of the upper limit to optical loss in the waveguide. Table 4.1 shows the range of loss values measured for the Ti:LN segmented waveguides using these two techniques.

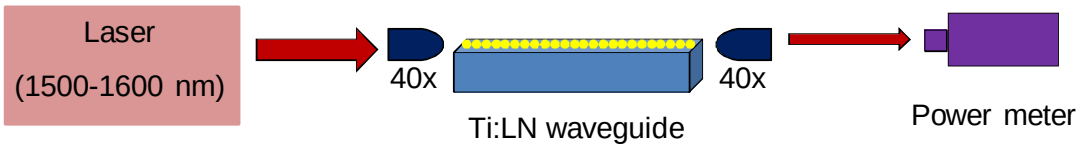

FIGURE 4.10: Experimental set-up used for measuring the loss of Ti:LN waveguides.

Both methods confirmed that large segment separations resulted in increased optical loss mainly due to poor confinement of the light inside the waveguide. The lowest propagation loss of $\sim$ 0.8 dB/cm was measured, using cut-back method, for transverse magnetic (TM) modes in the telecommunication wavelength range for waveguides written with a segment separation of 11 μm. For waveguides with segment separation of 7 μm the loss was measured to be $\sim$ 2.4 dB/cm and for waveguides having larger segment separations of $\geq$ 13 μm the measured loss was much much higher ($\sim$ 7 dB/cm) due to optical leakage of the guided wave to the substrate. Typical loss values reported in literature for Ti-indiffused waveguides are of order of $\sim$ 0.1 dB/cm. The factors that contributed to the higher losses from the waveguides produced by LIFT are thought to be i) the rough surface quality of the printed Ti dots and ii) the TiO_2 residue on the waveguide surface after diffusion. To improve the surface quality of the dots further optimisation of the deposition process is required and a thinner Ti donor film could result in little or no final TiO_2 residue. Apart from the rough surfaces of dots and TiO_2 residues the corrugations introduced in the waveguides by the circular geometry of Ti dots could also lead to additional scattering losses. Printing square or rectangular Ti segments (using the corresponding aperture) might help in bringing down the waveguide scattering losses. However, even with the non-optimal deposition quality and geometry, and after diffusion, residual losses as low as $\sim$ 0.8 dB/cm measured from the waveguides further confirms the potential of this technique for rapid prototyping of good quality optical waveguide devices.

Technique	Waveguides written with Ti dot separations in the range of (μm)	Range of loss values (dB/cm)
FP	10 - 13	1.5 - 7.7
Cut-back	11 - 15	0.8 - 7

TABLE 4.1: Waveguide losses measured using FP and cut-back methd at 1550 nm.

4.3.2 Mode profile characterization

The main feature of the optical waveguides fabricated by LIFT deposition was that the refractive index change along the length of the waveguides was not regular and continuous but there was a local refractive index increase within the volume where Ti metal had been diffused. The refractive index profile along the channel waveguide should, to some extent, reflect the Ti deposition pattern. The separation of the adjacent pixels or segments defines the average refractive index value along the waveguide hence different separations should result in different mode sizes. This was verified by characterizing the optical mode profiles of two distinct waveguides written with different speeds and hence different Ti segment separations. The experimental set-up used for capturing mode profiles of the waveguides was the same as that used for the cut-back method (fig. 4.10) but with the power meter being replaced with an infrared (IR) camera. The significantly different mode sizes of the fundamental modes obtained from these two waveguides at the probe wavelength of 1.532 μm is as shown in fig. 4.11. These waveguides were fabricated by scanning the samples at speed of 9 mm/s and 19 mm/s that corresponded to a segment separation of 9 μm (slight overlap) and 19 μm (complete separation) respectively for repetition rate of the laser set at 1 kHz. The average refractive index change for the more closely spaced depositions resulted in tighter confinement as observed in the mode profile shown in fig. 4.11 (a) while the less dense deposition resulted in a much larger waveguide mode profile shown in fig. 4.11 (b). In the case of waveguides with a partial overlap between successively deposited Ti-metal segments, any possible re-ablation of the deposited Ti metal segments would reduce the total amount of the deposited metal in the overlapping area. However for the range of overlaps used we observed that it was the segment separation that predominantly determined the mode profile of the resulting waveguide and the re-ablation had a negligible effect on it.

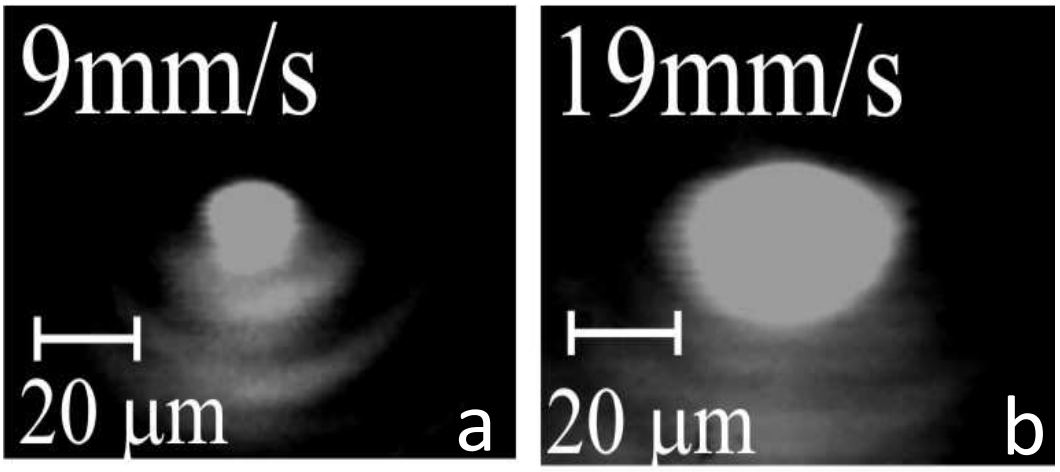

FIGURE 4.11: Near-field mode profiles of LIFT/diffused segmented Ti:LN waveguides corresponding to a) 9 μm and b) 19 μm segment separation.

As discussed above there should be some correlation between the refractive index profile along the channel waveguide and the Ti deposition pattern. It is possible to calculate the mode index of the waveguide by monitoring the mode profile and we used the method as discussed in (Ganguly et al., 2009) to do that [1]. The scalar wave equation for the fundamental mode of a waveguide is given by (McCaughan and Bergman, 1983):

$$\nabla^2 A(x,z) + [k^2 n^2(x,z) - \beta^2] A(x,z) = 0 \tag{4.1}$$

where

$$A(x,z) = [I(x,z)^{1/2}] \tag{4.2}$$

$$k = 2\pi/\lambda \tag{4.3}$$

I (x,z) is the normalized modal intensity, λ is the wavelength, n (x,z) is the refractive index of the waveguide, β is the propagation constant of the fundamental mode, x and z correspond to lateral and depth dimensions of the waveguide. Rearranging Eq. 4.1 gives

$$n^2(x,z) = (\frac{\beta^2}{k^2} - \frac{\nabla^2 A}{k^2 A}) \tag{4.4}$$

[1] These simulations were done by Dr. Pranabendu Gangopadhyay from the Indian Institute of Kharagpur, India

The refractive index change $\triangle n$ (x,z) of a single mode waveguide due to Ti in-diffusion is given by

$$\triangle n(x,z) = (\frac{\beta^2}{k^2} - \frac{\nabla^2 A}{k^2 A})^{1/2} - n_s \tag{4.5}$$

where n_s is the LN substrate refractive index. The refractive index change and mode index of the single-mode waveguides can be determined simultaneously using the following computation steps (Ganguly et al., 2009):

1. The measured near-field profile is fitted with a Gaussian distribution.
2. The result of the fit are used to compute the refractive index profile using Eq. 4.5, by taking the mode index equal to the substrate index.
3. Finally, the mode index value is increased to get the minimum refractive index change to be equal to zero outside the waveguide region.

We chose to fabricate the waveguides to be single moded at 633 nm in order to benefit from the measuring accuracy of our beam profiler (which has a silicon detector that is not sensitive to telecom wavelengths). The Ti donor layer used for the LIFT depositions was $\sim$ 150 nm thick, the laser repetition rate was set to 250 Hz, the segment separation was varied between 8 μm and 16 μm and the laser fluence used for transfer was $\sim$ 0.4 J/cm^2. The intensity profiles of these single mode waveguides (at 633 nm) were used for the calculation of the effective mode profiles using the method described above. The waveguide mode profiles were controlled just by varying the writing speeds. Figure 4.12 shows three different mode profiles which corresponded to three different segment separations as a result of different scanning speeds used during Ti deposition. It is clear that the mode changed from single to higher order mode by just changing the scanning speeds from 3.25 mm/s to 2 mm/s, which corresponded to segment separations of 13 μm and 8 μm respectively at 250 Hz. These results strengthens the versatility of this LIFT based technique for fabricating waveguides with pre-designed modal intensities. These results also suggested the possibility of changing the waveguide propagation characteristics along the length of the waveguide simply by manipulating the segment separation along the length to fabricate complex photonic devices such as mode filters and converters (discussed in the next chapter).

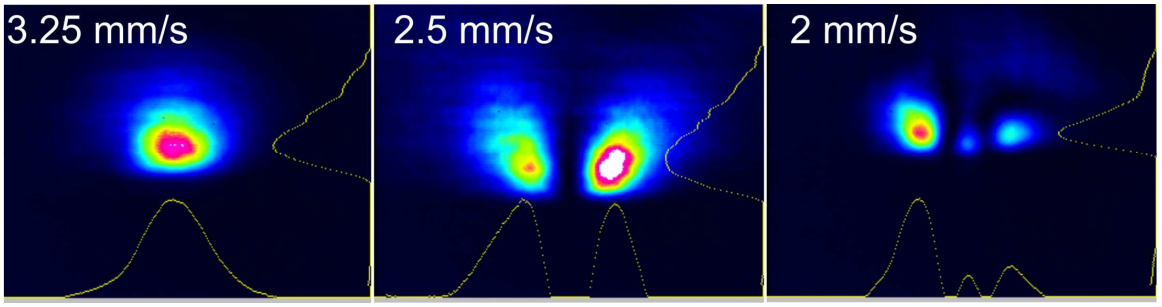

FIGURE 4.12: Near-field intensity profiles of three different waveguides fabricated with different segment separation by changing the deposition scanning speed as indicated in the figure.

Figure 4.13 shows a plot of the calculated effective indices (for TM modes) as a function of the segment separation. The extraordinary refractive index of LN is 2.13807 and the corresponding Δn value after Ti diffusion is 0.018. For segment separations longer than 16 μm there was no confinement of light (cut-off) while for separations less than 11 μm the waveguides became multi-moded. As expected the effective mode index decreased with increasing segment separation, as the average refractive index along the waveguide decreased, until cut-off was reached for a separation of 16 μm.

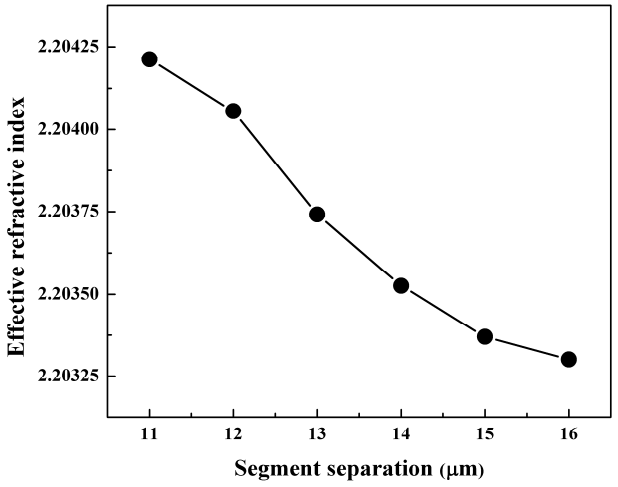

FIGURE 4.13: Calculated effective refractive indices of single mode waveguides as a function of segment separation. These effective indices correspond to TM modes.

In order to demonstrate the device fabrication functionality of this rapid prototyping method an X-coupler, which consisted of two straight channel waveguide crossing each other at a specific angle (Nakajima et al., 1982) was fabricated. The waveguides that constitute the X-couplers were fabricated by depositing Ti segmented lines at a writing

speed of 2.5 mm/s for a laser repetition rate of 250 Hz that corresponded to a segment separation of $\sim$ 10 μm. The angle between the two crossing waveguides was kept at a small value of 2 ^{0} for a reasonable overlap between them. Figure 4.14 (a) and 4.14 (b) show the schematic and an optical microscope image of the X-coupler fabricated respectively. The coupling ratio was measured at 1.55 μm by coupling light into one of the channels and measuring the power output of each channel on the opposite edge. The coupling ratio (for TM modes) was measured to be $\sim$ 0.2. The output edge of the X-coupler was imaged onto an IR camera.

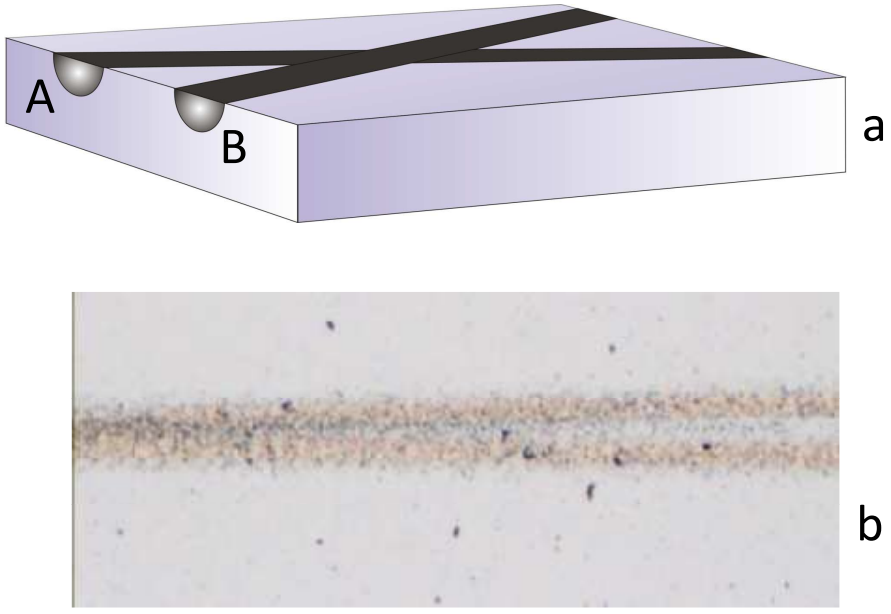

FIGURE 4.14: a) Schematic of the X-coupler b) optical microscope image of a 2 ^{0}coupler fabricated using the LIFT/diffusion process.

Figure 4.15 shows the images of the X-coupler output when light was launched into the waveguide A (4.15 (a)) and waveguide B (4.15 (b)) respectively, as indicated in the mode images. The mode profiles of A and B were not identical and the reason for this was an asymmetry in the fabrication of the constituent waveguides. This asymmetry was most likely due to the slight misalignment between the donor and the receiver assembly during the deposition process.

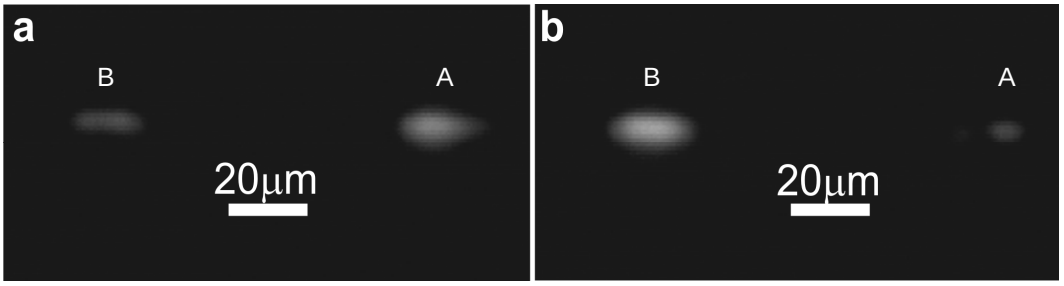

FIGURE 4.15: Near-field intensity profiles of the outputs of an X-coupler.

4.4 Conclusions

In this chapter we presented a method based on LIFT followed by thermal post-processing for the rapid prototyping of optical waveguide devices. Experimental set-up used for fabricating Ti in-diffused segmented waveguides in ferroelectric LN crystal was demonstrated in section 4.2. The characterisation of the fabricated channel waveguides that included loss and optical mode profile measurements of the waveguides were discussed in sub-sections 4.3.1 and 4.3.2 respectively of section 4.3. Losses as low as 0.8 dB/cm were obtained for some of the waveguides and the segment separation was observed to play a crucial role in determining the mode profiles of the waveguides. At smaller segment separations < 11 μm the waveguides were seen to be multimoded while for segment separations that increased up to 16 μm the waveguides became single moded with less tightly confined modes. Apart from straight channel waveguides fabrication and characterisation of X-couplers was also demonstrated using this method in section 4.3.2.

Bibliography

R. C. Alferness and L. L. Buhl. "Electro-Optic Wave-Guide TE-TM Mode Converter with Low Drive Voltage". *Optics Letters*, **5**:473, 1980.

D. P. Banks, K. S. Kaur, and R. W. Eason. "Etching and forward transfer of fused silica in solid-phase by femtosecond laser-induced solid etching (LISE)". *Applied Surface Science*, **255**:8343, 2009.

J. Bohandy, B. F. Kim, and F. J. Adrian. "Metal-Deposition from a Supported Metal-Film Using an Excimer Laser". *Journal of Applied Physics*, **60**:1538, 1986.

P. Ganguly, C. L. Sones, Y. J. Ying, H. Steigerwald, K. Buse, E. Soergel, R. W. Eason, and S. Mailis. "Determination of Refractive Indices From the Mode Profiles of UV-Written Channel Waveguides in $LiNbO_3$-Crystals for Optimization of Writing Conditions". *Journal of Lightwave Technology*, **27**:3490, 2009.

D. Hofmann, G. Schreiber, C. Haase, H. Herrmann, W. Grundkotter, R. Ricken, and W. Sohler. "Quasi-phase-matched difference-frequency generation in periodically poled Ti : $LiNbO_3$ channel waveguides". *Optics Letters*, **24**:896, 1999.

R. G. Hunsperger. *"Integrated Optics: Theory and Technology"*. Springer, New York, sixth edition, 1982.

L McCaughan and .E.E Bergman. "Index distribution of optical waveguides from their mode profile". *Journal of Lightwave Technology*, **1**:241, 1983.

H. Nakajima, T. Horimatsu, M. Seino, and I. Sawaki. "Crosstalk Characteristics of Ti-$LiNbO_3$ Intersecting Waveguides and Their Application as TE-TM Mode Splitters". *IEEE Journal of Quantum Electronics*, **18**:771, 1982.

R. Regener and W. Sohler. "Loss in Low-Finesse Ti-$LiNbO_3$ Optical Wave-Guide Resonators". *Applied Physics B-Photophysics and Laser Chemistry*, **36**:143, 1985.

J. Singh, J.T Schriempf, and E.D. Wolfe. “Electron Beam Physical Vapor Deposition Technology: Present and Future Applications”. Technical report, The Applied Research Laboratory, The Pennsylvania State University.

R. S. Weis and T. K. Gaylord. “Lithium-Niobate - Summary of Physical-Properties and Crystal-Structure”. *Applied Physics a-Materials Science & Processing*, **37**:191, 1985.

Chapter 5

Waveguide mode filter fabricated using LIFT

5.1 Introduction

In the previous chapter segmented waveguides fabricated using LIFT were presented and it was shown that the mode profile of the waveguides depends on the Ti segment separation: if the segment separation is varied along the length of the waveguide its propagation characteristics can be altered accordingly. Based on this idea a segmented waveguide mode filter was fabricated using LIFT and this is now discussed in this chapter. The mode control was achieved by adjusting the separation between adjacent Ti segments thus varying the average value of the refractive index along the length of the in-diffused channel waveguides. Mode filters are particularly important for non-linear applications such as frequency converters where it is difficult to have the single mode regime for all the interacting (especially the shorter pump) wavelengths. The common technique used for fabricating segmented mode filters is proton exchange (Jackel et al., 1982). However (as also discussed in the previous chapter) for cases that require rapid prototyping of devices more flexible and faster techniques are needed that allow rapid fabrication of good quality devices, particularly at the experimental level. Fabricating the mode filters using LIFT offers both the flexibility of the LIFT technique, and the large refractive index change, low optical loss and stability associated with the thermal diffusion method along with all the other advantages mentioned in the previous chapter.

The device fabrication details are provided in sub-section 5.2.1. This is followed by their characterization, that includes loss and optical mode profile measurements, in subsections 5.3.2 and 5.3.3, respectively. Theoretical simulation results discussing the devices performance and finally the conclusions are presented in sections 5.4 and 5.5 respectively.

5.2 Experiments and results

5.2.1 Fabrication

The process used for fabricating the index tapered mode filters was a two step process similar to that used for producing the channel waveguides with slight modifications in the writing conditions. As before segmented lines of Ti metal, formed from sequential Ti pixels, each $\sim$10 μm in diameter, were first printed on top of the -z face of LN substrates (18 x 18 mm; the receiver) along its crystallographic y-direction, using the LIFT technique as shown in fig. 5.1. The donor samples were prepared as earlier by depositing thin films ($\sim$ 150 nm) of Ti on top of transparent borosilicate glass substrates (50 x 50 x 1 mm; the carrier) by e-beam evaporation. The donor-receiver assembly was mounted on a high precision (10 nm resolution), fast (max velocity $\sim$ 100 mm/s), computer-controlled 3-axis (x,y,z) translation stages to achieve its relative movement with respect to the incoming laser pulses. All experiments were performed under a background pressure of 10^{-1} mbar. For details of the experimental set-up please refer to section 4.2 and fig. 4.2 of chapter 4. The laser threshold fluence value used for transfer of Ti dots was $\sim$ 0.4 J/cm^2 and the separation between donor and receiver was maintained at 1 μm using a Mylar spacer. After printing, the deposited metal lines were subsequently diffused into the LN crystal by heating it to 1050 ^{0}C in an oxygen atmosphere for 10 hours.

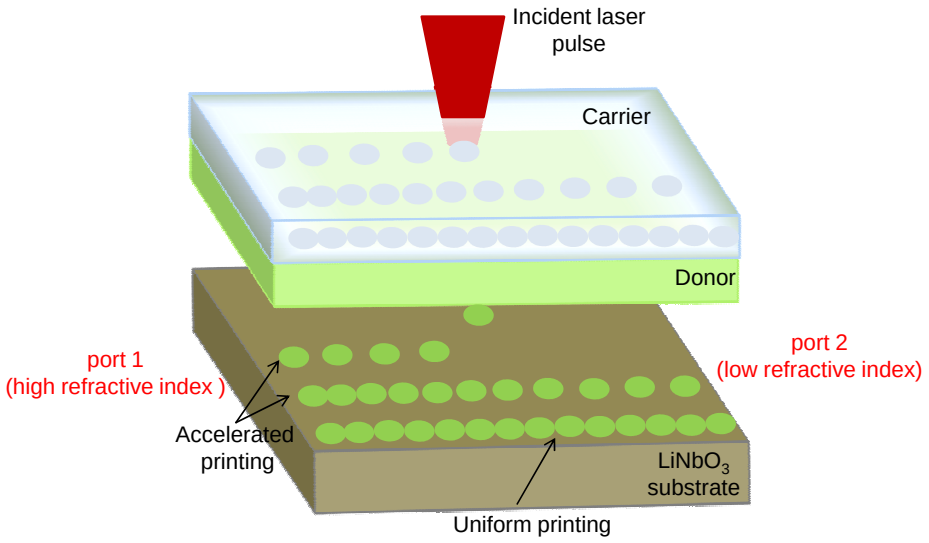

FIGURE 5.1: Schematic showing the LIFTing of segmented Ti lines onto LN substrates. The exaggerated version of how the Ti dots separate out by increasing speed from one end of the substrate to the other for fabrication of a tapered waveguide as well as constant velocity lines for comparison are also shown.

All the channel waveguides discussed in the previous chapter were fabricated by keeping the laser writing repetition rate or the stage scan speed constant along the length of the waveguide. To realize index tapered waveguides the segmented metal lines were written by varying the writing speeds across the segmented Ti lines at a constant acceleration. The reason for writing lines at constant acceleration was to avoid any sudden change in index to minimize losses and to obtain a smooth mode filter effect from the tapered waveguides. The idea was to have the ability to alter the behavior of the waveguides just by manipulating the scan speed and hence the segment separation along the length of the waveguides. The segment separation increased with increasing scan speed thereby decreasing the average amount of material deposited and then diffused per unit length which in turn decreased the average effective index of the mode. The mode confinement decreased with increasing speed and the waveguide modal behavior changed from multi-mode to single-mode. By increasing the segment separation and hence the index contrast a mode filter was realized that allowed only the fundamental mode to propagate. Three different values of constant acceleration 0.3, 0.4 and 0.5 mm/s^2 were used for fabricating the index tapered waveguides. The initial velocity was kept constant at 2.5 mm/s for all the tapers. Waveguides with a constant velocity of 2.5 mm/s that corresponded to

a segment separation of 10 μm were also written for comparison. A schematic of the index tapered waveguides fabricated by increasing the Ti dots separation from one end of the waveguide to the other along with the constant velocity segmented waveguides is shown in fig. 5.1. The samples were then end polished for optical characterisation and loss measurements.

5.2.2 Loss measurements

To measure the waveguide losses three different techniques were used namely FP (Castaldini et al., 2007); fibre mismatch (Tittelbach et al., 1993) and mode mismatch (Campbell, 1979). All these losses were measured at 1550 nm and the samples were 16 mm in length. In the FP method, the light from a tuneable laser (1500-1600 nm) was launched into the waveguide using a single mode fibre (SMF) and the output was collected by a detector that was controlled by a computer using LabView interface. The output was oscillatory in nature because of the standing waves formed inside the waveguide by tuning the wavelength. The contrast of the fringe pattern was used to calculate the propagation loss. It should be mentioned that due to uncertainty of the reflection coefficient of the end-facets, this method gave an upper limit on the optical loss in the waveguides. The loss measured in our samples was in the range of 4.6 $\pm$ 0.8 dB/cm at 1550 nm. In the fibre mismatch technique a SMF was used to launch the input light into the waveguide and the output was first collected using a similar SMF and then with a multimode fibre (MMF). The difference in the collection efficiency gave the coupling loss of 6 dB for the SMF. In this technique it was assumed that the MMF collected all the output light from the waveguide. The propagation loss was then calculated by taking the difference between the insertion loss (total loss due to the waveguide) and the coupling loss. The insertion loss of the waveguides was measured to be 11 dB resulting in a propagation loss of 3.1 $\pm$ 1 dB/cm. In the mode-mismatch technique, mismatch between the input fibre mode and the waveguide mode was calculated by performing an overlap integral between the two modes that gave an estimate of the coupling loss of 5 dB. The propagation loss of 3.7 $\pm$ 0.65 dB/cm was obtained again by taking the difference between the insertion loss (11 dB) and the coupling loss. All three techniques yielded almost similar waveguide loss within experimental error. The loss values measured for the tapered waveguides were more than those measured for the constant velocity waveguides presented in the previous chapter. These higher values of losses were attributed to the

variation in the velocity and hence average refractive index along the waveguide length for the tapers. The loss values measured for the index tapered waveguides using the three different techniques discussed above are listed in Table 5.1.

Measurement technique	Losses measured (dB/cm)
Fabry-Perot	4.6 ± 0.8
Fibre-mismatch	3.1 ± 1
Mode-mismatch	3.7 ± 0.65

TABLE 5.1: Losses measured for index-tapered waveguides using three different techniques at 1550 nm.

5.2.3 Optical characterization

For optical characterization of the waveguides the set-up shown in fig. 5.2 was used. Light from a tunable fiberised laser (1500-1600 nm, TM polarization) was coupled into the waveguides from port 1 using an objective lens (40 x). The output was collected using another objective lens (40 x) and the near-field mode profiles were observed using an IR camera. All these measurements were performed at 1550 nm and the waveguide samples and objective lenses were mounted on a 3-axis (x,y,z) translational stage.

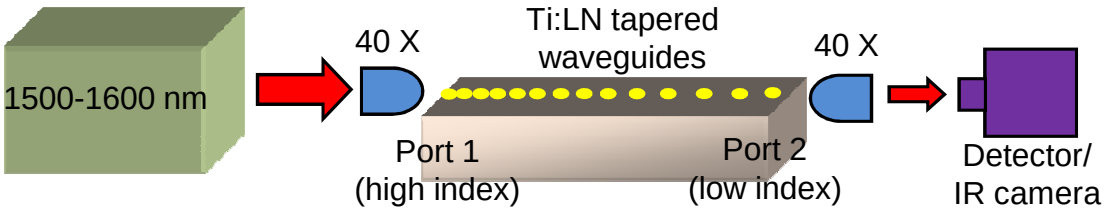

FIGURE 5.2: Experimental set-up used for optically characterizing the waveguides

Figure 5.3 (a) shows an optical mode profile of a segmented waveguide written with a constant velocity of 2.5 mm/s. The waveguides were multimode in nature and supported two modes (TM_{00} and TM_{01}). Figures 5.3 (b), (c) and (d) show the optical mode profiles of index tapered waveguides corresponding to Ti deposition with constant acceleration

of 0.3, 0.4 and 0.5 mm/s^2 respectively with an initial velocity of 2.5 mm/s when light was launched from port 1 as shown in fig. 5.2. The images clearly depict that the tapers supported only the fundamental mode (TM_{00}) thereby exhibiting the mode filtering operation. This was attributed to the fact that as the separation between the printed dots increased the average effective index decreased accordingly leading to the cut-off of the higher order modes leaving only the fundamental mode propagating. Similar results were obtained even when the coupling conditions were altered by moving the waveguides with respect to the input beam in the transverse direction to excite higher order modes indicating that port 2 of the tapered waveguides could support only the fundamental mode. When the acceleration value was increased beyond 0.5 mm/s^2 the waveguides ceased to guide all together due to the waveguide reaching its cut-off value. As the writing speed/acceleration was increased the mode size increased as well. The reason being the same as discussed in the previous chapter that the decrease in the index contrast with increasing segment separation lead to a broader and less tightly confined mode. The Gaussian fit for the mode profiles of tapers fabricated with 0.3, 0.4, 0.5 mm/s^{2}acceleration (shown in fig. 5.5) clearly depicted the increase in the mode field diameter (MFD) with increasing acceleration with the corresponding MFD values presented in table 5.2.

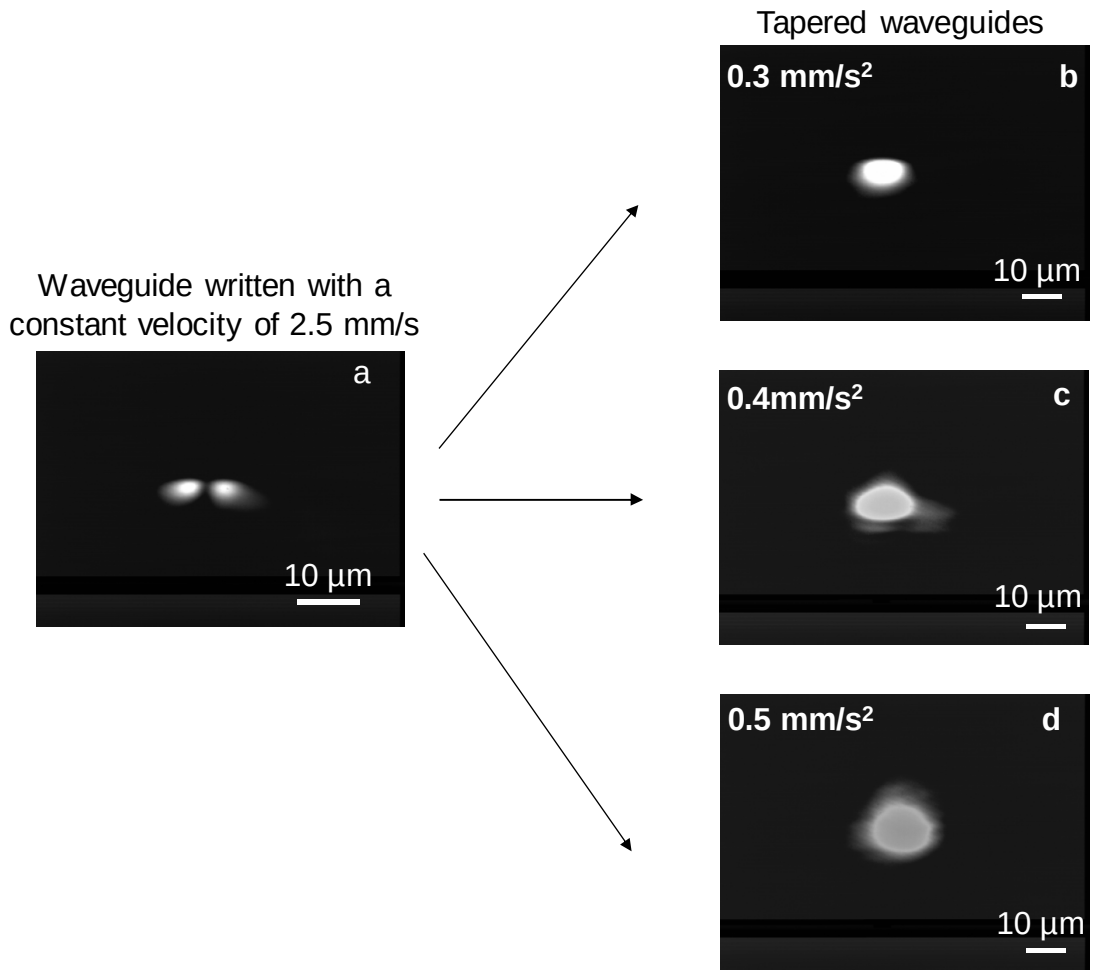

FIGURE 5.3: (a) Near field intensity profiles captured from a waveguide written with a constant velocity of 2.5 mm/s. (b-d) near field intensity profiles of tapered waveguides written at accelerations of 0.3, 0.4 and 0.5 mm/s^2 respectively when the light was launched from port 1.

When the laser light was launched from port 2 (fig. 5.2) a much more tightly confined fundamental mode was obtained on the higher index port 1 of the tapers as expected (shown in fig. 5.4 (a)). The Gaussian fit for this mode is also shown in fig. 5.5 with the corresponding value given in table 5.2. However upon altering the launching angle a higher order mode was monitored at the same port as shown in fig. 5.4 (b) for a waveguide written with an acceleration of 0.3 mm/s^2. This behavior is not expected for an adiabatic taper however the corrugation in the refractive index distribution along the waveguides caused by the shape of the printed Ti dots is believed to be responsible for this non-adiabatic behavior of the device. Modeling results, which will be discussed in the next section, confirmed this observation.

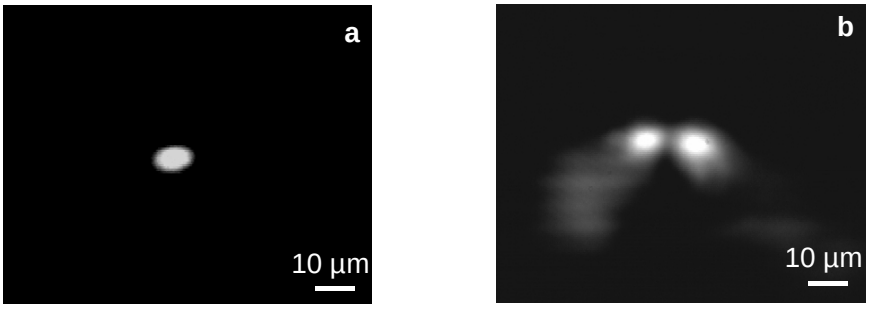

FIGURE 5.4: Near field intensity profiles corresponding to the waveguide written with an acceleration of 0.3 mm/s^2 when the light was launched from port 2.

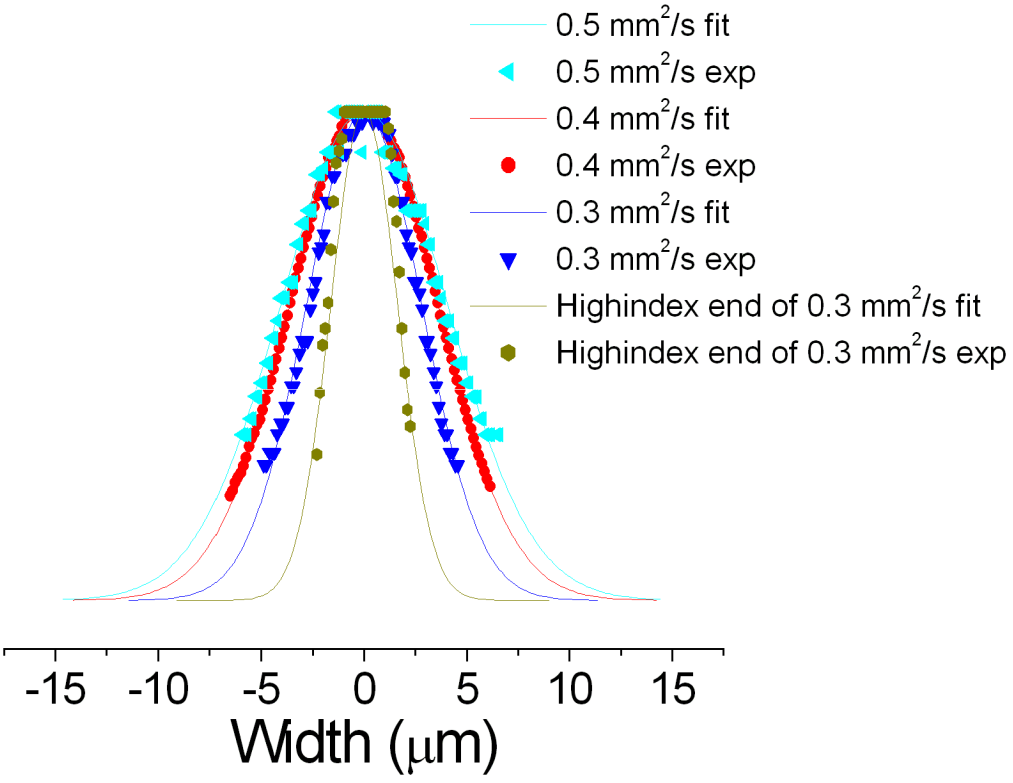

FIGURE 5.5: Shows the Gaussian fit to the experimental data for mode profiles captured for waveguides written with an acceleration of 0.3(▼), 0.4(●) and 0.5(◄) mm/s^2 respectively when the light was launched from port 1, thereby, clearly depicting the increase in the MFD with acceleration. The tighter confinement of the fundamental mode on the higher index port 1 is also shown for tapered waveguide written with 0.3 mm/s^2 (♦) acceleration when the light was launched from port 2.

Waveguides written with constant acceleration of	Intial and final edge to edge Ti dot separations (μm)	Gaussian fit MFD (μm)
0.3 mm/s^2 (light launched from the port 1)	0 - 3	$\sim$ 11.5
0.4 mm/s^2 (light launched from the port 1)	0 - 4.5	$\sim$ 14.5
0.5 mm/s^2 (light launched from the port 1)	0 - 5.8	$\sim$ 16.5
0.3 mm/s^2 (light launched from the port 2)	3 - 0	$\sim$ 8.5

TABLE 5.2: Gaussian fit MFD values for mode profiles captured from waveguides written with acceleration of 0.3, 0.4 and 0.5 mm/s^2 respectively when the light was launched from port 1, thereby, clearly depicting the increase in the MFD with acceleration; along with the MFD value for the fundamental mode on the higher index port 1 for tapered waveguide written with 0.3 mm/s^2 acceleration when light was launched from port 2. The corresponding intial and final Ti dot separations for the different accelerations are also presented in the second column.

5.3 Theoretical modeling

To understand the non-adiabatic nature of the tapers fabricated using LIFT the light propagation both along segmented Ti:LN and continuous index tapers was modeled. First a 3D model of Ti ion diffusion of LIFT-deposited dots at high temperature was developed with dot separation varying from zero to 3 μm in steps of 0.5 μm (edge to edge dot separation as shown in fig. 5.6) by solving the following partial differential equation for diffusion.

$$\frac{\partial C}{\partial t} = \nabla \left[D \nabla C \right] \tag{5.1}$$

where C is the Ti ion concentration, t is the time and D is the diffusivity of Ti ions in LN (1.1 x $10^{-4}\mu m^2 s^{-1}$ for all orientations in LN at 1050^0C (Filho et al., 1997) thereby simplifying equation 5.1 to:

$$\frac{\partial C}{\partial t} = D\nabla^2 C \tag{5.2}$$

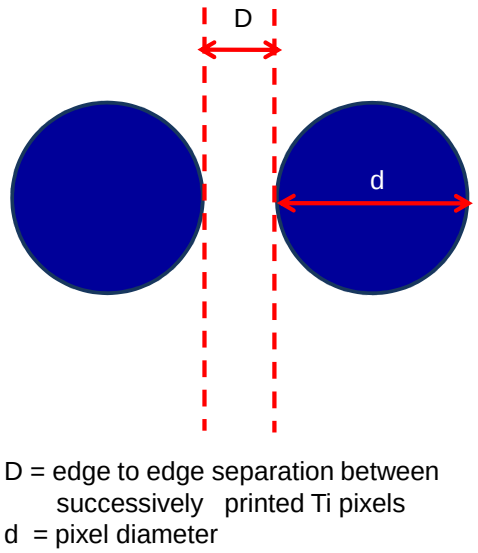

FIGURE 5.6: Schematic showing the edge to edge dot separation

The solution of equation 5.2 gave the 3D Ti ion concentration distribution which was then transferred to the corresponding 3D refractive index profile using the method discussed in (Fouchet et al., 1987). The zero and 3 μm separation values corresponded to the initial and final dot separation for the tapered waveguides written using 0.3 mm/s^2 acceleration. The maximum refractive index contrast values over this range of segment separation values varied from 0.0406 to 0.0322. In the actual experiments the samples were $\sim$ 16 mm long but theoretical modeling was not possible for these lengths due to excessively large computer memory requirements. The simulation of light propagation in the waveguides was therefore restricted to shorter lengths ($\sim$ 700 μm) and qualitative results were obtained using COMSOL multiphysics software. The structure was built by drawing 7 sections, each section containing 10 Ti discs with 0, 0.5, 1, 1.5, 2, 2.5, 3 μm separations respectively. The concentration distribution and the corresponding refractive index profile was first calculated for one quadrant of the dot for each set and the other 3 quadrants were obtained by mirror imaging as the boundary conditions were

symmetric. For the second dot the first dot was just mirror imaged along the y-axis and by continuing this process the whole set of 10 dots was obtained. Similar steps were followed for each of the remaining 6 sections to realize the whole structure. The corresponding refractive index profile of the structure is illustrated in fig. 5.7 (a) as variation of the intensity of the segments along the waveguide.

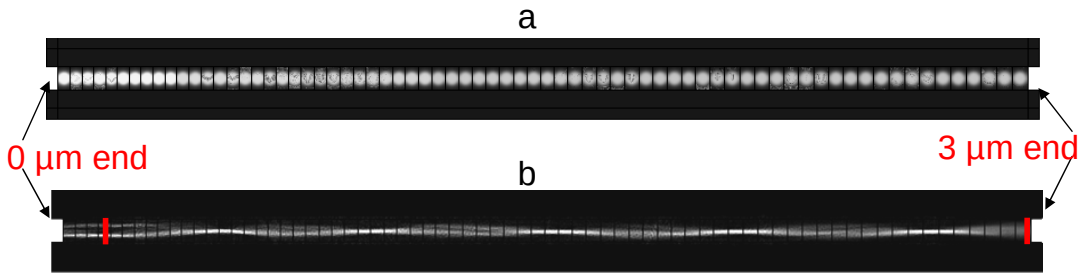

FIGURE 5.7: (a) Shows the refractive index profile for the segmented Ti:LN waveguide with the brighter regions corresponding to higher index. (b) Shows the light propagation pattern when TM_{00} mode was launched from the 3 μm end of the waveguide.

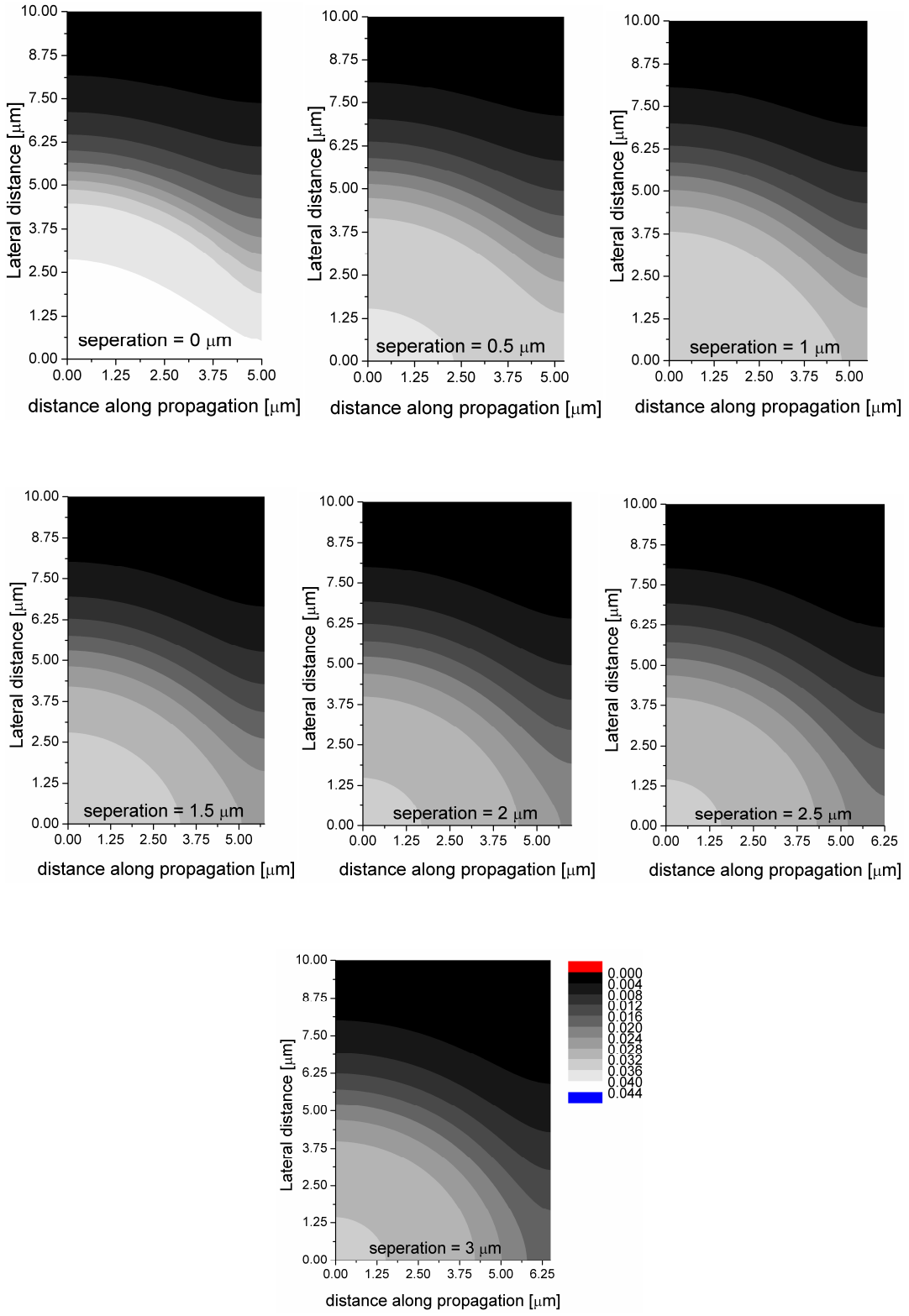

FIGURE 5.8: 3D refractive index profile (for a quadrant (1/4th) of Ti dot) corresponding to segment separations of 0, 0.5, 1, 1.5, 2, 2.5 and 3μm respectively.

The structure which is visible in some of the segments in fig. 5.7 (a) is due to limitations in the image generating capabilities of the software. Cross sections of the profiles showed a smooth refractive index profile as shown in fig. 5.8 (a-g) for segment separations from 0 to 3μm in steps of 0.5 μm respectively. The light propagation pattern as shown in fig. 5.7 (b) was obtained using a Gaussian (TM_{00}) distribution as an input to the port corresponding to the 3 μm separation side of the waveguides. The results revealed that during propagation, part of the TM_{00} mode gradually converted to TM_{01} mode at the zero separation port of the taper. The intensity profiles obtained from the 3 μm and zero separation ports of the tapered waveguide at the positions marked by red lines are shown in fig. 5.9 (i) and 5.9 (ii) respectively.

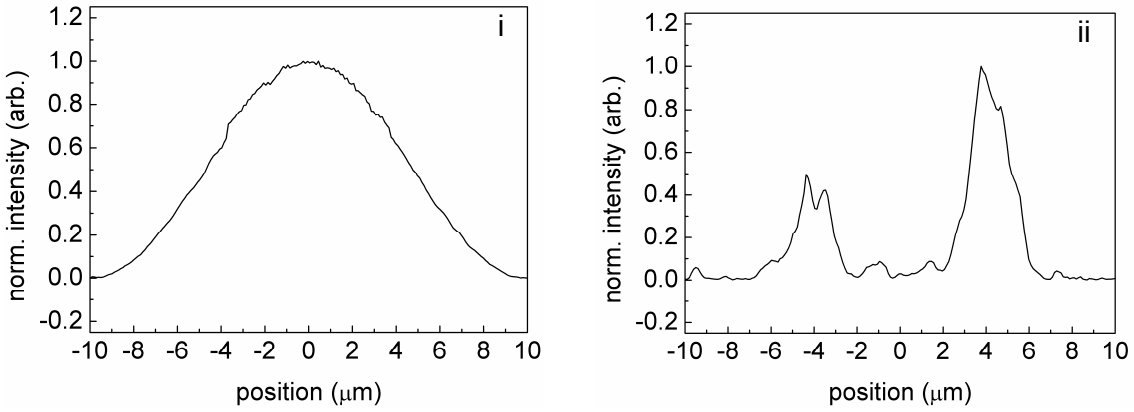

FIGURE 5.9: Mode profiles obtained, by launching a Gaussian distribution as input into the 3 μm port of the index tapered waveguide, from (i) the 3 μm end and (ii) the 0 μm end of the segmented Ti:LN waveguide. The positions where the modes were captured are marked as red in fig. 5.7 (b).

The case of light propagation through a continuous Ti:LN tapered waveguide was simulated using the beam propagation method (BPM) in the commercially available RSoft Beamprop software, with the refractive index contrast values varying linearly from 0.0406 to 0.0322 throughout the length ($\sim$ 1 cm in this case) of the taper. The results showed that the mode size increases from the higher index port of the taper to the lower index

port, as expected for an adiabatic taper. The mode sizes obtained from these simulated waveguides were comparable with the sizes obtained from experiments as presented in the previous section. The simulated mode profiles both for the higher and lower index ports are presented in figs. 5.10 (a) and 5.10 (b) respectively. This confirmed the dot-induced non-adiabatic refractive index structure observed for the segmented Ti:LN waveguides.

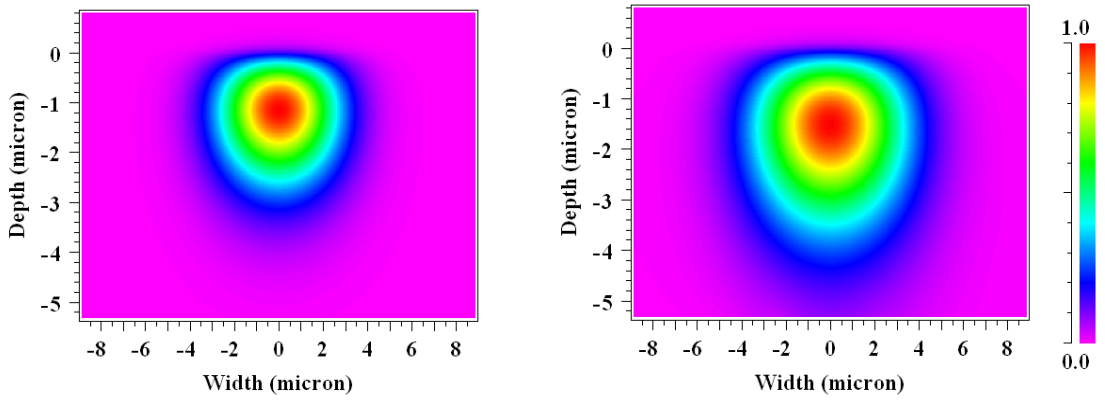

FIGURE 5.10: Calculated near field intensity profiles obtained from (a) the high index and (b) low index port of a continuous Ti:LN waveguide. The mode size increases as the refractive index decreases along the length of the waveguide.

5.4 Conclusions

Segmented tapered waveguides fabricated using a simple yet powerful technique based on the established LIFT and in-diffusion methods for mode filtering applications were presented in this chapter. The fabrication process used for producing the tapers, their loss and optical mode profile measurements were discussed in sub-sections 5.2.1, 5.2.2 and 5.2.3 respectively. The average propagation losses of the tapers measured using three different techniques was $\sim 3.8 \pm 0.8$ dB/cm at 1550 nm. The mode profile pictures captured confirmed the mode filtering action performed by the index tapered waveguides. The corrugations introduced in the refractive index profile due to the segmented geometry of the deposits induced a non-adiabatic behavior in the tapers. This was confirmed by theoretical modeling the light propagation along the taper waveguides and

their comparison with continuous Ti:LN waveguides and the results presented in section 5.3.

Bibliography

J. C. Campbell. "Coupling of Fibers to Ti-Diffused $LiNbO_3$ Waveguides by Butt-Joining". *Applied Optics*, **18**:2037, 1979.

D. Castaldini, P. Bassi, S. Tascu, G. Sauder, P. Aschieri, M.de Micheli, P. Baldi, K. Thyagarajan, and M.R. Shenoy. "All-in-one measurement set-up for fast and accurate charaterization of linear guided-wave optical devices". *Optical Engineering*, **46**:124601, 2007.

H.F. Filho, S.C. Zilio, and F.D. Nunes. "Modelling Ti in diffusion in $LiNbO_3$". *Journal of Physics: Condensed Matter*, **9**:357, 1997.

S. Fouchet, A. Carenco, C. Daguet, R. Guglielmi, and L. Riviere. "Wavelength Dispersion of Ti Induced Refractive-Index Change in $LiNbO_3$ as a Function of Diffusion Parameters". *Journal of Lightwave Technology*, **5**:700, 1987.

J. L. Jackel, C. E. Rice, and J. J. Veselka. "Proton-Exchange for High-Index Waveguides in $LiNbO_3$". *Applied Physics Letters*, **41**:607, 1982.

G. Tittelbach, B. Ricken, and W. Karthe. "Comparison of three transmission methods for integrated optical waveguide propagation loss measurement". *Pure Applied Optics*, **2**:683, 1993.

Chapter 6

Printing of pre-machined donor films

6.1 Introduction

In the conventional LIFT technique the donor material acts as its own propellant and the transfer is achieved either by completely melting it (for the case of a sufficiently thin donor) (Banks et al., 2006; Willis and Grosu, 2005) or ablating the top layer (the thick donor case) which then provides the required push for transfer (Zergioti et al., 2005). The complete melting or disintegration of the donor material during the transfer process is clearly a major drawback especially when printing of materials is required in solid and intact form e.g. single crystals, oriented films, single domain or other pre-structured donors. Also, due to the fact that the donor material from the irradiated zone has to shear itself from the remaining donor film that results in poor edge quality transfers, sometimes even shattering/fracturing the deposits (fig. 6.1 (a)). The thickness of the donor material that can be printed using the conventional LIFT technique is also restricted due to these limitations. Fig 6.1 depicts the advantages of using a machined donor film (fig. 6.1(b)) for intact printing of materials as compared to a non-machined donor film (fig. 6.1(a)).

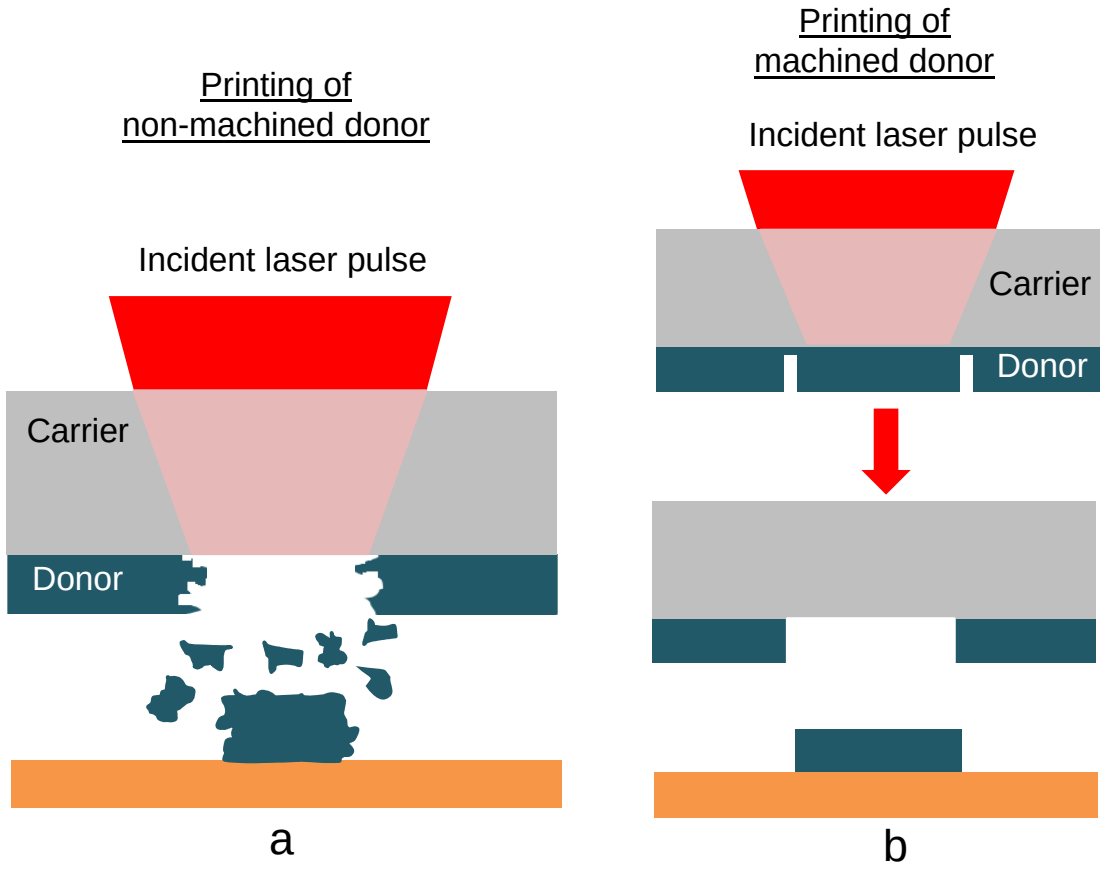

FIGURE 6.1: Illustration of the printing using non-machined donor films a) and machined donor films b).

To mitigate these problems and to achieve printing of materials both in solid and intact form, two complementary LIFT techniques called TP DRL-LIFT (Fardel et al., 2007; Banks et al., 2008b) and BLAST (Banks et al., 2008a) have been the most successful of all other variants of LIFT but there are still some challenges to be overcome. In the case of TP assisted LIFT as discussed in chapter 2, the dissociation temperature of TP is ~250 ^{0}C and solvents like chlorobenzene, cyclohexanone, toluene and acetone either dissolve the polymer or make it swell (Lippert and Dickinson, 2003; Nagel et al., 2007). This temperature and chemical sensitivity of TP imposes limits on the range of donor materials and their thickness that can be deposited while using TP as a DRL. In the BLAST technique, the areas to be printed are defined in the donor film, prior to printing, by weakening them using multiple spatially shaped pulses with fluence below the transfer threshold value (for more detail refer to chapter 2). However the problem with this technique is that the whole donor area to be printed is exposed to the multiple

pulses leading to a significant damage/melting of the deposits. So a more stringent control of the pulse-to-pulse spatial profile is required to improve the quality of the deposits printed using BLAST. In addition both these techniques do not eliminate the basic problem of the inevitable shearing or ripping of the donor film at the boundary of the illuminated region, which presents an unacceptable limitation to the use of LIFT where edge quality is of prime importance, for example in the case of printing multilayer donors.

In this chapter, a new complementary LIFT technique is presented that not only allows printing of solid donors in an intact form, but should also significantly extend the thickness limitation to beyond the current $\sim \mu$m level (Kaur et al., 2009), without using any DRL. The critical step is to pre-machine the donor with structures/patterns intended for printing prior to transfer to encourage separation and transfer of pre-determined shapes in intact and solid form (fig. 6.1 (b)). In this case, the focused ion beam (FIB) machining technique was used to pre-machine the patterns onto the donor films followed by LIFTing them. However, it is not necessary to machine through the entire depth of the donor for reasons discussed below and for an optimum depth of pre-machining onto the donor film, the pattern is transferred gently to the receiver substrate resulting in uniform and clean deposits. The FIB pre-machining would be an ideal candidate for LIFTing of oriented, pre-structured and single crystal materials where BLAST and TP-DRL techniques would not work. Especially for printing single crystals such as those grown via PLD which usually requires substrate heating to temperatures in excess of $\sim$600 ^{0}C to ensure single crystal thin film growth, and hence would be entirely unsuited to TP-DRL techniques.

Zinc oxide (ZnO), an environmental-friendly lead free piezoelectric was chosen as the trial donor material for the FIB assisted LIFT experiments, and our initial results are presented in this chapter. Section 6.2 provides the details of donor film preparation and pre-machining using FIB with a brief discussion of the significance of pre-machined donor depth value. This is followed by the results of printing ZnO pellets from the pre-machined donor films and a comparison with pellets printed using non-machined and using TP as a DRL in section 6.3 with the conclusions then presented in section 6.4.

6.2 Experimental details

The donor samples were prepared by sputtering 1 μm and 3 μm thick films of ZnO on top of quartz substrates at a pressure of 3 mTorr and a temperature of 200^{o}C. FIB machining was used to etch circular features first into the 1 μm thick sputtered donor films up to a depth of 0.8 μm with 5 μm and 10 μm diameters and centre-to-centre separation of 50 μm. Figure 6.2(a) shows the SEM image of the array of these machined ring patterns while fig. 6.2(b) shows a magnified image of one of the 5 μm rings. The poor quality of the images is attributed to the surface charging effect. It took $\sim$ 80 sec to machine each ring at a current value of 2.8 nA with a dosage of 2.81 nC/μm^2 per ring. The samples were machined using Ga^+ ions only without the use of any gas for enhanced etching.

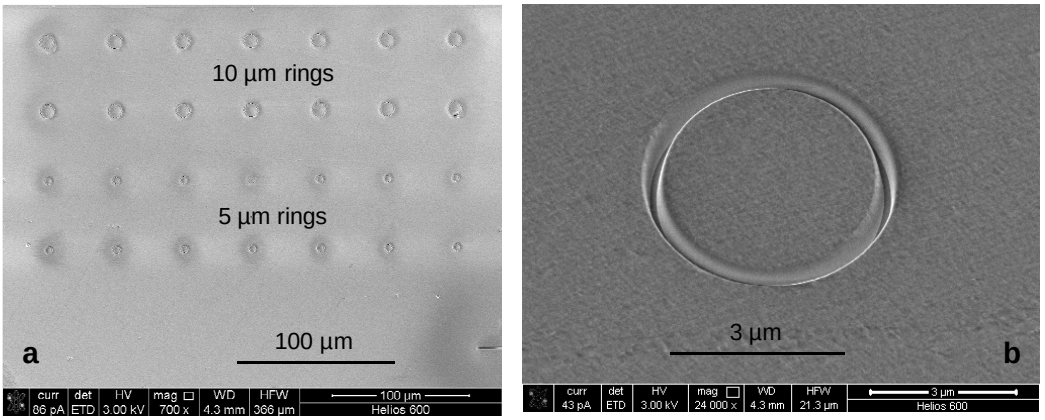

FIGURE 6.2: SEM images of the FIBbed ring patterns of 10 μm (top two rows) and 5 μm (bottom two rows) diameters in 1 μm thick ZnO donor film. (b) shows the magnified SEM image of one of the machined 5 μm rings.

An important parameter that needed to be determined for FIB assisted LIFT was the fractional pre-machined depth of donor required to ensure subsequent high quality transfer and printing. We defined a parameter 'Δ' to quantify the fractional etched depth for the donor:

$$\Delta = \frac{X}{Y} \tag{6.1}$$

where X is milled depth and Y is the donor thickness.

The Δ value chosen for our FIB pre-patterning technique experiments was 0.8. This value for Δ, while somewhat arbitrary, was based on the requirement to mill away a

substantial amount of material, without going to the extremes of $\Delta = 1$. A previous trial carried out by (Banks, 2008) on metals such as Au and Cr with Δ values= 1 (i.e. FIB machining all the way through the donor until the carrier) on the basis that machining away the entire thickness would be the best strategy to ensure easy detachment. In principle, for this case of $\Delta = 1$, only the residual donor-carrier adhesion force must be overcome to ensure donor transfer via the incident laser pulse, and there is no need for the irradiated donor section to shear itself from the rest of film. However, completely melted deposits which had very poor final spatial definition were obtained on LIFTing the pre-machined metallic donor films with Δ= 1 as shown in fig. 6.3 (b). The donor sample used for these experiments was a 200 nm thick Cr metal film and free standing rectangular grid patterns from 1x1 μm^2 to 10 x 10 μm^2 were pre-patterned into the film using the FIB technique as shown in fig. 6.3 (a).

One reason for the completely melted deposits may be due to the absence of lateral heat diffusion. When the donor film is machined at $\Delta = 1$, the incident laser-generated heat has no way to escape laterally, and as a result the temperature increase of the irradiated donor film can greatly exceed than that for the case of a film with $\Delta < 1$, hence overheating and consequent melting of the irradiated donor occurs. In addition to that values for Δ that approach (or exceed) 1 imply that any explosive propulsion force generated from LIFT is no longer constrained at the donor/carrier interface, and the propulsion force can leak around the milled slots leading to poor quality deposits (fig. 6.4(b)).

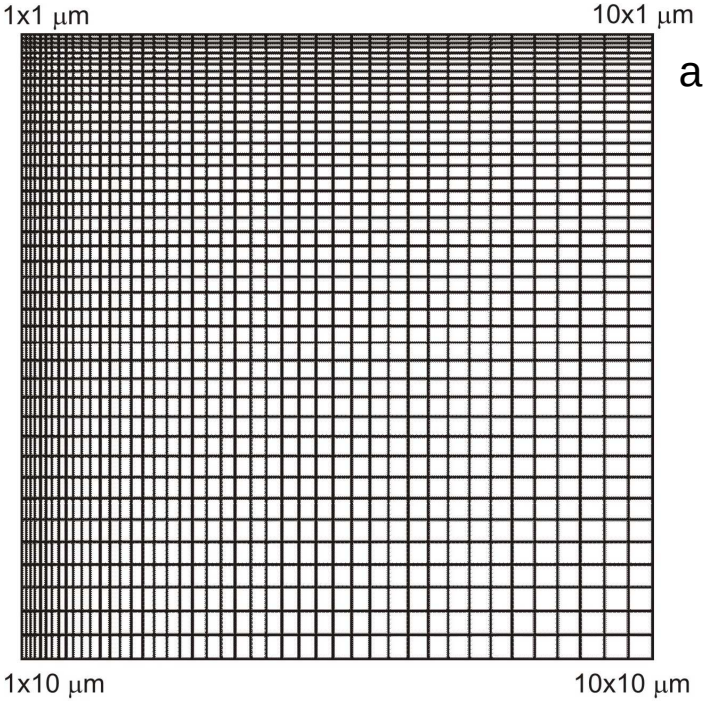

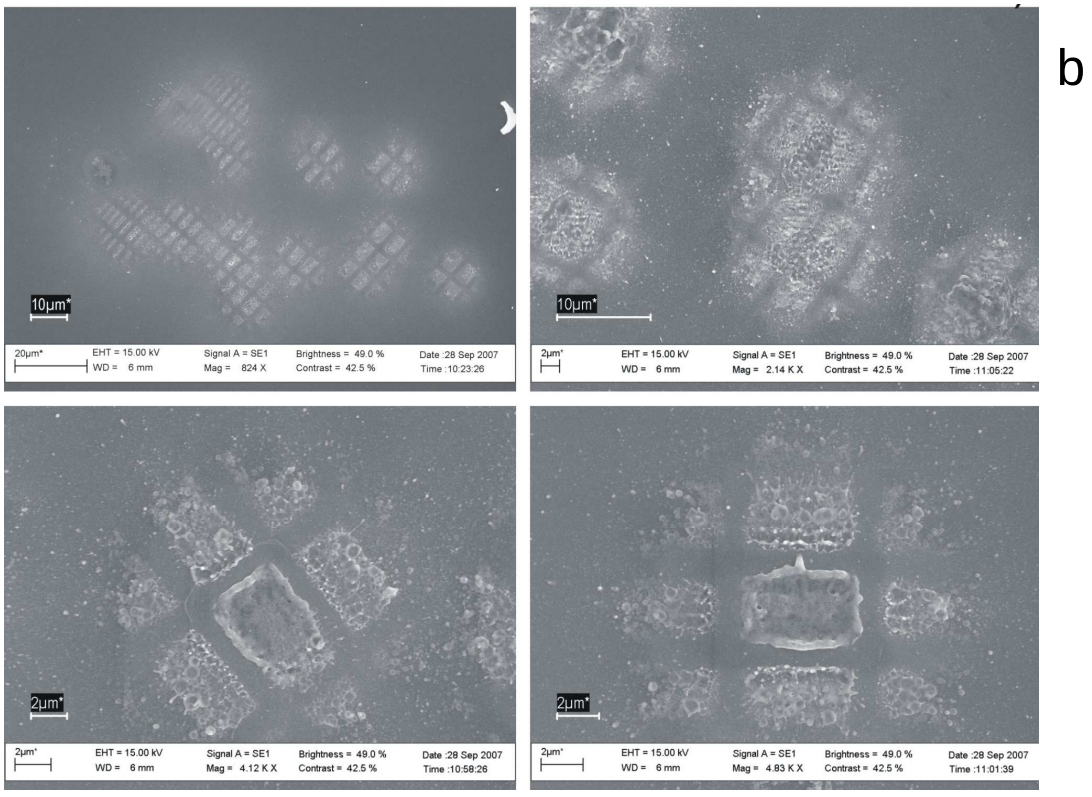

FIGURE 6.3: SEM micrograph images of Cr deposits on a Si receiver from pre-machined donors with a value of $\Delta = 1$ [Banks2008].

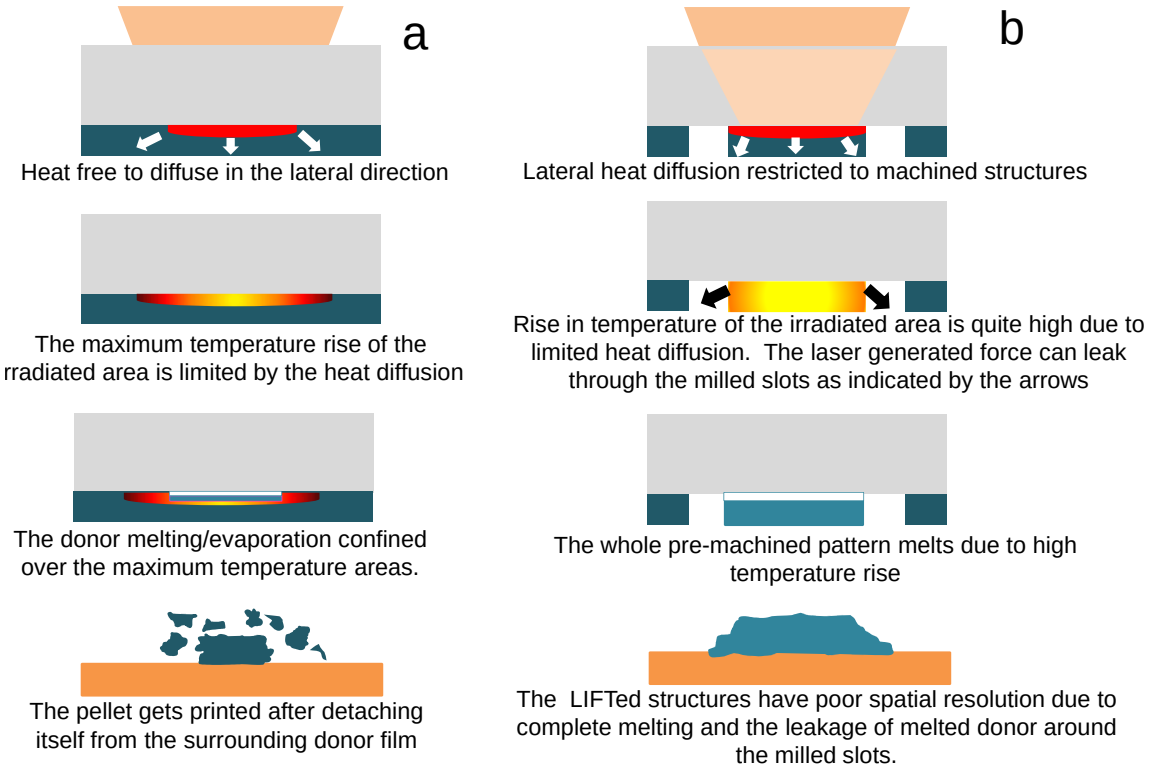

FIGURE 6.4: Illustration of the mechanisms involved during pellet transfer using the conventional LIFT technique [Banks2008].

Δ values of < 0.5, i.e. when the donor is machined less than half the way through, would also not be a good choice either as the irradiated donor section still has to experience considerable shearing from the surrounding non-irradiated donor layer. This inevitably results in considerable debris around the printed donor especially for thicker donor films, which again is less than desirable. For practical purposes therefore, to achieve debris-free deposits with smooth edge and surface quality, Δ should logically be within the range of $0.5 < \Delta < 1$. For this reason a trial value of 0.8 was chosen representing a reasonable compromise between removing too much material and insufficient removal, to ensure ideally debris free printing of the deposit.

For comparison, 1 μm and 3 μm thick ZnO films on top of 360 nm thick TP as a DRL and 1 μm and 3μm thick ZnO samples without any prior machining were also prepared for LIFTing. The donor substrates for the TP-DRL assisted LIFT case were not heated

during deposition due to temperature sensitivity of the polymer, keeping all the other conditions the same. The experimental set-up used for printing ZnO pellets was the same as described in fig. 2.1 of chapter 2. The spot size of the incident beam was $\sim$ 12 μm and all experiments were performed under a background pressure of 10^{-1} mbar. The beam size was chosen to be bigger than the FIBbed feature sizes (5 μm and 10 μm) for ease of alignment while printing. The donor receiver separation was maintained at $\sim$ 1 μm using Mylar spacers.

6.3 Results and discussion

6.3.1 TP-DRL assisted LIFT of ZnO

Figure 6.5 (a,b) shows optical microscope image of 1 μm thick ZnO donor film sputtered on top of 360 nm thick TP. About 80-85 % of the surface area of the donor films was cracked due to the thermal decomposition of TP while depositing the upper ZnO layer. Figure 6.6 (a-d) shows SEM images of ZnO deposits printed onto Si receivers using these films. Cracks were also clearly visible in the LIFTed deposits, and as the films were weaker around the cracks LIFTing preferentially occurred by the rupture along the cracks leading to non-circular deposits. The bad quality of the donor films resulted in shattered and irregular shaped pellets. Even though the substrates were not heated while sputtering ZnO on top of TP the prolonged exposure of the samples in a sputtering chamber can severely degrade the surface integrity of the film due to temperature sensitivity of TP while preparing thick films ($\sim$ μm thickness).

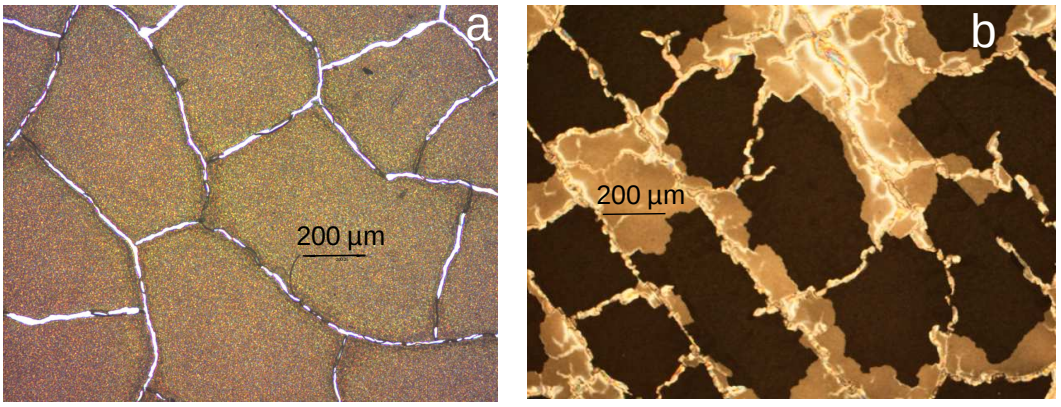

FIGURE 6.5: (a,b) Show optical microscope image of 1 μm and 3 μm thick ZnO donor films deposited on top of 360 nm thick TP respectively.

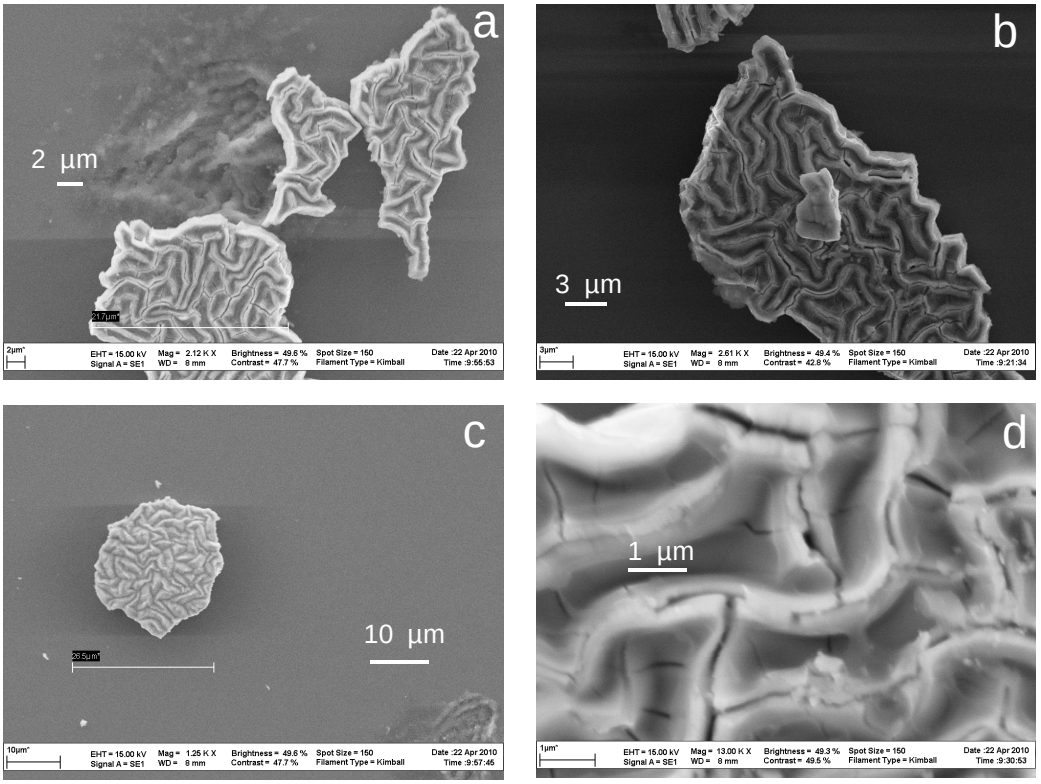

FIGURE 6.6: (a-d) Shows SEM images of cracked ZnO deposits printed on Si receiver from ZnO donor films deposited on top of TP as a DRL.

ZnO films on TP-coated unheated carriers were also prepared using the PLD technique as well. However, the quality of the resultant donor was poorer than that achieved via sputtering on uncoated carriers (i.e. no TP) (fig. 6.7(a)) and that resulted in bad quality deposits (fig. 6.7 (b)).

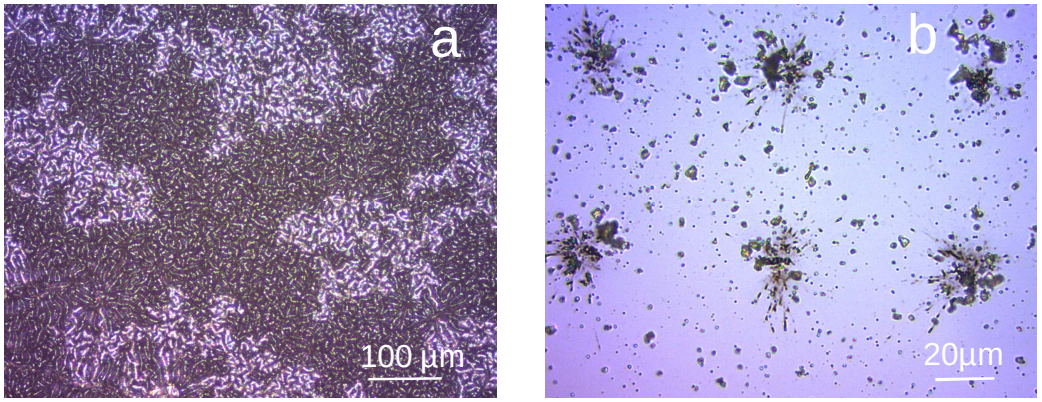

FIGURE 6.7: a) Optical microscope images of ZnO films deposited on top of TP as DRL and b) the deposits printed using these films.

6.3.2 LIFT of non-machined ZnO donors without any DRL

Figure 6.8 (a,b,c) shows SEM images of typical ZnO arrays printed from 1 μm thick donor films without any pre-machining at fluence values of $\sim$ 450, 470 and 500 mJ/cm^2, respectively. The transfers were incomplete at 450 mJ/cm^2 (fig. 6.8 (a)) suggesting that the fluence value was below the required threshold however as the fluence was increased the deposits became splashy, irregular with considerable amount of debris associated with them (fig. 6.8 (b,c)).

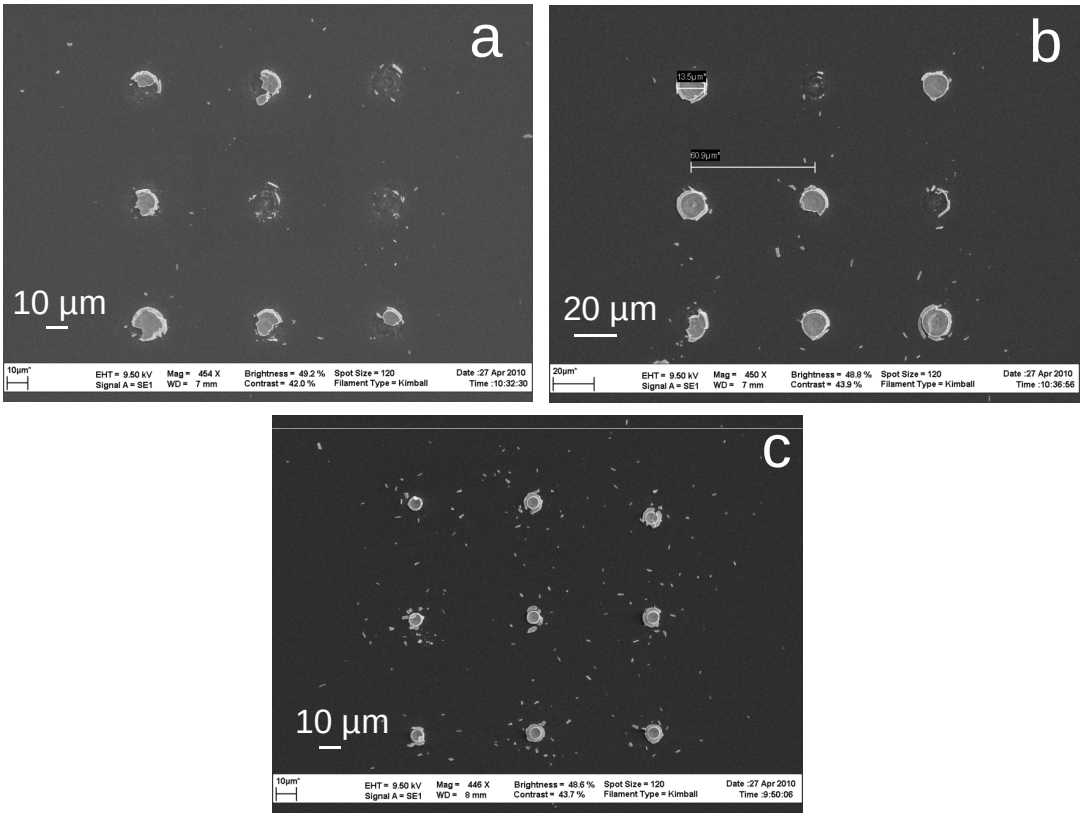

FIGURE 6.8: (a,b,c) SEM images of ZnO arrays LIFTed from a non-machined 1 μm thick ZnO donor film at fluence values of 450, 470 and 500 mJ/cm^2 respectively.

Figures 6.9 (a,b) show magnified images of two of such typical deposits. At fluence values of ∼1 J/cm^2 donut-shaped deposits were observed as shown in fig. 6.9 (c) . This change in deposit shape can be attributed to the greater momentum of the pellets during transfer at such high fluence values. However over this whole range of fluence values (from ∼450 mJ/cm^2 to 1 J/cm^2) the LIFTed ZnO deposits were in general splashy, with considerable amounts of debris and with very rough and ill-defined edges and irregular shapes.

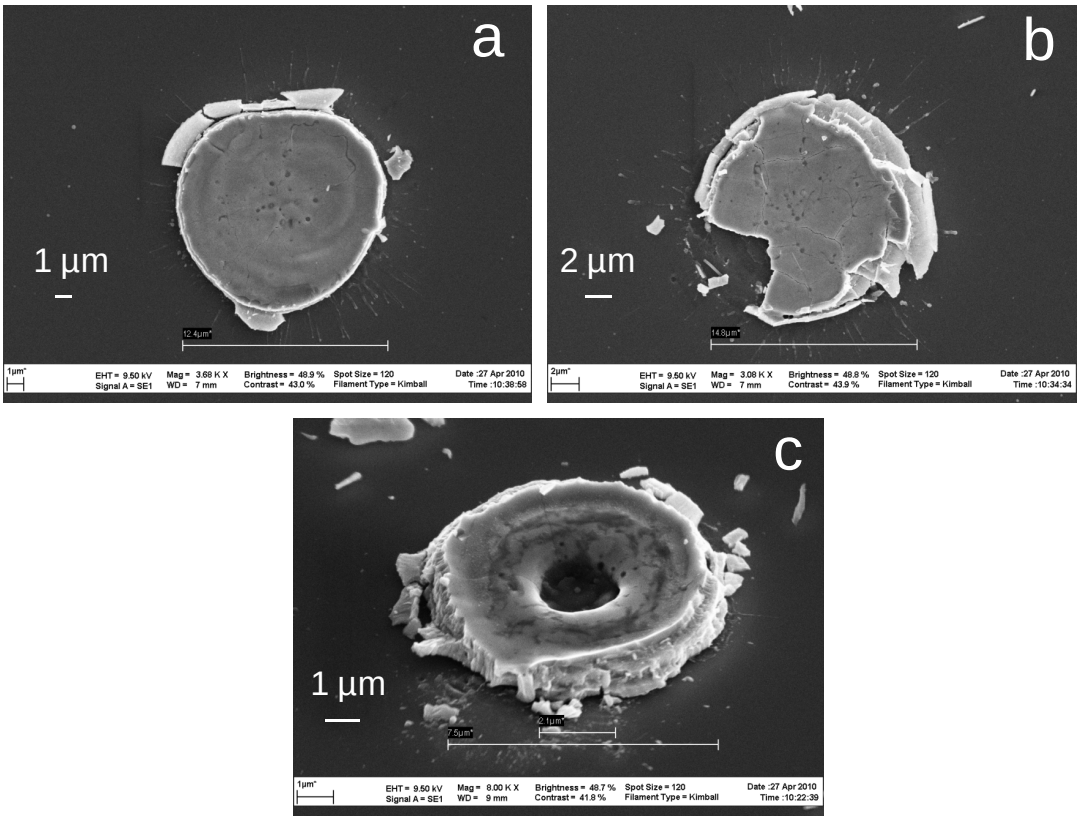

FIGURE 6.9: (a,b) Magnified SEM images of typical deposits printed using a 1μm thick non-machined ZnO donor film; (c) shows donut shaped deposits obtained at high fluence values of $\sim$ 1 J/cm^2.

The quality of the deposits was found to be even worse when printed using 3 μm thick ZnO non-machined donor films as shown in fig. 6.10 (a,b). This is attributed to the fact that as the donor thickness was increased the irradiated pellet had to shear itself from a considerably thicker surrounding film during LIFT printing that resulted in a violent transfer and hence a larger amounts of debris were associated with the deposits. These results highlight the problem of printing materials in solid and intact form especially from thicker donor films using conventional LIFT technique.

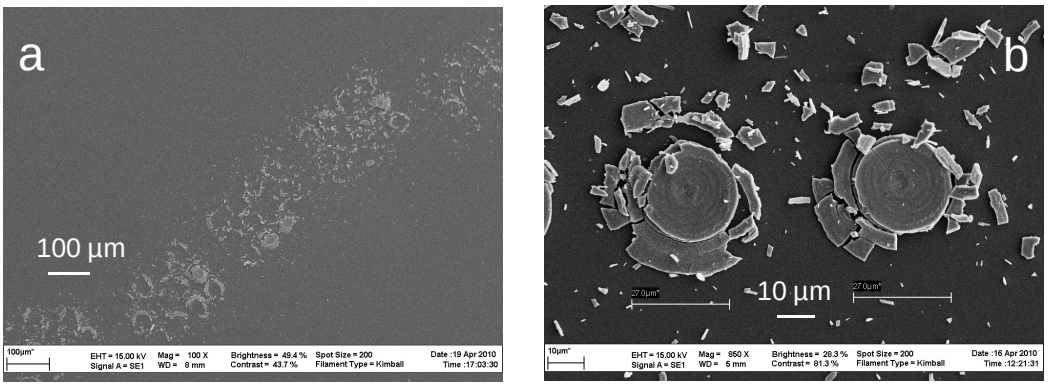

FIGURE 6.10: SEM images of a typical array printed from 3 μm thick non-machined ZnO donor film. b) shows a magnified image of the deposits.

6.3.3 LIFT of FIBbed ZnO donors without DRL

Figure 6.11 (a) and (b) show the SEM images of 10 μm diameter ZnO pellets printed from a pre-machined donor at fluence values of 450 mJ/cm^{2}and 470 mJ/cm^2, respectively. The pellets printed at 470 mJ/cm^2 were found to be cracked which was attributed to the higher impact and momentum during transfer at the higher fluence value. However there was no trace of any residual debris surrounding the pellets printed using pre-machined donor films even at higher value of fluences illustrating the capability of the FIB assisted LIFT technique in printing good quality deposits in solid and intact form. The deposits exhibited extremely good quality both in terms of surface uniformity and edge smoothness as shown by the SEM image of a typical 10 μm deposit, taken at 45 ^{0}, printed from a pre-machined donor at 450 mJ/cm^2 in fig. 6.11 (c). Figure 6.11 (d,e) show the SEM images, taken at 0 ^{0} and 45 ^{0} respectively, of 5 μm ZnO pellets printed from FIBbed donor films at a fluence value of 450 mJ/cm^2

Figure 6.11 (a-c) show the result for LIFTing 10 μm ZnO pellets onto a Si substrate, whereas in fig. 6.11 (d,e) a flexible compliant substrate (polystyrene) was used. The adhesion of ZnO to the plastic receiver was not as good as onto Si. Fortuitously however, the pellet LIFTed onto polystyrene flipped over while dismantling the donor-receiver assembly, allowing SEM examination of the quality of the front surface, and edge quality around the machined rim.

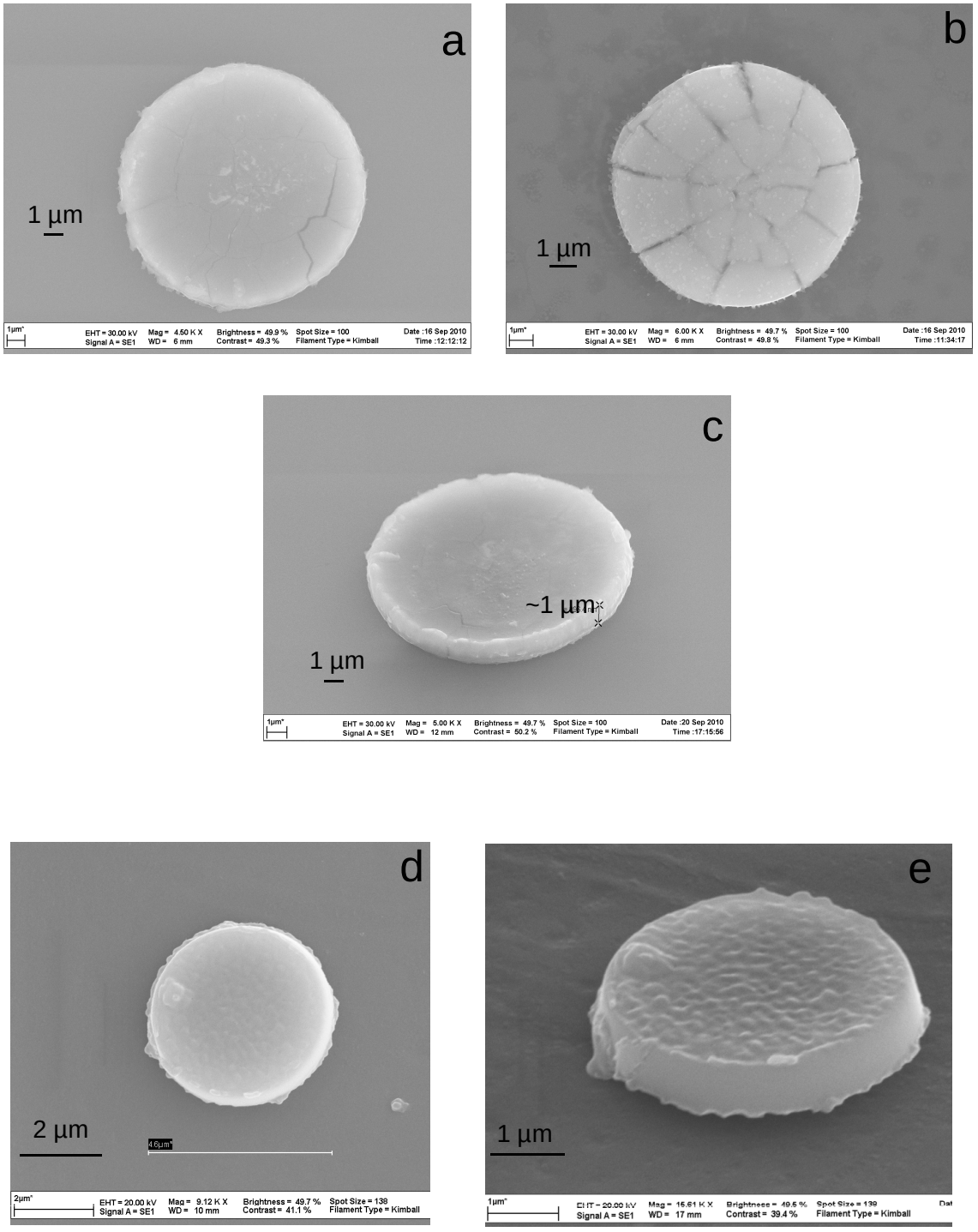

FIGURE 6.11: (a-c) SEM micrographs of 10 μm diameter ZnO pellets printed onto a Si receiver from a pre-machined 1 μm thick donor film. (d,e) shows SEM images of 5 μm ZnO pellets printed onto a plastic (polystyrene) receiver from a pre-machined 1 μm thick donor film.

A close inspection of the edges of the deposits revealed a tremendous improvement in the edge quality of the pellets printed using FIBbed donor films as compared to non-machined donors. Figure 6.12 (a) shows an SEM image of the edge quality of a typical printed pellet using non-machined ZnO donor films. For comparison fig. 6.12 (b,c) show SEM images of the edge quality of 10 μm ZnO pellet printed from a pre-machined donor, and this degree of smoothness was routinely seen in all SEM pictures taken. The 80% machined machined part of the donor film thickness was clearly observed in the images and is also highlighted in fig. 6.12 (c).

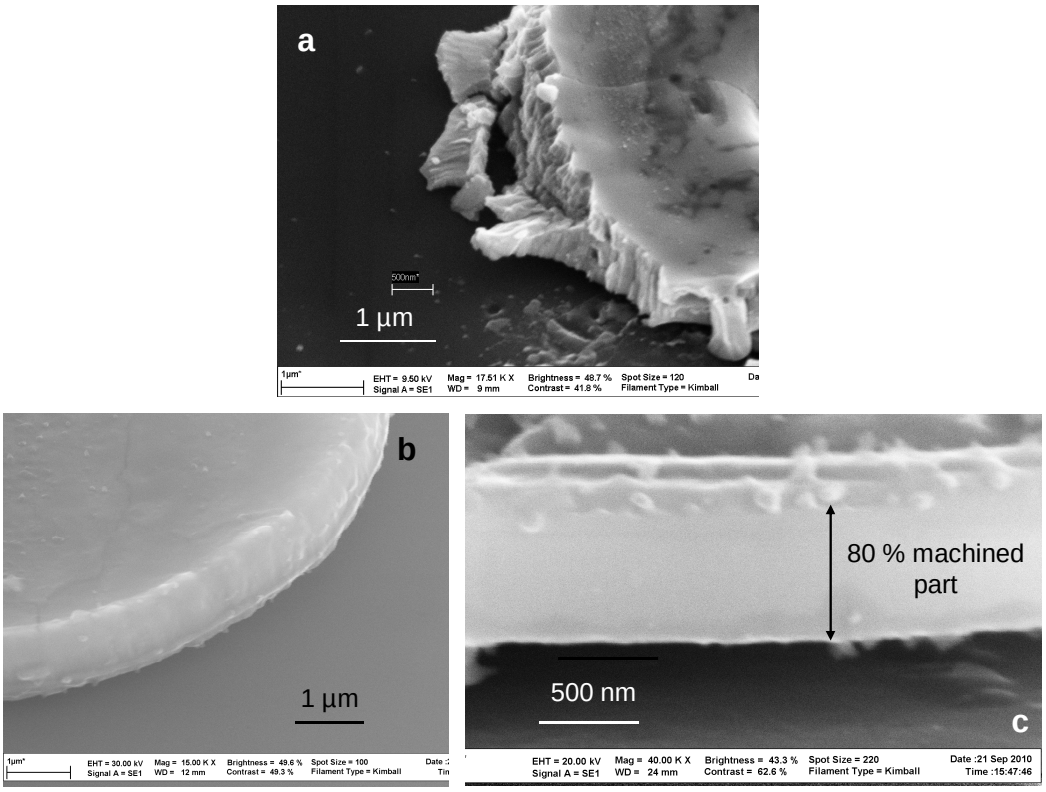

FIGURE 6.12: (a) Shows the rough edges of the ZnO deposits printed using non-machined donor films (b,c) magnified SEM images of the extraordinarily smooth edges of the deposits printed from the pre-machined ZnO donor.

The difference in the quality of deposits transferred from donors with and without pre-machining prior to LIFT was clearly seen for 1μm thick films. The incident laser pulse provided the required force to overcome the donor-carrier adhesion for both the machined and non-machined donor samples, but in the case of no prior machining, the donor pellet still had to shear itself from a considerable portion of the surrounding solid donor film,

resulting in shattering during transfer, rough edges, irregular shapes and considerable and unavoidable debris. For the pre-machined donor, the area to be printed had already been defined by FIB patterning which made the transfer process much gentler.

It should be mentioned that while a Δ value of 0.8 clearly produced impressive results, further experimentation or modelling is required to determine the optimum value for producing an optimum level of printing fidelity. For the cases where Δ approaches 1, detachment can occur with minimal (in best cases zero) residual debris, resulting in smooth and regular printing. It is also likely that this parameter is both donor material and thickness specific. Due to lack of time and non-availability of the FIB machine, the printing of ZnO pellets from a 3 μm thick FIBbed donor samples was not attempted. However, the striking difference in the quality of the deposits obtained clearly shows the great potential of this technique for printing thick and fragile donors in solid and intact format. FIB pre-machining is advantageous as it does not require any DRL so it should in principle be applicable to print any donor material as the range of donors that can be printed using this technique is not limited by the temperature or chemical sensitivity issues as in the case of DRL-assisted LIFT. In any future work, optimising the Δ value for a particular donor material would be an important step, as smaller values of Δ require less time for FIB machining, and as it stands, the 80 seconds per feature is still a comparatively long time. The rate of etching can also be increased considerably by using halogen containing gases thereby reducing the pre-machining time to perhaps $<$ ten of seconds per ring.

6.4 Conclusions

The results have been presented for printing micro-pellets of ZnO of excellent quality with extremely smooth and uniform edges using pre-machined donors to validate the proof-of-principle for the FIB-assisted LIFT technique. The donor films were machined to a depth of 0.8 μm by the FIB technique prior to LIFT and the Δ value of 0.8 was chosen based on the logic that it should be > 0.5 to avoid removing too much material and < 1 to avoid leaking of propulsion force through the milled slot and thermal damage of the donor due to excessive temperature increase as observed in the previous attempts of this technique. Printing results of non-machined ZnO donor films and films deposited on top of TP-DRL were also presented for comparison and they clearly indicated the

superior quality of transfer achievable using the FIB assisted LIFT technique. The initial results with $\Delta = 0.8$ were very encouraging suggesting the great potential of this pre-machining technique, however as mentioned earlier due to lack of time it was not possible to perform a complete and thorough optimisation of the Δ parameter and to study its dependence on donor thickness and donor material.

Bibliography

D. P. Banks, C. Grivas, J. D. Mills, R. W. Eason, and I. Zergioti. "Nanodroplets deposited in microarrays by femtosecond Ti : sapphire laser-induced forward transfer". *Applied Physics Letters*, **89**:193107, 2006.

D. P. Banks, C. Grivas, I. Zergioti, and R. W. Eason. "Ballistic laser-assisted solid transfer (BLAST) from a thin film precursor". *Optics Express*, **16**:3249, 2008a.

D. P. Banks, K. Kaur, R. Gazia, R. Fardel, M. Nagel, T. Lippert, and R. W. Eason. "Triazene photopolymer dynamic release layer-assisted femtosecond laser-induced forward transfer with an active carrier substrate". *Europeon Physics Letters*, **83**:38003, 2008b.

D.P Banks. *"Femtosecond laser-induced forward transfer techniques for the deposition of nanoscale, intact, and solid-phase material"*. PhD thesis, Optoelectronics Research Centre, 2008.

R. Fardel, P. Feurer, T. Lippert, M. Nagel, and A. Nuesch, F.and Wokaun. "Laser ablation of aryltriazene photopolymer films Effects of polymer structure on ablation properties". *Applied Surface Science*, **254**:1332, 2007.

K. S. Kaur, R. Fardel, T. C. May-Smith, M. Nagel, D. P. Banks, C. Grivas, T. Lippert, and R. W. Eason. "Shadowgraphic studies of triazene assisted laser-induced forward transfer of ceramic thin films". *Journal of Applied Physics*, **105**:113119, 2009.

T. Lippert and J. T. Dickinson. "Chemical and spectroscopic aspects of polymer ablation: Special features and novel directions". *Chemical Reviews*, **103**:453, 2003.

M. Nagel, R. Hany, T. Lippert, M. Molberg, F. A. Nuesch, and D. Rentsch. "Aryltriazene photopolymers for UV-laser applications: Improved synthesis and photodecomposition study". *Macromolecular Chemistry and Physics*, **208**:277, 2007.

D. A. Willis and V. Grosu. "Microdroplet deposition by laser-induced forward transfer". *Applied Physics Letters*, **86**:244103, 2005.

I. Zergioti, A. Karaiskou, D. G. Papazoglou, C. Fotakis, M. Kapsetaki, and D. Kafetzopoulos. "Time resolved schlieren study of sub-pecosecond and nanosecond laser transfer of biomaterials". *Applied Surface Science*, **247**:584, 2005.

Chapter 7

Printing of piezoelectric materials using LIFT

7.1 Introduction

In the past few years piezoelectric micro-energy harvesters have gained enormous attention both by academic and industrial researchers as alternative sources of energy to power small portable electronics (Beeby et al., 2006) by converting mechanical strain energy into electrical energy. Of all the piezoelectric materials lead zirconate titanate (PZT) is the most efficient in converting the mechanical energy into electrical energy so is a strong candidate for energy harvesters. The piezoelectric micro-generators are most commonly prepared by screen printing the PZT films and electrode layers followed by high temperature sintering (Glynne-Jones et al., 2001). PZT films have high value of d_{33} coefficients in the range of 10-250 pC/N as reported in the literature (Torah et al., 2004). However, when it is required to print onto polymer/flexible and pre-metalized substrates, screen printing is not the best option. In addition it is hard to print micron-scale features employing screen printing techniques, but such micron-sized deposits may easily be printed onto pre-structured substrates using the LIFT technique.

In this chapter details of the experiments and results obtained from LIFTing PZT donor films are presented. Non-lead based environment-friendly ZnO, another important piezoelectric material, was also printed using the LIFT technique. ZnO films have reasonable values of d_{33} (5-11 pC/N) (Yang et al., 2008) but not large in comparison to PZT but the

d_{33} values for ZnO can be increased by doping the films with V, Co, Ni and Fe (Wang et al., 2006). Sub-section 7.2.1 discusses the experimental set-up used for printing PZT using fs-LIFT followed by the attempts made to characterize the deposits using the piezoelectric force microscopy (PFM) technique in sub-section 7.2.2. Results of printing larger area deposits by fs-LIFT using a refractive beam shaper are presented in sub-section 7.2.3. Section 7.3 describes the experimental set-up used for printing PZT using ns-LIFT and the post-transfer d_{33} coefficient measurements after poling the deposits at high temperatures. Finally, the experimental details and results of transferring mm-sized ZnO pellets using ns-LIFT are discussed in section 7.4 followed by the conclusions in section 7.5.

7.2 Femtosecond DRL-LIFT of PZT donor films

7.2.1 Experimental details

The donor samples were prepared by depositing a 150 nm thick layer of PZT on top of fused silica carrier substrates (50 mm diameter and 3 mm thickness) previously coated with TP ($\sim$ 200 nm) using the PLD technique at room temperature (due to the low thermal decomposition temperature of TP $\sim$ 250 ^{0}C), at a pressure of 0.2 mbar and in an oxygen atmosphere. The experimental set-up used for fs DRL-LIFT of PZT was the same as described in fig. 2.1 of chapter 2 for printing Ti:LN channel waveguides. The incident beam spot size was $\sim$10 μm and all experiments were performed at a background pressure of 10^{-1} mbar. The separation between donor and receiver substrates was maintained at $\sim$1 μm using Mylar spacers. Silicon wafers of dimension $\sim$ 1 cm x 1 cm were used as receivers and the donor receiver assembly was mounted on 3-axis translation stages for relative movement with respect to the incoming laser pulses. The threshold fluence for printing PZT pellets was $\sim$ 365 mJ/cm^2. Figure 7.1 show an SEM image of a LIFTed PZT 1 x 8 array with the fluence value increasing from 365 mJ/cm^2 to 400 mJ/cm^2 in steps of 5 mJ/cm^2. The transfers were either incomplete or no transfer occurred at all below 365 mJ/cm^2. Magnified SEM images of PZT pellets transferred at 365 mJ/cm^{2}are shown in fig. 7.2 (a, b).

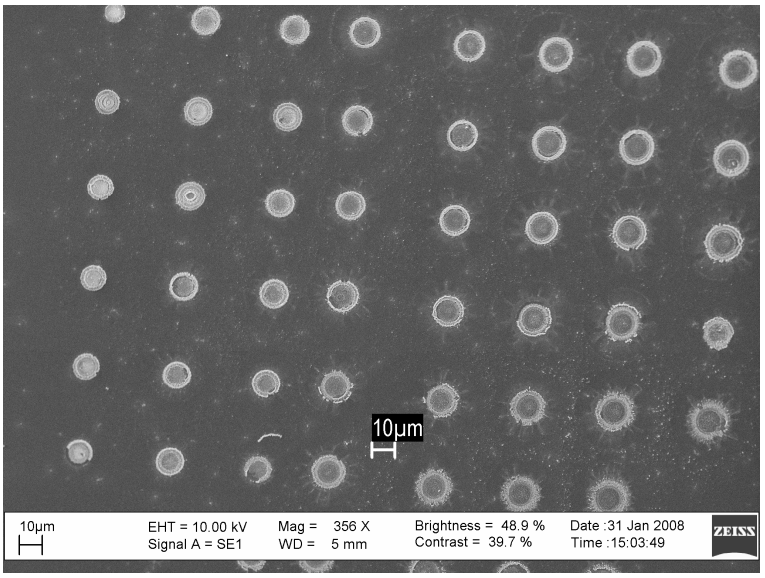

FIGURE 7.1: SEM image of a printed array of PZT pellets.

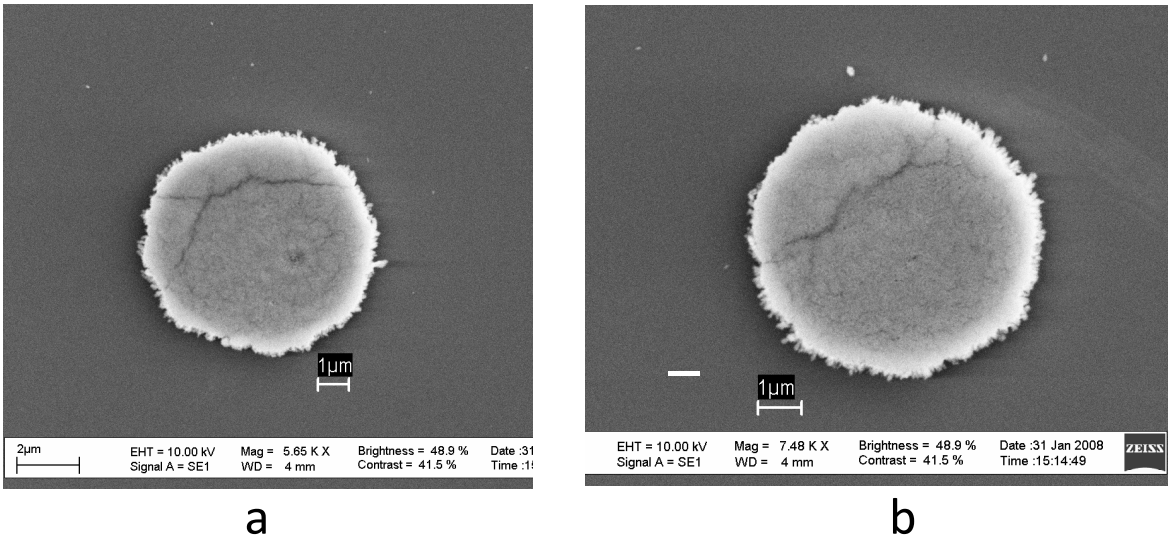

FIGURE 7.2: Magnified SEM images of PZT pellets printed at a fluence of 365 mJ/cm^2.

At higher values of fluence the morphology of deposits changed from circular to an annular ring type with a molten central region. The molten central region grew bigger on increasing the fluence value as shown in fig. 7.3 (a, b) for 370 mJ/cm^{2}and 385 mJ/cm^2 respectively.

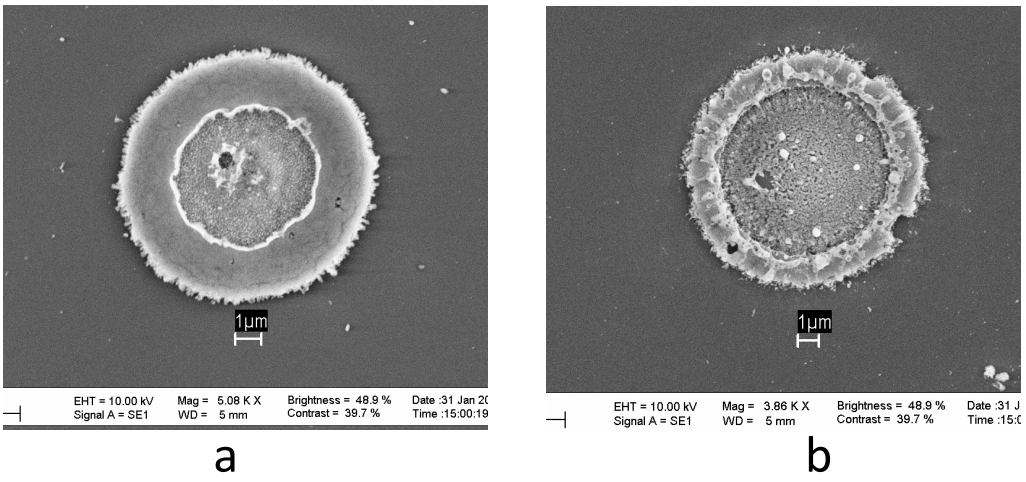

FIGURE 7.3: SEM images of PZT pellets printed at fluence values of 370 mJ/cm^2 and 385 mJ/cm^2 respectively.

7.2.2 Characterisation of the printed PZT pellets

The next step after transferring PZT deposits was to test their functionality by measuring their longitudinal d_{33} piezoelectric coefficients. These coefficients quantify the charge produced as a result of the applied dynamic force to the piezoelectric sample. Considering their small size (∼10 μm) it was rather tricky to deposit electrodes on top of the pellets (Si acting as the bottom electrode) so the piezoelectric force microscopy (PFM) (Wu, 2007) technique was employed to characterize the electromechanical properties of the printed PZT pellets. The samples were first baked at 200 ^{0}C in a tube furnace at a ramp rate of 2 ^{0}C /min and dwell time of 1 hour and then tested using PFM[1]. PFM is basically a modified atomic force microscopy (AFM) technique using a metalized AFM tip (cantilever) in contact mode (Wu, 2007). The piezoelectric sample under test deforms in response to an applied voltage. The sample expands locally when the domains are aligned and the internal polarization points in the same direction as the applied field, and the sample contracts locally if the internal polarization points in a direction opposite to the applied field. The local expansion or contraction causes the cantilever to deflect, which when measured, determines the piezoelectric coefficient value of the sample. The basic working principle of the technique is explained in fig. 7.4 .

[1]The PFM measurements were done by the colleagues at the Institute of Physics, University of Bonn, Germany.

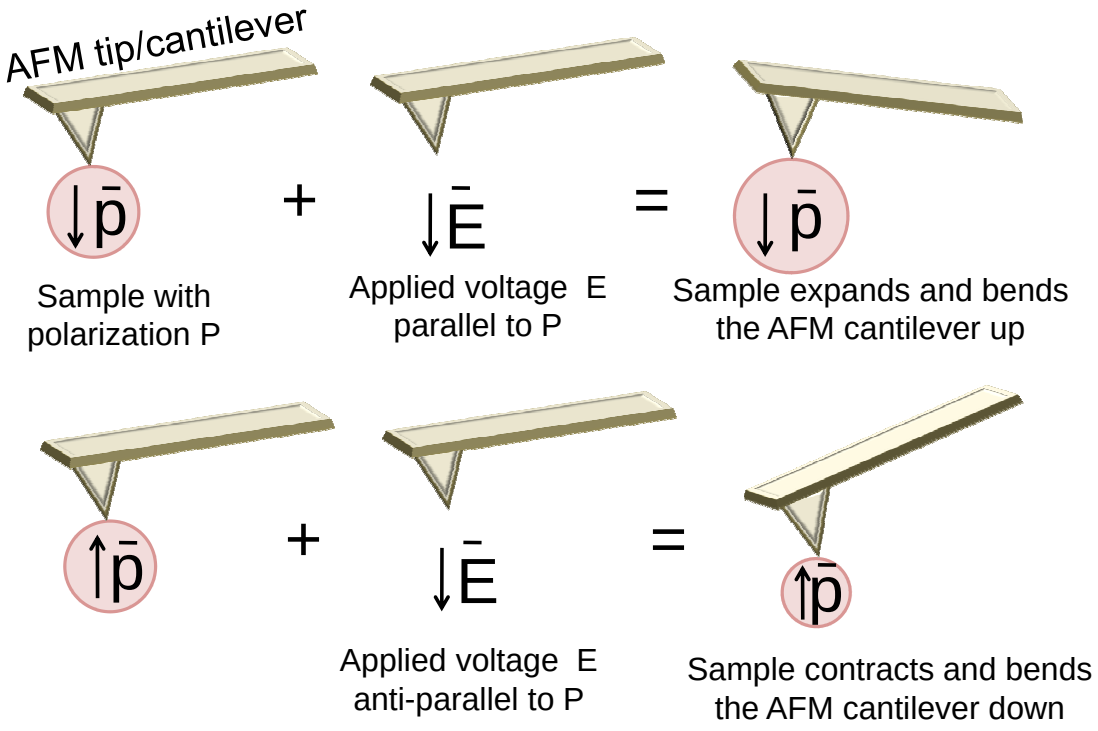

FIGURE 7.4: Schematic showing the basic principle of PFM technique adapted from (http://cp.literature.agilent.com/litweb/pdf/5989-7611en.pdf) .

Electrical voltages of + 100 and -100 V were applied to the sample for $\sim$ 20 s each through the conductive AFM tip but no PFM contrast/signal was recorded. Even baking the samples at a higher temperature of 500^0C for 1 hour did not result in any PFM signal. The reason for no mechanical response of the PZT pellets to the applied voltage was believed to be either due to a very small dimensional change in the pellets by the applied electric field to be detected or the absence of any net internal polarization in the pellets i.e. the domains were all randomly oriented. To surmount the latter problem in-situ heating and poling of the samples is required to align the domains along the applied field thereby allowing the samples/pellets to have an internal polarization. Additionally thicker donor films should be ideally used to overcome the former problem.

7.2.3 Printing larger area PZT deposits using femtosecond laser irradiation

For poling the PZT samples at higher temperatures larger size pellets of the order of mm^2 were required for ease of the deposition of upper electrodes on the transferred deposits. Printing mm size pellets was not possible with the experimental set-up used so far (fig. 2.2) as it involves clipping 90% of the incident Gaussian beam at the aperture for selecting the most homogeneous part of the beam and then demagnifying it by a factor of ∼40 to achieve the threshold fluence for transfer. A modified experimental set-up as shown in fig. 7.5 was used for printing bigger PZT pellets using fs-LIFT that employed a refractive beam shaper known as pi-shaper 6_6 (πshaper) (http://www.pishaper.com) in order to convert the beam profile of the incident collimated beam from Gaussian to a flattop collimated beam.

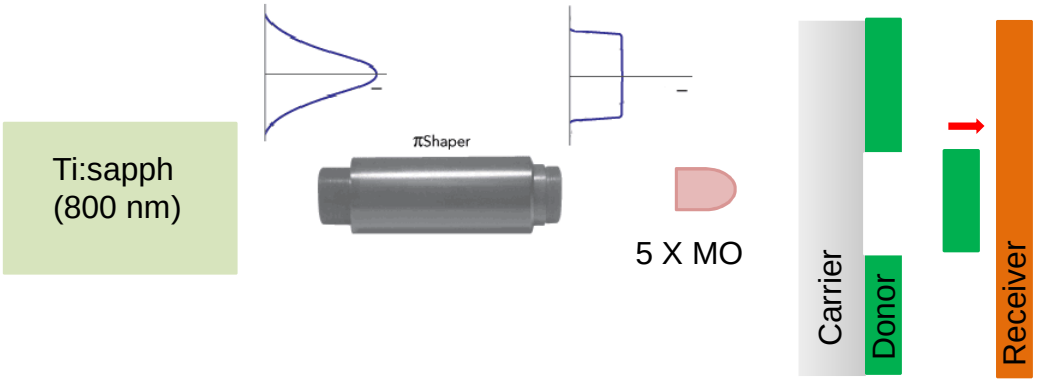

FIGURE 7.5: Experimental set-up using the πshaper for printing bigger areas by the fs-LIFT technique.

The input beam has to be of 6 mm FWHM and the πshaper converts it into a 6 mm FWHM flattop beam (http://www.pishaper.com). Figure 7.6 (a) and (b) show the intensity profiles of the incident beam before and after the πshaper respectively at a distance of 45 cm captured using a beam profiler. The output beam is much more homogeneous and has flattop profile except for the brighter rims. The reason for this is the non-perfect Gaussian intensity profile of the input beam and the low tolerance (± 0.1 mm) of the π shaper to the size of the input beam. The output beam from the π shaper was then centrally incident on a cicular aperture to get ∼ 1 mm size output

which was then imaged to the carrier-donor interface using a 5 x objective lens. The intensity profile of the beam just after the aperture is shown in fig. 7.7

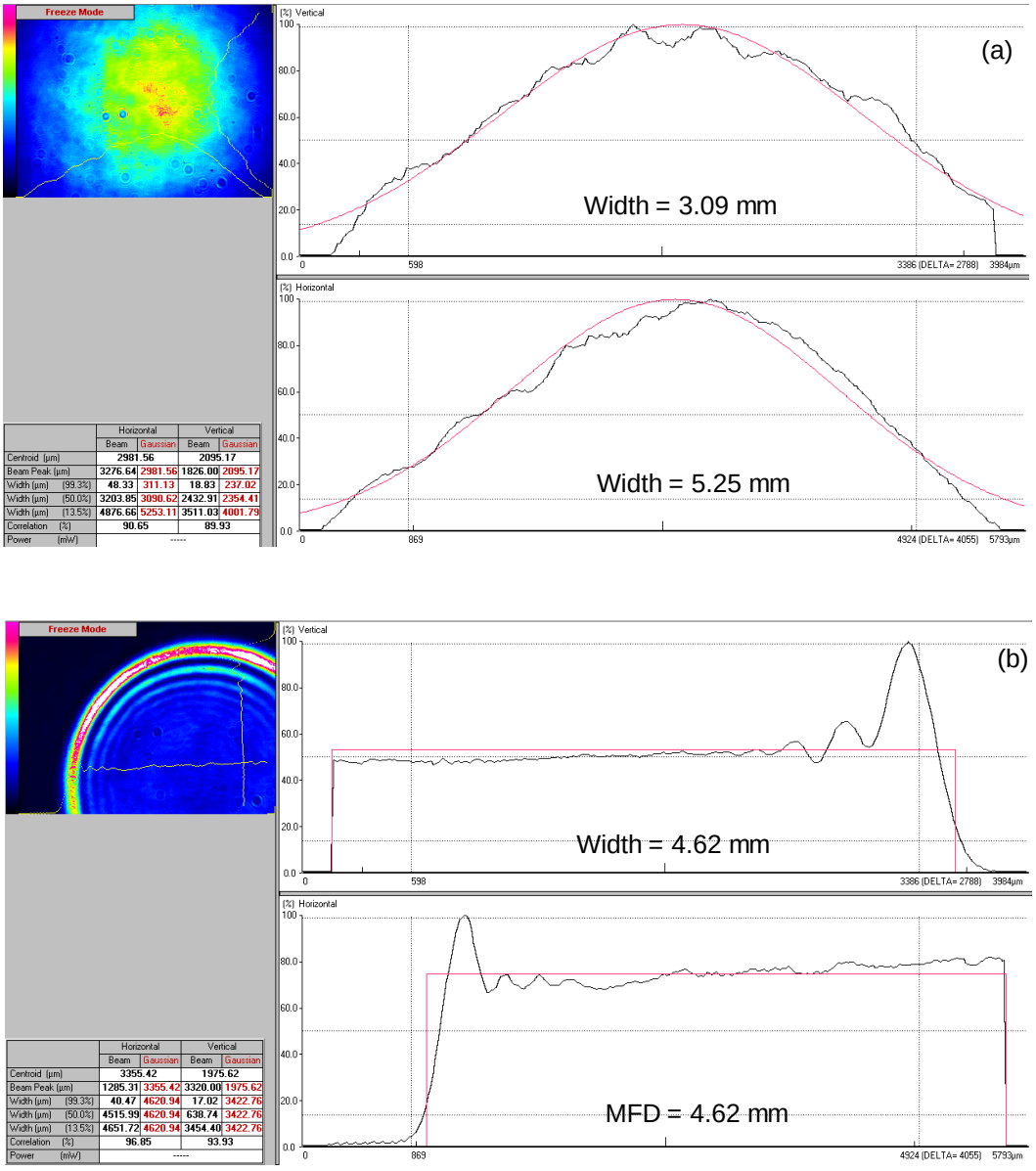

FIGURE 7.6: Intensity profiles of beam (a) before and (b) after the πshaper.

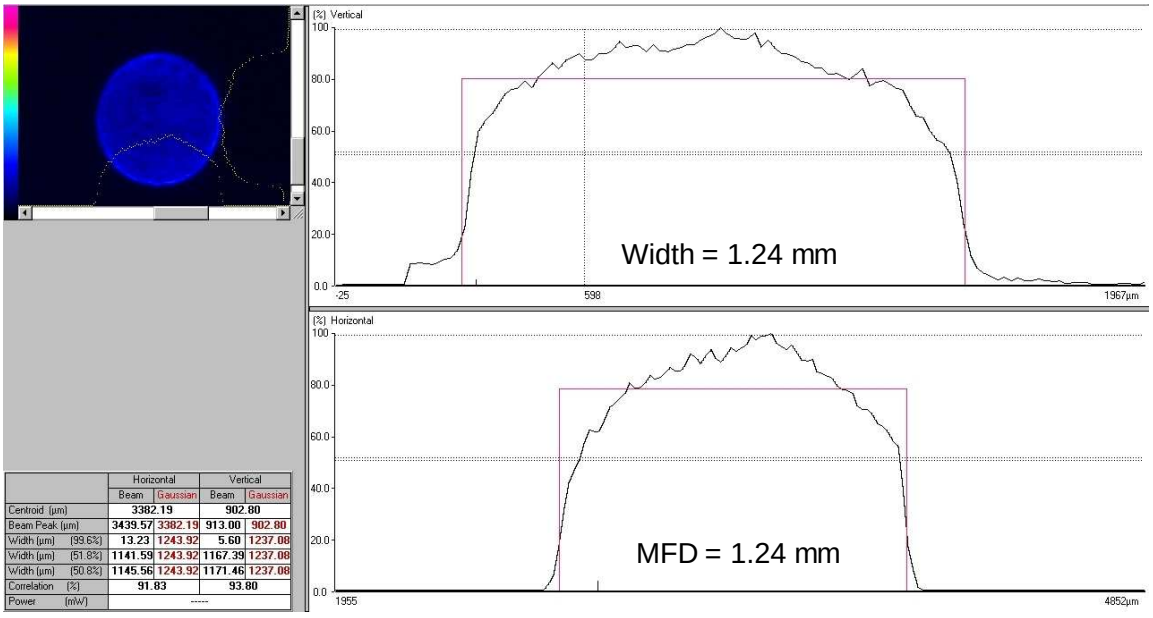

FIGURE 7.7: Intensity profile of beam just after the aperture.

For trial experiments, thin donor films of Ti (∼150 nm) on borosilicate glass carrier substrates were used and the SEM images of Ti deposits transferred using the πshaper onto Si receivers are shown in fig. 7.8 (b, c). The deposits had ring patterns associated with them which was due to the πshaper as it provided the collimated beam only up to a distance of $\leq$50 cm beyond which the beam started to have a ring pattern (Airy distribution) in it due to diffraction as shown in the intensity profile of the output beam from πshaper at a distance of 150 cm using the beam profiler in fig. 7.9. These ring patterns due to the beam profile were also clearly visible in the LIFTed deposits. Apart from the sensitivity of the πshaper to the input beam size and converting the Gaussian into a uniform collimated flattop beam only over a restricted distance, the maximum size that could be printed using the πshaper set-up was $\sim$ 200 μm which was much less than what was required ($\sim$ mm) for poling tests of PZT. So a simpler and easier solution of using a ns excimer laser that can print mm size pellets in a single shot was opted for, the details of which are discussed in the next section.

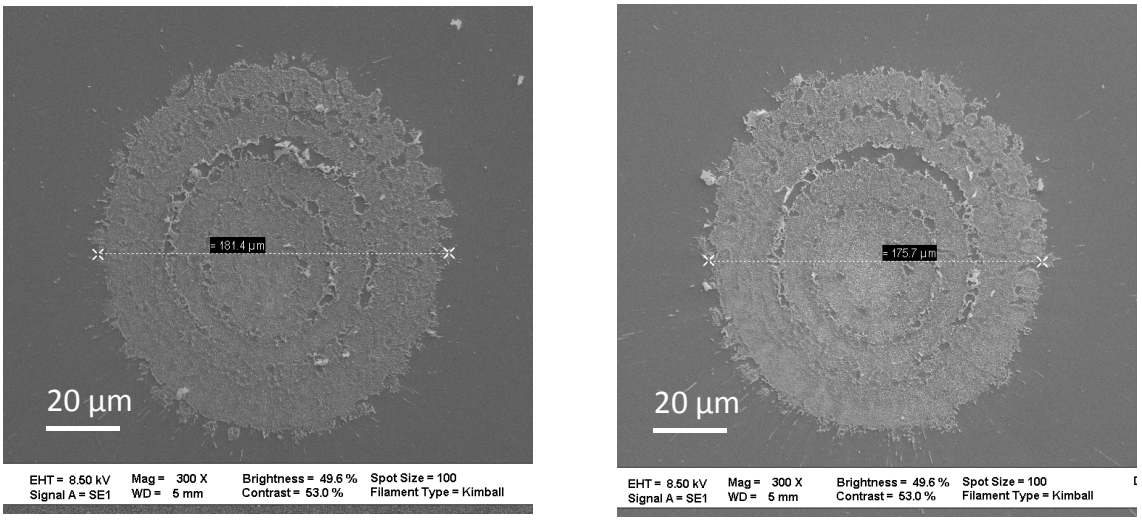

FIGURE 7.8: SEM images of Ti deposits printed using the πshaper set-up

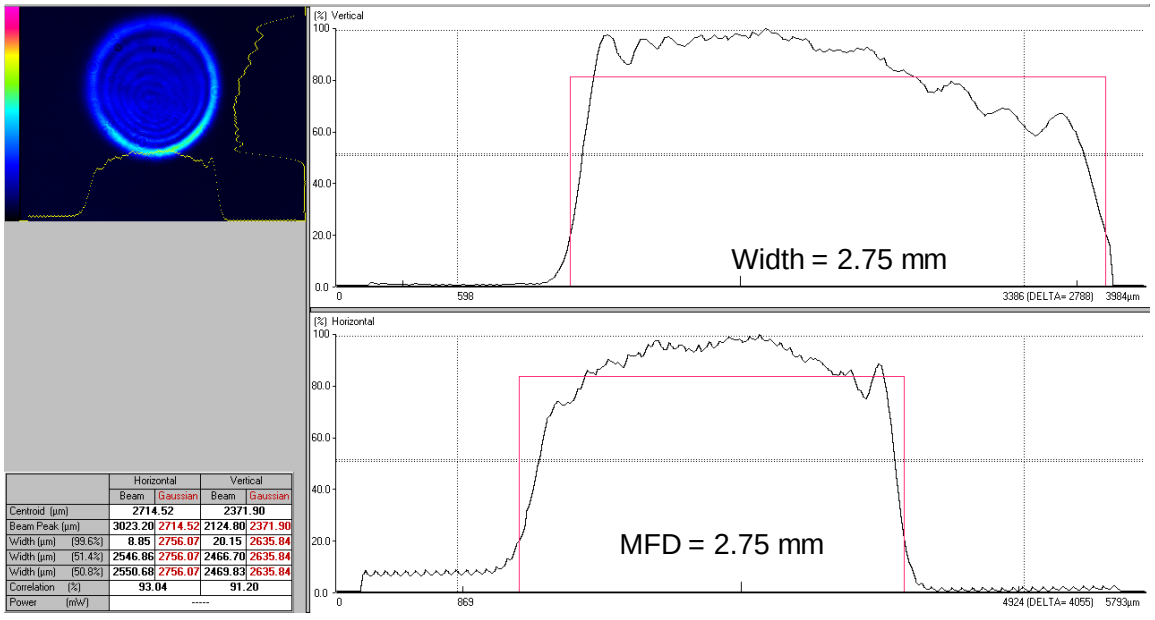

FIGURE 7.9: Ring pattern clearly visible in the intensity profile of an output beam from the πshaper measured at a distance of 150 cm.

7.3 Nanosecond DRL-LIFT of PZT donor films

7.3.1 Experimental details[2]

The experimental set-up used for printing mm size PZT pellets using ns DRL-LIFT is shown in fig. 7.10. Pulses from a XeCl excimer laser (λ = 308 nm, τ = 30 ns) were centrally incident on a square mask with an aperture of 4 mm resulting in a homogeneous beam. This uniform beam was then imaged by a lens (f = 250 mm) onto the sample with a demagnification of x 4, yielding a spot size of 1 mm x 1 mm. The pump laser energy incident on the target was controlled by a variable attenuator plate. The donor samples were prepared by depositing 150 nm and 1 μm thick films of PZT on top of TP coated (200 nm and 360 nm) fused silica carrier substrates using the PLD technique. Gold coated square Si wafers (1 cm x 1 cm) were used as receiver substrates.

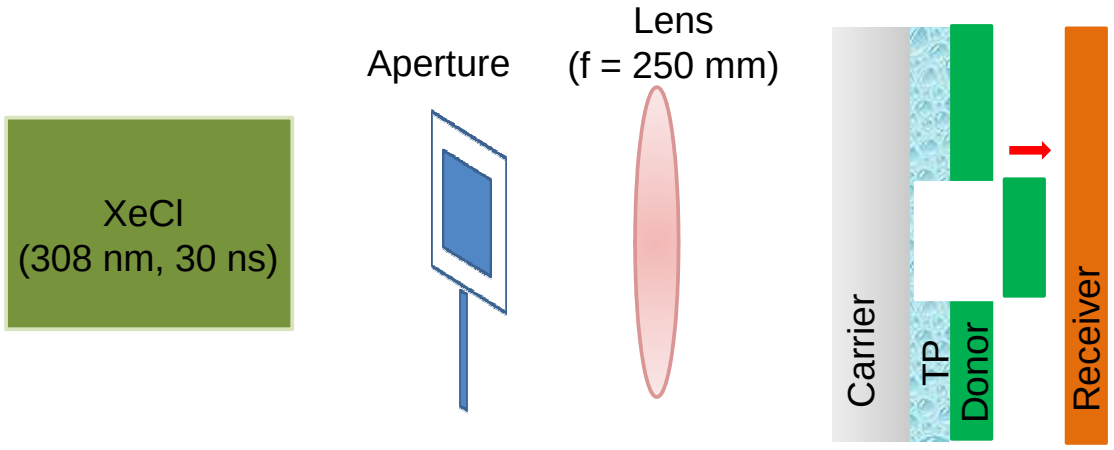

FIGURE 7.10: Schematic of ns-LIFT set-up used for printing PZT pellets.

Figure 7.11 (a, b) show the optical microscope images of typical PZT deposits transferred using ns DRL-LIFT at a fluence value of $\sim$ 380 mJ/cm^{2}and 1.5 mJ/cm^{2}for 150 nm and 1 μm thick films respectively. The deposits looked fragile and structured and this was attributed to the less than perfect quality of the donor films as shown in fig. 7.12.

[2]This work was done at the General Energy Research department, Paul Scherrer Institut, Villigen, Switzerland.

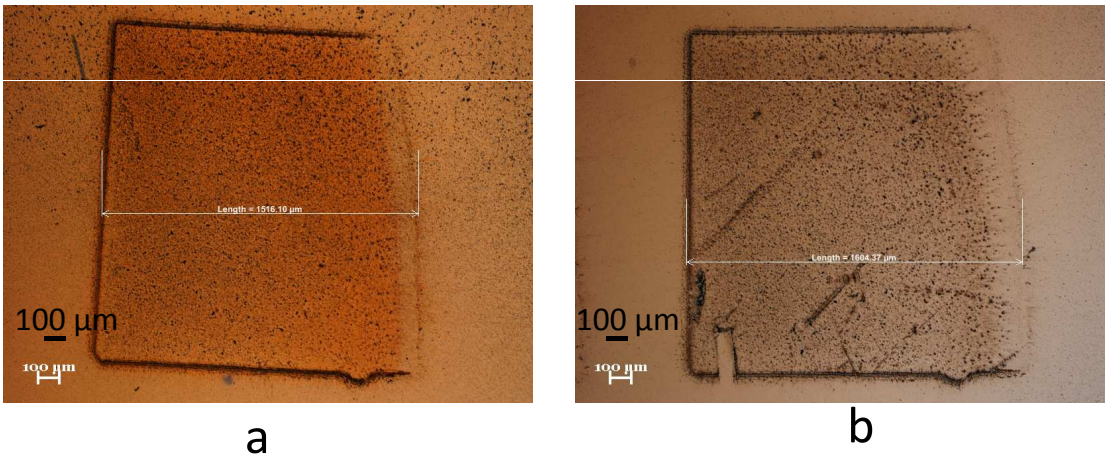

FIGURE 7.11: Optical microscope images of PZT deposits printed from 150 nm and 1 μm thick donor films respectively.

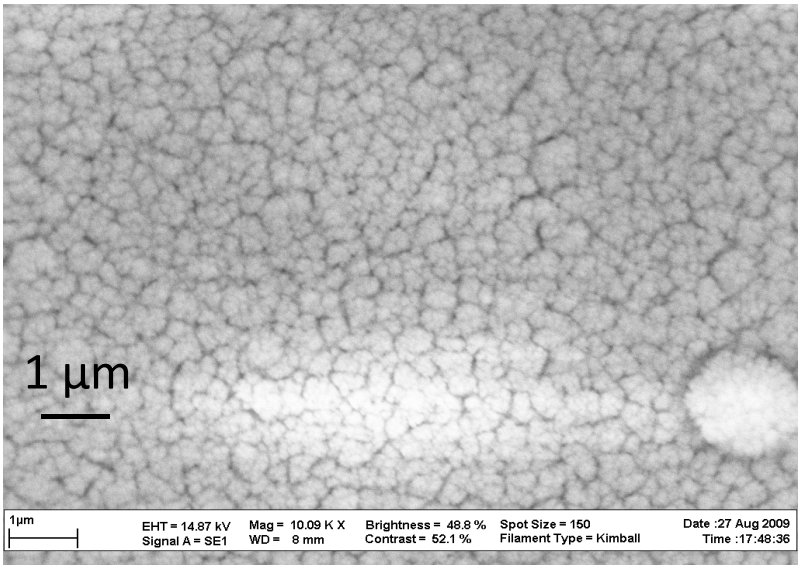

FIGURE 7.12: SEM image showing the textured surface quality of a 1 μm thick PZT donor film.

7.3.2 Characterization of the samples

A specially designed holder was used for poling the PZT samples at higher temperatures the schematic of which is shown in fig. 7.13. Au coated Si served as the lower electrode and a thin indium foil (0.5 mm x 0.5 mm x 0.1 mm) was used as the upper electrode.

The poling process was performed by placing the samples in a temperature controlled chamber and heating them to 150^0C with a field strength of 1 V/μm applied for 15 minutes. The samples were then allowed to cool to room temperature (RT) with the voltage applied continuously and once they reach RT the voltage was removed.

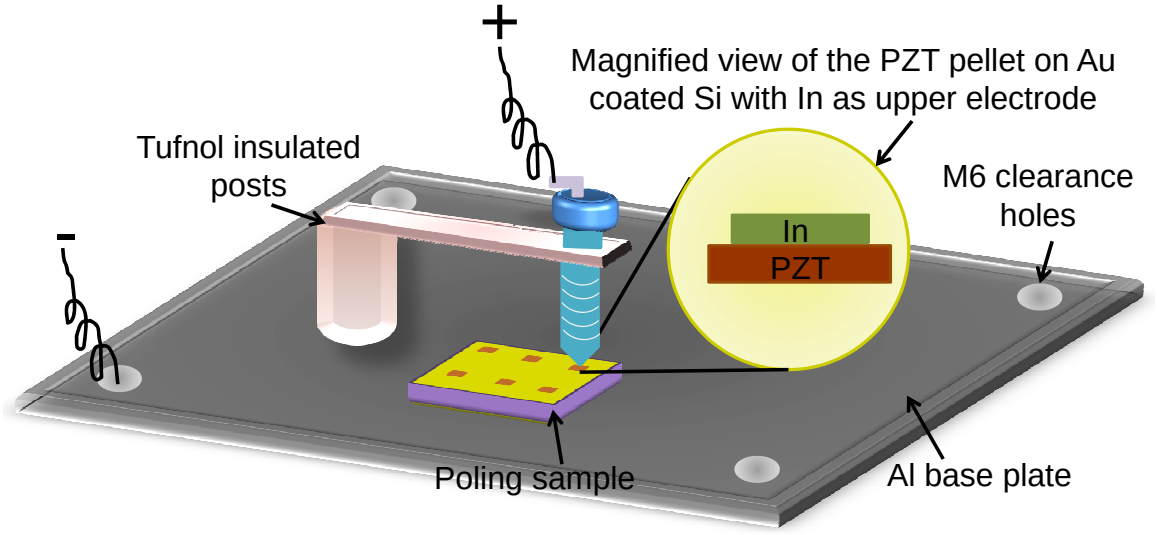

FIGURE 7.13: Schematic showing the holder used for poling the PZT samples.

The piezoelectric coefficients d_{33} of the samples were then measured using a Take Control PM35 piezometer (http://www.take control.demon.co.uk). The basic working principle of PM35 piezometer involves clamping the samples between two polished ball bearings and applying a low frequency oscillatory force to them. The electrical signals from the sample, if any, are then processed and on comparison with a built-in reference enables the system to give a direct reading of d_{33} coefficients (http://www.take control.demon.co.uk). Small values of ~19 - 20 pC/N were measured for 1μm thick PZT samples while nothing was recorded for 150 nm thick samples. The absence of any recorded d_{33} coefficient for 150 nm samples again suggested that thicker films/pellets are required for post-transfer processing and characterization and to realize functional devices. Even the 1 μm thick films/pellets were quite fragile and tend to short-circuit and get damaged while performing poling and d_{33} coefficient measurements so the experiments/measurements couldn't be repeated. Additionally, putting an indium foil on top of the pellets as an upper electrode is not an optimum method either. To address these shortcomings attempts were made to deposit better quality PZT donor films (~

1 μm) along with Al pads (∼100 nm) underneath which would serve both as a DRL during transfer and as the upper electrode for post transfer measurements (fig. 7.14). However for reasons not yet clear the films were found to be lead deficient as indicated by the EDX measurements (Table 7.1).

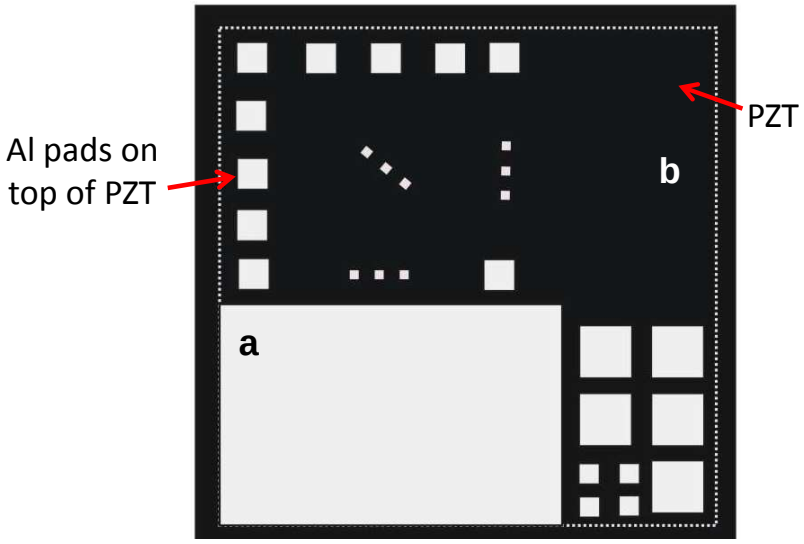

FIGURE 7.14: Schematic of PZT donor film (∼ 1 μm) with Al pads (100 nm) on top.

Element	Atomic % measured at point 'a' on the film	Atomic % measured at point 'b' on the film
Pb	0.77	0.12
Zr	10.99	10.71
Ti	13.21	15.47
O	61.15	61.92
Si	9.7	10.82
Al	3.22	0.02
Nb	0.97	0.94

TABLE 7.1: EDX measurements clearly showing the Pb deficiency in the PZT donor films.

7.4 Nanosecond LIFT of ZnO donor films

The schematic of the set-up used for printing non-lead based piezoelectric ZnO films onto Au coated Si receivers using ns-LIFT is shown in fig. 7.15[3]. Pulses from a KrF excimer laser (λ = 248 nm, τ = 20 ns) were centrally incident on a square mask with an aperture of 6 mm resulting in a homogeneous beam. This uniform beam was then imaged by a lens (f = 300 mm) onto the sample with a demagnification of 5x, yielding a spot size of 1.2 mm x 1.2 mm. The donor samples were prepared by sputtering 3 μm thick films of ZnO on top of fused silica substrates at a pressure of 3 mTorr and a temperature of 200^0C. The separation between donor and receiver substrates was maintained ~3.5 μm using Mylar spacers.

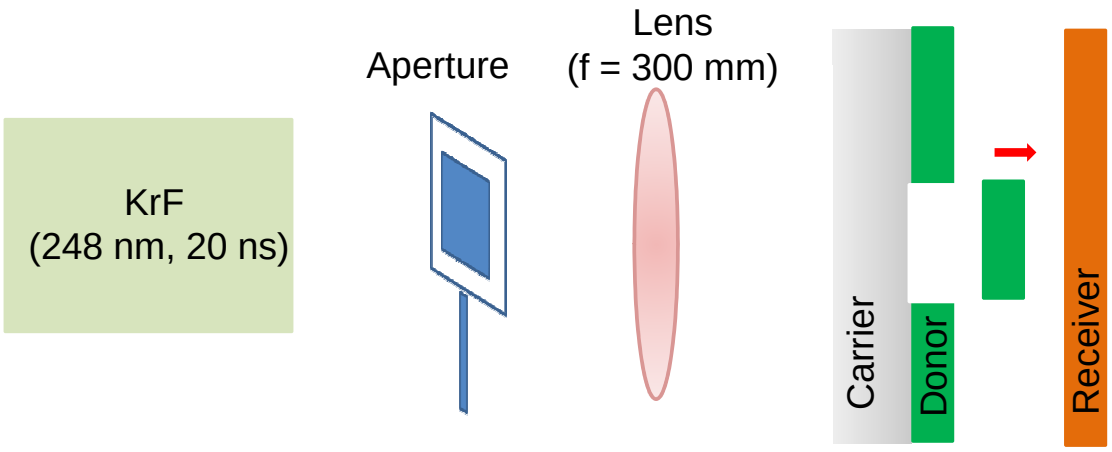

FIGURE 7.15: Experimental set-up used for printing ZnO donor films.

Figure 7.16 (a, b) show the SEM images of typical ZnO deposits printed using ns-LIFT at a fluence value of 0.9 J/cm^2 with fig 7.16 (c) showing the optical microscope image of the corresponding hole in the donor film. However the adhesion of ZnO deposits was so poor that the deposits couldn't stand the "blow test". Some of the pellets were collected onto carbon stubs for inspection under optical and electron microscopes that lead to significant cracking and damage of the pellets as shown in fig. 7.16 (a, b). The adhesion did not improve when printing was tried on different receiver substrates such as Si wafers without Au coating, plastic and cover glass slides. Due to the poor adhesion of

[3]Note that this work was performed prior to our use of FIB for pre-patterning. Additionally the time required to pre-pattern ~ mm^2 samples would be prohibitive.

the deposits it was not possible to perform any post-transfer characterization via poling and d_{33} coefficient measurements.

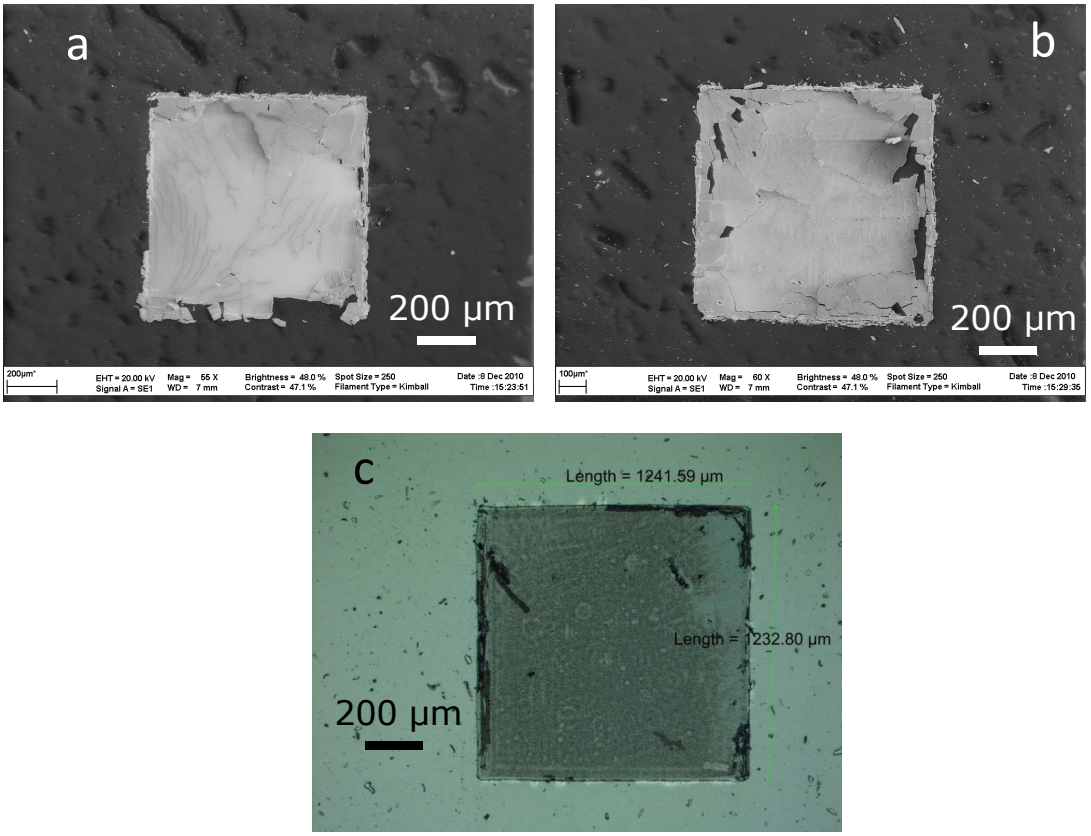

FIGURE 7.16: (a, b) SEM images of ZnO transferred ZnO deposits; (c) optical microscope image of the corresponding hole in the donor film.

7.5 Conclusions

Printing of lead based (PZT) and non-lead based piezoelectric (ZnO) materials using the conventional ns/fs-LIFT and ns/fs-DRL-LIFT technique was discussed in this chapter. Micron-sized PZT deposits were transferred from 150 nm thick film using fs-LIFT but post-transfer characterization for measuring the piezoelectric coefficients was difficult due to the small thickness and size of the deposited features so ns-LIFT was opted for to resolve this issue. The ns-LIFT enabled printing of mm size PZT pellets both using 150 nm and 1 μm thick donor films and the samples were poled at 150^0C before measuring

their d_{33} coefficients. A small value of 19-20 pC/N was recorded for 1 μm thick PZT films only. Due to the fragile nature of the deposits they tend to get damaged during measurements. To avoid this damage of the deposits and to get repeatable and more reliable post transfer measurements better quality films with metal pads underneath for use as the subsequent upper electrodes were sputtered but there were issues with Pb deficiency of the films. Finally, ns-LIFT of mm-sized ZnO pellets was presented but the deposits had very poor adhesion onto receiver substrates. The issues of Pb content in PZT films and poor adhesion of ZnO pellets need to be addressed in future before any viable micro-energy harvester can be realized using the LIFT technique.

Bibliography

S. P. Beeby, M. J. Tudor, and N. M. White. "Energy harvesting vibration sources for microsystems applications". *Measurement Science & Technology*, **17**:R175, 2006.

P. Glynne-Jones, S. P. Beeby, and N. M. White. "Towards a piezoelectric vibration-powered microgenerator". *IEE Proceedings-Science Measurement and Technology*, **148**:68, 2001.

http://www.pishaper.com.

http://www.take control.demon.co.uk.

R. N. Torah, S. P. Beeby, and N. M. White. "Improving the piezoelectric properties of thick-film PZT: the influence of paste composition, powder milling process and electrode material". *Sensors and Actuators a-Physical*, **110**:378, 2004.

X.B Wang, C. Song, D.M. Li, K.W. Geng, F. Zeng, and F. Pan. "The influence of different doping elements on microstructure piezoelectric coefficient and resistivity of sputtered ZnO film.". *Applied Surface Science*, **253**:1639, 2006.

S. Wu. http://cp.literature.agilent.com/litweb/pdf/5989-7611en.pdf. Technical report, Agilent Technologies, 2007.

Y. C. Yang, C. Song, X. H. Wang, F. Zeng, and F. Pan. "Giant piezoelectric d_{33} coefficient in ferroelectric vanadium doped ZnO films". *Applied Physics Letters*, **92**, 2008.

Chapter 8

Conclusions and Future Work

8.1 Introduction

In this chapter conclusions from the work presented in the previous chapters of the thesis are presented in section 8.2 and the suggestions for further work are discussed in section 8.3.

8.2 Conclusions

8.2.1 Time Resolved Study of LIFT

The effect of various key operating parameters such as laser fluence, donor and TP-DRL thickness on the transfer process and the quality of the ejected flyer for solid phase ceramics Gd-Ga-O and Yb:YAG was studied using the ns time-resolved shadowgraphy technique for different donor (200 nm and 1 μm) and TP (50, 150 and 360 nm) thicknesses over a range of 60 - 700 mJ/cm^2 fluence values and the results were presented in chapter 3. Both the shockwave and flyer were found to travel further and faster with increasing laser fluence value and the donor film quality was also observed to affect the flyer and shockwave properties. The flyer propagation distance also tended to decrease with increasing the donor film thickness. Theoretical values for propagation distance and velocity of flyer/shockwaves computed using simple analytical models agreed quite well with the experimental results obtained. It was observed that the flyer delaminates

earlier from the target surface and both the flyer and shockwave travelled greater distance for thicker (360 nm) films of TP-DRL as compared to thinner (50 nm) TP films however, more debris were found to be associated with the former case. Also, the flyers were seen to disintegrate and deform in shape with increasing distance from the target.

8.2.2 Rapid Prototyping of Photonic Devices using LIFT

Chapter 4 described the fabrication and characterization of Ti:LN segmented channel waveguides and X-couplers using the LIFT technique followed by thermal diffusion. Optical losses measured for channel waveguides were as low as $\sim$ 0.8 dB/cm showing great potential for the LIFT-based technique for fabricating photonic devices. The segment separation was observed to play a key role in determining the modal characteristics of the segmented waveguides. As the segment separation was increased to and beyond 16 μm the waveguide modal behavior was found to change from multi-moded to single moded and the size of the mode increased as well. This was attributed to the fact that the index contrast decreased on increasing the segment separation thereby decreasing the mode confinement and number of modes being supported. The dependence of the mode profile of the waveguides on the Ti segment separation formed the basis for fabricating index-tapered mode filters by varying the scan speed only along the length of the waveguides as discussed in chapter 5. The average optical loss of the waveguides was measured to be $\sim$3.8 $\pm$ 0.8 dB/cm with the mode filtering action confirmed by the captured mode profile images. Interestingly, the segmented geometry of the deposits tend to make the tapered waveguides non-adiabatic in nature and this was further confirmed by theoretical models developed using commercial software COMSOL and RSoft.

8.2.3 LIFTing of Pre-Machined Donor Films

Shearing and ripping of the donor material from the surrounding solid film at the boundary of the incident pulse resulting in poor edge quality deposits associated with unwanted debris is a basic problem related to both the conventional and complementary LIFT techniques. In order to mitigate this problem LIFTing of pre-machined donor films was presented in chapter 6. Results of printing micron-sized ($\sim$ 10 μm) deposits from 1 μm thick ZnO donor films etched to a depth of 0.8 μm using the FIB technique prior to LIFT were discussed. The deposits exhibited extremely smooth and uniform edges with

no debris associated with them thereby clearly demonstrating the advantages of LIFT using pre-machined donors. Comparison with the results obtained from printing ZnO pellets using the conventional and TP-DRL assisted LIFT techniques further highlighted the great potential of this technique. Additionally, no sacrificial or DRL material was required so in principle it can be used for printing any solid donor material unlike DRL-LIFT technique where the range of donor materials is limited by the temperature and chemical sensitivity of the chosen DRL material.

8.2.4 Printing Piezoelectrics using LIFT

In chapter 7 deposition and post-transfer characterization of both lead based (PZT) and non-lead based (ZnO) piezoelectric materials using the ns/fs-LIFT and ns/fs TP-DRL-LIFT technique was discussed. Micron-sized ($\sim$ 10 μm) 150 nm thick pellets of PZT were printed using fs DRL-LIFT but due to their small size and thickness post-transfer characterization of the deposits was not possible. A πbeam shaper (http://www.pishaper.com) incorporated in a fs-LIFT set-up resulted in increased size of the deposits but only up to $\sim$200μm so the ns-LIFT technique was then investigated to print thicker and larger area pellets. Measurements of d_{33} coefficients for 1 μm thick PZT pellets printed using ns-LIFT followed by poling at 150^0C resulted in small values of $\sim$ 19 - 20 pC/N for d_{33} coefficients. The pellets tend to get damaged during the poling and d_{33} measurements due to their fragile nature. In order to avoid this damage to the pellets PZT films were prepared with Al metal pads sputtered on top of them, with the intention to have the Al layer acting both as a DRL and top electrode, however for reasons not clear the films were found to be Pb deficient. For the case of non-lead based ZnO films the adhesion of the printed pellets (1.5 x 1.5 x 0.003 mm) was the major issue.

8.3 Future Work

In this section suggestions for work that can be carried out in the future based on the results presented in this thesis are discussed. The ns-shadowgraphy experiments can be performed by including a receiver in the set-up to collect the ejected flyers for investigating the presence of any residual TP in the debris and/or in the flyer. This will also help to understand the effect of receiver, if any, on the flyer quality. A more

thorough study of TP thickness parameter can be performed to completely understand its effect on the process dynamics. Additionally, a fs-time-resolved study of LIFT can be performed for a better understanding of the dynamics of the fs-LIFT transfer process and to compare it with its ns counterpart.

The optical losses of the segmented channel waveguides prepared using LIFT followed by post thermal treatment can be reduced further by optimising the deposition and post-processing parameters and more complex geometries and devices such as interferometers, 1 x N splitters etc. can be fabricated. Rare-earth dopants such as Nd, Er and Yb can be printed locally on pre-existing ridge waveguides or Ti:LN waveguides for lasing applications. Spatial selective deposition of multiple donor materials e.g. Ti and a rare-earth element either in one go or sequentially can also be investigated.

The initial results of LIFTing pre-machined donors using the trial value of $\Delta = 0.8$ were very promising. However a more thorough optimisation of the Δ parameter is required and its dependence on donor material and thickness needs to be studied. This method can be very helpful to print micron-sized crystals, which are nearly impossible to print using conventional LIFT or with any complementary LIFT technique, by using crystalline donor films with patterns etched in them prior to LIFT. Currently LIFTing of crystalline YIG ($Y_3Fe_5O_{12}$) grown onto YAG substrates using the PLD technique is being investigated.

The time required to etch features into the donor film using the FIB technique is a drawback of the FIB-assisted LIFT technique and this etch rate can be reduced by employing gas-assisted milling. Another method that can be employed to reduce the etching time is the use of spatially shaped laser pulses for defining the pattern in the donor film prior to transfer e.g for printing a circular feature the first few ring shaped pulses can be used to define and weaken the donor region to be printed followed by a top-hat profile pulse for pushing this weakened part of the donor to the receiver. This approach is similar to that used in the BLAST technique (Banks et al., 2008) however the significant damage to the deposits as observed in the BLAST technique can be avoided by controlling the spatial profile of each incoming pulse using a spatial light modulator (SLM). A DLP Discovery 3000 system by Texas Instruments (http://www.dmddiscovery.com) was used for spatially shaping the incident pulses. The discovery kit included a 0.7" digital micro mirror device (DMD) with an array of 1024 x 768 addressable mirrors plus a hardware

(Discovery 3000) and a controller board for communication with the DMD chip. Few preliminary experiments were performed to ablate complex patterns in gold donor films ($\sim$ 80 nm) by projecting static images on to the DMD as shown in fig. (8.1(a-c)).

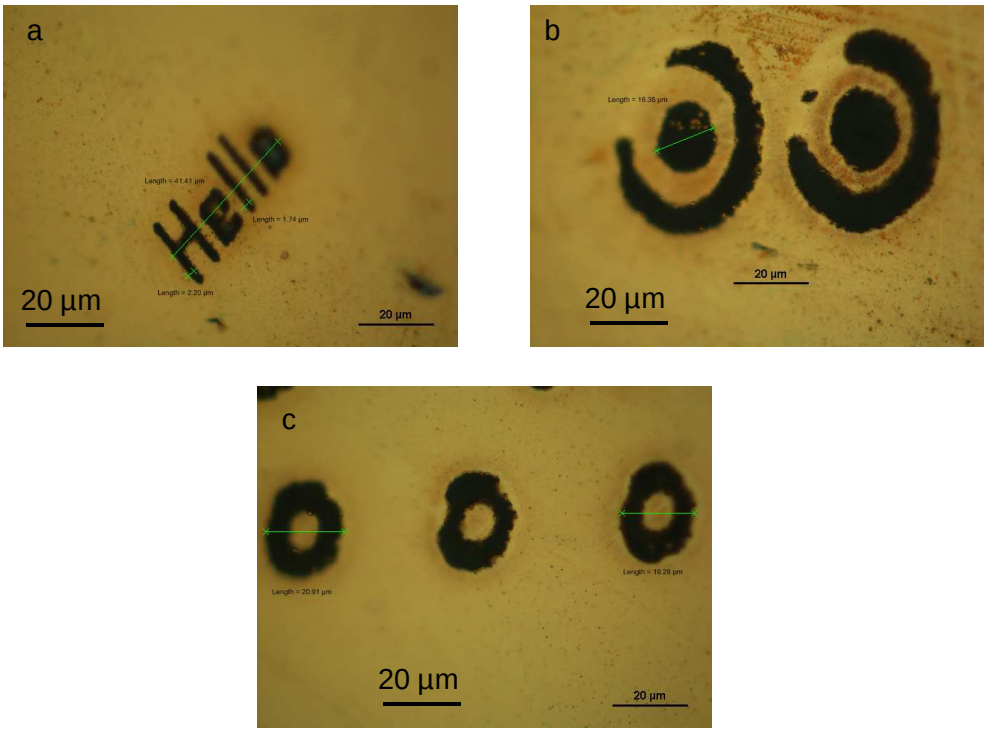

FIGURE 8.1: Optical microscope images of patterns ablated in Au donor films by spatially shaping the laser pulses using DMD.

However the DMD chip behaved erratically under fs laser irradiation and the reason was believed to be the sensitivity of the chip and the electronics underneath to electrostatic discharge, so further LIFT experiments couldn't be undertaken. A more robust DMD chip with better ESD compatibility called the Pico Projector (http://www.dlp.com/pico projector/) is being tested at present for spatially shaping the laser pulses.

For facilitating the measurements of d_{33} coefficients of PZT pellets post-transfer better quality donor films need to be deposited with adequate Pb content. To avoid damage to the pellets during the poling, oriented/aligned films and hence final LIFTed deposits can be achieved which will omit the need for poling the samples before piezoelectric

coefficient measurements. The adhesion of ZnO deposits onto the receiver substrates can be improved by chemical or surface treatment of the receiver substrate or coating the receiver substrate with an adhesion promoting thin film.

Finally, all the experiments discussed in this thesis were carried out either with fs laser with maximum rep rate of up to 1 kHz or with excimer laser with rep rate of 10-20 Hz. However for any real commercial applications, where a rapid prototyping and fast mass-production is a must, a higher rep-rate is necessary. Few attempts were made to print Ti films ($\sim$ 150 nm thick) using fs amplifier (Rega 9000) that can go up to 250 kHz. Figure 8.2 (a, b) show SEM images Ti line printed onto Si receiver substrates by tuning the rep-rate of the amplifier to 50 kHz.

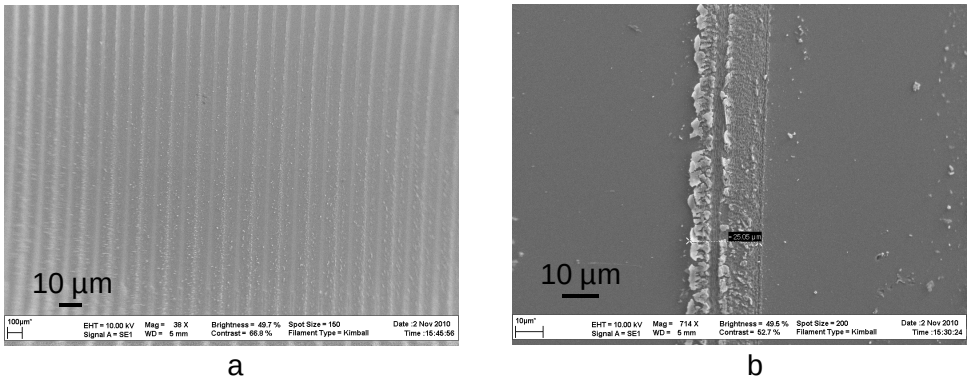

FIGURE 8.2: (a) SEM image of Ti lines printed onto Si receivers at a rep-rate of 50 kHz (b) magnified image of one of the lines.

The quality of the deposit however is very poor and the reason for this being the re-ablation of the printed metal deposits by successive pulses. The stages used to move the donor-receiver assembly relative to the incoming pulses couldn't be made to run faster than 30 mm/s due to problems with the stage software and this lead to $\sim$ 94% overlap between successive pulses resulting in ablation of the transferred deposits. Once the software issue is resolved LIFTing can be performed at a much faster rate and this technique can be used to cover bigger areas in competitive time scales.

Bibliography

D. P. Banks, C. Grivas, I. Zergioti, and R. W. Eason. "Ballistic laser-assisted solid transfer (BLAST) from a thin film precursor". *Optics Express*, 16:3249, 2008.

http://www.dlp.com/pico projector/.

http://www.dmddiscovery.com.

http://www.pishaper.com.

List of Publications

Journals

1. **K.S. Kaur**, M. Feinaeugle, D.P. Banks, J.Y. Ou, F. Di Pietrantonio, E. Verona, C.L. Sones, R.W.Eason, "Laser-induced forward transfer of focussed ion beam pre-machined donors," Applied Surface Science, **257**, 6850 (2011).

2. **K.S. Kaur**, A.Z. Subramanian, D.P. Banks, C.L. Sones, S. Mailis, and R.W. Eason, "Waveguide more filters fabricated using laser-induced forward transfer," Optics Express, **19**, (2011).

3. C.L. Sones, **K.S. Kaur**, P. Ganguly, D.P. Banks, Y.J. Ying, R.W. Eason, S. Mailis, "Laser-Induced-Forward-Transfer: A rapid prototyping tool for fabrication of photonic devices," Applied Physics A, **101**, 333 (2010).

4. D.P. Banks, **K.S. Kaur**, R.W.Eason, "Etching and forward transfer of fused silica in solid-phase by femtosecond laser-induced solid etching (LISE)," Applied Surface Science, **255**, 8343 (2009).

5. D.P. Banks, **K.S. Kaur**, R.W.Eason, "Influence of optical standing waves on the femtosecond laser-induced forward transfer of transparent thin films," Applied Optics, **48**, 2058 (2009).

6. **K.S. Kaur**, R. Fardel, T.C. May-Smith, M. Nagel, D.P. Banks, C. Grivas, T. Lippert, R.W. Eason, "Shadowgraphic studies of triazene assisted laser-induced forward transfer of ceramic thin films," Journal of Applied Physics, **105**, 113119 (2009).

7. D. Banks, **K.S. Kaur**, R.Gazia, R.W. Eason, R. Fardel, M. Nagel, T. Lippert, "Triazene photopolymer dynamic release layer-assisted femtosecond laser-induced forward transfer with an active carrier substrate," Europhysics Letters, **83**, 38003 (2008).

International Conferences

1. C. L. Sones, **K. S.Kaur**, M. Feinaeugle Feinaugle, K . A. Sloyan, T. C. M. Smith, R. W. Eason , " Printing of amorphous and crystalline materials pre-machined using focussed ion beam ", CLEO Europe 22-26th May 2011.

2. **K.S. Kaur**, M. Feinaeugle, D.P. Banks, J.Y. Ou, F. Di Pietrantonio, E. Verona, C.L. Sones, R.W.Eason ,"Laser-Induced Forward Transfer of Pre-Machined Donor Films", CLEO 2011 Baltimore 1-6th May 2011.

3. **K.S. Kaur**, A.Z. Subramanian, D.P. Banks, C.L. Sones, S. Mailis, and R.W. Eason "Waveguide Mode Filter Fabricated Using Laser-Induced Forward Transfer", CLEO 2011 Baltimore 1-6th May 2011.

4. S. Mailis, C.L. Sones, P. Ganguly, Y.J. Ying, **K.S. Kaur**, D.P. Banks, R.W. Eason "Laser-Induced-Forward-Transfer: A rapid prototyping tool for fabrication of photonic devices", COLA 09 Singapore 22-27 Nov 2009.

5. D.P.Banks, **K.S.Kaur**, C.Grivas, R.W.Eason, "Femtosecond laser-induced solid etching (LISE) of silicon and silica", EMRS Spring Meeting Strasbourg 8-12 Jun 2009.

6. D.P. Banks, **K.S. Kaur**, C. Grivas, C.L. Sones, P. Gangopadhyay, C. Ying, J.D. Mills, S. Mailis, I. Zergioti, R. Fardel, M. Nagel, T. Lippert, X. Xu, S.P. Banks, R.W. Eason "Femtosecond laser-induced forward transfer for the deposition of nanoscale transparent and solid-phase materials", 5th International Congress on Laser Advanced Materials Processing (LAMP) Kobe, Japan 29th Jun - 2nd Jul 2009

7. D.P. Banks, **K. Kaur**, C. Grivas, R. Fardel, M. Nagel, T.K.M. Lippert, I. Zergioti, R.W. Eason "Femtosecond laser induced forward transfer for the deposition of nanoscale transparent and solid-phase materials" LAMP 2009 Kobe 29 Jun - 2 Jul 2009 (Invited talk).

8. **K. Kaur**, R. Fardel, T.C. May-Smith, M. Nagel, D.P. Banks, C. Grivas, T. Lippert, R.W.Eason "Time resolved study of photopolymer assisted laser-induced forward transfer of thin ceramic films", LAMP 2009 Kobe 29 Jun-2 Jul 2009.

9. **K.S. Kaur**, R. Fardel, T.C. May-Smith, D.P. Banks, M. Nagel, C. Grivas, T. Lippert, R.W.Eason "Nanosecond-shadowgraphic imaging of laser induced forward transfer of ceramics using a triazene polymer sacrificial layer", EMRS 2009 Spring Meeting Strasbourg 8-12 Jun 2009.

10. **K. Kaur**, D.P. Banks, R. Gazia, C. Grivas, R. Fardel, M. Nagel, T. Lippert, R.W.Eason "Femtosecond laser-induced forward transfer of thin films using a Triazene polymer sacrificial layer and an active carrier", EMRS 2008 Strasbourg 26-30 May 2008.

A Letters Journal Exploring the Frontiers of Physics

August 2008

EPL, **83** (2008) 38003 www.epljournal.org
doi: 10.1209/0295-5075/83/38003

Triazene photopolymer dynamic release layer-assisted femtosecond laser-induced forward transfer with an active carrier substrate

D. P. Banks[1(a)], K. Kaur[1], R. Gazia[1], R. Fardel[2,3], M. Nagel[2], T. Lippert[3] and R. W. Eason[1]

[1] *Optoelectronics Research Centre, University of Southampton - Southampton SO17 1BJ, UK, EU*
[2] *General Energy Research Department, Paul Scherrer Institut - 5232 Villigen PSI, Switzerland*
[3] *EMPA, Swiss Federal Laboratories for Materials Testing and Research, Laboratory for Functional Polymers Überlandstrasse 129, 8600 Dübendorf, Switzerland*

received 18 March 2008; accepted in final form 13 June 2008
published online 23 July 2008

PACS 81.15.Fg – Laser deposition
PACS 64.70.km – Polymers
PACS 42.65.Ky – Frequency conversion; harmonic generation, including higher-order harmonic generation

Abstract – Discs of solid material have been forward transferred from thin films on transparent carrier substrates using femtosecond Ti:sapphire laser-induced forward transfer (fs-LIFT) with a triazene polymer dynamic release layer (DRL). The fluence threshold for fs-LIFT was found to be only ≈ 20% of the DRL ablation threshold at the laser wavelength. This decrease is attributed to ultrafast shock-wave generation in the constrained polymer layer under femtosecond irradiation being the driving force for fs-LIFT with the polymer DRL. The result is very different from the nanosecond regime, where the LIFT threshold is observed to be slightly above the polymer ablation threshold. White-light continuum generation in a carrier substrate is observed and its influence on the fs-LIFT process is discussed.

Introduction. – The deposition of patterned thin films of various materials is important for both fundamental research and technical (*i.e.* micro-electro-mechanical) applications. Most techniques applied for this purpose lack lateral resolution on micron and smaller scales, so separate deposition and patterning stages are necessary. Direct-write (DW) methods are attractive for microdeposition applications as deposition and patterning can be achieved simultaneously.

A very promising technique offering sub-micron lateral resolution deposition of a wide variety of materials is laser-induced forward transfer (LIFT) (fig. 1(a)) [1]. In LIFT, a thin film of the material to be deposited (the donor) is coated onto a transparent carrier substrate. The coated carrier is placed in close contact with a receiving substrate and one or more focused or demagnified laser pulses are used to transfer a well-defined section of the film. The laser induces ablation at the carrier-film interface to propel material to the receiver.

Whilst LIFT is readily applied for metal films [1,2] and materials that are heat-resistant, sensitive materials such as biomaterials, organic dyes, and semiconducting polymers can be damaged by the laser irradiation. The high pressures and temperatures that are experienced by the donor during transfer can result in photo- or thermo-chemical reactions, phase-changes and evaporation. As such, it is now relatively common practice in LIFT experiments to include a sacrificial propellant material, either in the form of a supporting matrix (Matrix-Assisted Pulsed Laser Evaporation-Direct Write

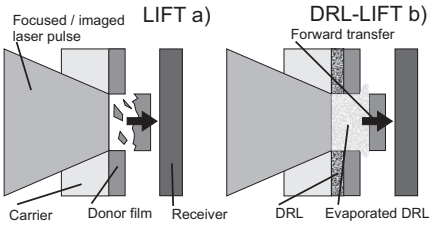

Fig. 1: Schematics of LIFT (a) and DRL-assisted LIFT (b).

(a) E-mail: dpb@orc.soton.ac.uk

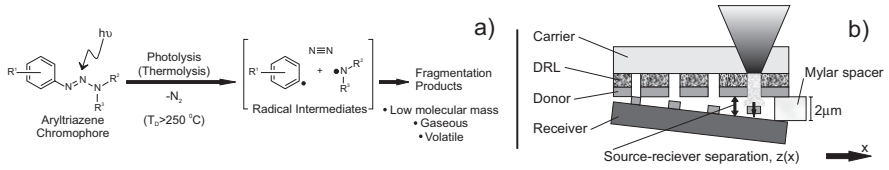

Fig. 2: Photolytic cleavage pathway of a triazene chromophore (the chromophore can also experience thermal decomposition above about 250 °C) (a) [7]. Experimental layout used to study femtosecond LIFT with TP DRL (b).

(MAPLE-DW)) [3,4], or as a separate layer between carrier and donor (a dynamic release layer (DRL)) [5], to protect the active material during transfer. DRL-LIFT is shown schematically in fig. 1(b).

Dynamic release layers. – To be suitable for use as a DRL, a material must have a low ablation threshold, high-absorption coefficient, and avoid excessive thermalization of the absorbed photons to facilitate transfer with low thermal impact on the donor. The DRL should also dissociate upon irradiation to avoid contamination of the transferred donor with residual DRL material. A particularly well-suited material for DRL applications is the triazene polymer (TP), which exhibits clean and well-defined photofragmentation into small, volatile, gaseous, molecular fragments. The fragmentation process releases N_2, providing the thrust required for LIFT [6,7]. This thrust, which originates from the pressure increase, allows a precise "cutting" of well-defined regions from the film. The photolytic cleavage pathway of a TP chromophore is shown in fig. 2(a) [7]. The TP chromophore can also experience the same decomposition pathway if the temperature is raised above $\approx 250\,^{\circ}\mathrm{C}$.

The TP has a very low ablation threshold of $25\,\mathrm{mJ/cm^2}$ at 308 nm irradiation (with ns pulses) meaning that transfer can be achieved with low thermal impact on sensitive donors using UV wavelengths [8]. The IR damage threshold of the TP has been measured to be $\approx 500\,\mathrm{mJ/cm^2}$ at 800 nm with 130 fs pulses, with multi-photon absorption believed to be the dominant absorption mechanism [9]. The quality of the structures obtained with fs laser ablation is also quite high, with strong indication that the fs-pulse induced decomposition also produces mainly gaseous ablation products (similar to 308 nm, ns irradiation) [8].

The TP has been used as a DRL in a number of LIFT studies for forward transfer of other polymers [10], cells [11], quantum dots [12], and organic LEDs [13]. Other materials have also been used as DRLs, including metals [14,15], hydrogenated silicon [16], and other polymers [5,17]. An important point to note is that in all these studies, which used nanosecond pulsed lasers, the fluence threshold required for LIFT was slightly greater than the normal ablation threshold of the DRL material. This result should not be surprising as, to achieve forward transfer, sufficient DRL material must be ablated to provide LIFT thrust.

In this work, we present results using the TP as a DRL for the forward transfer of "hard" donor films. An 800 nm femtosecond pulsed laser is used, representing the first ultrashort-pulsed TP DRL results. The different transfer mechanisms in the nanosecond and femtosecond regimes will be discussed. Before the fs-LIFT results are presented, we shall discuss the occurrence of nonlinear optical phenomena in the carrier. Such phenomena are unavoidable in a typical fs-LIFT setup, but their potential consequences have not yet been considered in the literature.

Experimental. – For all LIFT experiments, single pulses from a Ti:sapphire laser (800 nm, ≈ 130 fs) were used. Spatially-Gaussian laser pulses of ≈ 4 mm diameter (FWHM) were centrally incident on a $450\,\mu$m circular aperture, resulting in a circular beam; the intensity difference between the centre and the edge of the beam was $\approx 5\%$. A highly demagnified image of the aperture was relayed to the target using a reverse projection microscope resulting in an $\approx 12\,\mu$m diameter circular spot at the carrier-film interface, as measured by the laser damaged area. The image plane of the microscope was adjusted to coincide with the best image of the aperture and the depth of focus of the laser was measured to be $\approx 200\,\mu$m.

The TP was synthesized as described by Nagel *et al.* [6] and was then prepared by spin coating from a solution in chlorobenzene and cyclohexanone (1 : 1, w/w). The thickness of the TP was controlled by adjusting the viscosity of the solution and spin speed to yield a DRL with a thickness of ≈ 100 nm. The carrier substrates were a fused quartz disc (diameter 50 mm, thickness 3 mm) and the receiver was a Si wafer ≈ 10 mm square. All experiments were performed under vacuum at ≈ 0.1 mbar. The separation between the donor film and the receiver, z, was controlled by the insertion of a single $2\,\mu$m thick Mylar spacer. This resulted in a variation of the separation with position across the LIFT setup, $z(x)$, as shown in fig. 2(b). Donor-receiver separation was measured interferometrically using the microscope's white-light source.

On top of each DRL, a donor film of ≈ 150 nm of a transparent amorphous GdGaO material was grown by pulsed laser deposition (PLD). The PLD target was single crystal gadolinium gallium garnet ($Gd_3Ga_5O_{12}$). The films were deposited at room temperature and in an oxygen

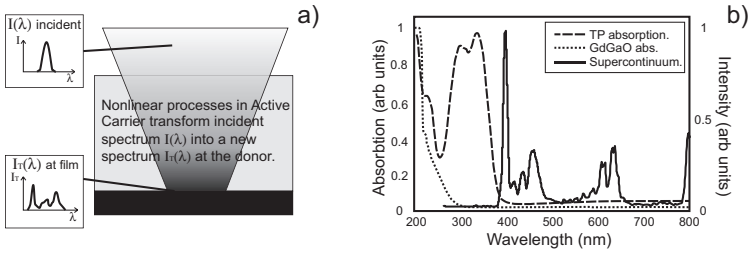

Fig. 3: Schematic of the active carrier technique (a). Typical measured supercontinuum spectrum (solid line), and TP (dashed line) and GdGaO (dotted line) film absorption curves (b).

atmosphere at a pressure of 4×10^{-2} mbar. The GdGaO was chosen as a sample material to study the fs-LIFT of "hard" donor films using the TP-DRL. It is interesting because it can be grown under conditions that do not damage the polymer and LIFTed in the amorphous state before post-transfer annealing to crystallise it (results not presented here). As such it may provide a template for the micro-deposition of single-crystal material by fs-LIFT.

Active carriers. – The measured ablation threshold of the TP at 800 nm corresponds to an intensity of $\approx 10^{12}\,\mathrm{W/cm^2}$ [9]. Reported intensity thresholds for femtosecond LIFT are also typically $\geqslant 10^{11}\,\mathrm{W/cm^2}$ (see *e.g.* [2,18–21]). It is well-known that, when ultrashort laser pulses are focused inside transparent media, supercontinuum generation can occur, resulting in a significant broadening of the laser spectrum [22]. The intensity threshold for the onset of supercontinuum generation with 800 nm in silica has been measured to be $\approx 10^{11-12}\,\mathrm{W/cm^2}$ and, a spectrum from $\approx$ 400–950 nm is generated [23]. Hence, in a fs-LIFT arrangement it is unavoidable that, at some point within the carrier, the laser intensity will be great enough to generate a supercontinuum. Such a setup, where the normally passive carrier substrate plays an active role by modifying the laser spectrum, may be termed active carrier LIFT (AC-LIFT). The principle of AC-LIFT is indicated in fig. 3(a).

To measure the spectrum and intensity of the supercontinuum generated in the current experiment, the laser was imaged onto the rear surface of an uncoated carrier in exactly the same geometry as used for all fs-LIFT experiments. Two IR cut-off filters (cut-off wavelength $\approx$ 670 nm; effective transmission (800 nm) $\leqslant 1\%$, ($\leqslant$ 670 nm) $\geqslant 90\%$) were inserted after the uncoated carrier to remove residual 800 nm light. The threshold for supercontinuum generation was measured to be $\approx 110\,\mathrm{mJ/cm^2}$ ($\cong 7 \times 10^{11}\,\mathrm{W/cm^2}$). The conversion efficiency (including all wavelengths $\leqslant$ 670 nm) was $\approx$ 1–1.5%. The solid trace in fig. 3(b) shows a typical spectrum; the supercontinuum displayed a strong peak around 400 nm with an intensity $\leqslant 1\%$ of the incident laser. The new wavelengths generated in the AC represent another possible source of laser-induced damage to the donor material that must be considered when choosing the combination of donor and DRL materials, and laser wavelength.

The absorption spectrum of the GdGaO donor film is also shown in fig. 3(b), dotted line. As can be seen, the material was essentially transparent to wavelengths longer than 300 nm; hence the donor could not be damaged either directly by the laser or by the AC-generated supercontinuum. The absorption spectrum of the TP polymer is represented by the dashed line in fig. 3(b) [9]. The TP did not significantly absorb the AC-generated supercontinuum. The absorption coefficients at 400 nm and 800 nm were approximately equal; hence, given the $\approx 1\%$ conversion efficieny from 800 $\rightarrow$ 400 nm, it can be concluded that the AC did not affect linear absorption of the laser in the TP-DRL. The measured ablation threshold for a 100 nm thick TP film with no overlying donor irradiated through a carrier substrate was found to be $\approx 500\,\mathrm{mJ/cm^2}$. This value was in good agreement with the normal ablation threshold at 800 nm and significantly above the threshold for onset of supercontinuum generation, deomnstrating that the presence of the continuum did not significantly affect the TP ablation.

GdGaO results. – The threshold for forward transfer of the GdGaO donor was measured to be $\approx 90\,\mathrm{mJ/cm^2}$ with the TP-DRL and $\approx 110\,\mathrm{mJ/cm^2}$ without it. Figure 4(a) shows an SEM image of transferred GdGaO material using $\approx 120\,\mathrm{mJ/cm^2}$ without the DRL, and fig. 4(b,c) show SEM micrographs of GdGaO discs deposited with the DRL; fluence $\approx$ 90–100 $\mathrm{mJ/cm^2}$. The donor-receiver separation was $\approx$ 100–200 nm. The benefits of using the TP-DRL for the LIFTing of solid material from hard donor films are apparent. Surface profiling of typical discs transferred using the DRL, similar to those in fig. 4(b,c), is shown in fig. 4(d). The deposits were reproducibly $\approx$ 130 nm thick, closely matching the original thickness of the GdGaO donor and indicating that little or no DRL remained on the deposit post-transfer. Another reproducible feature of the deposits was a slightly raised region around the edge, which is believed to be a result of

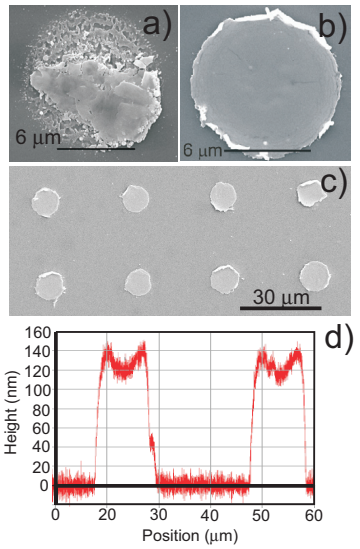

Fig. 4: SEM micrographs of GdGaO deposition without a TP-DRL ($\approx 120\,\mathrm{mJ/cm^2}$) (a), and with the DRL (≈ 90–$100\,\mathrm{mJ/cm^2}$) (b,c); donor-receiver separation of ≈100–200 nm. Surface profiling of deposits like those shown in (c) (d).

how the deposits were transferred, which will be discussed later.

The most important thing to note with regards to the GdGaO depositions is the significant difference in laser fluence threshold for forward transfer and direct ablation of the TP ($\approx 500\,\mathrm{mJ/cm^2}$ [9]); the LIFT threshold was only about 20% of the direct ablation threshold. This was very different from the case of nanosecond polymer DRL-assisted LIFT where the LIFT threshold has been consistently found to be slightly above the polymer ablation threshold. Hence a totally new process is observed when using femtosecond pulses for TP DRL-LIFT. The reason for the dramatically lower LIFT threshold with femtosecond pulses is hypothesised as follows, and shown schematically in fig. 5.

1. fig. 5(1): The incident laser energy was absorbed in the TP DRL through multi-photon absorption of the 800 nm laser; for reasons discussed earlier, the AC-generated supercontinuum is not thought to play a significant role. Furthermore, interface effects and multiple reflections from the TP-donor and donor-vacuum interfaces, and the Si receiver may have slightly increased absorption in the DRL.

2. fig. 5(2): As the absorption depth of the laser significantly exceeded the film thickness, absorption throughout the irradiated region was approximately homogeneous.

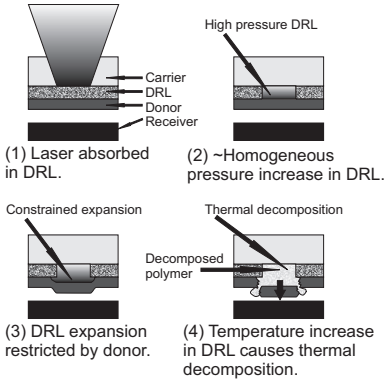

Fig. 5: Hypothesised process leading to low forward transfer threshold fluence when using ultrashort pulses.

3. fig. 5(3): The absorption of ultrashort duration pulses in polymers initiates a rapid pressure jump in the target due to the pulse energy being deposited faster than the target can fully relax (see *e.g.*, [24]). This is in sharp contrast to exposure to longer duration pulses, where the relatively slow rate of energy deposition predominantly results in a temperature increase. However, even with ultrashort pulses, with free surface ablation this pressure increase can be somewhat relaxed by expansion of the target. In a DRL-LIFT arrangement, particularly with a hard donor film, significant expansion of the polymer is restricted by the overlying layer. Hence in this case, the pressure of the TP DRL was raised sharply by absorbing the femtosecond pulse. The increase could not be easily relaxed by polymer expansion, so a sharp temperature increase in the TP occurred.

4. fig. 5(4): This temperature increase resulted in the DRL temperature rising above $\approx 250\,^\circ\mathrm{C}$ and thermolytic decomposition of the DRL occurred.

Hence we envisage a situation where absorption of the femtosecond pulse initiated a rapid pressure jump in the TP which could not be easily relaxed due to the overlying donor layer. The polymer temperature then increased and thermal decomposition of the TP chromophores occurred well below the DRL ablation threshold.

To further support the hypothesis of thermal decomposition resulting from constrained pressure increase being the driving force for sub-ablation threshold forward transfer with femtosecond pulses, the influence of donor-receiver separation on any resultant GdGaO depositions was studied. The results are shown in fig. 6. Figure 6(a) shows

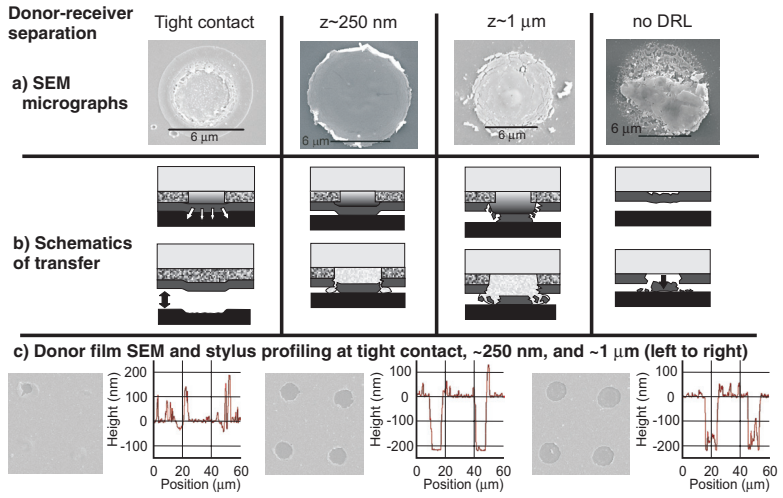

Fig. 6: SEM micrographs (a) and schematics of the forward transfer process (b) with varying donor-receiver separation. (c) SEM and stylus profiling of donor film after LIFT in tight contact (left), at optimal separation, and with greater than optimal separation (right).

SEM micrographs of deposits obtained with tight-contact between donor and receiver (left column), and separations of $\approx 250\,\text{nm}$ & $\approx 1\,\mu\text{m}$. Figure 6(b) shows diagrams of the envisaged transfer process in the different donor-receiver separation regimes. The case of no DRL is also shown for comparison (right column).

When donor and receiver were in tight contact, no discs of donor material were obtained. The TP decomposed due to the large pressure increase, however the tight contact with the receiver prevented expansion of the decomposed polymer, which was necessary to shear the donor. Instead the high pressure build up in the irradiated region just caused some damage to the underlying receiver. EDX analysis and surface-profiling confirmed that there was little or no GdGaO deposited onto the receiver. With a small donor-receiver separation ($\leqslant 500\,\text{nm}$), there was sufficient space for a small amount of expansion of the decomposed polymer which allowed for relatively clean shearing and transfer of a clean disc of donor. The slight deformation of the donor film prior to shearing also explains the slightly raised edges seen around clean disc deposits (see fig. 4(d)). As the separation was increased, the brittle donor experienced increased deformation due to the pressure of the trapped decomposed DRL. With separations of $\approx 1\,\mu\text{m}$, the amount of deformation became sufficiently great that the donor disc shattered during transfer, resulting in a more particulate deposit.

In this case, the optimal donor-receiver separation was found to be around 250 nm. However, it should be noted that the optimal separation is expected to vary with a number of properties including DRL and donor materials and layer thicknesses; for example, less brittle donors should be able to withstand increased deformation without shattering. The size of the laser spot will also affect the deformation of the donor and should have an influence on the dependence of the transfer process on separation.

Figure 6(c) shows SEM and stylus profiling observations of the donor film after LIFT in tight contact (left), at optimal separation, and at greater than optimal separation (right). It can be seen that, in tight contact, most of the GdGaO film remained on the carrier, although a significant roughening of the donor surface was apparent in the irradiated areas. When the separation was increased to optimal, the donor material was completely removed from the carrier apart from small sections around the edge of the irradiated region, which, although fragmented, remained partially attached to the donor film. At greater than optimal separation, complete removal of material in the irradiated region was also seen, but the fragments around the edge were no longer visible attached to the donor and appeared instead as debris on the carrier and donor. The fragmentation of donor material around the edge of the transferred region supports the hypothesis of deformation of the donor, primarily at the edge, occurring as a result of increased pressure of the underlying polymer. We conclude therefore that the Si receiver also played a critical role in determining the final quality of deposited material. The receiver had to be close enough to constrain deformation of the brittle donor and restrict shattering around the edge due to excessive bending. However, a

small separation between donor and receiver was necessary to allow the donor to shear.

A final point to note is that, at optimal donor-receiver separation, stylus profiling results indicated that the TP was completely removed during LIFT (see fig. 4(d) and fig. 6(c)), which is important to avoid contamination of transferred material.

Conclusions. – Discs of GdGaO of $\approx 10\,\mu$m diameter have been deposited by TP DRL-assisted femtosecond LIFT. The use of the TP-DRL allowed for the deposition of pellets of GdGaO in solid phase with no shattering when the donor and receiver were at the optimal separation. In contrast, when no DRL was used GdGaO material was transferred in many fragments due to explosive ablation of the donor material being the driving force for LIFT.

The threshold transfer fluence with the TP-DRL was found to be $\approx 90\,\mathrm{mJ/cm^2}$, only $\approx 20\%$ of the polymer ablation threshold at the laser wavelength. This was in stark contrast to nanosecond DRL-LIFT using this polymer where the transfer threshold is reproducibly found to be slightly greater than the ablation threshold. A model to explain the reduced fluence threshold of TP-DRL fs-LIFT has been proposed based on a rapid increase of the polymer DRL pressure following irradiation that cannot be easily relaxed due to the presence of the overlying donor film and receiver. The model has been supported by the observed morphology of the transferred material and donor film after LIFT. The optimal donor-receiver separation was found to be around 250 nm, although this optimal value is predicted to vary with donor and DRL materials and feature size. The TP has been observed to be removed completely during LIFT.

Supercontinuum generation in the carrier substrate has been observed at the typical transfer fluences. Although the influence of the continuum has been shown to be negligible within this study, the presence of a supercontinuum in a fs-LIFT setup cannot be neglected as the generated wavelengths may be absorbed by the DRL or donor.

* * *

The authors are grateful to the Engineering and Physical Sciences Research Council, UK, for research funding under Grant No. EP/C515668/1. The financial support of the Swiss National Science Foundation is acknowledged.

REFERENCES

[1] Bohandy J., Kim B. F. and Adrian F. J., *J. Appl. Phys.*, **60** (1986) 5138.

[2] Banks D. P., Grivas C., Mills J. D., Zergioti I. and Eason R. W., *Appl. Phys. Lett.*, **89** (2006) 193107.

[3] Piqué A., Chrisey D. B., Auyeung R. C. Y., Fitz-Gerald J., Wu H. D., McGill R. A., Lakeou S., Wu P. K., Nguyen V. and Duignan M., *Appl. Phys. A (Suppl.)*, **69** (1999) S279.

[4] Arnold C. B., Kim H. and Piqué A. , *Appl. Phys. A*, **79** (2004) 417.

[5] Tolbert W. A., Lee I.-Y. S., Doxtader M. M., Ellis E. W. and Dlott D. D., *J. Imaging Sci. Technol.*, **37** (1993) 411.

[6] Nagel M., Hany R., Lippert T., Molberg M., Nüesch F. A. and Rentsch D., *Macromol. Chem. Phys.*, **208** (2007) 277.

[7] Fardel R., Feurer P., Lippert T., Nagel M., Nüesch F. A. and Wokaun A., *Appl. Surf. Sci.*, **254** (2007) 1332.

[8] Karnakis D. M., Lippert T., Ichinose N., Kawanishi S. and Fukumura H., *Appl. Surf. Sci.*, **127-129** (1998) 781.

[9] Bonse J., Solis J., Urech L., Lippert T. and Wokaun A., *Appl. Surf. Sci.*, **253** (2007) 7787.

[10] Mito T., Tsujita T., Masuhara H., Hayashi N. and Suzuki K., *Jpn. J. Appl. Phys.*, **40** (2001) 805.

[11] Doraiswamy A., Narayan R. J., Lippert T., Urech L., Wokaun A., Nagel M., Hopp B., Dinescu M., Modi R., Auyeung R. C. Y. and Chrisey D. B., *Appl. Surf. Sci.*, **252** (2006) 4743.

[12] Xu J., Liu J., Cui D., Gerhold M., Wang A. Y., Nagel M. and Lippert T., *Nanotechnology*, **18** (2007) 025403.

[13] Fardel R., Nagel M., Nüesch F., Lippert T. and Wokaun A., *Appl. Phys. Lett.*, **91** (2007) 061103.

[14] Serra P., Colina M., Fernández-Pradas J. M., Sevilla L. and Morenza J. L., *Appl. Phys. Lett.*, **85** (2004) 1639.

[15] Hopp B., Smausz T., Antal Zs., Kresz N., Bor Zs. and Chrisey D., *J. Appl. Phys.*, **96** (2004) 3478.

[16] Toet D., Thompson M. O., Smith P. M. and Sigmon T. W., *Appl. Phys. Lett.*, **74** (1999) 2170.

[17] Kattamis N. T., Purnick P. E., Weiss R. and Arnold C. B., *Appl. Phys. Lett.*, **91** (2007) 171120.

[18] Bähnisch R., Gross W. and Menschig A., *Microelectron. Eng.*, **50** (2000) 541.

[19] Bera S., Sabbah A. J., Yarbrough J. M., Allen C. G., Winters B., Durfee C. G. and Squier J. A., *Appl. Opt.*, **46** (2007) 4650.

[20] Papakonstantinou P., Vainos N. A. and Fotakis C., *Appl. Surf. Sci.*, **151** (1999) 159.

[21] Zergioti I., Papazoglou D. G., Karaiskou A., Fotakis C., Gamaly E. and Rode A., *Appl. Surf. Sci.*, **208-209** (2003) 177.

[22] Brodeur A. and Chin S. L., *J. Opt. Soc. Am. B*, **16** (1999) 637.

[23] Nagura C., Suda A., Kawano H., Obara M. and Midorikawa K., *Appl. Opt.*, **41** (2002) 3735.

[24] Hare D. E., Franken J. and Dlott D. D., *J. Appl. Phys.*, **77** (1995) 5950.

Shadowgraphic studies of triazene assisted laser-induced forward transfer of ceramic thin films

K. S. Kaur,[1,a)] R. Fardel,[2,3] T. C. May-Smith,[1] M. Nagel,[3] D. P. Banks,[1] C. Grivas,[1] T. Lippert,[2] and R. W. Eason[1]
[1]*Optoelectronics Research Centre, University of Southampton, Southampton SO17 1BJ, United Kingdom*
[2]*General Energy Research Department, Paul Scherrer Institut, 5232 Villigen PSI, Switzerland*
[3]*Laboratory for Functional Polymers, EMPA–Swiss Federal Laboratories for Materials Testing and Research, Überlandstrasse 129, 8600 Dübendorf, Switzerland*

(Received 4 December 2008; accepted 20 April 2009; published online 9 June 2009)

The laser-induced forward transfer process of solid ceramic donor materials (gadolinium gallium oxide and ytterbium doped yttrium aluminium oxide) was studied using triazene polymer as a sacrificial layer by means of a time-resolved nanosecond-shadowgraphy technique. The dependence of the ablation dynamics and quality of the ejected donor material on the laser fluence and thickness of the sacrificial and donor layers were investigated and discussed. © *2009 American Institute of Physics*. [DOI: 10.1063/1.3132822]

I. INTRODUCTION

The laser-induced forward transfer (LIFT) method has received a great deal of attention in the past two decades as an additive laser direct-write technique due to its simplicity, versatility, and the potential advantages it offers. The basic working principle of LIFT involves the focusing of a laser pulse through a transparent support substrate (the carrier) onto the rear side of a thin film of the material to be LIFTed (the donor). Another substrate (the receiver) onto which the donor material is to be transferred is placed in close proximity to the coated carrier (the target).[1–4] However, in the conventional LIFT process the donor material acts as its own propellant, which leads to its unavoidable damage during the transfer process. A variation in the original LIFT technique employed to overcome this problem utilizes an intermediate sacrificial layer called the dynamic release layer (DRL), which is sandwiched between the carrier and the donor to absorb the incident pulse energy.[5]

A tailor-made UV absorbing triazene polymer (TP) has recently gained much favor as a DRL material due to its attractive properties such as low ablation threshold and photolytic dissociation. Upon dissociation, the TP releases N_2 gas along with other molecular gaseous fragments, which provide the required push for forward transfer of the overlying donor layer.[6] Living biological cells,[7] organic light emitting diodes (OLEDs),[8] quantum dots,[9] and ceramic materials[10] have been transferred using TP as the DRL.[11] In all these cases the receiver was placed either in contact or in close proximity to the target. However, for an ease in mechanical handling in industrial applications such as those involving transfer of donors for building stacks of different materials, the donor and receiver need to be separated by a relatively large distance. Time-resolved techniques can be used to study the dynamics of the LIFT process for such cases and the quality of the ablated donor material during transfer.[12,13] These observations help in improving understanding of both the ablation and the transfer mechanisms that are directly related to the end scientific and technological applications.

In this paper, conventional nanosecond-shadowgraphy imaging of the TP-DRL assisted LIFT is reported for the solid phase ceramic materials gadolinium gallium oxide (Gd–Ga–O) and ytterbium doped yttrium aluminium oxide (Yb:YAG). The time evolution of the LIFT process and the influence of various operating parameters such as the laser fluence and thicknesses of the donor and DRL materials on the quality of the opaque transferred disc (referred to as the "flyer") were also investigated and the results are discussed.

II. EXPERIMENTAL

The samples for the nanosecond-shadowgraphic studies were prepared by depositing films of the donor materials Gd–Ga–O and Yb:YAG on top of previously TP coated fused silica substrates. The TP was synthesized by the method described in Ref. 14 and spin-coated on the silica substrates from solutions of TP in chlorobenzene and cyclohexanone (1:1 w/w). The donor material layer was then deposited on top by pulsed laser deposition (PLD). All the donor films were prepared under room temperature conditions and in an oxygen atmosphere (7×10^{-2} mbar for Gd–Ga–O and 2×10^{-3} mbar for Yb:YAG). Due to the temperature sensitivity of the TP, which decomposes at 250 °C,[14] Gd–Ga–O and Yb:YAG were chosen as the donor materials because they can be deposited at room temperature. Several samples with different TP thicknesses (50, 150, and 350 nm) and different donor thicknesses (200 and 1000 nm) were prepared to study the effect of the relative thicknesses of the DRL and donor material on the quality of the ablated flyer.

The pump-probe setup used for the experiments is shown in Fig. 1. A XeCl excimer laser (Compex, Lambda Physik, $\lambda=308$ nm, $\tau=30$ ns) was used as the pump source. The reason for choosing this laser was the strong absorption of the TP at this wavelength.[6] The second harmonic of a

a)Author to whom correspondence should be addressed. Electronic mail: kak@orc.soton.ac.uk.

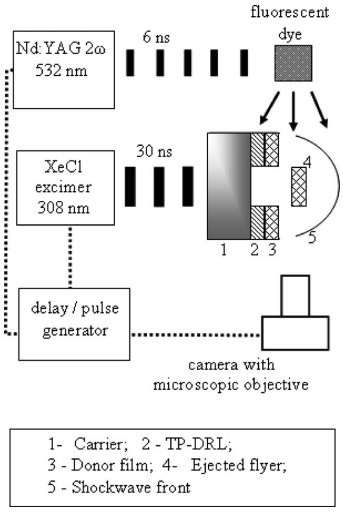

FIG. 1. Schematic of the nanosecond-shadowgraphy setup.

Nd:YAG laser ($\lambda=532$ nm, $\tau=6$ ns) was used as the probe beam. The pump pulses were centrally incident on a square mask with an aperture of 2 mm, resulting in an approximately homogeneous beam. This uniform beam was then imaged by a lens onto the sample with a demagnification of 4×, yielding a spot size of 500×500 μm^2. The pump laser energy incident on the target was controlled by a variable attenuator plate and was measured by a pyroelectric energy meter (Molectron J4–09 or Gentec QE 50) placed at the end of the beam line. The target was mounted on a motorized translation stage, with the film facing away from the laser beam for back-side ablation.

Visualization of the process was achieved by a complementary metal-oxide semiconductor (CMOS) camera with a microscope objective placed perpendicular to the laser beam (i.e., parallel to the sample surface). The probe beam generated fluorescence from a Rhodamine dye in a quartz cuvette placed on the camera axis on the opposite side of the sample, which in turn illuminated the ejected flyer and the released shockwave. It is well known that an incoherent source is better suited for shadowgraphy than a coherent light source, so the fluorescent dye was used for illumination purposes rather than the direct irradiation from the Nd:YAG laser.[15] The delay between the pump and the probe beam was controlled using a digital pulse/delay generator (Stanford Research Systems DG535).

III. RESULTS AND DISCUSSION

For all the experiments the pump laser was raster-scanned across the sample to selectively ablate an array of square holes with each row corresponding to a different laser fluence value. A computer-controlled system allowed variation in the fluence, exposed position of the sample, the delay time between the pump and probe beam, and capture of a sequence of frames showing the generated shockwave and the ejected flyer. Each picture was recorded using a different pulse and corresponded to a different position on the sample. Figure 2 shows the schematic of the ablated matrix generated on the sample, and the inset to the figure shows one of the ablated square patterns (500×500 μm^2) observed under an optical microscope. The results corresponding to the study of the effect of the laser fluence, TP-DRL, and donor thicknesses on the flyer dynamics are discussed below.

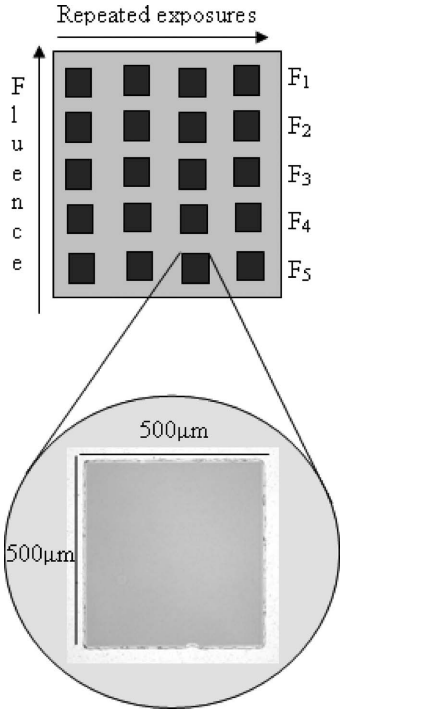

FIG. 2. Schematic of the donor sample ablated using different fluence values (from F_1 to F_5) for each row (inset shows the optical microscope image of an ablated region on the donor).

A. Laser fluence dependence

Figure 3 shows time-resolved shadowgraphs of the target having a 1 μm thick Gd–Ga–O film deposited on top of a 350 nm thick TP at fluence values of (a) ~60 and (b) ~600 mJ/cm^2. The time delay between the pump and the probe pulses was varied from 400 to 2400 ns with a delay step of 400 ns. Figures 4(a) and 4(b) show the images for the second donor material Yb:YAG (1 μm thick) with all other conditions kept the same.

The shockwave released by the huge pressure jump at the ablation site and the opaque flyer ejected from the target surface are clearly visible in all the pictures. It is clear from these images that the higher the fluence, the farther the shockwave and flyer propagate away from the target surface.

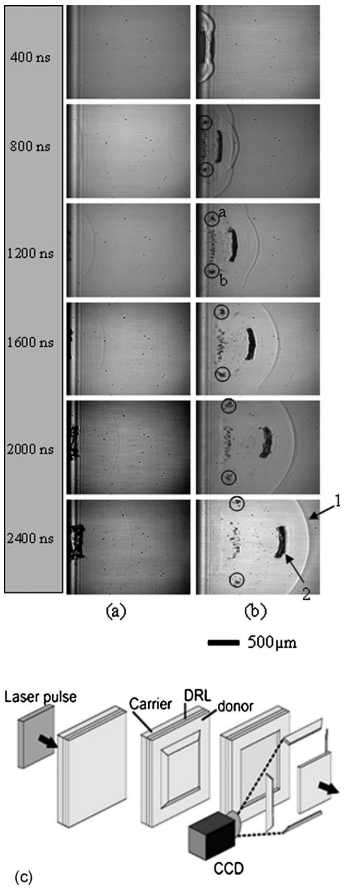

FIG. 3. Shadowgraphs recorded for 1 μm thick Gd–Ga–O target with 350 nm TP for fluence values of (a) 60 and (b) 600 mJ/cm^2 at delay times of 400–2400 ns between the pump and the probe. The shockwave front and the flyer have been marked as 1 and 2, respectively, as an example in (b). Also the solid chunks of the Gd–Ga–O layer from the shattered edges of its flyer are circled and marked as (a) and (b). The 3D schematic of the donor shearing process is shown in (c).

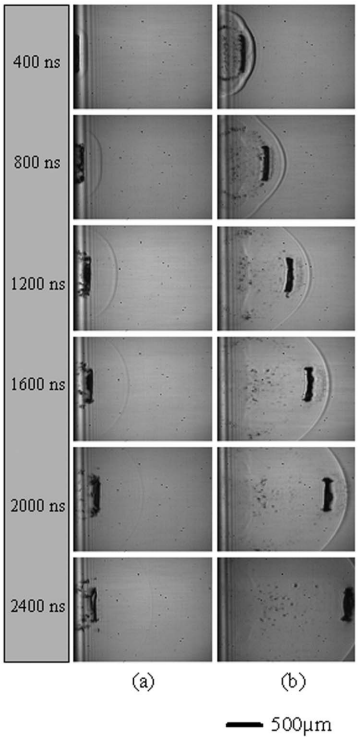

FIG. 4. Images for the 1 μm thick Yb:YAG target with 350 nm TP for fluence values of (a) 60 and (b) 600 mJ/cm^2 at delay times of 400–2400 ns between the pump and the probe.

In Figs. 3(a) and 4(a), for a delay time of 800 ns, while the flyer had just started to delaminate from the surface at an irradiance of 60 mJ/cm^2 pulse, it had already moved a substantial distance from the target surface for a $\sim$10$\times$ higher fluence (600 mJ/cm^2) [see Figs. 3(b) and 4(b)]. This can be attributed to the fact that at low fluence the pressure generated by the decomposed polymer was not sufficient to expel the flyer far from the surface. However, as the fluence was increased, the ablation depth also increased, which in turn decomposed a larger fraction of the TP film, and this released more gaseous fragments and hence an increased pressure was exerted on the top donor layer.

Also observed was a distorted shockwave front at the higher fluence value (600 mJ/cm^2) for both the materials. The reason for this is believed to be the decomposed TP escaping out from the sides of the flyer at the time of ejection due to an extremely high pressure present at the ablation spot, which led to the overlapping side shockwaves. After time delays of around 1600 ns the shockwave appeared to regain the hemispherical shape [refer to Fig. 3(b)].

On comparing the shadowgraphs of the two ceramic materials it is evident that the Yb:YAG flyer was traveling farther than that of the Gd–Ga–O flyer at all delay times for both fluences. Two additional much smaller flyers were also observed in the case of the Gd–Ga–O donor layer [circled and marked as (a) and (b) in Fig. 3(b)]. These observations can be attributed to the difference in the quality of the two donor films as analyzed by a scanning electron microscope. The Yb:YAG film was somewhat porous and had substantial surface texturing, while the Gd–Ga–O was a much smoother and flatter film. The solid Gd–Ga–O film is likely to offer more resistance to shearing than the porous Yb:YAG layer, which was relatively easily detached, resulting in a cleaner and less violent shearing process. Comparatively less force was therefore required to forward transfer the Yb:YAG layer and hence the greater distance of travel observed by the flyer from this film for the same fluence. The solid material re-

sulted from the comparatively violent shearing of the flyer from the nonporous solid Gd–Ga–O film, which in turn may have disrupted the edges of the flyer during its detachment from the donor surface. These shattered edges appear as the two smaller flyers when captured by the camera mounted perpendicular to the target surface as depicted in Fig. 3(c). However only fragments are observed for the case of Yb:YAG due to the relatively less violent shearing process and difference in the surface quality. This clearly explains the lesser amount of debris seen in the case of the flyer from the Yb:YAG film.

The graphs shown in Figs. 5(a) and 5(b) show the distance propagated by the shockwave and the flyer, respectively, as a function of delay time for a range of pump laser fluence values for the 1 μm thick Yb:YAG on top of 350 nm TP-DRL target sample. The solid lines in Figs. 5(a) and 5(b) are simple guides to the eye. The experimental data for the shockwave propagation follow the similar qualitative trend [shown in Fig. 5(c)] as predicted by the theoretical model,[16,17] which is based on Eq. (1),

$$R = \{[1.5C_5(E_0)^{1/2}t + C_4^{3/2}]^{2/3} - C_4\}/C_5, \quad (1)$$

where

$$C_4 = \frac{A\delta}{8}\left(\frac{2}{\gamma+1}\right)^2\rho_s,$$

$$C_5 = \frac{\rho_0 A}{\gamma+1}\left(\frac{1}{\gamma-1} + \frac{4}{\gamma+1}\right).$$

Here R is the propagation distance, E_0 is the laser energy, γ is the specific heat ratio of the atmosphere, A is the laser-ablated area, ρ_s is the TP density, δ is the ablation depth, ρ_0 is the atmospheric density, and t is the delay time. However, quantitatively the experimental and theoretical values differ by ~60% as shown in Fig. 5(c). The reason for this discrepancy is the overlying donor layer in the present case, while the theoretical model takes the TP layer into account only. The generated shockwave has to travel through the donor layer, which results in the lower values of distance propagated.

For the case of the flyer the range of incident energy densities spans more than one order of magnitude, and while a straight line fit appears to be appropriate for the lowest incident energy density results (60 mJ/cm^2), the data points for the 680 mJ/cm^2 are seen to depart from a simple straight line fit, as shown in Fig. 5(b). Given that the flyer will experience a frictional damping force from the surrounding air, it is to be expected that some slowing down will occur, particularly for the higher velocities recorded, as the drag experienced by an object is proportional to (velocity)^2. For this reason, the fits (which remain as guides to the eye) are not shown as straight lines.

The variation in the propagation velocity for both the shockwave and the flyer with the fluence at a delay time of 800 ns is also shown in Figs. 6(a) and 6(b), respectively, for a sample with 1 μm thick Gd–Ga–O donor film on top of a 350 nm TP-DRL. The velocities for both the shockwave and the flyer increase monotonically with the laser fluence. The

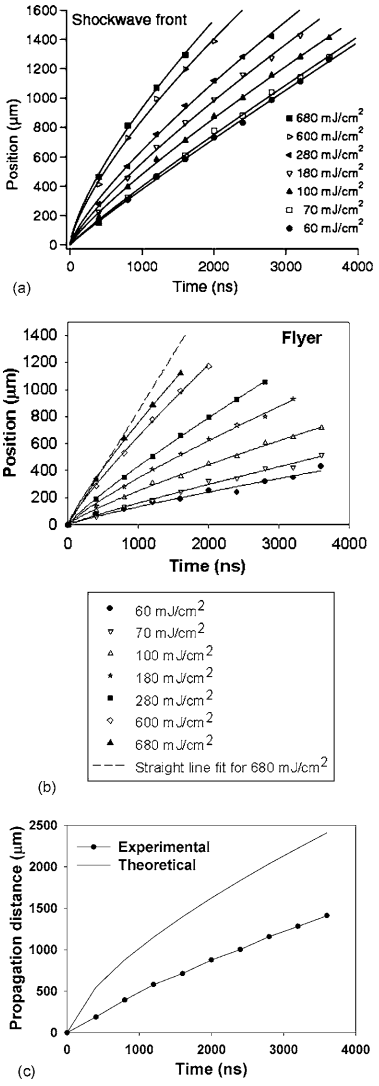

FIG. 5. Variation in the position of the (a) shockwave and the (b) flyer as functions of the pump fluence at different delay times for the sample with 1 μm thick Yb:YAG on top of a 350 nm TP. The flyer is shown to slow down and depart from a constant velocity straight line fit for a fluence of 680 mJ/cm^2 in (b). (c) Plot showing the variation in propagation distance of shockwave as a function of delay time as predicted by the theory and that given by experimental values for 1 μm thick Yb:YAG on top of a 350 nm TP with fluence of 100 mJ/cm^2.

solid line drawn through the experimental data points for the shockwave is just a guide to the eye [Fig. 6(a)]. However the dashed curve drawn along the flyer data points in the log-log plot in Fig. 6(b) is a theoretical fit based on the following model.

The energy density of the incident laser pulse was used to decompose the TP-DRL layer into gaseous fragments,

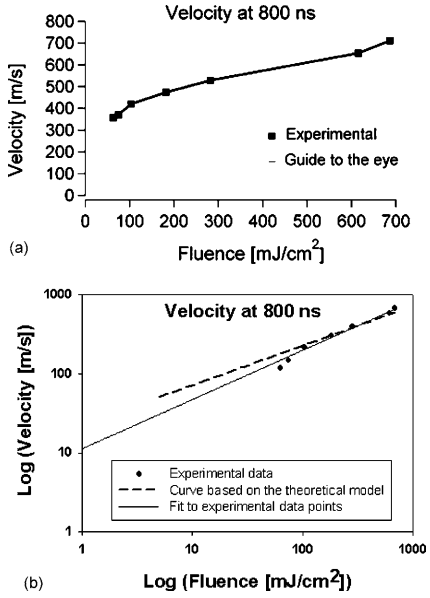

FIG. 6. Variation in the propagation velocity of the (a) shockwave and the (b) flyer as functions of the pump fluence at a delay time of 800 ns for a sample with 1 μm thick Gd–Ga–O donor film on top of a 350 nm TP-DRL.

which in turn pushed the irradiated donor film forward. Assuming that the incident absorbed energy of the laser pulse was proportional to the kinetic energy of the ejected flyer, i.e.,

$$E_{\text{pulse}} \propto \tfrac{1}{2}mv^2, \tag{2}$$

where E_{pulse}, m, and v are energy of the laser pulse, mass, and velocity of the ejected flyer, respectively. For fixed values of m

$$E_{\text{pulse}} \propto v^2,$$

$$\therefore v = K\sqrt{E_{\text{pulse}}} \tag{3}$$

where K is the proportionality constant. Equation (3) represents the analytical dashed plot of Fig. 6(b), and it is consistent with the experimental data. However it should be mentioned that the experimental data points corresponding to low fluences depart from the theoretical straight line fit based on the above model. This is due to the fact that at these fluence values the laser energy is not sufficient to completely decompose the TP layer; hence a lesser forward push acts on the flyer, leading to a lower value of the flyer velocity.[18,19] A similar trend in the variation in propagation distance and velocity with laser fluence was observed for all the other samples irrespective of the TP-DRL and donor material (Gd–Ga–O or Yb:YAG) and their thicknesses.

Based on the previous analysis, we now consider the overall energy budget for the entire LIFT process to better understand the relative pathways for conversion of the incident absorbed laser energy into the kinetic energy of the flyer, the shockwave, and the physical processes behind the DRL decomposition and rupture of the donor film. The efficiency of energy conversion from incident pulse energy to kinetic energy of the flyer was directly inferred from the fit to the experimental data points as shown in Fig. 6(b) for a 1 μm thick Gd–Ga–O donor film on top of a 350 nm TP-DRL at a fluence of 600 mJ/cm^2. The kinetic energy of the flyer resulted in ~20% of the pulse energy using the slope (~0.62) and the y-intercept (~11.2) of the fit.

The TP decomposition process is exothermic and the amount of energy released is 6.97×10^5 J/kg. The thermal energy released by the decomposition of a 500×500 μm^2 region of a 350 nm thick TP film is therefore ~68 μJ (density of triazene$=1.12\times10^3$ kg/m^3). This is only 4% of the incident laser energy (for a fluence of 600 mJ/cm^2), so the energy released during TP decomposition can be considered to contribute little to the energy balance equation.

What remains therefore is the energy required to rupture or shear the donor film and the residual energy contained within the multiple shockwaves generated. However it should be added that functional devices such as OLEDs [8] and viable biomaterials[7] have been transferred using triazene as a DRL and no thermal damage to the printed features was observed/reported.

Apart from the laser fluence, the thickness of the donor (ceramic material) and the underlying TP layer should also play an important role in determining the dynamics of the flyer. For example, if the ablation depth exceeded the TP layer thickness, then the donor would be damaged and the basic idea of achieving an intact transfer using a DRL is defeated. Also for a thicker donor film the flyer would travel a smaller distance as compared to the flyer from a sample with a thinner donor film due to the greater force required to shear a thicker film. The study of the effect of these parameters is discussed in the next two subsections.

B. Donor thickness dependence

The influence of the donor thickness on the quality of the ejected flyer was studied by performing pump-probe experiments with the delay time between the pump and the probe pulses set at a constant value of 1600 ns. Pump pulses with a constant energy density were raster-scanned across the sample, and the shadowgraphs of the ejected flyer and the shockwave were recorded. For the case of a constant donor thickness the distance propagated by the shockwave or the flyer as a function of the position on the donor should also be constant, provided the DRL film had a uniform thickness. In the present case, a very homogeneous layer of TP-DRL on the silica substrate was obtained by spin-coating. However, the donor layer deposited by PLD had a radial thickness variation. Any deviation from the straight line behavior can thus be attributed to the thickness variation in the donor film and not the TP. Figure 7(a) shows such a plot for a Gd–Ga–O sample having a maximum thickness (~1.7 μm) at the center and a minimum thickness (~1 μm) around the edges, and Fig. 7(b) shows the schematic of the target with varying donor thickness. The TP thickness was 350 nm and the fluence was ~100 mJ/cm^2. The layer thicknesses were mea-

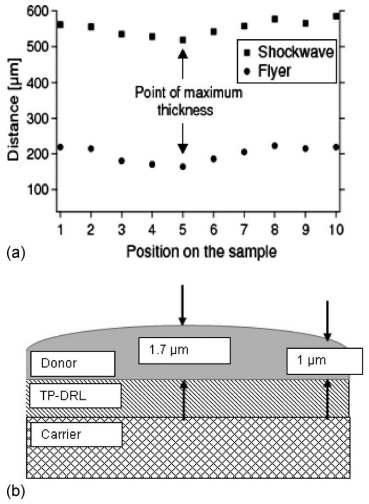

FIG. 7. (a) Plot showing the dependence of the position of the shockwave and the flyer on the donor thickness for fixed values of TP thickness (350 nm) and delay time (1600 ns) for a Gd–Ga–O sample having a maximum thickness (~1.7 μm) at the center and a minimum thickness (~1 μm) around the edges. The *x*-axis corresponds to the position on the sample with varying thickness as shown in (b).

sured using a stylus profiler. The dip at the center of the plot (arrowed) coincides with the point of maximum thickness on the target, which suggests a clear dependence of the transfer mechanism on the donor thickness. The graph depicting the decrement of the distance traveled by the flyer with the donor thickness, for the above discussed sample, is shown in Fig. 8. The dashed line represents the analytical fit to the experimental data points. It was obtained using the following simple model.

As mentioned in the previous section the energy of the laser pulse is proportional the kinetic energy of the flyer [Eq. (2)], so for different donor film thicknesses X_1 and X_2,

$$E_{\text{pulse}} \propto \tfrac{1}{2}m_1v_1^2 = \tfrac{1}{2}m_2v_2^2,$$

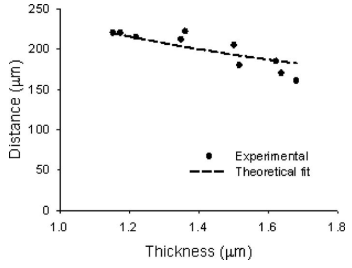

FIG. 8. The propagation distance of the flyer plotted against the thickness of the donor film of Gd–Ga–O for fixed values of TP (350 nm) and delay time (1600 ns). The curve clearly shows that thicker films have slower velocities, as expected.

$$\therefore \frac{m_1}{m_2} = \frac{v_2^2}{v_1^2}, \tag{4}$$

where m_1 and m_2 are the masses of the ejected flyer corresponding to the thicknesses X_1 and X_2, respectively, and v_1 and v_2 are the corresponding velocities. For a given distance d traveled by the flyer and at a given time t,

$$d = vt,$$

$$\therefore v^2 = \frac{d^2}{t^2},$$

$$\Rightarrow v^2 \propto d^2. \tag{5}$$

From Eqs. (4) and (5) we obtain

$$\therefore \frac{m_1}{m_2} = \frac{d_2^2}{d_1^2},$$

$$\Rightarrow \frac{d_2}{d_1} = \sqrt{\frac{m_1}{m_2}} = \sqrt{\frac{X_1}{X_2}},$$

$$\therefore d_2 = d_1\sqrt{\frac{X_1}{X_2}}. \tag{6}$$

Here d_1 and d_2 represent the distances traveled by the flyer corresponding to thicknesses X_1 and X_2, respectively. Equation (6) represents the theoretical curve plotted in Fig. 8 and is consistent with the experimental data.

C. TP thickness dependence

To examine the effect of the DRL layer thickness on the transfer process, shadowgraphy experiments were performed for target samples with two different thickness values of TP (50 and 350 nm) while keeping the central thickness of the donor material approximately constant (1 μm Yb:YAG). Figures 9(a) and 9(b) show the recorded time-resolved images of the Yb:YAG flyers with pulses of ~100 mJ/cm^2 and at delay times of 0–3600 ns between the pump and the probe for these two thickness values of TP. Although we have only studied two different thicknesses of TP, we present the key observations and our qualitative conclusions from these shadowgraphs, which are stated below.

(a) It appears that the delamination of the donor material started earlier for samples with a thicker TP layer (350 nm) as compared to those with thinner TP layer (50 nm). For example, even after 400 ns only a weak shockwave was visible for the sample with a 50 nm TP-DRL, while the flyer and shockwave were both clearly visible for the 350 nm TP sample.

(b) The ejected flyer traveled a significantly greater distance for the sample with the thicker TP-DRL film (350 nm) than for the one with the thinner TP layer (50 nm). For example, after 1600 ns the flyer from the former sample was already hundreds of microns away from the donor surface, while the flyer from the latter target was barely detached from the surface of the donor.

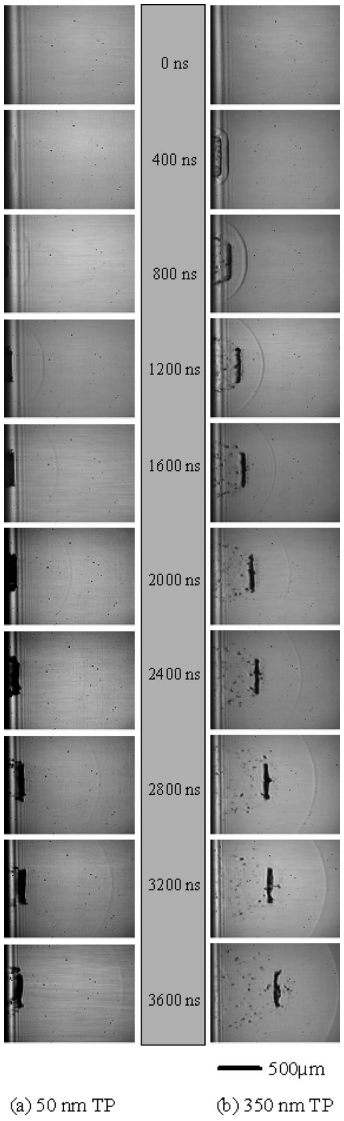

FIG. 9. Shadowgraphs recorded for targets with (a) 50 and (b) 350 nm TP-DRL while keeping the donor (Yb:YAG) thickness constant (~1 μm) at the delay times of 0–3600 ns between the pump and the probe and a fluence of 100 mJ/cm^2.

(c) The flyer from the sample with the thicker TP appears to be associated with noticeably more debris than the one from the thinner TP.
(d) The flyer started to disintegrate and deform in shape with increasing distance. This effect was more prominent for targets with thicker TP layers.

The explanation for these observations is based on the decomposition of the DRL layer beneath the donor film into gaseous fragments by the pump pulse, which then exerted a forward push on the donor material. The thicker TP layer applied a greater force on the ejected flyer causing its early delamination and providing it with a greater kinetic energy to propagate farther from the sample surface. This long distance travel of the flyer is useful for any practical industrial applications that require large donor-receiver separations, e.g., for transferring multilayers of dissimilar materials sequentially. In contrast, the lesser pressure exerted on the flyer for the sample with a thinner TP layer explains the smaller distance traveled by the flyer and its delayed delamination. The pump pulse decomposed the TP-DRL layer over the irradiated region, thereby shearing the flyer apart from the donor surface by the exerted pressure. For the thicker TP-DRL sample the huge pressure exerted on the flyer made this shearing a violent process and shattered the edges of the flyer during its detachment from the surface, and this may well explain the debris seen in the images for the thicker TP samples.

It should be mentioned that the ablation depth depends not only on the fluence but on TP-DRL thickness as well.[18] For a given fluence the absolute amount of ablated TP increases with increasing film thickness, thereby providing more thrust for flyer ejection with thicker DRLs; however beyond a certain value of thickness (beyond the ablation depth), the relative percentage of undecomposed TP increases.[19] For example, at 100 mJ/cm^2 a 50 nm TP film is completely dissociated, while ~30% of the TP remains undecomposed for the sample with a 350 nm TP-DRL layer (data interpolated from that presented in Ref. 18). So the flyer from this sample was bilayered, i.e., consists of both the ceramic material (Yb:YAG or Gd–Ga–O) and the remaining TP. This undissociated TP could also be a possible cause of the debris seen in the shadowgraphs apart from the shattered edges of the flyer. The actual reason behind this debris is not known for the present case; however this can be very well investigated using an experimental setup including a receiver substrate to collect the flyer along with the debris.

Also the quality of the flyer deteriorated as it moved away from the target surface. Therefore, for an intact long distance transfer of the flyer, an optimal thickness of the sacrificial layer has to be chosen, taking into account the fluence, donor material, and thickness. As stated earlier however, these experiments were only performed for two different TP thicknesses, and hence definitive and fully quantitative conclusions must await a much more systematic study of what is actually a complex and coupled problem.

IV. CONCLUSION

The dependence of the TP-DRL assisted LIFT process on laser fluence and thickness of the donor and the TP-DRL was studied using a time-resolved nanosecond-shadowgraphy technique for solid phase ceramic Gd–Ga–O and Yb:YAG materials. The propagation distance and velocity for both the shockwave and the flyer were found to increase with the laser fluence. The distance travelled by the ejected flyer decreases with increasing donor film thickness. Finally, the investigation of the effect of the thickness of the

TP layer on the process revealed that an optimal value of the TP-DRL thickness is required and that the optimal thickness varied with donor material, donor thickness, and the laser energy.

ACKNOWLEDGMENTS

Financial support from the Engineering and Physical Sciences Research Council (EPSRC), UK (under Grant No. EP/C515668/1), and the Swiss National Science Foundation is gratefully acknowledged.

[1]J. Bohandy, B. F. Kim, and F. J. Adrian, J. Appl. Phys. **60**, 1538 (1986).
[2]K. D. Kyrkis, A. A. Andreadaki, D. G. Papazoglou, and I. Zergioti, in *Recent Advances in Laser Processing of Materials*, edited by J. Perrière, E. Millon, and E. Fogarassy (Elsevier, Amsterdam, 2006).
[3]D. P. Banks, C. Grivas, J. D. Mills, R. W. Eason, and I. Zergioti, Appl. Phys. Lett. **89**, 193107 (2006).
[4]I. Zergioti, S. Mailis, N. Vainos, C. Fotakis, S. Chen, and C. Grigoropoulos, Appl. Surf. Sci. **127–129**, 601 (1998).
[5]W. A. Tolbert, I.-Y. S. Lee, M. M. Doxtader, E. W. Ellis, and D. D. Dlott, J. Imaging Sci. Technol. **37**, 411 (1993).
[6]T. Lippert, Adv. Polym. Sci. **168**, 51 (2004).
[7]A. Doraiswamy, R. Narayan, T. Lippert, L. Urech, A. Wokaun, M. Nagel, B. Hopp, M. Dinescu, R. Modi, R. Auyeung, and D. Chrisey, Appl. Surf. Sci. **252**, 4743 (2006).
[8]R. Fardel, M. Nagel, F. Nüesch, T. Lippert, and A. Wokaun, Appl. Phys. Lett. **91**, 061103 (2007).
[9]J. Xu, J. Liu, D. Cui, M. Gerhold, A. Y. Wang, M. Nagel, and T. K. Lippert, Nanotechnology **18**, 025403 (2007).
[10]D. P. Banks, K. Kaur, R. Gazia, R. Fardel, M. Nagel, T. Lippert, and R. W. Eason, Europhys. Lett. **83**, 38003 (2008).
[11]M. Nagel, R. Fardel, P. Feurer, M. Häberli, F. Nüesch, T. Lippert, and A. Wokaun, Appl. Phys. A: Mater. Sci. Process. **92**, 781 (2008).
[12]I. Zergioti, A. Karaiskou, D. Papazoglou, C. Fotakis, M. Kapsetaki, and D. Kafetzopoulos, Appl. Surf. Sci. **247**, 584 (2005).
[13]M. Hauer, D. J. Funk, T. Lippert, and A. Wokaun, Opt. Lasers Eng. **43**, 545 (2005).
[14]M. Nagel, R. Hany, T. Lippert, M. Molberg, F. Nüesch, and D. Rentsch, Macromol. Chem. Phys. **208**, 277 (2007).
[15]G. S. Settles, *Schlieren and Shadowgraph Techniques: Visualizing Phenomena in Transparent Media* (Springer-Verlag, Berlin, 2001).
[16]D. A. Freiwald, J. Appl. Phys. **43**, 2224 (1972).
[17]L. S. Bennett, T. Lippert, H. Furutani, H. Fukumura, and H. Masuhara, Appl. Phys. A: Mater. Sci. Process. **63**, 327 (1996).
[18]R. Fardel, M. Nagel, T. Lippert, F. Nüesch, A. Wokaun, and B. S. Luk'yanchuk, Appl. Phys. A: Mater. Sci. Process. **90**, 661 (2008).
[19]R. Fardel, M. Nagel, F. Nüesch, T. Lippert, and A. Wokaun, Appl. Surf. Sci. **255**, 5430 (2009).

Applied Surface Science 255 (2009) 8343–8351

Contents lists available at ScienceDirect

Applied Surface Science

journal homepage: www.elsevier.com/locate/apsusc

Etching and forward transfer of fused silica in solid-phase by femtosecond laser-induced solid etching (LISE)

David P. Banks *, Kamal S. Kaur, Robert W. Eason

Optoelectronics Research Centre, University of Southampton, Building 46, Highfield, Southampton SO17 1BJ, UK

ARTICLE INFO

Article history:
Received 23 March 2009
Received in revised form 1 May 2009
Accepted 21 May 2009
Available online 29 May 2009

PACS:
42.82.Cr
52.77.Bn
46.50.+a
42.62.−b

Keywords:
Femtosecond
Forward transfer
Etching
Fracture
Deposition

ABSTRACT

We present a femtosecond laser-based technique for etching and forward transfer of bulk transparent materials in solid-phase. Femtosecond laser pulses with $\lambda = 800$ nm were focused through a fused silica block onto an absorbing thin film of Cr. A constraining Si wafer was pressed into tight contact with the Cr film to prevent lift-off of the film. A combination of the high temperature and pressure of the Cr, and compressive stress from the Si, resulted in etching of smooth features from the fused silica by cracking. Unlike in conventional ablative or chemical etching, the silica was removed from the bulk as single solid-phase pieces which could be collected on the Si. Using this so-called laser-induced solid etching (LISE) technique, 1–2 μm deep pits and channels have been produced in the silica surface, and corresponding dots and lines deposited on the Si. The threshold fluence for etching was found to be $\approx 0.4\,J/cm^2$ with ≈ 130 fs duration pulses. The morphology of the etched features are investigated as functions of fluence and exposure to multiple pulses.

1. Introduction

Laser-induced forward transfer (LIFT) techniques offer a simple and versatile method for the micro-deposition of a range of materials [1–6]. Although metals [1,7,8], polymers [9,10], oxides [11], semiconductors [12], superconductors [13], diamond [14], carbon nanotubes [15], and biomaterials [16,17] have now been successfully deposited using LIFT, the forward transfer of solid transparent materials is still challenging.

In LIFT, focused or demagnified laser pulses are used to drive pixelated transfer of a single- or multi-component source film (the *donor*) coated onto the backside of a transparent (*carrier*) substrate. The forward transferred donor material is then collected on another substrate placed nearby (typically ≤ 5 μm away: the *receiver*) (see Fig. 1). Typically LIFT techniques rely on direct absorption of the laser light used in the printing process in the donor material, which necessarily leads to transfer of film material by melting or ablation [7]. In a recent work, we demonstrated the transfer of Cr in solid, single-pieces by using multiple low energy pulses to gently delaminate and release the donor material [8].

Multi-photon absorption of femtosecond duration pulses has recently allowed for the LIFT of transparent donors. Zergioti et al. and Mailis et al. have demonstrated transfer of transparent ITO films [18,19], and recently we reported the transfer of a transparent gadolinium gallium oxide (GdGaO) film [20]. However, the resultant deposits in all these cases exhibited significant surface roughness and appeared to have been transferred as molten fragments. Much smoother and unshattered deposits of GdGaO were obtained using a sacrificial dynamic release layer (DRL [2]) of nitrogen-releasing triazene polymer (TP [21]) to provide the thrust for LIFT [20]. However, the TP dissociates at around 250 °C [21] and is sensitive to solvent treatment, thereby limiting the choice of donor materials that can be deposited on top. Using more robust materials such as metals for the DRL (see e.g. [16]) can result in residual, undecomposed DRL being mixed with, or remaining on top of, the transferred donor [22].

In this work, we present a new LIFT technique (which we call laser-induced solid etching (LISE)) that allows transparent material to be transferred in solid-phase contiguous pieces. By utilising controlled laser cracking rather than direct ablation, LISE allows for the forward transfer of transparent materials with surface smoothness comparable to the best achievable with DRL-LIFT [20]. The key difference from conventional LIFT is that the material transferred is etched from the transparent carrier

* Corresponding author. Tel.: +44 2380593144.
E-mail address: dpb@orc.soton.ac.uk (D.P. Banks).

0169-4332/$ – see front matter © 2009 Elsevier B.V. All rights reserved.
doi:10.1016/j.apsusc.2009.05.060

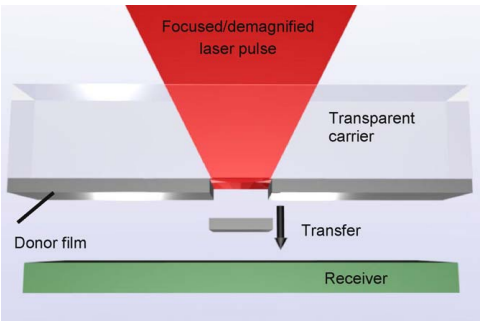

Fig. 1. Schematic of the LIFT technique.

substrate instead of the donor film. Using LISE, the forward transfer deposition of fused silica has been achieved for the first time. Furthermore, as the transferred material is etched from the bulk carrier, the features deposited on the receiver correspond exactly to structures etched into the backside of the carrier. Hence, LISE can also be used as a method of direct-writing onto the backside of UV-transparent substrates. Again, the LISE method compares well in terms of processing speed, simplicity, and feature quality with existing backside writing techniques [23,24].

1.1. Backside writing

To process UV-transparent materials with nanosecond or longer pulsed lasers, it is possible to use either extremely high powers [25], or to include a laser absorbing material. This absorber can be in the form of a dopant, but in many real applications doping of the target material is undesirable, or as a thin film coating that must be removed after patterning.

An alternative approach that has been extensively investigated is backside etching. This approach utilises laser absorption in an absorbing material in contact with the UV-transparent substrate. The processing laser is focused through the substrate onto the absorber–substrate interface where rapid boiling of the absorber etches away some of the substrate. This technique is known as laser-induced backside wet etching (LIBWE [23,26]) or dry etching (LIBDE [24,27]) depending on whether the absorber is a solution or solid (often metallic) film. With LIBWE, etch rates of tens of nm/pulse are typically reported [23,26] and the resultant features can be very smooth and uniform. However, the process requires a specialised liquid chamber, potentially harmful solvents, and can be complicated to carry out in practice. LIBDE has been shown to be capable of a much higher etch rate ($\approx$500 nm/pulse for a single pulse [24] up to $\approx$1 μm with 3–5 pulses [28]) and is much simpler, but the etched features are typically somewhat rougher than with LIBWE. Both these backside etching techniques eliminate the problem of redeposited debris inherent with ablative microstructuring.

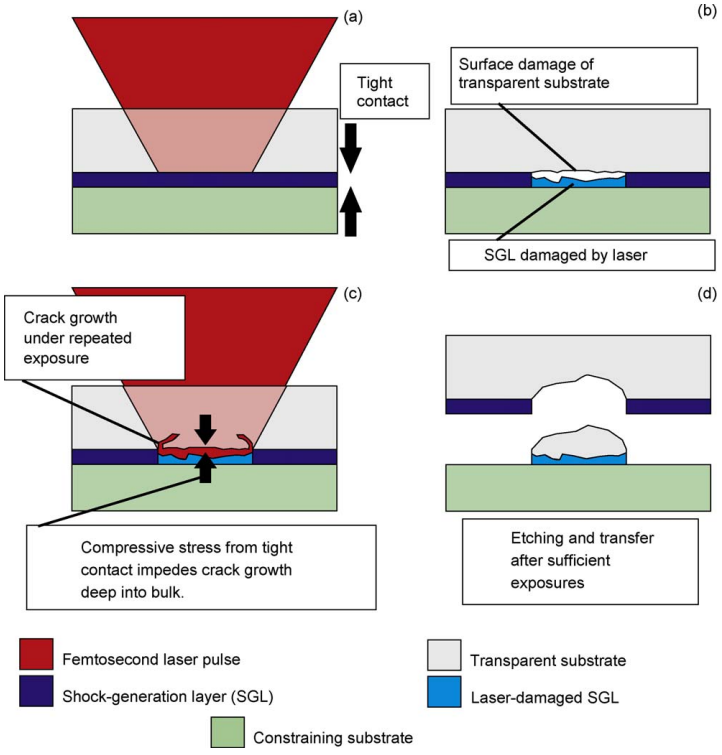

Fig. 2. Schematic of the LISE technique.

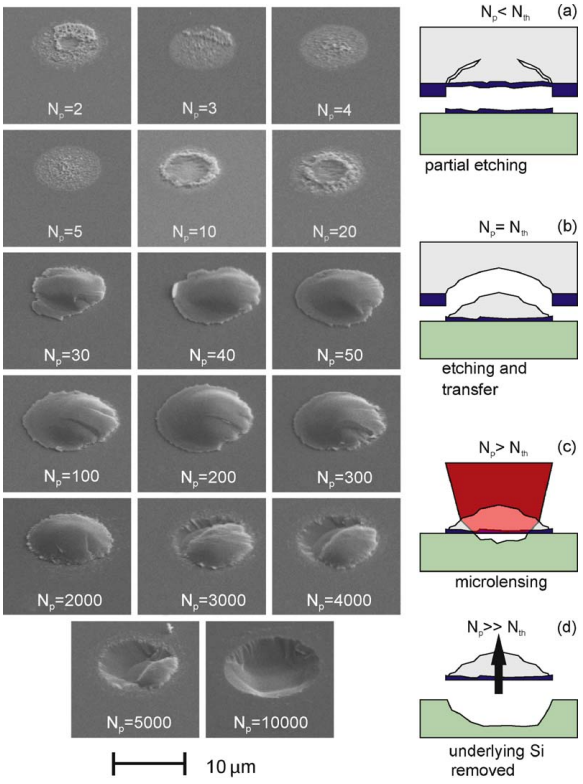

Fig. 3. SEM micrographs of deposits of fused silica produced with indicated values of N_p; fluence 0.4 J/cm^2. (a)–(d) Schematics showing envisaged transfer process as N_p varies relative to N_{th}.

1.2. Laser-induced cracking

The formation and growth of cracks in, particularly, fused silica has been studied extensively in recent years because of the impact on the lifetime of high power and remote (e.g. satellite-based) optical systems [29–31]. It has been observed that exposure to multiple laser pulses leads to a crack originating on the surface of transparent substrates. Once a surface crack has formed, it causes a hoop stress to form in its immediate surroundings. This stress reduces the local strength of the material, which facilitates further, and increasingly catastrophic, crack growth into the bulk [31].

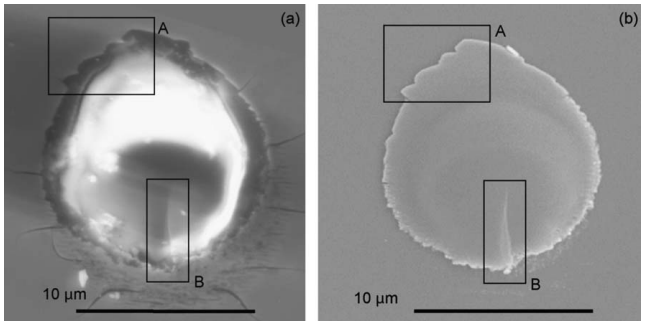

Fig. 4. SEM micrographs of a hole in fused silica (a) and corresponding silica deposit on Si (b). $N_p = 500$, fluence 0.4 J/cm^2.

Dahmani et al. [30,31] have observed a dependence of the crack morphology on stress applied parallel to the laser propagation axis. This dependence is thought to arise because applying an external stress field breaks the hoop stress symmetry around the crack, thus offsetting the localised decrease in material strength. Hence, the cracking now preferentially occurs at the edge of the laser irradiated area where the strain is greatest. Indeed, it was observed that, when no external stress was applied, cracks with a diameter of approximately the laser spot size at the substrate surface penetrating mm into the silica were seen. However, if the applied stress was increased to $\approx$41 kPa, the silica damage was manifested as a smooth-sided 100–200 μm deep pit, again with a diameter approximately the same as the spot size [30]. This stress-suppressed cracking forms the basis of the LISE process.

1.3. Laser-induced solid etching (LISE)

The LISE process combines elements of LIFT, LIBDE, and laser cracking for the solid-phase etching and forward transfer of brittle, transparent bulk substrates (Fig. 2). An absorbing thin film (referred to as a *shock-generation layer* (SGL)) is coated onto the backside of a transparent substrate, as in LIFT or LIBDE, and a second bulk substrate, akin to the receiver in a LIFT setup, is pressed into tight contact with the thin film. Femtosecond laser pulses are then focused or demagnified through the transparent substrate onto the film, where they are absorbed, leading to very large and rapid pressure and temperature increases in the film (Fig. 2(a)). The film can reach pressures up to tens or thousands of GPa [32–35], and temperatures of up to thousands of K [36,37].

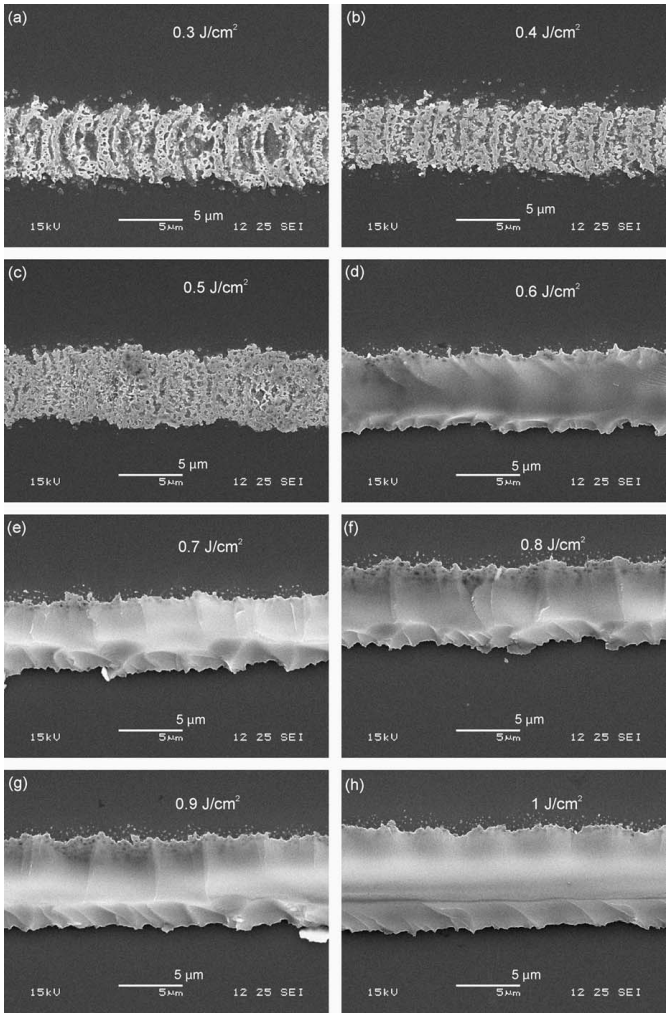

Fig. 5. SEM micrographs of line structures obtained by raster-scanning laser at $v = 1.1$ mm/s with indicated fluence.

The extremely high temperature and pressure in the SGL can cause secondary damage to the surface of the transparent substrate, as in LIBDE [24] (Fig. 2(b)). This damage, which is localised to the irradiated area, then acts as the seed for crack propagation into the bulk of the substrate [29,31]. However, because of the tight contact between the substrates and the SGL, there is a compressive stress on the bulk substrates. Hence, crack propagation into the bulk is impeded, and instead the etched features appear as smooth pits on the surface after exposure to multiple pulses, like those reported by Dahmani et al. [30] (Fig. 2(c) and (d)). Note that these features are transferred in one piece after several laser pulses, and not as a gradual build-up of individual thin layers over successive laser pulses (Fig. 2(d)). Hence, the deposited material maintains the same underlying microscopic structure as the original bulk substrate, meaning that LISE may be suitable for forward transferring materials with long-range order that cannot be readily deposited with established techniques. Note also that the feature size is limited only by the laser spot size as, for reasons described in the previous sub-section, cracking occurs around the edge of the laser irradiated region when an external stress field is applied.

2. Experimental

To study the LISE process, 50 mm diameter, 6 mm thick discs of fused silica were coated with $\approx$80 nm of Cr by thermal evaporation. The coated face of a silica disc was pressed into tight contact with a Si wafer in a vacuum cell held at a pressure of $\approx$10 Pa. Note that the silica acted as the top window of the vacuum cell. Hence, the pressure difference across the silica window was around 10^5 Pa and so when the Si wafer was brought into tight contact, the compressive stresses on the silica was similar to tens of kPa applied to get relatively smooth silica pits by Dahmani et al. [30]. Note also that it can be expected that there is an optimal value of the SGL thickness which will be determined by the materials involved and the desired feature size. No attempt has been made here to find the optimal material or value of the thickness for the current configuration, instead an 80 nm thick Cr film was chosen simply to ensure there was no laser damage of the underlying Si.

Femtosecond duration pulses (800 nm, 110 fs) with a Gaussian spatial profile ($1/e^2$ diameter of $\approx$4 mm) from a Ti:sapphire laser (Coherent MIRA and Legend) illuminated an $\approx$450 μm circular aperture at a repetition rate of 250 Hz. An image of the aperture was then relayed to the silica–Cr interface by a reverse-projection microscope to give an $\approx$10 μm diameter, roughly uniform intensity circular spot. The vacuum cell was mounted on a 3-axis, computer-controlled translation stage and a high-speed mechanical shutter (Uniblitz LS3) was used to control laser exposure.

3. Results and discussion

3.1. LISE of fused silica domes

The first experiments concerned the transfer of single, $\approx$10 μm spots of silica onto the Si substrate by LISE. It was observed that two thresholds existed for the LISE process; a threshold fluence below which no transfer occurred, and a minimum number of pulses that were required to etch the silica. The threshold fluence was measured to be 0.37 J/cm^2, which approximately coincided with the onset of ablation in the SGL [7].

Fig. 3 shows a sequence of SEM micrographs of silica deposits on the Si surface after exposure to an increasing number of pulses, N_p, at a fluence of 0.4 J/cm^2, i.e. just above the transfer threshold. It can be seen that the first few pulses (up to around $N_p = 20$) simply repeatedly melted and ablated the SGL, leaving some remaining on the Si and some on the silica (Fig. 3(a)). The threshold for silica transfer in this case appeared around $N_p = N_{th} = 20$–30. This threshold can be thought of as the number of pulses required to grow the cracks sufficiently that they intersect and a single piece of silica was transferred (Fig. 3(b)). It is worth noting that etched features in fused silica approximately an order of magnitude larger

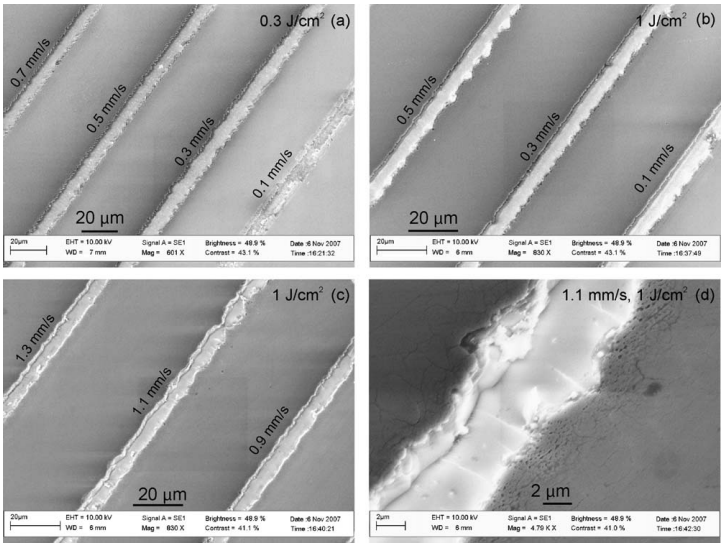

Fig. 6. SEM micrographs of channels in fused silica substrate after exposure to 0.3 J/cm^2(a) and 1 J/cm^2(b and c) with indicated raster speeds. Close up of channel with 1 J/cm^2 written at 1.1 mm/s (d).

than the depositions in Fig. 3 have been observed after exposure to 200–300 pulses (i.e. also an order of magnitude more pulses) [30].

For $N_p \geq N_{th}$, domed deposits of fused silica that had been etched from the bulk substrate were consistently seen on the Si surface. Similar deposits were obtained over a very broad range of N_p, up to 1000–2000. The reason that exposure to more pulses did not significantly alter the morphology of the deposits was that there was no absorption in the silica of these pulses. Instead, after transfer, the silica domes formed a microlens on the Si surface (Fig. 3(c)). Observation of the deposits obtained with $N_p \geq 2000$ (i.e. $N_p \gg N_{th}$) revealed that exposure to very high numbers of pulses resulted in damage to the underlying Si. Hence, it can be concluded that pulses incident after transfer (i.e. $N_p \geq N_{th}$) did not damage the transferred transparent material, but instead ablated the underlying absorbing substrate. Once the Si underneath the deposit had been machined away (i.e. $N_p \gg N_{th}$), the silica could no longer remain bonded to the Si wafer, and was removed from the substrate (see Fig. 3(d)). This finding suggested that, when using LISE for forward transfer, particularly onto a substrate that absorbs at the laser wavelength, it is important to use only sufficient pulses to transfer the transparent material as any subsequent pulses can pass through the deposited material and damage the underlying substrate.

An interesting point to note is that the machined features in the silicon obtained with large N_p appeared to be much smoother than those usually seen with direct ablation. As such it is believed that these structures were the result of LISE of the Si substrate. It appears therefore, that LISE may be suitable for the etching of smooth structures in the surface of absorbing substrates as well.

It would be tempting to conclude that the dome-shaped features were the result of redeposition of particulate material gradually etched out of the transparent substrate by boiling of the SGL (as in LIBDE). However, closer inspection revealed that many of the silica deposits exhibited sharp features and edges that could only have been the result of the deposit being etched from the transparent substrate and transferred as a single, solid piece (see, e.g. $N_p = 100, 200, 300, 2000$; Fig. 3). These features could also be seen in the corresponding holes in the silica substrate, confirming that the deposits must have been transferred as a single piece. Fig. 4(a) shows an SEM micrograph of a silica hole and Fig. 4(b) shows a micrograph of the corresponding deposit on the Si after exposure to 500 pulses with fluence 0.4 J/cm^2. A couple of features can be seen in Fig. 4 that conclusively prove etching as a single, solid-phase piece; firstly, the edges of the hole and deposit corresponded exactly (e.g. the boxed regions marked 'A' in the figure), and second, sharp discontinuities could be seen in both the hole and the deposit (e.g. regions 'B').

Obtaining good adherence of material deposited by forward transfer techniques is a challenge. With the current LISE setup, the repeatedly melted and resolidified Cr SGL between the silica and Si substrates provided an excellent bonding layer. The silica deposits were observed to remain on the Si surface after 5 min in an ultrasound bath in deionised water at 40 °C.

3.2. LISE of silica lines

The second half of our initial study of the LISE of fused silica concentrated on the direct-writing of continuous lines. These structures were obtained using an identical setup as described above except that the laser was raster scanned across the sample with speed v mm/s (recall that the laser repetition rate was 250 Hz and the spot diameter at the silica–SGL interface was $\approx 10\,\mu$m).

Fig. 5 shows SEM micrographs of the resultant structures seen on the Si surface after exposure to fluences from 0.3 J/cm^2 (Fig. 5(a)) to 1 J/cm^2 (Fig. 5(h)) with a raster speed of $v = 1.1$ mm/s. The direct ablation threshold of the silica was measured to be ≈ 1.1 J/cm^2, hence LISE was not possible for fluences above this value. As was the case with the dome-shaped structures in the previous section, a well-defined fluence threshold was observed; in this case the threshold was between 0.5 and 0.6 J/cm^2. Below this fluence threshold, only the SGL was transferred to the Si, resulting in relatively uniform Cr lines. Once the LISE threshold fluence was reached, continuous silica lines 1–2 μm in height were deposited. It was observed that the smoothness of the lines improved with increasing fluence. This was in agreement with the cracking results of Dahmani et al., where it was observed that increasing the compressive stress on the transparent substrate resulted in smoother pits [30].

The higher fluence threshold for LISE measured with the lines than with the silica domes can be partially explained by the fact that, due to rastering of the laser, there was less overlapping of multiple pulses when writing the lines. However, with the dome-shaped deposits, it was observed that a minimum of 10–20 pulses were required to LISE the silica. The lines shown in Fig. 5 were written with $v = 1.1$ mm/s, which with a spot size of $\approx 10\,\mu$m and repetition rate of 250 Hz, corresponded approximately to a $\approx$55–60% overlap between successive pulses. Therefore, we must conclude that the lines were the result of a cumulative cracking process that was initiated at the point where the translation stage was accelerating, and hence where there was more overlapping of multiple pulses. The channel formed by the cracking then propagated along the silica surface, becoming incrementally longer with each successive pulse, as the laser was scanned across the target.

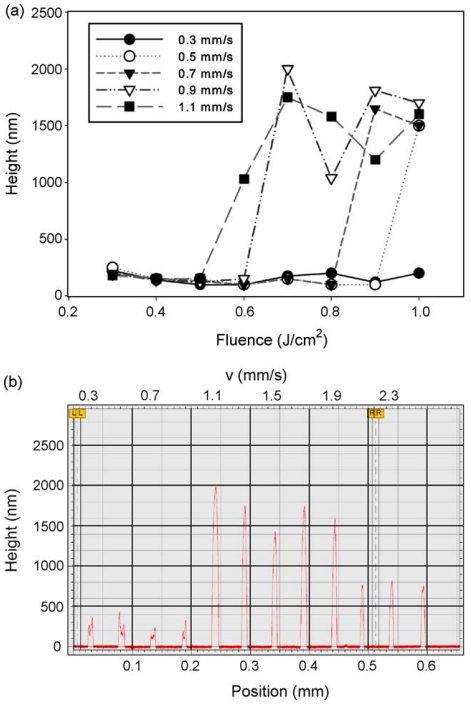

Fig. 7. Plot of maximum height of silica lines as a function of fluence and raster speed.

Clearly the silica deposition process corresponded to etching of the transparent substrate and so there were channels left in the silica surface after LISE. A detailed study of the channels as a function of processing parameters will be reported separately; here we just present a visual examination of the channels. Fig. 6 shows SEM micrographs of the Cr-coated silica surface after LISE (the Cr was left on to prevent surface charging in the SEM). With fluence below the LISE threshold (0.3 J/cm^2: Fig. 6(a)), the Cr was not completely removed in the irradiated area and the silica was not etched. When the fluence was increased to greater than the previously identified LISE threshold to 1 J/cm^2, and the raster speed was slow ($\leq$ 0.9 mm/s: Fig. 6(b)), the Cr was completely removed from the silica surface, but again no channel was observed. Instead channel formation was only observed when the raster speed was increased above a well-defined threshold; in this case $\approx$0.9 mm/s (Fig. 6(c)). Closer examination of the channels (Fig. 6(d)) revealed them to be smooth-sided, V-shaped features with only minimal evidence of redeposited material in the channel. The sharpness of the features again supported the hypothesis of etching by solid-phase cracking rather than ablation or boiling of the Cr.

Clearly, as with the silica domes, there were two thresholds for the LISE of the silica lines; a fluence threshold (which was higher for the lines than the domes because of fewer overlapping pulses) and a raster speed threshold (related to the overlapping of successive pulses). To understand how these two thresholds were related, the maximum heights of the lines on the Si were measured by stylus profiling as functions of fluence and raster speed. The results are shown in Fig. 7 (a).

From Fig. 7(a), it can be seen that, at the lowest raster speed (0.3 mm/s), no silica lines were deposited, independent of fluence. As the raster speed was increased, the threshold fluence for LISE of the silica was observed to decrease. Fig. 8(a)–(h) shows SEM micrographs of the lines deposited with a fluence of 0.7 J/cm^{2}while varying v; at this fluence, the threshold for LISE of continuous silica

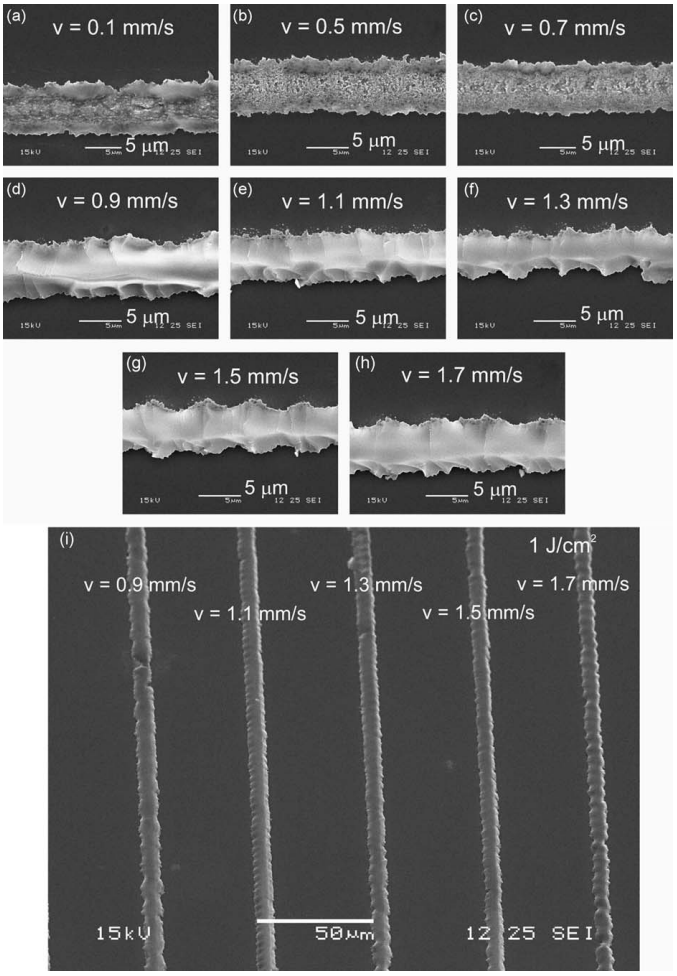

Fig. 8. SEM micrographs of line structures obtained by varying raster speed v with fluence 0.7 J/cm^2(a–h) and zoomed-out view of silica lines with 1 J/cm^2 (i).

lines was around $v = 0.9$ mm/s. Observation of the lines obtained with v less than the raster speed threshold (Fig. 8(a)–(c)) indicate why a raster speed threshold existed. The line produced with $v = 0.1$ mm/s (Fig. 8(a)) in particular exhibited an obviously damaged central region and edges where the deposited material appeared to be LISE-deposited silica. At this speed, approximately 10 incident pulses overlapped at any given point. Hence, we conclude that the observed line was the result of a LISE-deposited silica line that was subsequently destroyed and partially redeposited in the original channel by exposure to too many high energy pulses, causing cracking after etching. When the raster speed was increased to $v = 0.9$ mm/s (Fig. 8(d)), only 2 successive pulses overlapped at any given point. As a result, the LISE-deposited silica line was not destroyed by exposure to pulses incident after etching had occurred. Hence we can conclude that the LISE line-writing process has a fluence threshold that determines if LISE occurs, and a raster speed threshold to prevent post-etching damage of the transferred material.

Fig. 7(b) shows an example of the stylus trace for lines produced with fluence 0.7 J/cm^2. The lines produced with the slowest raster speeds were on the order of hundreds of nm high with rough top surfaces. Some lines also exhibited a central region that was lower than the edges. This observation is consistent with our model of LISE-deposited silica lines that have been damaged by exposure to further pulses after etching. For $0.9 \leq v \leq 1.9$ mm/s, lines with a rounded-cone cross-section and a maximal thickness of between 1.5 and 2 μm were obtained reproducibly. The thickness variation along the length of a LISE-deposited line was measured to be $\approx 10\%$. There was some evidence of the line thickness decreasing slightly with increasing raster speed; this may have been due to less pulse-to-pulse overlap at higher speeds. For $v \geq 2$ mm/s, the lines became discontinuous, with many gaps. The maximal heights of the discontinuous LISE deposits was observed to be only about 40–50% of that of the continuous lines.

Observing the lines obtained as v was increased further (Fig. 8(e)–(h)) revealed a periodic variation of the edges of the lines with a period that matched the spacing between successive pulses. For example, with $v = 1.5$ mm/s (Fig. 8(g)) the pulse-to-pulse separation was around 6 μm, closely matching the periodicity seen in the line structure. It was observed previously that LISE was not possible with single pulses. Hence, it is believed that the lines were the result of successive pulses propagating cracks in the silica along the line length. Once the raster speed became sufficiently great that the pulse-to-pulse spacing was large compared to the spot size, continuous silica lines were not observed (the maximum speed was found to be $v \approx 2$ mm/s at all studied fluences).

As a final point to note, with the correct exposure conditions, the uniformity of the silica lines was observed to be very good, with only small variation observed over the full 0.5 mm writing length. As an example, Fig. 8(i) shows an SEM micrograph of lines obtained with fluence 1 J/cm^2 with $v = 0.9$ (left), 1.1, 1.3, 1.5, and 1.7 (right) mm/s. The SEM micrograph in Fig. 8(i) also clearly shows the variation in line morphology with increasing v. Lines written at slower speeds appeared to have smoother tops and straighter edges, while faster speeds resulted in increasingly segmented structures. At the highest speed in Fig. 8(i) ($v = 1.7$ mm/s), the contribution of each successive pulse adding a small section to the end of the line is clearly visible.

4. Conclusions

We have presented initial studies of the LISE of fused silica. The high pressures and temperatures generated in a thin Cr film under femtosecond laser pulse irradiation combined with the compressive stress from tight contact with a Si wafer under vacuum resulted in etching of very smooth features in the silica. It was found that the threshold fluence required for etching (≈ 0.4 J/cm^2) approximately corresponded to the onset of ablation of the Cr. The etched silica was deposited onto the Si, allowing for the use of LISE as a solid-phase forward transfer technique. Adherence of the transferred material was found to be very good due to the presence of resolidified Cr SGL between the Si substrate and deposited silica.

LISE appears to be a potentially useful technique for the etching and forward transfer deposition of micron and larger scale features of transparent materials (the resolution of the technique appears only to be limited by the laser spot size). The technique is easy to carry out in an ordinary lab environment without the need for a specialised processing setup; harmful chemicals and clean room facilities are not needed. All that is required for etching is an absorbing coating on the transparent substrate and an externally-applied compressive stress (which does not have to be the low vacuum used here; the process also works in air ambient).

Forward transfer deposition of the etched transparent material in single, solid-phase pieces can be achieved by placing another substrate in contact with the absorbing film. Forward transfer of solid-phase transparent materials is very challenging by other methods so this is where we envisage the main advantages of LISE. Potential applications include the direct-writing of microlenses, and rib and strip-loaded waveguides. As material deposited by LISE is transferred as a single piece, the underlying microscopic structure of the original substrate is preserved. Hence, LISE may allow for the single-step direct-writing of crystalline materials (and others with long-range order); a capability not available with any existing forward transfer techniques. Materials such as single-crystals that exhibit preferential shearing, or cleaving, directions may be even more suited to LISE deposition than amorphous materials such as fused silica.

Further work should focus on optimising the shock-generation layer material and thickness. The deposition/etching of more complex patterns and other kinds of transparent materials are also important future studies.

Acknowledgement

The authors are grateful to the Engineering and Physical Sciences Research Council, UK, for research funding under Grant No. EP/C515668/1.

References

[1] J. Bohandy, B. Kim, F. Adrian, J. Appl. Phys. 60 (1) (1986) 1538–1539.
[2] W. Tolbert, I. Lee, M. Doxtader, E. Ellis, D. Dlott, J. Imag. Sci. Technol. 37 (4) (1993) 411–421.
[3] H. Fukumura, Y. Kohji, K. Nagasawa, H. Masuhara, J. Am. Chem. Soc. 116 (1994) 10304–10305.
[4] A. Pique, D. Chrisey, R. Auyeung, J. Fitz-Gerald, H. Wu, R. McGill, S. Lakeou, P. Wu, V. Nguyen, M. Duignan, Appl. Phys. A 69 (Suppl.) (1999) 279–S284.
[5] D. Toet, M. Thompson, P. Smith, T. Sigmon, Appl. Phys. Lett. 74 (15) (1999) 2170–2172.
[6] G. Blanchet, Y.-L. Loo, J. Rogers, F. Gao, C. Fincher, Appl. Phys. Lett. 82 (3) (2003) 463–465.
[7] D. Banks, C. Grivas, J. Mills, I. Zergioti, R. Eason, Appl. Phys. Lett. 89 (2006) 193107.
[8] D. Banks, C. Grivas, I. Zergioti, R. Eason, Opt. Express. 16 (2008) 3249–3254.
[9] J. Lee, S. Lee, Adv. Mater. 16 (1) (2004) 51–54.
[10] B. Thomas, A. Alloncle, P. Delaporte, M. Sentis, S. Sanaur, M. Barret, P. Collot, Appl. Surf. Sci. 254 (2007) 1206–1210.
[11] I. Zergioti, S. Mailis, N. Vainos, P. Papakonstantinou, C. Kalpouzos, C. Grigoropoulos, C. Fotakis, Appl Phys. A 66 (1998) 579–582.
[12] P. Mogyorosi, T. Szorenyi, K. Ball, Z. Toth, I. Hevesi, Appl. Surf. Sci. 36 (1989) 157–163.
[13] E. Fogarassy, C. Fuchs, F. Kerherve, G. Hauchecorne, J. Perriere, J. Appl. Phys. 66 (1) (1989) 457–459.
[14] S. Pimenov, G. Shafeev, A. Smolin, V. Konov, B. Vodolaga, Appl. Surf. Sci. 86 (1995) 208–212.
[15] S. Chang-Jian, J. Ho, J. Cheng, C. Sung, Nanotechnology 17 (2006) 1184–1187.
[16] P. Serra, M. Colina, J. Fernandez-Pradas, L. Sevilla, J. Morenza, Appl Phys. A 85 (9) (2004) 1639–1641.

[17] Y. Tsuboi, Y. Furuhata, N. Kitamura, Appl. Surf. Sci. 253 (2007) 8422–8427.
[18] S. Mailis, I. Zergioti, G. Koundourakis, A. Ikiades, A. Patentalaki, P. Papakonstantinou, N. Vainos, C. Fotakis, Appl. Opt. 38 (11) (1999) 2301–2308.
[19] I. Zergioti, D. Papazoglou, A. Karaiskou, N. Vainos, C. Fotakis, Appl. Surf. Sci. 197–198 (2002) 868–872.
[20] D. Banks, K. Kaur, R. Gazia, R. Fardel, M. Nagel, T. Lippert, R. Eason, Europhys. Lett. 83 (2008) 38003.
[21] M. Nagel, R. Hany, T. Lippert, M. Molberg, F. Nuesch, D. Rentsch, Macromol. Chem. Phys. 208 (2007) 277–286.
[22] T. Smausz, B. Hopp, G. Kecskemeti, Z. Bor, Appl. Surf. Sci. 252 (2006) 4738–4742.
[23] J. Wang, H. Niino, A. Yabe, Appl. Phys. A 68 (1) (1999) 111–113.
[24] B. Hopp, C. Vass, T. Smausz, Z. Bor, J. Phys. D: Appl. Phys. 39 (2006) 4843–4847.
[25] J. Ihlemann, B. Wolff-Rottke, Appl. Surf. Sci. 106 (1996) 282–286.
[26] J. Wang, H. Niino, A. Yabe, Appl. Surf. Sci. 87 (2000) 45–53.
[27] B. Hopp, C. Vass, T. Smausz, Appl. Surf. Sci. 253 (2007) 7922–7925.
[28] T. Smausz, T. Csizmadia, N. Kresz, C. Vass, Z. Marton, B. Hopp, Appl. Surf. Sci. 254 (2007) 1091–1095.
[29] A. Salleo, R. Chinsio, F. Genin, Proc. SPIE 3578 (1998) 456–471.
[30] F. Dahmani, S. Burns, J.L.S. Papernov, A. Schmid, Opt. Lett. 24 (8) (1999) 516–518.
[31] F. Dahmani, J. Lambropoulos, A. Schmid, S. Papernov, S. Burns, Appl. Opt. 38 (33) (1999) 6892–6903.
[32] T. Sano, H. Mori, O. Sakata, E. Ohmura, I. Miyamoto, A. Hirose, K. Kobayashi, Appl. Surf. Sci. 247 (2005) 571–576.
[33] R. Evans, A. Badger, F. Fallis, M. Mahdieh, T. Hall, P. Audebert, J.-P. Geindre, J.-C. Gauthier, A. Mysyrowicz, G. Grillon, A. Antonetti, Phys. Rev. Lett. 77 (16) (1996) 3359–3362.
[34] D. Moore, K. Gahagan, J. Reho, D. Funk, S. Buelow, R. Rabie, T. Lippert, Appl. Phys. Lett. 78 (1) (2001) 40–42.
[35] D. Funk, D. Moore, S. McGrane, K. Gahagan, J. Reho, S. Buelow, J. Nicholson, G. Fisher, R. Rabie, Thin Solid Films 453–454 (2004) 542–549.
[36] J. Hohlfeld, S.-S. Wellershoff, J. Gudde, U. Conrad, V. Jahnke, E. Matthias, Chem. Phys. 251 (2000) 237–258.
[37] E. Gamaly, A. Rode, B. Luther-Davies, V. Tikhonchuk, Phys. Plasmas 9 (3) (2002) 949–957.

Influence of optical standing waves on the femtosecond laser-induced forward transfer of transparent thin films

David P. Banks,* Kamal Kaur, and Robert W. Eason

Optoelectronics Research Centre, University of Southampton, Southampton SO17 1BJ, UK

*Corresponding author: dpb@orc.soton.ac.uk

Received 7 January 2009; revised 18 March 2009; accepted 20 March 2009;
posted 20 March 2009 (Doc. ID 105581); published 2 April 2009

The effects of the formation of an optical standing wave during femtosecond laser-induced forward transfer of transparent films is analyzed using a numerical interference model. The dependence of the intensity distribution on a number of easily controllable experimental parameters is investigated. Results of the model are compared to experimental studies of the transfer of gadolinium gallium oxide (GdGaO) with a polymer sacrificial layer. The model allows us to explain the observed variation in deposit morphology with the size of the air gap, and why forward transfer of the GdGaO was possible below the ablation thresholds of polymer and oxide. © 2009 Optical Society of America

OCIS codes: 350.3390, 190.4180, 310.6860, 160.2750, 160.5470.

1. Introduction

The laser-induced forward transfer (LIFT) technique (as shown in Fig. 1) was initially proposed by Bohandy *et al.* as a method for microdepositing metal for the repair of damaged photomasks [1]. In LIFT, a thin film of the material to be deposited (the *donor film*) is coated onto one face of a transparent support substrate (known as a *carrier*) and brought into close contact (typically the separation is on the order of a few micrometers) with another substrate (the *receiver*). Transfer of the donor film to the receiver is effected by focusing or demagnifying a laser through the carrier onto the carrier–donor interface. The laser initiates melting [2] or ablation [3,4] of the donor film, providing the thrust required to propel material to the receiver.

LIFT has been successfully applied for the direct writing of metals (e.g., see [1,2,5–11] among others), polymers [12], oxides [13,14], superconductors [15], diamond [16], carbon nanotube field emission cathodes [17], conducting polymers [18], and an adenosine triphosphate sensor fabricated from luciferase [19]. Recently, a number of groups have also investigated the effects of using ultrashort (subpicosecond) pulses for LIFT (so-called fs-LIFT) [13,20–24]. The majority of work has focused on achieving the smallest possible structures, but fs-LIFT has also been shown to be capable of transferring viable biomaterial [25] and contiguous solid-phase sections of donor film [26] without requiring a sacrificial matrix or protective layer.

A. LIFT of Transparent Materials

For materials that do not absorb linearly at the laser wavelength, other techniques have been developed that utilize ablation of absorbing sacrificial materials to provide the thrust for forward transfer [27–31]. Although these techniques have vastly expanded the range of materials that can be deposited using forward transfer, they also introduce extra complexity to the process. For example, one commonly applied approach is to include a sacrificial layer between the carrier and the donor, which is often referred to as a dynamic release layer (DRL) [28]. Metallic layers are often used as DRLs [28,29], but, as metals do not dissociate cleanly, contamination

0003-6935/09/112058-09$15.00/0

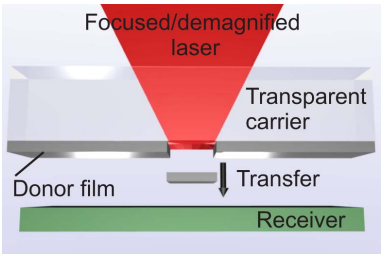

Fig. 1. (Color online) Schematic of the LIFT technique.

of deposited donor material by residual DRL is possible [32]. Although this problem can be minimized using optimized polymeric DRLs [30,33,34], such materials can limit the range of available donors due to sensitivity to high temperatures or solvent treatment. Clearly, therefore, it would be desirable to have a technique capable of transferring transparent materials directly.

In a recent work, we demonstrated that by utilizing multiphoton absorption of femtosecond duration pulses at $\lambda = 800\,\mathrm{nm}$, forward transfer of an effectively transparent (absorption depth several orders of magnitude greater than the film thicknesses), amorphous gadolinium gallium oxide (GdGaO) donor was possible [35]. Furthermore, by including a triazene polymer (TP) DRL [36], also transparent to the laser wavelength, it was possible to forward transfer very clean discs of GdGaO with no evidence of residual DRL. An interesting observation was that the transfer threshold using the DRL was only ≈20% of the TP ablation threshold at $\lambda = 800\,\mathrm{nm}$.

B. Optical Standing Waves

An important consideration when transferring transparent films by fs-LIFT is the formation of an optical standing wave due to interference between forward- and backward-propagating waves reflecting off the various interfaces between carrier, DRL, donor, air gap, and receiver. The result is potentially a large intensity modulation along the laser propagation direction within the thin films. Hence, the local intensity can vary significantly from the incident intensity, which will affect the transfer threshold and may cause unintentional damage to the transferred material.

In this work we will consider the fs-LIFT of transparent films in more detail. A model for the intensity profile in arbitrary stacks of DRL and donor film(s) is presented. The effects of various material and experimental parameters on the peak intensity within the film(s) are discussed in terms of their potential impact on the LIFT process. Lastly, the model is applied to the case of fs-LIFT of GdGaO with a TP-DRL. We investigate whether the formation of a standing wave can explain the surprisingly low transfer threshold observed previously [35]. Also studied are the effects of varying the size of the air gap in the setup on the resultant GdGaO depositions.

2. Standing Wave Model

The formation of standing waves in thin films has been considered by a number of authors for the case of lithographic patterning (see, e.g., [37]). In particular, an analytical description of the standing wave intensity pattern in stacks of arbitrary numbers of thin films has been developed by Mack [38]. Note that, in the following, we are assuming normal, nonconvergent incidence of the laser contrary to that shown in Fig. 1 and Fig. 3, below. Typically, in a LIFT setup, the thickness of the donor and DRL films is small ($\leq 1\,\mu\mathrm{m}$) compared to the depth of field (≈0.1 mm). Hence, this approximation is valid, and for modeling purposes we can neglect angular-dependent reflection coefficients. Note also that the following treatment is applicable to femtosecond duration pulses when the coherence length is significantly greater than the optical path length of the multiple reflections. Later we will consider pulses with a coherence length around $30\,\mu\mathrm{m}$, which is appreciably larger than the few micrometers optical path length of the first few reflections that dominate the standing wave pattern.

A. Single-Film Case

It is relatively simple to determine the intensity profile in a single thin film between two, effectively infinite, dielectric media, as shown in Fig. 2. The film is exposed through layer 1 (refractive index, $\mathbf{n_1} = n_1 + i\kappa_1$) to a normally incident monochromatic plane wave, $\mathbf{E_{In}}(\mathbf{z}) = E_{In}\exp(-ik_1 z)$. For simplicity, it is chosen to set $z = 0$ at the first interface, Γ_{12}. The wave is partially transmitted into the film where it undergoes multiple reflections off Γ_{23} and Γ_{12}. Note that, although the theory is for monochromatic illumination, the femtosecond Ti:sapphire laser used in the experiments described later had a bandwidth of around 10 nm. The result of using a source with a finite bandwidth would be to reduce the standing wave amplitude relative to the monochromatic case. However, because the laser bandwidth was small

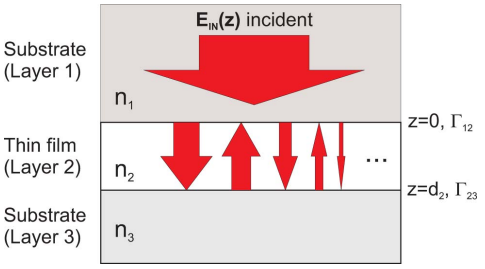

Fig. 2. (Color online) Schematic of multiple reflections in a single transparent thin film under monochromatic, plane-wave illumination. Multiple reflections have been spatially separated for ease of viewing.

compared to the standing wave period (≈100) s nm, the model still provided an acceptable level of accuracy for comparison between experimental and numerical results.

A geometrical approach yields a series of forward- and backward-propagating waves in the film, $\mathbf{E}^{+}(\mathbf{z})$ and $\mathbf{E}^{-}(\mathbf{z})$, respectively, of the form

$$\mathbf{E}_{\mathbf{a}}^{+}(\mathbf{z}) = E_{In} t_{12} r_{23}^{a-1} r_{21}^{a-1} \tau_2^{2(a-1)} \exp(-ik_2 z), \quad (1)$$

$$\mathbf{E}_{\mathbf{a}}^{-}(\mathbf{z}) = E_{In} t_{12} r_{23}^{a} r_{21}^{a-1} \tau_2^{2a} \exp(ik_2 z), \quad (2)$$

where $t_{ij} = 2\mathbf{n}_i/(\mathbf{n}_i + \mathbf{n}_j)$ is the transmission coefficient at Γ_{ij}, $r_{ij} = (\mathbf{n}_i - \mathbf{n}_j)/(\mathbf{n}_i + \mathbf{n}_j)$ is the reflection coefficient at Γ_{ij}, $\tau_j = \exp(-ik_j d_j)$ is the internal transmittance of layer j, d_j is the thickness of layer j, $k_j = 2\pi\mathbf{n}_j/\lambda$ is the propagation constant in layer j, λ is the wavelength, and a denotes multiple reflections.

The total electric field in the thin film, $\mathbf{E}_{\mathbf{film}}(\mathbf{z})$, is then just the summation of all these forward- and backward-propagating waves:

$$\mathbf{E}_{\mathbf{film}}(\mathbf{z}) = \sum_{a=1}^{\infty} (\mathbf{E}_{\mathbf{a}}^{+}(\mathbf{z}) + \mathbf{E}_{\mathbf{a}}^{-}(\mathbf{z})). \quad (3)$$

Substituting Eqs. (1) and (2) into (3), it is then straightforward to show that

$$\mathbf{E}_{\mathbf{film}}(\mathbf{z}) = E_{In} t_{12} [\exp(-ik_2 z_2) + r_{23}\tau_2^2 \exp(ik_2 z_2)] S, \quad (4)$$

where $S = 1 + r_{21} r_{23} \tau_2^2 (1 + r_{21} r_{23} \tau_2^2 (1 + \ldots))$, is a geometrical series. Hence, noting that $r_{21} = -r_{12}$, we arrive at [38]

$$\mathbf{E}_{\mathbf{film}}(\mathbf{z}) = E_{In} t_{12} \left(\frac{\exp(-ik_2 z) + r_{23}\tau_2^2 \exp(ik_2 z)}{1 + r_{12} r_{23} \tau_2^2} \right). \quad (5)$$

Finally, the intensity in the film, $\mathbf{I}_{\mathbf{film}}(\mathbf{z})$, is found by squaring the magnitude of $\mathbf{E}_{\mathbf{film}}(\mathbf{z})$,

$$\mathbf{I}_{\mathbf{film}}(\mathbf{z}) = I_{\text{film}} |\mathbf{E}_{\mathbf{film}}(\mathbf{z})|^2, \quad (6)$$

where I_{film} is a constant.

B. Multiple-Film Case

The above analysis can be extended to the case of multiple thin films between two substrates. Consider now the case of $m - 1$ thin films (i.e., $m + 1$ layers including the two substrates). The substrates are layers 1 and $m + 1$. The field in layer 2, the first thin film, is then given by [38]

$$\mathbf{E}_{\mathbf{2}}(\mathbf{z}) = E_{In} t_{12} \frac{\exp(-ik_2 z) + r'_{23}\tau_2^2 \exp(ik_2 z)}{1 + r_{12} r'_{23} \tau_2^2}. \quad (7)$$

Note that the electric field in layer 2 is almost identical in the single- and multiple-film cases except that the reflection coefficient at Γ_{23} in Eq. (5) is replaced by an effective reflection coefficient between layer 2 and all the subsequent layers, r'_{23}.

Similarly, if it is desired to know the field in the jth layer, $\mathbf{E}_{\mathbf{j}}(z)$, this is given by [38]

$$\mathbf{E}_{\mathbf{j}}(\mathbf{z}) = E_{In,j} t'_{j-1,j} \frac{\exp(-ik_j z_j) + r'_{jj+1}\tau_j^2 \exp(ik_j z_j)}{1 + r^*_{j-1,j} r'_{jj+1} \tau_j^2}. \quad (8)$$

Here, $E_{In,j}$ is the effective fluence incident on layer j, and $r^*_{j-1,j}$ is the effective reflection coefficient between layer j and all the preceding layers. $r^*_{j-1,j}$, r'_{jj+1}, and $E_{In,j}$ can be calculated from the refractive indices and thicknesses of all the layers in the structure as described in [38]. z_j is the local depth in layer j, such that $z_j = 0$ at $\Gamma_{j-1,j}$ and $z_j = d_j$ at Γ_{jj+1}. Note that, in layer m (the last thin film), r'_{jj+1} is just equal to r_{jj+1}.

The intensity in the top or the jth layer can then be found by squaring the magnitude of Eq. (7) or (8), respectively:

$$\mathbf{I}_{\mathbf{2}}(\mathbf{z}) = I_2 |\mathbf{E}_{\mathbf{2}}(\mathbf{z})|^2, \quad (9)$$

$$\mathbf{I}_{\mathbf{j}}(\mathbf{z}) = I_j |\mathbf{E}_{\mathbf{j}}(\mathbf{z})|^2, \quad (10)$$

where I_2 and I_j are constants.

3. Implications of Standing Waves for fs-LIFT

Using the above, multilayered model, it is simple to determine the standing wave intensity profile in a typical fs-LIFT setup. Consider first the case of a single donor film of refractive index $\mathbf{n}_{\mathbf{donor}}$ and thickness d_{donor} on a silica carrier ($\mathbf{n}_{\mathbf{carrier}} \approx 1.47 + 0i$) separated by an air gap of thickness d_{air} from a receiver with a surface reflection coefficient r_{rec}, as shown in Fig. 3. Clearly the carrier is equivalent to layer 1 in the above model; the donor is layer 2, the air gap layer 3, and the receiver layer 4.

For the simulations, the laser wavelength was chosen to be 800 nm, in accordance with experiments. E_{In}, I_2, and I_j were all set to 1 for simplicity, and hence the incident intensity at the carrier–donor interface ($z = 0$) was also unity. For the donor, a material similar to the GdGaO was chosen, so

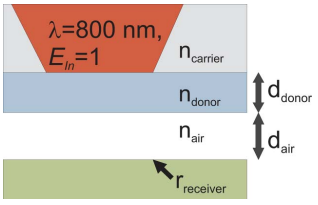

Fig. 3. (Color online) Fs-LIFT of a single film.

$\mathbf{n_{donor}} = n_{donor} + i\kappa_{donor} \approx 1.95 - 0.03i$; the value of κ_{donor} corresponded to a $1/e$ absorption depth of approximately $2\,\mu$m.

There are essentially three variable parameters in this setup, d_{donor}, d_{air}, and r_{rec} ($\mathbf{n_{donor}}$ is obviously fixed by the application). Figure 4 shows the variation of maximum intensity in the donor, $I_{(donor,Max)}$, as a function of d_{air} for a range of donor film thicknesses, with receivers approximately corresponding to silica [$r_{rec} = -0.2$, Fig. 4(a)] and silicon [$r_{rec} = -0.57$, Fig. 4(b)]. The most obvious trend that can be seen is that $I_{(donor,Max)}$ varied approximately sinusoidally with d_{air} with a period of around $\lambda/2$. This result was intuitive as interference in the donor film due to the first reflection off the receiver was constructive for $2d_{air} = \lambda/2, 3\lambda/2, \ldots$ and destructive for $2d_{air} = 0, \lambda, 2\lambda, \ldots$ (note the π-phase shift upon reflection from the air–receiver interface).

The dependence on d_{donor} was also relatively easy to explain. Due to interference between the forward-propagating incident wave and the two backreflections off the donor–air interface and the receiver surface, a pattern of maxima and minima was formed in the donor film with a period of $\lambda/2n_{donor} \approx 200$ nm. Consider Fig. 5, which shows the calculated intensity profiles in the donor and air layers with $(d_{donor}(\mu m), d_{air}(\mu m))$ equal to (0.05,0.125) (a), (0.05,0.375) (b), (0.5,0.2) (c), and (0.5,0.4) (d). The receiver reflectivity was $r_{rec} = -0.57$, and the refractive index profile is included as a dashed line to indicate the donor–air boundary.

The necessity to have an intensity minimum at the receiver surface meant that d_{air} determined the positions of the maxima and minima in the donor layer. For very thin films ($d_{donor} \le \lambda/2n_{donor}$), the film thickness was less than the standing wave period, so whether there was a maximum or minimum in the donor was determined by d_{air} [see Figs. 5(a) and 5(b)]. As a result, the maximum intensity in very thin films was highly dependent on d_{air} (see Fig. 4). For thicker films with $d_{donor} > \lambda/2n_{donor}$, there was always a standing wave maximum in the donor, and so the dependence on d_{air} decreased. However, there was still a significant, approximately sinusoidal, dependence of the maximum on d_{air}.

LIFT techniques are well known to be highly sensitive to the applied laser fluence (see, e.g., [1,21]). Hence, having the maximum intensity in the donor highly dependent on d_{air} represents a problem as d_{air} is then another parameter that must be accurately controlled for reproducible results. It is convenient to define the parameter β as the ratio of the maximum to the minimum value of $I_{donor,Max}$ as d_{air} is varied, i.e.,

$$\beta = \frac{\max(I_{donor,Max}(d_{air}))}{\min(I_{donor,Max}(d_{air}))}. \tag{11}$$

β then quantifies the variation of the maximum intensity in the donor with d_{air}. Ideally we want $\beta = 1$ so there is no dependence of $I_{donor,Max}$ on d_{air} and

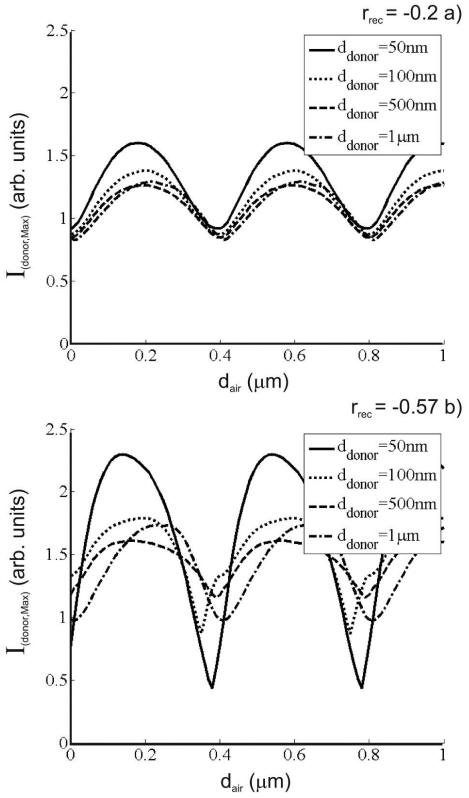

Fig. 4. Variation of the maximum intensity in the donor with d_{air} and d_{donor} assuming $r_{rec} = -0.2$ (a) and -0.57 (b).

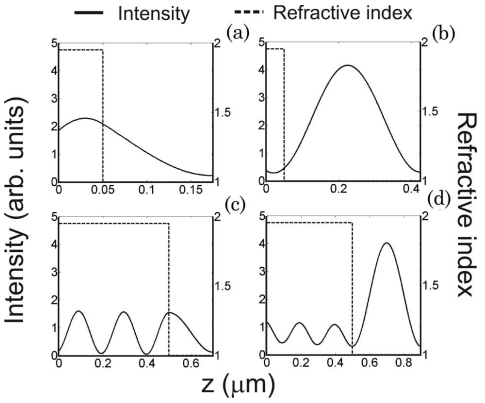

Fig. 5. Intensity (solid lines) and refractive index (dashed lines) profiles with $(d_{donor}(\mu m), d_{air}(\mu m))$ equal to (0.05, 0.125) (a), (0.05, 0.375) (b), (0.5, 0.2) (c), and (0.5, 0.4) (d).

critical control of the size of the air gap is not necessary.

Figure 6 shows plots of β as functions of r_{rec} (a) and d_{donor} (b) with all other parameters fixed. There were clearly strong dependences on both parameters. For receivers with very low reflection coefficients, the backreflection off the receiver was comparatively small compared to the standing wave in the film due to the strong backreflection off the donor–air interface. Hence, the variation of β with d_{donor} was small for values of $|r_{rec}| \leq 0.1$ [Fig. 6(a)].

As $|r_{rec}|$ was increased, the influence of the backreflection off the receiver was enhanced, and hence the value of β also began to rise. For very thin films (with $d_{donor} \leq \lambda/2n_{donor}$ as before), the increase in β was monotonic due to the lack of the formation of complete fringes in the donor [Fig. 6(b)]. For thicker donors ($d_{donor} \geq \lambda/2n_{donor}$), β increased to a peak at $r_{rec} \approx -0.35$ [Fig. 6(b)]. The value of r_{rec} at which this peak occurred was observed to be virtually independent of d_{donor} but strongly dependent on $\mathbf{n_{donor}}$. The origin of the peak was due to the relative amplitudes of the backreflections from the donor–air interface and the receiver. A wave passing through the donor–air interface, reflecting off the receiver, and then reentering the donor layer experienced an effective reflection coefficient, r_{eff}, of $t_{23}r_{rec}t_{32}$. A simple calculation then yields $r_{rec} \approx -0.35$, which corresponds to $r_{eff} \approx r_{23}$. Hence, interference was almost completely destructive for $2d_{air} = 0, \lambda, 2\lambda, \ldots$ and fully constructive for $2d_{air} = \lambda/2, 3\lambda/2, \ldots$ when $r_{rec} \approx -0.35$. This led to the largest possible variation of $I_{donor,Max}$ with d_{air}, and hence a maximum in the value of β.

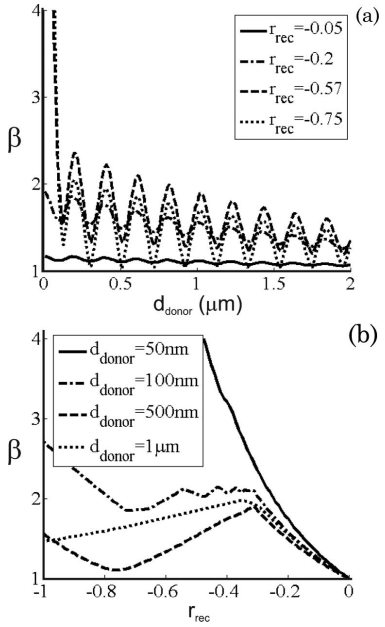

Fig. 6. Plot of β as functions of d_{donor} (a) and r_{rec} (b) with other parameters fixed.

For $r_{rec} \geq r_{eff}$, the value of β began to fall to a minimum [Fig. 6(b)]. Note that, for certain values of d_{donor}, the minimum was at an unphysical value of $|r_{rec}| > 1$. To understand this behavior, it is necessary to consider the higher-order reflections that can occur. For example, consider the second-order reflection off the donor–carrier interface for backward-propagating waves in the donor. The relative strength of this reflection will depend on whether there is a minimum or a maximum at this interface, which in turn depends on whether there is a minimum or a maximum at the donor–air interface. The important point to note is that, if $d_{donor} = m\lambda/4\mathbf{n_{donor}}$, $m = 1, 3, 5, \ldots$ then there will always be a minimum at the donor–carrier interface if there is a maximum at the donor–air interface and vice versa [see Figs. 5(c) and 5(d)]. For $d_{donor} = m\lambda/4\mathbf{n_{donor}}$, $m = 2, 4, 6, \ldots$ the opposite is true. Hence, for $m = 1, 3, 5, \ldots$, the reflection off the donor–carrier interface acts to counter the variation in $I_{donor,Max}$ due to d_{air}, while for $m = 2, 4, 6, \ldots$ the two effects combine to increase the variation. Thus the second-order reflection explains why a periodic behavior of β with d_{donor} is observed with a period of $\lambda/2\mathbf{n_{donor}}$ [Fig. 6(a)]. Similarly, the reason why β begins to increase again above a certain, d_{donor}-dependent value of $|r_{rec}|$ can be explained by considering even higher-order reflections. One final observation to note is that, for all values of r_{rec}, $\beta \to 1$ as $d_{donor} \to \infty$ due to the small amount of absorption in the donor film.

To conclude this section, fs-LIFT of transparent films is complicated by the formation of an optical standing wave. The effect of this standing wave is a dependence of $I_{donor,Max}$ on d_{air} that is not observed with absorbing films and means that d_{air} must be accurately controlled to achieve reproducible results. However, using the above model, it is possible to identify sets of experimental parameters that minimize this problem. If the application allows for variation of r_{rec}, then the problem can be reduced significantly. If only control of d_{air} and d_{donor} is available, as is likely in many real applications, then it is still possible to use the model to find optimal values of these parameters.

4. fs-LIFT of Transparent GdGaO: Influence of d_{air}

In Section 3 it was demonstrated theoretically that the formation of an optical standing wave during fs-LIFT of transparent films led to a strong dependence of the peak intensity in the film(s) on the size of the air gap. It was shown that great care must be taken to choose optimal values of the various experimental parameters to obtain reproducible results. In this section we will consider how significant the effect is in practice by investigating the transfer of a sample transparent donor and how the deposited structures on the receiver vary with d_{air}.

As a sample donor material, a GdGaO film transparent to all wavelengths greater than ≈300 nm was used. In a recent work we demonstrated the fs-LIFT of this material using multiphoton absorption of an 800 nm Ti:sapphire laser (130 fs) [35]. However, it was observed that direct transfer of the donor resulted in poor quality depositions, which would be difficult to analyze in terms of damage caused by localized high intensities corresponding to standing wave maxima. By including a TP-DRL, transparent to wavelengths longer than 400 nm, it was possible to transfer clean discs of GdGaO. Hence we will use the same setup already described in [35] (DRL, TP 100 nm thick; donor, GdGaO 150 nm thick) for our studies here.

The above model can easily be extended to include the DRL by including an extra layer between the carrier and the donor. The TP-DRL is now layer 2, with refractive index $\mathbf{n_{DRL}} = n_{\mathrm{DRL}} + i\kappa_{\mathrm{DRL}} \approx 1.7 - 0.06i$ [39]; the GdGaO donor is layer 3, the air layer 4, and the receiver layer 5. Note that in Section 3 the value of n_{donor} was taken to be 1.95. This corresponds to the refractive index of single crystal gadolinium gallium garnet. However, because the donor in this experiment had to be grown at room temperature to protect the heat-sensitive TP-DRL, the resultant film was amorphous. The refractive index of this amorphous GdGaO is not known so it was chosen to use the value of $n_{\mathrm{donor}} = 1.95$ as an approximation.

In this multiple-film geometry, the parameter β is important in both the DRL and donor films. Similar calculations to those performed above again yielded periodic dependences of β on the films' thicknesses in the DRL and donor, as shown in Figs. 7(a) and 7(b), respectively. This behavior can be easily explained considering the relative intensities of the multiple reflections as before.

Assuming the best guesses of n_{DRL} and n_{donor} given above for the TP and the GdGaO, the model gives $\beta = 3.0717$ in the DRL and $\beta = 1.7882$ in the donor for $d_{\mathrm{DRL}} = 100$ nm and $d_{\mathrm{donor}} = 150$ nm. When n_{DRL} and n_{donor} were allowed to vary while the film thicknesses was kept constant [Fig. 7(c)], it was found that, although there were dependences of β in both layers on the refractive indices, these dependences was comparatively weak. Hence, the most important parameters in determining the values of β in the two films appear to be the film thicknesses. In this case the minimum values of β were ≈1.25 and ≈1.4 in the DRL and donor layers, respectively. However, given the uncertainty in the values of $\mathbf{n_{DRL}}$ and $\mathbf{n_{donor}}$, such numerical results should be treated with caution.

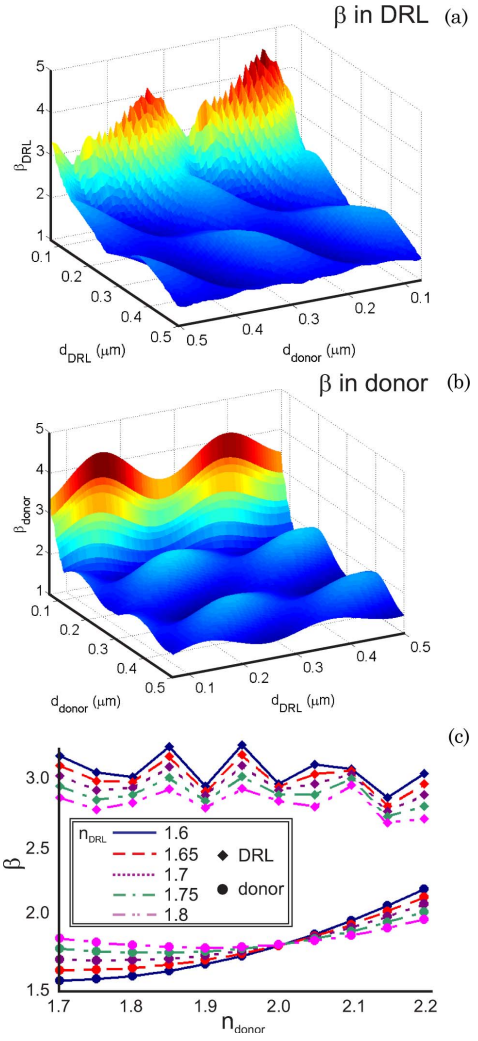

Fig. 7. (Color online) Plots of β in the TP-DRL (a) and in the GdGaO donor (b) as functions of d_{donor} and d_{DRL} with other parameters fixed, and variation of β in the DRL (diamonds) and donor (circles) layers as function of n_{DRL} and n_{donor} (c).

A. Experiments with GdGaO

All experiments were performed under vacuum at a pressure of ≈0.1 mbar. The donor and receiver were separated by a single, 8 μm thick Mylar spacer at one edge. This resulted in a variation of d_{air} across the donor sample from tight contact at the edge with no spacer, to ≈8 μm. The fs-LIFT experiments were performed using a micromachining workstation (modified New Wave UP-266) fitted with a white light source and a CCD camera for viewing the workpiece. As the DRL and donor films were transparent to the white light, thin film interference of the white light occurred that was observed as colored fringes on the CCD. Estimating the reflection coefficients of the interfaces using the previously given refractive indices yielded $r_{12} \approx -0.07$, $r_{23} \approx -0.07$, $r_{34} \approx 0.32$, and $r_{45} = r_{\mathrm{rec}} \approx -0.57$. Hence, the backreflections off the

donor–air and air–receiver interfaces were by far the strongest, and so we can conclude that the visible fringes were primarily the result of thin film interference in the air gap. Therefore, it was possible to estimate d_{air} from the color of the fringe, λ_f, and the fringe number, f. For example, for the first green fringe, $\lambda_f \approx 530$ and $f = 1$, $d_{\mathrm{air}} = f\lambda_f/4 \approx 130\,\mathrm{nm}$.

The accuracy of the method described above for measuring d_{air} depended entirely on accurately estimating the wavelength of the observed colored fringes. We estimated that the accuracy of the wavelength measurement we were able to achieve with the micromachiner color CCD was around $\pm 25\,\mathrm{nm}$. This corresponded to an error in d_{air} of $\pm 7\,\mathrm{nm}$.

Figure 8 shows scanning electron microscope (SEM) micrographs of deposited GdGaO as a function of d_{air}. For reasons described in [35], it is believed that all the TP-DRL was removed during the forward transfer process. Observation of these results revealed a periodic dependence of the GdGaO deposit morphology on d_{air}. With donor and receiver in tight contact [$d_{\mathrm{air}} \approx 0$, Fig. 8(a)] no deposits were obtained. This was believed to be due to the fact that the donor layer did not have sufficient room to deform and shear due to the close proximity of the receiver [35]. Increasing d_{air} to around 50 or 100 nm [Fig. 8(b)] resulted in the good-quality, unshattered discs reported previously [35]. For $d_{\mathrm{air}} \approx 200\,\mathrm{nm}$, the deposited structures were very different, exhibiting significant laser damage and splattered material transferred around the main deposit [Fig. 8(c)]. Further increasing d_{air} resulted in a gradual reduction in the amount of apparent laser damage [Fig. 8(d)] until around $d_{\mathrm{air}} \approx 400\,\mathrm{nm}$ when similar good-quality discs to those observed at $d_{\mathrm{air}} \leq 100\,\mathrm{nm}$ were seen again [Fig. 8(e)]. However, at this separation, there was evidence of more (solid phase) debris, believed to be due to shattering during transfer [35].

When d_{air} was increased to greater than 400 nm, similar behavior was observed. Firstly, the amount of laser damage to the GdGaO increased with d_{air} up to $d_{\mathrm{air}} \approx 600\,\mathrm{nm}$ [Fig. 8(f)], before decreasing again until relatively clean discs were seen for $d_{\mathrm{air}} \approx 800\,\mathrm{nm}$ [Fig. 8(g)]. This periodic variation of deposits continued with the donor–receiver separation, with good-quality deposits obtained when $d_{\mathrm{air}} \approx 400, 800, \ldots\,\mathrm{nm}$ and significantly damaged material when $d_{\mathrm{air}} \approx 200, 600, \ldots\,\mathrm{nm}$.

It is simple to explain the observed variation in deposited material by considering the effect of multiple reflections. In previous work, the forward transfer threshold of a 150 nm GdGaO donor on a 100 nm TP-DRL was measured to be around $90\,\mathrm{mJ/cm^2}$, compared to ablation thresholds of 110 and $500\,\mathrm{mJ/cm^2}$ for the GdGaO and TP, respectively [35]. Figure 9 shows a plot of the variation of maximum fluence in the DRL (solid line) and donor (dashed line) layers with d_{air} calculated using the material properties described above and assuming an incident fluence of $90\,\mathrm{mJ/cm^2}$ (achieved by setting $E_{In} = 10.229$). The SEM micrographs A–G show

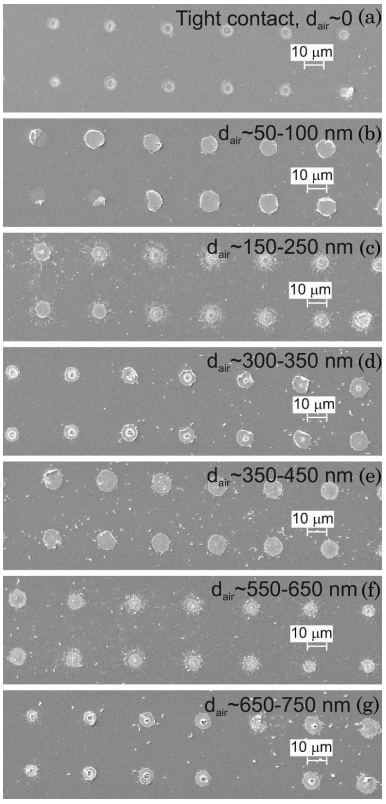

Fig. 8. SEM micrographs of GdGaO deposits on Si as a function of d_{air} transferred with fluence $\approx 90\,\mathrm{mJ/cm^2}$.

typical deposits obtained at values of d_{air} indicated by A–G on the graph. As would be expected, the relatively undamaged deposits coincided with values of d_{air} where destructive interference resulted in relatively low fluences in the DRL and donor (see A, D, G). Similarly, the most obviously damaged deposits were obtained when d_{air} corresponded to constructive interference in the films (B, E).

The results in Fig. 9 also provide a likely explanation for the surprisingly low (below the ablation threshold) transfer thresholds of GdGaO when a TP-DRL was included [35]. As can be seen from the plot in Fig. 9, assuming an incident fluence of $90\,\mathrm{mJ/cm^2}$, the maximum fluence in the TP-DRL varied from ≈ 80 to $\approx 250\,\mathrm{mJ/cm^2}$ as d_{air} changed, and hence the fluence was never sufficient to photolytically decompose the TP-DRL. However, the fluence in the donor was consistently above $110\,\mathrm{mJ/cm^2}$ (i.e., greater than the measured ablation threshold). This observation suggested that the forward transfer of GdGaO resulted from absorption of the laser in, and associated heating of, the donor; the hot donor

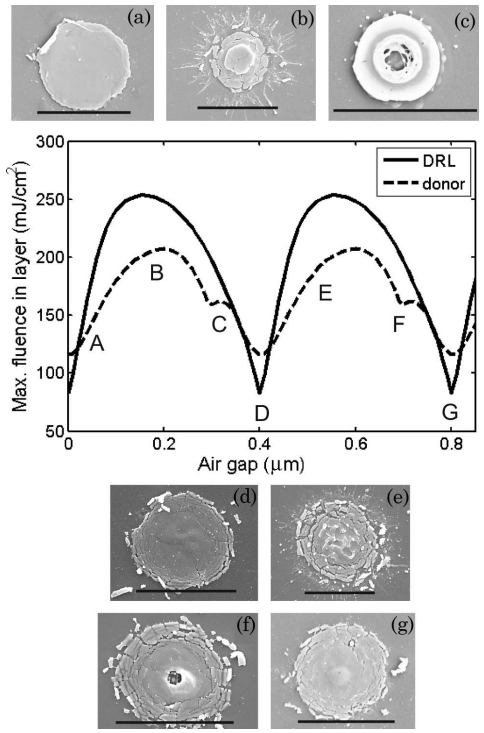

Fig. 9. Main graph: variation of maximum fluence in TP-DRL (solid line) and GdGaO donor (dashed line) as functions of d_{air} assuming incident fluence 90 mJ/cm^2. SEM micrographs show deposited material at approximately indicated separations; scale bars represent 10 μm.

film then conductively heated the TP-DRL, which subsequently thermally decomposed. Note that these results indicate that it is possible to get good-quality transfer of donor material, even when the donor has a lower ablation threshold than the DRL at the laser wavelength, provided that the donor can withstand heating to the DRL ablation/decomposition temperature. Note also the apparent disparity between the numerical results in Fig. 9 and the measured ablation threshold of the GdGaO. The model predicted fluences in the donor well above its ablation threshold for most values of d_{air}, but no evidence of laser damage was seen in the deposits at $d_{air} \approx 0, 400, 800, \ldots$ nm. This can be explained by the fact that the model does not take into account the increase in κ_{donor} as the fluence approached the ablation threshold and the GdGaO began to absorb the laser nonlinearly.

5. Conclusions

To conclude, a thin film interference model has been used to predict the standing wave intensity distribution formed during the femtosecond LIFT of transparent films. The model has been used to investigate the effects of varying a number of experimental parameters, including the thicknesses of the donor, DRL, and air layers, and the receiver reflectivity. An important consideration that has been identified was the dramatic variation of the fluence in the DRL and donor layers as d_{air} was changed. We have shown that, in principle, it is possible to minimize this effect with the proper choice of film thicknesses (and receiver reflectivity, if this parameter can be varied).

The results of the model have been compared to experimental results of the transfer of a GdGaO donor on a TP-DRL. The model appeared to explain the periodic variation in the morphology of GdGaO deposits with d_{air}. Also, the model provided an explanation of the below ablation threshold transfer of GdGaO. The transfer process is now believed to be a thermolytic decomposition of the TP layer due to conductive heating from the overlying donor, which nonlinearly absorbed the laser at a lower fluence. Taken together, the experimental and numerical results indicate that fs-LIFT is a viable method for the transfer of transparent materials. However, extra care must be taken with regards to the formation of a standing wave and the relative damage thresholds of the DRL and donor materials.

The authors are grateful to the Engineering and Physical Sciences Research Council (EPSRC), UK, for research funding under grant EP/C515668/1. We also thank Thomas Lippert at the Paul Scherrer Institut and Romain Fardel and Matthias Nagel at EMPA in Switzerland for providing the TP-DRL layers.

References

1. J. Bohandy, B. Kim, and F. Adrian, "Metal deposition from a supported metal film using an excimer laser," J. Appl. Phys. **60**, 1538–1539 (1986).
2. D. Willis and V. Grosu, "Microdroplet deposition by laser-induced forward transfer," Appl. Phys. Lett. **86**, 244103 (2005).
3. F. Adrian, J. Bohandy, B. Kim, A. Jette, and P. Thompson, "A study of the mechanism of metal deposition by the laser-induced forward transfer process," J. Vac. Sci. Technol. B **5**, 1490–1494 (1987).
4. R. Baseman and N. Froberg, "Minimum fluence for laser blow-off of thin gold films at 248 and 532 nm," Appl. Phys. Lett. **56**, 1412–1414 (1990).
5. Z. Toth, Z. Kantor, P. Mogyorosi, and T. Szorenyi, "Surface patterning by pulsed laser induced transfer of metals and compounds," Proc. SPIE **1279**, 150–157 (1990).
6. H. Esrom, J. Zhang, U. Kogelschatz, and A. Pedraza, "New approach of a laser-induced forward transfer for deposition of patterned thin metal films," Appl. Surf. Sci. **86**, 202–207 (1995).
7. I. Zergioti, D. Papazoglou, A. Karaiskou, C. Fotakis, E. Gamaly, and A. Rode, "A comparative schlieren imaging study between ns and sub-ps laser forward transfer of cr," Appl. Surf. Sci. **208–209**, 177–180 (2003).
8. Y. Nakata and T. Okada, "Time-resolved microscopic imaging of the laser-induced forward transfer process," Appl. Phys. A **69**, S275–S278 (1999).

9. R. Bahnisch, W. Gross, and A. Menschig, "Single-shot, high repetition rate metallic pattern transfer," Microelectron. Eng. **50**, 541–546 (2000).
10. B. Tan, K. Venkatakrishnan, and K. Tok, "Selective surface texturing using femtosecond pulsed laser induced forward transfer," Appl. Surf. Sci. **207**, 365–371 (2003).
11. L. Landstrom, J. Klimstein, G. Schrems, K. Piglmayer, and D. Bauerle, "Single-step patterning and the fabrication of contact masks by laser-induced forward transfer," Appl. Phys. A **78**, 537–548 (2004).
12. I. Lee, W. Tolbert, D. Dlott, M. Doxtader, D. Foley, D. Arnold, and E. Ellis, "Dynamics of laser ablation transfer imaging investigated by ultrafast microscopy," J. Imaging Sci. Technol. **36**, 180–187 (1992).
13. I. Zergioti, S. Mailis, N. Vainos, P. Papakonstantinou, C. Kalpouzos, C. Grigoropoulos, and C. Fotakis, "Microdeposition of metal and oxide structures using ultrashort laser pulses," Appl. Phys. A **66**, 579–582 (1998).
14. H. Sakata, S. Chakraborty, E. Yokoyama, M. Wakaki, and D. Chakravorty, "Laser-induced forward transfer of tio-au nanocomposite films for maskless patterning," Appl. Phys. Lett. **86**, 114104 (2005).
15. E. Fogarassy, C. Fuchs, F. Kerherve, G. Hauchecorne, and J. Perriere, "Laser-induced forward transfer of high- T_c ybacuo and bisrcacuo superconducting thin films," J. Appl. Phys. **66**, 457–459 (1989).
16. S. Pimenov, G. Shafeev, A. Smolin, V. Konov, and B. Vodolaga, "Laser-induced forward transfer of ultra-fine diamond particles for selective deposition of diamond films," Appl. Surf. Sci. **86**, 208–212 (1995).
17. S. Chang-Jian, J. Ho, J. Cheng, and C. Sung, "Fabrication of carbon nanotube field emission cathodes in patterns by a laser transfer method," Nanotechnology **17**, 1184–1187 (2006).
18. B. Thomas, A. Alloncle, P. Delaporte, M. Sentis, S. Sanaur, M. Barret, and P. Collot, "Experimental investigations of laser-induced forward transfer process of organic thin films," Appl. Surf. Sci. **254**, 1206–1210 (2007).
19. Y. Tsuboi, Y. Furuhata, and N. Kitamura, "A sensor for adenosine triphosphate fabricated by laser-induced forward transfer of luciferase onto a poly(dimethylsiloxane) microchip," Appl. Surf. Sci. **253**, 8422–8427 (2007).
20. L. Yang, C. Wang, X. Ni, Z. Wang, W. Jia, and L. Chai, "Microdroplet deposition of copper film by femtosecond laser-induced forward transfer," Appl. Phys. Lett. **89**, 161110 (2006).
21. D. Banks, C. Grivas, J. Mills, I. Zergioti, and R. Eason, "Nanodroplets deposited in microarrays by femtosecond ti:sapphire laser induced forward transfer," Appl. Phys. Lett. **89**, 193107 (2006).
22. S. Bera, A. Sabbah, J. Yarbrough, C. Allen, B. Winters, C. Durfee, and J. Squier, "Optimization study of the femtosecond laser-induced forward-transfer process with thin aluminium films," Appl. Opt. **46**, 4650–4659 (2007).
23. C. Germain, L. Charron, L. Lilge, and Y. Tsui, "Electrodes for microfluidic devices produced by laser induced forward transfer," Appl. Surf. Sci. **253**, 8328–8333 (2007).
24. F. Claeyssens, A. Klini, A. Mourka, and C. Fotakis, "Laser patterning of zn for zno nanostructure growth: Comparison between laser induced forward transfer in air and in vacuum," Thin Solid Films **515**, 8529–8533 (2007).
25. I. Zergioti, A. Karaiskou, D. Papazoglou, C. Fotakis, M. Kapsetaki, and D. Kafetzopoulos, "Time resolved schlieren study of sub-pecosecond and nanosecond laser transfer of biomaterials," Appl. Surf. Sci. **247**, 584–589 (2005).
26. D. Banks, C. Grivas, I. Zergioti, and R. Eason, "Ballistic laser-assisted solid transfer (blast) from a thin film precursor," Opt. Express **16**, 3249–3254 (2008).
27. A. Pique, D. Chrisey, R. Auyeung, J. Fitz-Gerald, H. Wu, R. McGill, S. Lakeou, P. Wu, V. Nguyen, and M. Duignan, "A novel laser transfer process for direct writing of electronic and sensor materials," Appl. Phys. A **69**, S279–S284 (1999).
28. W. Tolbert, I. Lee, M. Doxtader, E. Ellis, and D. Dlott, "High-speed color imaging by laser ablation transfer with a dynamic release layer: fundamental mechanisms," J. Imaging Sci. Technol. **37**, 411–421 (1993).
29. P. Serra, M. Colina, J. Fernandez-Pradas, L. Sevilla, and J. Morenza, "Preparation of functional DNA microarrays through laser-induced forward transfer," Appl. Phys. Lett. **85**, 1639–1641 (2004).
30. G. Blanchet, Y.-L. Loo, J. Rogers, F. Gao, and C. Fincher, "Large area, high resolution, dry printing of conducting polymers for organic electronics," Appl. Phys. Lett. **82**, 463–465 (2003).
31. R. Fardel, M. Nagel, F. Nuesch, T. Lippert, and A. Wokaun, "Fabrication of organic light-emitting diode pixels by laser-assisted forward transfer," Appl. Phys. Lett. **91**, 061103 (2007).
32. T. Smausz, B. Hopp, G. Kecskemeti, and Z. Bor, "Study on metal microparticle content of the material transferred with absorbing film assisted laser induced forward transfer when using silver absorbing layer," Appl. Surf. Sci. **252**, 4738–4742 (2006).
33. R. Fardel, M. Nagel, F. Nuesch, T. Lippert, and A. Wokaun, "Laser forward transfer using a sacrificial layer: influence of the material properties," Appl. Surf. Sci. **254**, 1322–1326 (2007).
34. N. Kattamis, P. Purnick, R. Weiss, and C. Arnold, "Thick film laser induced forward transfer for deposition of thermally and mechanically sensitive materials," Appl. Phys. Lett. **91**, 171120 (2007).
35. D. Banks, K. Kaur, R. Gazia, R. Fardel, M. Nagel, T. Lippert, and R. Eason, "Triazene photopolymer dynamic release layer-assisted femtosecond laser-induced forward transfer with an active carrier substrate," Europhys. Lett. **83**, 38003 (2008).
36. M. Nagel, R. Hany, T. Lippert, M. Molberg, F. Nuesch, and D. Rentsch, "Aryltriazene photopolymers for uv-laser applications: Improved synthesis and photodecomposition study," Macromol. Chem. Phys. **208**, 277–286 (2007).
37. F. Dill, "Optical lithography," IEEE Trans. Electron Devices **ED-22**, 440–444 (1975).
38. C. Mack, "Analytical expression for the standing wave intensity in photoresist," Appl. Opt. **25**, 1958–1961 (1986).
39. J. Bonse, J. Solis, L. Urech, T. Lippert, and A. Wokaun, "Femtosecond and nanosecond laser damage thresholds of doped and undoped triazenepolymer thin films," Appl. Surf. Sci. **253**, 7787–7791 (2007).

Appl Phys A (2010) 101: 333–338
DOI 10.1007/s00339-010-5827-5

Applied Physics A
Materials Science & Processing

Laser-induced-forward-transfer: a rapid prototyping tool for fabrication of photonic devices

C.L. Sones · K.S. Kaur · P. Ganguly · D.P. Banks · Y.J. Ying · R.W. Eason · S. Mailis

Received: 4 November 2009 / Accepted: 10 May 2010 / Published online: 17 June 2010

Abstract We propose a rapid prototyping method for the fabrication of optical waveguides based on the direct laser-printing method of ultrafast Laser-Induced Forward Transfer (LIFT) followed by further processing. The method was implemented for the fabrication of titanium in-diffused lithium niobate channel waveguides and X-couplers by LIFT-depositing titanium metal followed by diffusion. Propagation loss as low as 0.8 dB/cm was measured in preliminary experiments.

1 Introduction

A popular method for the fabrication of optical waveguide circuits in materials such as lithium niobate (LN) is by spatially selective deposition of titanium metal followed by thermal diffusion. This fabrication method is ideally compatible with current wafer-scale parallel techniques used by the microelectronics industry, such as photolithographic patterning and lift-off, which is of course excellent for mass production of devices.

However, these parallel techniques are somewhat inflexible in the device development stage where a fast production turnover of fundamentally different devices is required for conceptual testing. This creates a niche for simple prototyping production methods which are flexible enough to allow for rapid fabrication of good quality devices, particularly at the experimental one-off level.

LIFT is a rapid prototyping method which was first proposed by Bohandy et al. [1] and has since been utilized for the deposition of a variety of metals, semiconductors, superconductors, dielectrics, and biomaterials on a wide range of substrates [2–5]. The simple, non-stringent laboratory-environment based operational conditions for LIFT together with its single-step pattern-definition and material-transfer ability offer some significant experimental advantages inherently available by its usage. Additionally, this approach has some unique capabilities such as patterning of non-planar substrates [6], 3-d printing or stacking of dissimilar materials [7], and even the possibility of transfer of single-crystal materials with desired orientations. However, the pulsed nature and the quality of LIFT deposition are inhibiting factors for the direct deposition of superior quality waveguide layers.

In this paper, we propose the use of LIFT for the spatially selective deposition of materials onto optical substrates which can produce optical waveguides by further processing, e.g. thermal diffusion. Such a method will combine the flexibility of direct waveguide writing methods, which are suitable for rapid prototyping, with the large refractive index, longevity, and low propagation loss which is associated with conventional waveguide fabrication methods such as metal diffusion.

The use of a pulsed deposition method such as LIFT allows for further control over the optical waveguide structure by enabling the fabrication of higher refractive index segments the spatial distribution of which determines the average refractive index along the optical waveguide. By varying the spatial distribution of the segments (i.e. the separa-

C.L. Sones · K.S. Kaur · D.P. Banks · Y.J. Ying · R.W. Eason · S. Mailis (✉)
Optoelectronics Research Centre, University of Southampton, Southampton, SO17 1BJ, UK
e-mail: sm@orc.soton.ac.uk
Fax: +44-23-80593141

P. Ganguly
Advanced Technology Development Centre, Indian Institute of Technology, Kharagpur, 721302, India

tion between adjacent segments), it is possible to change the average refractive index along the optical waveguide. The impact of the segmentation on the waveguide propagation is demonstrated in some of the experimental results which are presented here.

Other advantages of this method include the ability to deposit more than one material or composite materials during a single deposition session and also the deposition of diffusion sources on non-planar (for example already microstructured) surfaces for the fabrication of rib waveguides which is challenging for conventional photolithographic methods.

Herein, we present our preliminary, proof-of-principle, results which demonstrate the feasibility of using a LIFT based material printing methodology in conjunction with high temperature post-processing for rapid prototyping of Ti-indiffused waveguides in LN [8, 9]. LN has a distinctive combination of inherent physical properties and is used in a diverse range of applications [10] and has consequently been the work-horse of the optoelectronics industry for switching applications and nonlinear frequency generation.

2 Experiments and results

The first step for the fabrication of channel optical waveguides in LN requires the spatially selective deposition of titanium metal onto LN substrates using ultrafast LIFT. The carrier-donor-substrate complex rests on a set of 2D translation stage and can be scanned with respect to the focussed or de-magnified incident beam. As illustrated in the schematic shown in Fig. 1, the transfer of the donor material (in this case Ti) onto the substrate, referred to as the receiver, is achieved on a pixel-by-pixel basis by scanning the donor-receiver assembly in front of a focussed pulsed laser source, resulting in a dot-matrix-like printing of individual donor-material pixels that are detached from the carrier and printed on the receiver. In the case for Ti printing here, melting of the donor occurs and a molten droplet is ejected onto the receiver. The dimension of the deposited droplet is similar to the dimensions of the incident laser spot. The melting and super-heating of the metal vapour trapped between the carrier and the donor film provides the required driving force to forward transfer the rest of the donor material, within the interaction volume, onto the receiver substrate. The laser system used to transfer the Ti-metal deposits was a fs laser operating at 800 nm, with a pulse duration of 130 fs and a repetition rate that could be tuned from single shot to 1 kHz. It is however, the high repetition rate of this laser source rather than the pulse width that made it suitable for the demonstration of this rapid prototyping method. The titanium donor film with a thickness of ∼150 nm had been previously deposited onto a transparent (borosilicate glass) carrier substrate via e-beam evaporation.

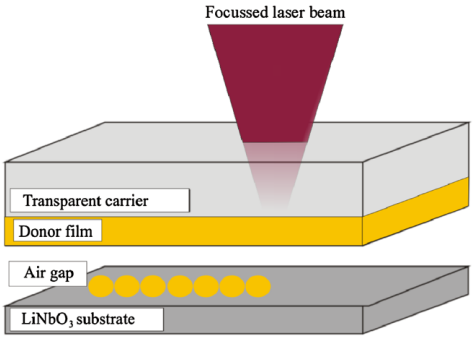

Fig. 1 Schematic of the LIFT deposition process. The carrier-donor-substrate complex rests on a set of 2D translation stage and can be scanned with respect to the focussed or de-magnified incident beam

Ti-metal line patterns were printed on the $-z$ faces of congruent undoped z-cut LN samples along the crystallographic y-directions. Several linear arrays of Ti metal pixels were deposited using different conditions for the intensity (or fluence) of the incident laser pulse and the separation between the centre of adjacent pixels which could be controlled by adjusting either the laser repetition rate or the scan speed. The separation of the centres of adjacent pixels varied from 5 μm (overlapping) to 20 μm (completely separated) while the laser fluence at the carrier/donor interface was in the range of 0.4–1.2 J/cm^2.

The deposited metal pixels were approximately circular in shape and had a diameter of ∼10–15 μm. The holes which were created by missing metal on the carrier substrate (which correspond to the illuminating spot size) matched the size of the deposited metal dots as expected for deposits of this size. The distance between the donor-carrier composite and the receiver was maintained at less than 1 μm.

These variations of the writing parameters were aimed at identifying the optimum conditions for LIFT of Ti-metal onto the LN substrates under the reasonable assumption that there is a direct relationship between the metal deposition characteristics and the final optical waveguide mode profiles following the in-diffusion step. The metal line-patterns were successively in-diffused into the LN substrates by heating the LN substrates to a temperature of 1050°C in an O_2 environment for 10 hours.

A typical example of the deposited linear arrays of titanium pixels is shown in the optical microscope image of Fig. 2(a). The separation of the adjacent metal deposits in Fig. 2(a) has been varied from a slight overlap (top line) to complete separation (bottom line) by changing the scanning speed. The same area of the sample after the diffusion process is shown in the optical microscope image of

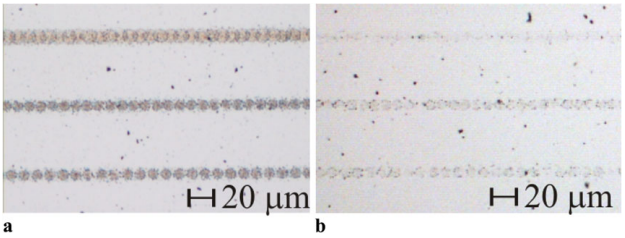

Fig. 2 (**a**) Optical microscope image of linear pixelated titanium LIFT-deposits at different separations. (**b**) The same surface of the sample after diffusion has taken place

Fig. 2(b). The outline of the deposited metal is still visible after diffusion due to the presence of TiO_2 residue on the surface of the sample. Note that the TiO_2 residue is not the same for all deposited lines. The top line showed significantly less residue possibly because the overlap between adjacent deposited metal pixels resulted in a partial re-ablation process for each subsequent laser pulse which removed metal from the sample surface thus reducing the available diffusion source.

The in-diffused LN substrates were subsequently edge-polished perpendicular to the titanium lines to enable characterization of the optical waveguides produced. For this purpose, laser radiation was coupled through one of the end-polished edges using a microscope objective into the waveguides and the near-field mode profile was monitored by imaging the opposite polished end of the waveguide onto a CCD camera.

The main feature of the optical waveguides which were fabricated by LIFT deposition is that the refractive index change along the length of the waveguide is not regular and continuous: there is a local refractive index increase within the volume where titanium metal has been diffused. Hence, the refractive index profile along the channel waveguide should reflect, to some extent, the titanium deposition pattern.

The separation of the adjacent pixels or segments should in principle define the average refractive index value along the waveguide. Hence, different separations should result in different waveguide confinement characteristics, and thereby different mode sizes. This was verified by the optical mode profile characterization results. The mode profiles for two distinct waveguides which correspond to different separation of the titanium segments are shown in Fig. 3. Both waveguides were single moded at the probe wavelength of 1.532 μm however, as shown in Fig. 3, the mode size of the waveguides varies significantly.

These waveguides were fabricated by scanning the sample at rates of 9 mm/sec and 19 mm/sec which corresponds to segment separation of 9 μm (and hence a slight overlap) and 19 μm (full separation), respectively (the laser repetition rate was 1 kHz in this experiment). Hence, the average refractive index change for the more closely spaced depositions, results in tighter confinement as observed in the

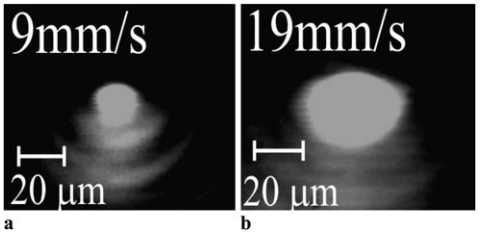

Fig. 3 Near-field waveguide mode profiles (at 1.532 μm) of LIFT/diffused segmented Ti:LN waveguides corresponding to different segment separation; (**a**) overlapped segments, (**b**) separated segments

mode profile shown in Fig. 3(a) while the less dense deposition results in a much larger waveguide mode profile shown in Fig. 3(b). In the case of waveguides with a partial overlap between successively deposited adjacent segments, any possible re-ablation of the deposited Ti-metal segments would reduce the total amount of the deposited metal in the overlapping area. However, our experimental results suggest that, for the range of overlaps used, it is the segment separation that predominantly determines the mode profile of the resulting waveguide, hence if any re-ablation does occur, it has negligible effect on the guiding conditions.

It was mentioned in the previous paragraph that there should be some correlation between the refractive index profile along the channel waveguide and the titanium deposition pattern. In reality, the diffusion process will distribute titanium over an area which is (for Ti in LN) roughly 10% larger than the deposited pixel area and this process will smooth out any sharp features contained in the original deposited metal spot. As a result, the diffused profile will be much smoother than the deposited pattern which is beneficial to the waveguide performance because the elimination of sharp features is expected to keep the scattering losses of the waveguides at low level.

The optical loss of the waveguides was estimated by two different methods which were (i) cut-back and (ii) Fabry–Perot. Cut-back [11], which involves repetitive measurement of throughput for progressively shorter channel lengths, is clearly a destructive, time consuming method,

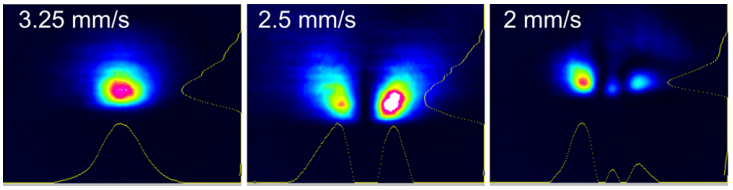

Fig. 4 Near-field mode profiles (at 633 nm) of three different waveguides fabricated with different segment separation by changing the deposition scanning speed as indicated in the figure

and is therefore of limited utility for measurement of waveguide loss. The second method relies on the formation of a low finesse Fabry–Perot cavity between opposite end faces of the waveguide. The contrast of the fringes of this optical cavity gives an estimate of the upper limit of the optical loss [12].

Both methods confirmed that large segment separations resulted in increased optical loss mainly due to poor confinement of the light inside the waveguide. The lowest propagation loss of ∼0.8 dB/cm (for TM modes in the telecommunication wavelength range) was measured for waveguides written with a segment separation of 11 μm. For waveguides having larger segment separations of ≥13 μm, the measured loss was much higher (∼7 dB/cm) due to optical leakage of the guided wave to the substrate. However, even for these preliminary attempts, with deposition quality being far from optimal, a loss measurement as low as ∼0.8 dB/cm measured for some of the waveguides is very encouraging, further confirming the potential of this method for rapid prototyping of good quality optical waveguide devices. Typical loss values reported in literature for Ti-indiffused waveguides are of order ∼0.1 dB/cm.

In order to evaluate the effective refractive index as a function of the fabrication conditions, it is necessary to fabricate single mode waveguides with different mode sizes. By monitoring the waveguide mode profile, it is possible to calculate the mode index of the waveguide [13]. We chose to fabricate the waveguides to be single moded at the wavelength of 633 nm in order to benefit from the measuring accuracy of our optical beam profiler (which has a silicon detector that is not sensitive to telecom wavelengths). The titanium donor layer used for the LIFT depositions was 150 nm thick, the laser repetition rate was 250 Hz and the laser fluence was in the range of 0.4 to 0.8 J/cm^2 while the segment separation varied between 8 μm and 16 μm.

Once again by varying the writing speed, it was possible to control the waveguide mode profile. Figure 4 shows three different mode profiles which correspond to different segment separation as a result of different scanning speeds during deposition. As can be seen in Fig. 4, the mode changed from single to higher order by just changing the scanning speed from 3.25 mm/sec to 2 mm/sec, which corresponds to segment separations of 13 μm and 8 μm, respectively (at 250 Hz laser repetition rate). This result reiterates the versatility of LIFT in the creation of waveguides with predesigned modal profiles.

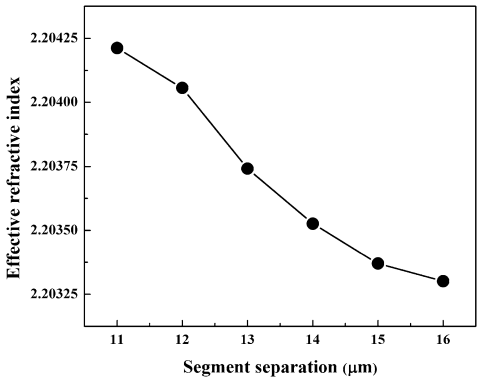

Fig. 5 Calculated effective refractive indices of single mode waveguides as a function of segment separation. These effective indices correspond to TM modes

The intensity profiles of the single mode waveguides (at 633 nm) which were fabricated using the conditions described in the previous section were used for the calculation of the effective mode profiles of the corresponding waveguides using the method which is described in [13]. A plot of the calculated effective mode indices (for TM modes) as a function of the segment separation is shown in Fig. 5. For segment separations longer than 16 μm, there was no confinement of light (cut-off) while for separation less than 11 μm the waveguides become multi-moded.

However, it seems that there is a good scope for manipulation of the effective mode index within the segment separation range that corresponds to single mode waveguides as shown in Fig. 5.

As expected the effective mode index decreases with increasing segment separation, as the average refractive index along the waveguide decreases, until cut-off is reached for a separation of 16 μm.

One of the advantages of using a method such as the one described here is the possibility of changing the waveguide propagation characteristics along the length of the waveguide by simply manipulating the segment separation along the length. However, with our current setup, it

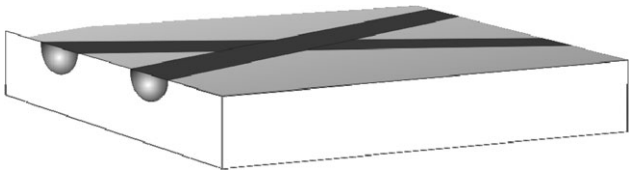

Fig. 6 Schematic of an X-coupler

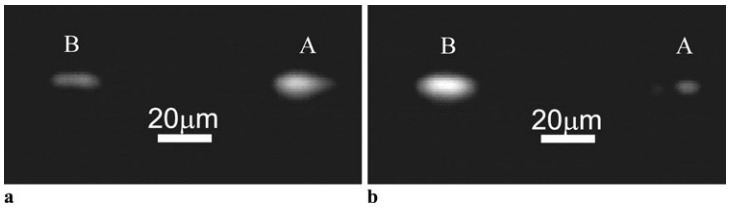

Fig. 7 Near-field intensity profiles of the X-coupler output

was not possible to demonstrate this capability during these initial experiments.

In order to demonstrate the device fabrication functionality of our rapid prototyping method, we chose to fabricate an X-coupler which consists of two straight waveguide channels crossing each other at a specific angle [14].

The waveguides that constitute the X-coupler, a schematic of which is shown in Fig. 6, were fabricated by LIFT depositing titanium metal with an incident laser fluence of 1 J/cm^2 at a writing speed of 2.5 mm/s which, for a laser repetition rate of 250 Hz, corresponds to segment separation of 10 μm. The angle between the two crossing waveguides was kept at a small value (2°) to maximize their overlap.

The coupling ratio was measured at telecom wavelengths (1.55 μm) by coupling light into one of the channels and measuring the power output of each channel on the opposite edge. The coupling ratio (for TM modes) was measured to be ∼0.2.

The output edge of the X-coupler was imaged onto an infrared camera and the images are shown in Fig. 7. Figures 7(a) and (b) show the device output when launching light into waveguide A (Fig. 7(a)) and waveguide B (Fig. 7(b)), respectively, as indicated in the mode images. Note that the mode profiles of A and B are not identical indicating an asymmetry in the fabrication of the constituent waveguides. This asymmetry was confirmed by investigation of the waveguides under an optical microscope and was attributed to a slight accidental misalignment of the LIFT apparatus during the deposition process.

3 Conclusions

We have proposed a method for the rapid prototyping of optical waveguide devices which is based on LIFT deposition followed by post processing and have demonstrated the utility of the method by fabricating good quality titanium in-diffused segmented channel waveguides and X-couplers in ferroelectric LN crystals. The preliminary results are encouraging and opens up a route for exploitation of this fabrication process not only as a rapid prototyping tool but also as a waveguide fabrication method to assist in situations where the waveguide propagation constant should change along the waveguide length, repair, or trim existing waveguides by co-doping, deposit overlayers for fine trimming of the waveguide mode, etc. Additionally, the inherent capability of the method to produce segmented waveguides can be used for the fabrication of long period gratings or even for quasi-phasematching of non-linear processes in waveguides by periodic variation of the propagation constant.

Other possibilities include the single-step multi-layer donor deposition process to produce, rare-earth (e.g. Er, Yb, and Nd) doped waveguide structures for optical amplifiers and lasers, and finally the selective deposition and subsequent waveguide fabrication on non-planar or microstructured surfaces which is normally challenging or impossible by conventional methods.

Acknowledgements We gratefully acknowledge the Royal Society for the International Fellowship of Dr. P. Ganguly (No. IIF-2007/R2), the Engineering and Physical Sciences Research Council (EPSRC) for the research funding under grant number EP/C515668, and the financial support of the European Union for funding under the STREP "3-D DEMO".

References

1. J. Bohandy, B.F. Kim, F.J. Adrian, J. Appl. Phys. **60**, 1538–1539 (1986)
2. D.P. Banks, C. Grivas, J.D. Mills, R.W. Eason, I. Zergioti, Appl. Phys. Lett. **89** (2006)
3. D.P. Banks, C. Grivas, I. Zergioti, R.W. Eason, Opt. Express **16**, 3249–3254 (2008)

4. A. Pique, D.B. Chrisey, R.C.Y. Auyeung, J. Fitz-Gerald, H.D. Wu, R.A. McGill, S. Lakeou, P.K. Wu, V. Nguyen, M. Duignan, Appl. Phys. A **69**, S279–S284 (1999)
5. W.A. Tolbert, I.Y.S. Lee, M.M. Doxtader, E.W. Ellis, D.D. Dlott, J. Imaging Sci. Technol. **37**, 411–422 (1993)
6. S. Mailis, I. Zergioti, G. Koundourakis, A. Ikiades, A. Patentalaki, P. Papakonstantinou, N.A. Vainos, C. Fotakis, Appl. Opt. **38**, 2301–2308 (1999)
7. R. Fardel, M. Nagel, F. Nuesch, T. Lippert, A. Wokaun, Appl. Phys. Lett. **91**, 3 (2007)
8. R.C. Alferness, L.L. Buhl, Opt. Lett. **5**, 473–475 (1980)
9. D. Hofmann, G. Schreiber, C. Haase, H. Herrmann, W. Grundkotter, R. Ricken, W. Sohler, Opt. Lett. **24**, 896–898 (1999)
10. R.S. Weis, T.K. Gaylord, Appl. Phys. A **37**, 191–203 (1985)
11. R.G. Hunsperger, *Integrated Optics: Theory and Technology* (Springer, New York, 1982)
12. R. Regener, W. Sohler, Appl. Phys. B **36**, 143–147 (1985)
13. P. Ganguly, C.L. Sones, Y.J. Ying, H. Steigerwald, K. Buse, E. Soergel, R.W. Eason, S. Mailis, J. Light Technol. **27**, 3490–3497 (2009)
14. H. Nakajima, T. Horimatsu, M. Seino, I. Sawaki, IEEE J. Quantum Electron. **18**, 771–776 (1982)

Applied Surface Science 257 (2011) 6650–6653

Contents lists available at ScienceDirect

Applied Surface Science

journal homepage: www.elsevier.com/locate/apsusc

Laser-induced forward transfer of focussed ion beam pre-machined donors

K.S. Kaur[a,*], M. Feinaeugle[a], D.P. Banks[a], J.Y. Ou[a], F. Di Pietrantonio[b], E. Verona[b], C.L. Sones[a], R.W. Eason[a]

[a] Optoelectronics Research Centre, University of Southampton, Southampton SO17 1BJ, UK
[b] Institute of Acoustics and Sensors, CNR 100 00133 Rome, Italy

ARTICLE INFO

Article history:
Received 5 January 2011
Received in revised form 21 February 2011
Accepted 22 February 2011
Available online 26 February 2011

Keywords:
Laser induced forward transfer (LIFT)
Focussed ion beam (FIB)
ZnO
DRL

ABSTRACT

In this paper we report femtosecond laser-induced forward transfer (LIFT) of pre-machined donor films. 1 μm thick zinc oxide (ZnO) films were first machined using the focussed ion beam (FIB) technique up to a depth of 0.8 μm. Debris-free micro-pellets of ZnO with extremely smooth edges and surface uniformity were subsequently printed from these pre-machined donors using LIFT. Printing results of non-machined ZnO donor films and films deposited on top of a polymer dynamic release layer (DRL) are also presented for comparison, indicating the superior quality of transfer achievable and utility of this pre-machining technique.

1. Introduction

Laser induced forward transfer (LIFT) is a versatile direct-write method for spatially selective printing of a wide range of materials [1–3]. In the conventional LIFT technique a thin film (usually of thickness <1 μm) of the material (the *donor*) to be printed is deposited on top of a substrate (the *carrier*) which is transparent to the incident laser wavelength. A laser pulse is then focussed/imaged onto the carrier–donor interface which induces the necessary impulsive force to push the donor onto a substrate placed nearby (the *receiver*) either by melting it (for the case of a sufficiently thin donor) [4,5] or ablating the top layer (the thick donor case) [6]. The complete melting or disintegration of the donor material during the transfer process is clearly a major drawback especially when printing is required of materials in solid and intact form (e.g. single crystals), oriented films, single domain or other pre-structured donors.

One technique that has met with considerable success to mitigate the above mentioned problems of damage to the donor layer is dynamic release layer (DRL)-LIFT. In DRL-LIFT a sacrificial layer called the dynamic release layer is introduced between the carrier and the donor film to avoid direct exposure of the donor to the incident laser. This DRL can be a metal [7,8] or a polymer film [9,10], a light-to-heat conversion layer as in laser induced thermal imaging (LITI) [11] or a specially engineered nanomaterial layer as in nanomaterial enabled laser transfer (NELT) [12]. These complementary LIFT methods have demonstrated the transfer of biomaterials [8,10], conductive polymers [11], OLED pixels [9,12] ceramics [13] and semiconductor bare dies [14]. Recently printing of SiO_x was also reported by coating the receiver film directly onto the donor to reduce the debris associated with the deposits [15]. However these techniques do not eliminate one of the basic problems in LIFT printing, namely the inevitable shearing or ripping of the donor film at the boundary of the illuminated region, which may present an unacceptable limitation to the use of LIFT where edge quality is of prime importance, for example where multilayer donors are used. Spatially shaped multiple pulses to define weakened regions into the donor film before printing have been used to reduce this problem in another complementary LIFT technique called ballistic laser-assisted solid transfer (BLAST) [16]. Complete micro-dissection of biological samples prior to transfer to avoid contamination has also been reported in the literature [17].

In this paper we introduce a new variant to the LIFT technique that allows debris-free printing of solid donors in an intact form without using any DRL. The critical step is to pre-machine the donor using, in our case, focussed ion beam (FIB) machining to encourage separation and transfer of predetermined shapes in intact and solid form. It is not necessary to machine throughout the entire depth of the donor however as this would prevent the laser-induced pressure build-up behind the material intended for transfer. For the optimum depth of pre-machining into the donor, uniform and clean deposits are printed onto the receiver. This technique should also significantly extend the thickness limitation for donor layers to beyond the current ~μm level: with a maximum value of ~1 μm

* Corresponding author. Tel.: +44 2380 59 29091.
E-mail address: kak@orc.soton.ac.uk (K.S. Kaur).

0169-4332/$ – see front matter © 2011 Elsevier B.V. All rights reserved.
doi:10.1016/j.apsusc.2011.02.094

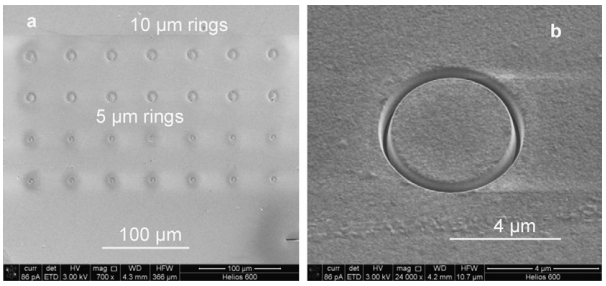

Fig. 1. (a) SEM images of the FIBbed ring patterns of 10 μm (top two rows) and 5 μm (bottom two rows) diameters in 1 μm thick ZnO donor film. (b) The magnified SEM image of one of the machined 5 μm rings.

being reported to date using a triazene polymer (TP) DRL [18]. Zinc oxide (ZnO), an environmental-friendly lead free piezoelectric was chosen as the trial donor material for these LIFT experiments, and we report our first results below.

2. Experiments and results

The donor samples were prepared by sputtering 1 μm thick films of ZnO on top of quartz substrates (the *carrier*) at a pressure of 3 mTorr and a temperature of 200 °C. FIB machining was used to etch circular features into 1 μm thick sputtered donor films up to a depth of 0.8 μm with 5 μm and 10 μm diameters and centre-to-centre separation of 50 μm. We defined a parameter 'Δ' to quantify the fractional etched depth for the donor:

$$\Delta = \frac{\text{milled depth}}{\text{donor thickness}} \quad (1)$$

The Δ value chosen for our trial demonstration of this FIB pre-patterning technique was 0.8. It took ~80 s to machine each ring at a current value of 2.8 nA with a dosage of 2.81 nC/μm^2 per ring. These first samples were machined using Ga^+ ions only without the use of any gas for enhanced etching. If halogen containing gases were used, then the rate of etching can be increased considerably, reducing the pre-machining time to perhaps tens of seconds per ring. The value of 0.8 for Δ was chosen based on the requirement to mill away a substantial amount of material, without going to the extremes of $\Delta = 1$. A previous trial had been carried out on other donors that included metals such as Au and Cr, and Δ values exceeding 1.0 (i.e. FIB machining through the donor and into the carrier itself) had been tried on the basis that machining away the entire thickness would be the best strategy to ensure easy detachment [19]. Values for $\Delta \geq 1.0$ however mean that any explosive propulsion force generated from LIFT is no longer constrained at the donor/carrier interface, and the propulsion force can leak around the milled slot. For this reason we chose a trial value of 0.8, which was felt to represent a reasonable compromise between removing too much material, and not removing sufficient, so that debris would still present possible problems.

In any future work, optimising the Δ value for a particular donor material would be an important step, as smaller values of Δ require less time for FIB machining. As it stands, the 80 s per feature is still a fairly long time. However, as will be seen later, this does result in side-walls for the LIFTed pellet that are extremely smooth, and for certain applications, where printing of a limited number of pellets is required, in a debris-free manner, this time may not be considered particularly restrictive. Fig. 1(a) shows the SEM image of an array of machined ring patterns while Fig. 1(b) shows a magnified image of one of the 5 μm rings.

For comparison 1 μm thick ZnO films on top of TP as a DRL and 1 μm thick ZnO samples without any prior machining were also prepared for LIFTing. For all the experiments a commercial mode-locked Ti:sapphire femtosecond laser was used. Single laser pulses with a Gaussian spatial profile (800 nm, 150 fs, FWHM ~4 mm) were first centred on a 450 μm diameter circular aperture resulting in a reasonably spatially uniform incident pulse profile with spot size of ~12 μm. The beam size was chosen to be bigger than the FIBbed feature sizes (5 μm and 10 μm) for ease of alignment while printing. A highly de-magnified image of the aperture was then relayed onto the carrier–donor interface using a commercial micro-machining workstation (New Wave UP266, USA) thereby printing micro-pellets of ZnO onto silicon (Si) receivers at a donor–receiver separation of 1 μm, using Mylar spacers. All the experiments were performed under a background pressure of 10^{-1} mbar.

Fig. 2(a) shows an optical microscope image of a 1 μm thick ZnO donor film sputtered on top of 360 nm thick TP. About 80–85% of the surface area of the donor films was cracked due to the thermal

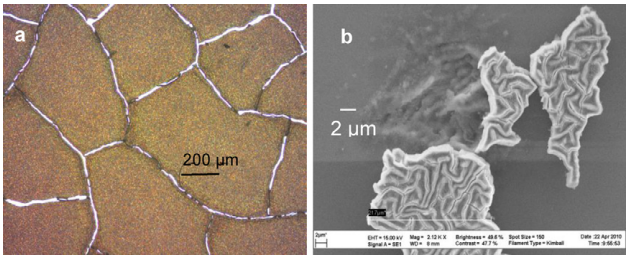

Fig. 2. Optical microscope image of 1 μm thick ZnO donor film deposited on top of 360 nm thick TP (a). SEM image of deposits printed from this donor film (b).

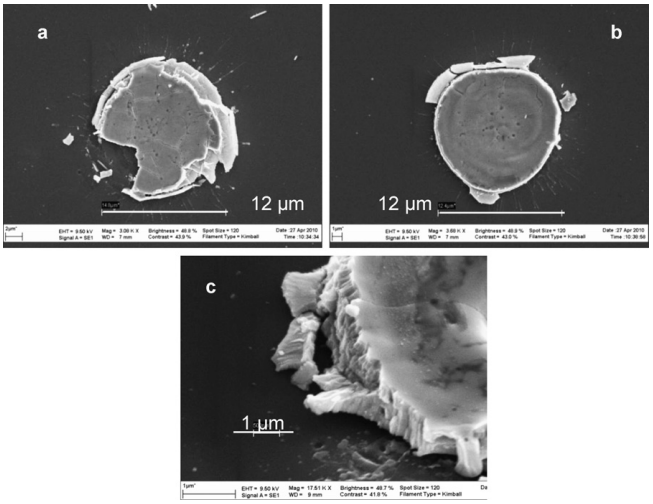

Fig. 3. (a and b) SEM images of 12 μm ZnO pellets printed form a non-machined 1 μm thick donor. The shattering of the pellets during transfer produced non-uniform, irregular shaped and splashy deposits, clearly depicted in the images. (c) The rough edges of the printed deposits.

decomposition of TP while depositing the upper ZnO layer. Fig. 2(b) shows an SEM image of ZnO deposits printed using these films. Cracks were also clearly visible in the LIFTed deposits, and as the film was weaker around the cracks LIFTing preferentially occurred by rupture along the cracks leading to non-circular deposits. The bad quality of the donor films in this case resulted in shattered and irregular shaped pellets. We have also tried to deposit ZnO on TP-coated unheated carriers using other techniques including pulsed laser deposition (PLD). Again however, the quality of the resultant donor was less good than that achieved via sputtering on uncoated carriers. The degradation temperature of TP is of the order of 250 °C, and for thick films (∼μm thicknesses) prolonged exposure in a sputtering chamber can severely degrade the surface integrity. This is another reason why FIB pre-machining can be advantageous as it does not require any DRL use. It should in principle be applicable to print any donor material as the range of donors that can be printed using this technique is not limited by any temperature or chemical sensitivity issues as is the case for DRL-assisted LIFT.

Fig. 3(a) and (b) shows SEM images of typical and the best LIFTed deposits, respectively, of 12 μm diameter ZnO pellets printed from a 1 μm thick donor without any pre-machining, while Fig. 3(c) shows the edge quality of a typical deposit. The deposits were in general splashy, with considerable amounts of debris and with very rough and ill-defined edges and irregular shapes. However, the deposits from a pre-machined donor exhibited extremely good quality both in terms of surface uniformity and edge smoothness. Under the optimum conditions for LIFTing, there was no trace of any residual debris surrounding the transferred pellets. Fig. 4(a) and (b) shows the SEM images of 10 μm and 5 μm ZnO pellets, respectively, printed from a pre-machined donor. Note here that Fig. 4(a) shows the result for LIFTing onto a Si substrate, whereas Fig. 4(b) used a flexible compliant substrate (polystyrene). The adhesion of ZnO to the plastic receiver was not as good as onto Si. So far we have not made any adhesion tests for the printed pellets using this pre-patterning approach, and the use of flexible receivers appears to be non-optimum. Fortuitously however, the pellet LIFTed onto polystyrene has flipped over while dismantling the donor–receiver assembly, allowing SEM examination of the quality of the front surface, and edge quality around the machined rim.

Fig. 5 shows an SEM image of the edge quality of a printed 10 μm ZnO pellet, and this degree of smoothness was routinely seen in all SEM pictures taken. The high edge quality pellets from the pre-machined ZnO donors were transferred at an incident laser fluence

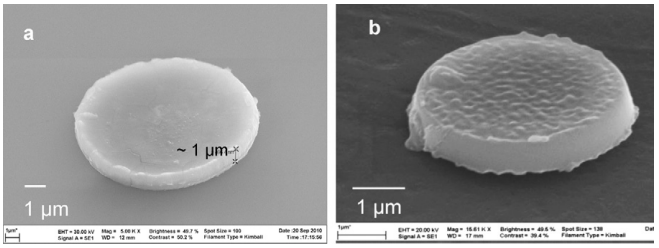

Fig. 4. SEM micrographs of 10 μm (a) and 5 μm (b) ZnO pellets printed onto Si and plastic receiver, respectively, from a pre-machined 1 μm thick donor film.

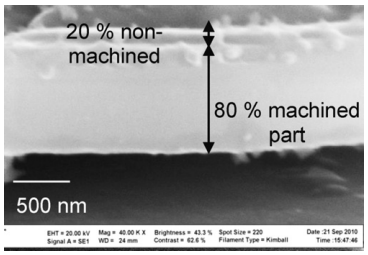

Fig. 5. Magnified SEM image of the extraordinarily smooth edge of one of the deposits printed from the pre-machined ZnO donor.

of ~450 mJ/cm^2 (Fig. 5) which is less than half the value (~1 J/cm^2) used to transfer the shattered and rough edge quality deposits from the non-machined donors (Fig. 3(c)).

The difference in the quality of deposits transferred from donors with and without pre-machining prior to LIFT is clearly seen. For both cases the incident laser pulse provides the required force to overcome the donor–carrier adhesion, but in the case of no prior machining, the donor pellet still has to shear itself from a considerable portion of the surrounding solid donor film, resulting in shattering during transfer, rough edges, irregular shapes and considerable and unavoidable debris. In case of the pre-machined donor, the area to be printed is already defined by FIB patterning which makes the transfer process much gentler. For cases where Δ approaches 1, detachment can occur with minimal (in optimum cases zero) residual debris, and smooth, regular printing can occur.

It should be mentioned that while a Δ value of 0.8 has clearly produced impressive results, without further experimentation or modelling, it is not yet apparent which value produces the optimum level of printing fidelity. It is also likely that this parameter is both donor material and thickness specific. However, the striking difference in the quality of the deposits obtained clearly shows the great potential of this technique for printing thick and fragile donors in solid and intact format. Finally, we also mention that LIFTing of single crystal materials, such as those grown via PLD which usually requires substrate heating to temperatures in excess of ~600 °C to ensure single crystal thin film growth, and hence would be entirely unsuited to TP-DRL techniques, would also be an attractive prospect. FIB pre-machining is an ideal candidate to try here, and experiments are currently under way. We are not aware of any other reports of LIFTing of single crystal PLD-grown thin films, and this may well be a good example where FIB pre-patterning presents a useful, if slightly time-consuming process.

3. Conclusions

Micro-pellets of ZnO of excellent quality with extremely smooth and uniform edges were printed from pre-machined donors. The donor films were machined to a depth of 0.8 μm by the FIB technique prior to LIFT. To the best of our knowledge, this is the first time that materials have been printed using the FIB pre-patterning LIFT technique. The initial results presented here were to validate the proof-of-principle for the technique, and further optimisation studies using donors with different Δ values, different thicknesses and donor materials are currently in progress.

Acknowledgements

Financial support from the Engineering and Physical Sciences Research Council (EPSRC), UK, (under grants no. EP/C515668/1 and EP/G060363/1) and the European community (under grant no. 508581101, e-LIFT) are gratefully acknowledged.

References

[1] J. Bohandy, B.F. Kim, F.J. Adrian, Metal deposition from a supported metal film using an excimer laser, J. Appl. Phys. 60 (1986) 1538.
[2] K.D. Kyrkis, A.A. Andreadaki, D.G. Papazoglou, I. Zergioti, in: J. Perrière, E. Millon, E. Fogarassy (Eds.), Recent Advances in Laser Processing of Materials, Elsevier, Amsterdam, 2006.
[3] A. Pique, D. Chrisey, R. Auyeung, J. Fitz-Gerald, H. Wu, R. McGill, S. Lakeou, P. Wu, V. Nguyen, M. Duignan, A novel laser transfer process for direct writing of electronic and sensor materials, Appl. Phys. A 69 (1999) S279–S284 (Suppl.).
[4] D.P. Banks, C. Grivas, J.D. Mills, R.W. Eason, I. Zergioti, Nanodroplets deposited in microarrays by femtosecond Ti:sapphire laser induced forward transfer, Appl. Phys. Lett. 89 (2006) 193107.
[5] D.A. Willis, V. Grosu, Microdroplet deposition by laser-induced forward transfer, Appl. Phys. Lett. 5713 (2005) 90–96.
[6] I. Zergioti, A. Karaiskou, D. Papazoglou, C. Fotakis, M. Kapsetaki, D. Kafetzopoulos, Time resolved schlieren study of sub-pecosecond and nanosecond laser transfer of biomaterials, Appl. Surf. Sci. 247 (2005) 584–589.
[7] B. Hopp, T. Smausz, Z. Antal, N. Kresz, Z. Bor, D. Chrisey, Absorbing film assisted laser induced forward transfer of fungi (trichoderma conidia), J. Appl. Phys. 96 (6) (2004) 34783481.
[8] P. Serra, M. Colina, J.M. Fernández-Pradas, Preparation of functional DNA microarrays through laser-induced forward transfer, Appl. Phys. Lett. 85 (9) (2004) 1639–1641.
[9] R. Fardel, M. Nagel, F. Nüesch, T. Lippert, A. Wokaun, Fabrication of organic light-emitting diode pixels by laser-assisted forward transfer, Appl. Phys. Lett. 91 (2007) 061103.
[10] N.T. Kattamis, P.E. Purnick, R. Weiss, C.B. Arnold, Thick film laser induced forward transfer for deposition of thermally and mechanically sensitive materials, Appl. Phys. Lett. 91 (2007) 171120.
[11] G.B. Blanchet, J.A. Yueh-Lin Loo, F. Rogers, C.R. Gao, Fincher, Large area, high resolution, dry printing of conducting polymers for organic electronics, Appl. Phys. Lett. 82 (3) (2003) 463–465.
[12] S.H. Ko, Pan, S.G. Ryu, N. Misra, C.P. Grigoropoulos, H.K. Park, Nanomaterial enabled laser transfer for organic light emitting material direct writing, Appl. Phys. Lett. 93 (2008) 151110.
[13] D.P. Banks, K. Kaur, R. Gazia, R. Fardel, M. Nagel, T. Lippert, R.W. Eason, Triazene photopolymer dynamic release layer-assisted femtosecond laser-induced forward transfer with an active carrier substrate, Europhys. Lett. 83 (2008) 38003.
[14] S.A. Mathews, N.A. Chaipar, K. Metkus, A. Piqué, Manufacturing microelectronics using 'lase-and-place, Photon. Spectra 41 (10) (2007) 70–74.
[15] J. Ihlemann, R.W. Schriever, Laser-induced congruent forward transfer of SiO_x-layers, Appl. Phys. A 101 (2010) 483–486.
[16] D.P. Banks, C. Grivas, I. Zergioti, R.W. Eason, Ballistic laser-assisted solid transfer (BLAST) from a thin film precursor, Opt. Exp. 16 (2008) 3249–3254.
[17] K. Schütze, G. Lahr, Identification of expressed genes by laser-mediated manipulation of single cells, Nat. Biotechnol. 16 (8) (1998) 737–742.
[18] K. Kaur, R. Fardel, T.C. May-Smith, M. Nagel, D.P. Banks, C. Grivas, T. Lippert, R.W. Eason, Shadowgraphic studies of triazene assisted laser-induced forward transfer of ceramic thin films, J. Appl. Phys. 105 (2009) 113119.
[19] D.P. Banks, Femtosecond laser induced forward transfer techniques for the deposition of nanoscale, intact, and solid-phase material, University of Southampton, personal communication, (2008).

Waveguide mode filters fabricated using laser-induced forward transfer

K. S. Kaur,[1,*] A. Z. Subramanian,[1] Y. J. Ying,[1] D. P. Banks,[1] M. Feinaeugle,[1] P. Horak,[1] V. Apostolopoulos,[2] C. L. Sones,[1] S. Mailis,[1] and R. W. Eason[1]

[1]*Optoelectronics Research Centre, University of Southampton, Southampton SO17 1BJ, UK*
[2]*School of Physics and Astronomy, University of Southampton, Southampton SO17 1BJ, UK*
**kak@orc.soton.ac.uk*

Abstract: Titanium (Ti)-in-diffused lithium niobate waveguide mode filters fabricated using laser-induced forward transfer followed by thermal diffusion are presented. The mode control was achieved by adjusting the separation between adjacent Ti segments thus varying the average value of the refractive index along the length of the in-diffused channel waveguides. The fabrication details, loss measurements and near-field optical characterization of the mode filters are presented. Modeling results regarding the device performance are also discussed.

OCIS codes: (140.3390) Laser materials processing; (140.7090) Ultrafast lasers; (230.7370) Waveguides: laser-induced forward transfer.

References and links

1. R. S. Weis and T. K. Gaylord, "Lithium niobate: summary of physical properties and crystal structure," Appl. Phys., A Mater. Sci. Process. **37**(4), 191–203 (1985).
2. R. C. Alferness and L. L. Buhl, "Electro-optic waveguide TE–TM mode converter with low drive voltage," Opt. Lett. **5**(11), 473–475 (1980).
3. D. Hofmann, G. Schreiber, C. Haase, H. Herrmann, W. Grundkötter, R. Ricken, and W. Sohler, "Quasi-phase-matched difference-frequency generation in periodically poled Ti:$LiNbO_3$ channel waveguides," Opt. Lett. **24**(13), 896–898 (1999).
4. C. L. Sones, K. S. Kaur, P. Ganguly, D. P. Banks, Y. J. Ying, R. W. Eason, and S. Mailis, "Laser-Induced-Forward-Transfer: A rapid prototyping tool for fabrication of photonic devices," Appl. Phys., A Mater. Sci. Process. **101**(2), 333–338 (2010).
5. J. Bohandy, B. F. Kim, and F. J. Adrian, "Metal deposition from a supported metal film using an excimer laser," J. Appl. Phys. **60**(4), 1538–1539 (1986).
6. K. D. Kyrkis, A. A. Andreadaki, D. G. Papazoglou, and I. Zergioti, *Recent Advances in Laser Processing of Materials*, J. Perrière, E. Millon, and E. Fogarassy, eds. (Elsevier, 2006), p. 213.
7. D. P. Banks, C. Grivas, J. D. Mills, R. W. Eason, and I. Zergioti, "Nanodroplets deposited in microarrays by femtosecond ti:sapphire laser induced forward transfer," Appl. Phys. Lett. **89**(19), 193107 (2006).
8. S. Mailis, I. Zergioti, G. Koundourakis, A. Ikiades, A. Patentalaki, P. Papakonstantinou, N. A. Vainos, and C. Fotakis, "Etching and printing of diffractive optical microstructures by a femtosecond excimer laser," Appl. Opt. **38**(11), 2301–2308 (1999).
9. A. Piqué, D. Chrisey, R. Auyeung, J. Fitz-Gerald, H. Wu, R. McGill, S. Lakeou, P. Wu, V. Nguyen, and M. Duignan, "A novel laser transfer process for direct writing of electronic and sensor materials," Appl. Phys., A Mater. Sci. Process. **69**(Suppl.), S279–S284 (1999).
10. K. Kaur, R. Fardel, T. C. May-Smith, M. Nagel, D. P. Banks, C. Grivas, T. Lippert, and R. W. Eason, "Shadowgraphic studies of triazene assisted laser-induced forward transfer of ceramic thin films," J. Appl. Phys. **105**(11), 113119 (2009).
11. I. Zergioti, A. Karaiskou, D. Papazoglou, C. Fotakis, M. Kapsetaki, and D. Kafetzopoulos, "Time resolved schlieren study of sub-picosecond and nanosecond laser transfer of biomaterials," Appl. Surf. Sci. **247**(1-4), 584–589 (2005).
12. G. Tittelbach, B. Richter, and W. Karthe, "Comparison of three transmission methods for integrated optical waveguide propagation loss measurement," Pure Appl. Opt. **2**(6), 683–700 (1993).
13. D. Castaldini, P. Bassi, P. Aschieri, S. Tascu, M. De Micheli, and P. A. Baldi, "High performance mode adapters based on segmented SPE:$LiNbO_3$ waveguides," Opt. Express **17**(20), 17868–17873 (2009).
14. S. Fouchet, A. Carenco, C. Daguet, R. Guglielmi, and L. Riviere, "Wavelength dispersion of Ti induced refractive index change in $LiNbO_3$ as a function of diffusion parameters," J. Lightwave Technol. **5**(5), 700–708 (1987).

1. Introduction

Lithium Niobate (LN) is a very important optical material which is widely used by the photonics industry mainly due to its excellent electro/acousto-optical properties [1]. Channel waveguides, which are at the heart of any photonics circuit, are fabricated in LN by doping it with titanium (Ti) metal using the in-diffusion technique where Ti is locally deposited on a LN substrate using photolithography and lift off methods followed by thermal treatments [2,3]. This method is suitable for mass production of devices and is compatible with the wafer-scale parallel techniques used in the microelectronics industry. However, for cases that require rapid prototyping of devices more flexible and faster techniques are needed.

In our recent work the laser-induced forward transfer (LIFT) technique was used to deposit segmented Ti metal lines onto LN substrates which produced low loss optical waveguides after thermal diffusion [4]. LIFT is a direct-write technique first demonstrated by Bohandy et al [5,6] for depositing metals to repair damaged photomasks. Due to its simplicity and flexibility its use was quickly extended to print a variety of metals, semiconductors, dielectrics, ceramics and biomaterials [7–11]. This new approach offers both the flexibility, less stringent experimental conditions and rapid prototyping associated with LIFT, and the large refractive index change, low optical loss and stability of the waveguides associated with the thermal diffusion method. Additionally, printing of multiple diffusion sources in a single shot, from specifically tailored donors and deposition on non-planar substrates are the other advantages offered by this technique. In this paper, we present results of fabrication and optical characterisation of index-tapered waveguides produced by this method by adjusting the density of adjacent titanium segments during the LIFT process that defines the average refractive index which light experiences in different sections of the waveguide. We demonstrate here the use of such a refractive index tapered waveguide as a mode filter thereby taking this technique into a new realm of fabricating custom-made complex refractive index profiles and photonic devices.

2. Experiments

The fabrication of tapered waveguides using LIFT was a two-step process. Firstly, a linear arrangement of Ti metal segments was printed on top of LN substrates using the LIFT technique as shown in Fig. 1. The LIFT samples were prepared by depositing thin films (~150 nm) of Ti (the *donor*) on top of transparent glass substrates (the *carrier*) by e-beam evaporation. Femtosecond pulses with a Gaussian spatial profile from a mode-locked Ti: sapphire laser (800 nm, 150 fs, FWHM ~4 mm) were centred on a 450 µm diameter circular aperture resulting in a reasonably spatially uniform incident pulse profile. A highly de-magnified image of the aperture was then relayed onto the *carrier-donor* interface using a commercial micromachining workstation (New Wave UP266, USA) thereby printing circular Ti discs of diameter ~10 µm (comparable to the incident laser spot size) onto a congruent undoped z-cut LN substrate on the –z face along the crystallographic y-direction. The separation between the carrier and the donor was maintained at ~1 µm separation using a Mylar spacer. The donor-receiver assembly was mounted on a 3-axis precision (10 nm resolution), fast (max. speed ~250 mm/s) computer-controlled translation stage to allow the *carrier-donor* complex to be scanned in front of the incoming laser pulses. All experiments were performed under a background pressure of 10^{-1} mbar. Single laser pulses were used to print each Ti dot and the laser was operated at 250 Hz. The laser threshold fluence for transfer of Ti discs was ~0.4 J/cm^2. The separation between two adjacent Ti dots was controlled by varying the scan speed of the translation stages. After printing, the deposited metal lines were diffused into the LN crystal by heating it to 1050°C in an oxygen atmosphere for 10 hours.

Index tapered waveguides were produced by varying the writing speed along the segmented Ti lines at a constant acceleration. The reason for writing lines at constant acceleration was to avoid sudden changes in the final refractive index profiles to minimize losses and obtain a smooth mode filter effect from the tapered waveguides. The idea behind this technique is to have the ability to alter the behaviour of the waveguides just by

manipulating the scan speed and hence the segment separation along the length of the waveguides. The amount of material deposited and then diffused per unit length decreases with increasing scan speed, which in turn decreases the average effective index of the mode. The mode confinement should therefore decrease with increasing speed and the waveguide modal behavior should change from multi-mode to single-mode. By increasing the segment separation and hence decreasing the index contrast along the waveguide a mode filter can be produced that allows only the fundamental mode to propagate. In the present set of experiments three different values of constant acceleration of 0.3, 0.4 and 0.5 mm/s^2 were used for fabricating the tapered waveguides. The initial velocity was kept constant at 2.5 mm/s for all the tapers. Uniform waveguides were also fabricated for comparison by depositing Ti segments with a constant separation (10 µm between the centres of adjacent segments) obtained by scanning the sample with a constant velocity of 2.5 mm/s (Fig. 1). The samples were then end-polished for optical characterisation and loss measurements.

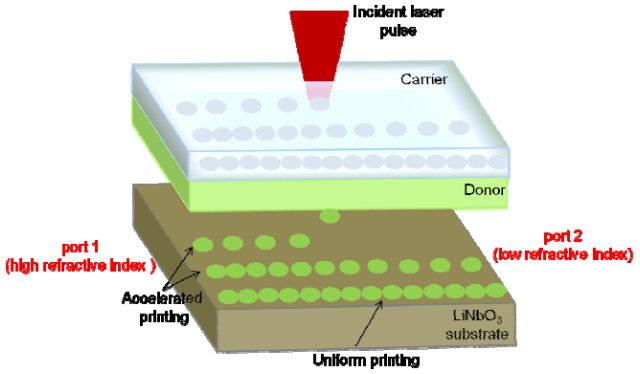

Fig. 1. Schematic of the LIFT technique for printing segmented Ti lines onto LN substrates. The exaggerated version of how the Ti dots separate out by increasing speed from one end (port 1) of the substrate to the other (port 2) for fabrication of a tapered waveguide along with constant velocity lines for comparison are also shown.

The waveguide losses at 1550 nm were measured using the fibre mismatch technique [12]. Light from a tuneable laser (1500-1600 nm) was launched into the waveguides using a single mode fibre (SMF) and the output was first collected using a similar SMF and then with a multimode fibre (MMF). The difference in the collection efficiency gave the coupling loss of 6 dB for the SMF. In this technique it is assumed that the MMF collects all the output light from the waveguide. The propagation loss was then calculated by taking the difference between the insertion loss (total loss due to the waveguide) and the coupling loss. The insertion loss of the waveguides was measured to be 11 dB resulting in a propagation loss of ~3.1 dB/cm, (the waveguide length was 16 mm). The variation in the velocity along the waveguide length leads to higher values of optical loss in tapered waveguides than the previously reported constant velocity waveguides [4]. In comparison, overall optical losses of 1.6 dB and 1.05 dB have been reported for mode filters with lengths of 0.6 mm and 1.6 mm respectively prepared using soft proton exchange (SPE) method [13].

The optical characterization of the waveguides was performed using the set-up outlined in Fig. 2. Light from a tuneable fiberised laser (1500-1600 nm, TM polarization) was coupled into the waveguides from port 1 using an objective lens (40 x). The output was collected using another objective lens (40 x) and the mode profiles were observed using an IR camera. All these measurements were performed at 1550 nm. The waveguide samples and objective lenses were mounted on a 3-axis (x-y-z) translational stage.

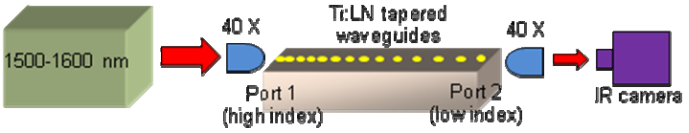

Fig. 2. Experimental set-up used for optically characterizing the waveguides.

Figure 3(b) shows optical mode profiles of segmented waveguides corresponding to Ti deposition at constant velocity (2.5 mm/s). The waveguides supported two modes (TM_{00} and TM_{01}). Figure 3 (d), (e) and (f) show the optical mode profiles of index tapered waveguides corresponding to Ti deposition with constant acceleration of 0.3, 0.4 and 0.5 mm/s^2 respectively with an initial velocity of 2.5 mm/s when light was launched from port 1 (Fig. 2). The images clearly show that the tapers supported only the fundamental mode (TM_{00}) thereby exhibiting the mode filtering operation. Similar results were obtained even when the coupling conditions were altered by moving the waveguides with respect to the input beam in the transverse direction to excite higher order modes indicating that the port 2 of the tapered waveguides could support only the fundamental mode. When the acceleration value was increased beyond 0.5 mm/s^2 the waveguides ceased to guide altogether due to the waveguide reaching its cut-off value. Another important feature to be noticed in these images is that as the writing speed/acceleration was increased the mode size increased as well, as a direct consequence of the decrease in the index contrast with increasing segment separation that lead to a broader and less tightly confined mode. The Gaussian function fit mode field diameter (MFD) values for mode profiles captured from tapers fabricated with 0.3, 0.4 and 0.5 mm/s^2 acceleration respectively are presented in Table 1. It clearly depicts the increase in the MFD with increasing acceleration value.

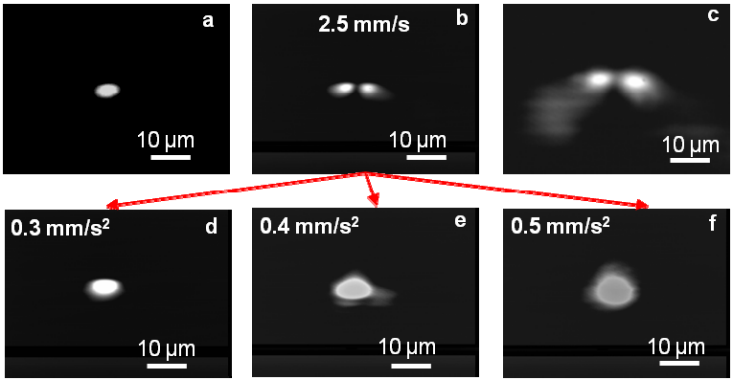

Fig. 3. (b) Near field intensity profiles captured from a waveguide written with a constant velocity of 2.5 mm/s. (d-f): near field intensity profiles of tapered waveguides written at accelerations of 0.3, 0.4 and 0.5 mm/s^2 respectively when the light was launched from port 1. (a) and (c): near field intensity profiles corresponding to the waveguide written with an acceleration of 0.3 mm/s^2 when the light was launched from port 2.

When the laser light was launched from port 2 (Fig. 2) a much better confined fundamental mode was obtained on the higher index port 1 of the tapers (Fig. 3 (a)) as expected. The Gaussian fit MFD value for this mode is also presented in Table 1. However upon altering the launching angle a higher order mode was monitored at the same port as shown in Fig. 3 (c) for a waveguide written with an acceleration of 0.3 mm/s^2. This behavior

is not expected for an adiabatic taper however the corrugation in the refractive index distribution along the waveguides caused by the shape of the printed Ti dots is believed to be responsible for this non-adiabatic behavior of the device. Modeling results, which will be discussed in the next section, confirmed this observation.

Table 1. Gaussian Fit MFD Values for Mode Profiles Captured from Waveguides Written with Acceleration of 0.3, 0.4 and 0.5 mm/s^2 Respectively When the Light was Launched from Port 1 Along with the MFD Value for the Fundamental Mode on the Higher Index Port 1 for Tapered Waveguide Written with 0.3 mm/s^2 Acceleration When Light was Launched from Port 2

Waveguides written with constant acceleration of	Gaussian fit MFD (μm)
0.3mm/s^2 (light launched form the port 1)	~11.5
0.4 mm/s^2 (light launched form the port 1)	~14.5
0.5 mm/s^2 (light launched form the port 1)	~16.5
0.3 mm/s^2 (light launched form the port 2)	~8.5

3. Theoretical modeling

To understand the non-adiabatic nature of the segmented tapers fabricated using LIFT the light propagation both along segmented Ti:LN and continuous index tapers was modeled. First a 3D model of Ti diffusion of LIFT-deposited dots at high temperature was developed with dot separation varying from zero to 3 μm in steps of 0.5 μm. This Ti distribution was then converted to the corresponding 3D refractive index profile using the method discussed in [14]. The zero and 3 μm separation values corresponded to the initial and final Ti dot separation for the tapered waveguides written using 0.3 mm/s^2 acceleration. The maximum refractive index contrast values over this range of segment separation vary from 0.0406 to 0.0322. In the actual experiments the samples were ~16 mm long but theoretical modeling was not possible for these lengths due to excessively large computer memory requirements. The simulation of light propagation in the waveguides was therefore restricted to shorter lengths (~700 μm) and qualitative results were obtained using Comsol multiphysics software. The structure was built by drawing 7 sections each section containing 10 Ti discs with 0, 0.5, 1, 1.5, 2, 2.5 and 3 μm separations respectively. The corresponding refractive index profile was calculated and is illustrated in Fig. 4 (a) as variation of the intensity of the segments along the waveguide. The structure which is visible in some of the segments in Fig. 4 (a) is due to limitations in the image generating capabilities of the software. Cross sections of the profiles showed a smooth refractive index distribution. The light propagation pattern as shown in Fig. 4 (b) was obtained using a Gaussian (TM_{00}) distribution as an input to the port corresponding to the 3 μm separation side of the waveguides. The results revealed that during propagation, part of the TM_{00} mode gradually converted to TM_{01} mode at the zero separation port of the taper. The intensity profiles obtained from the 3 μm and zero end of the tapered waveguide at the positions marked by red lines are shown in Fig. 5 (i) and 5 (ii) respectively.

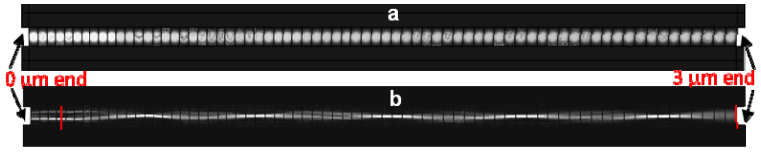

Fig. 4. (a) Shows the refractive index profile for the segmented Ti:LN waveguide with the brighter regions corresponding to higher index. (b) Shows the light propagation pattern when TM_{00} mode was launched from the 3 μm end of the waveguide.

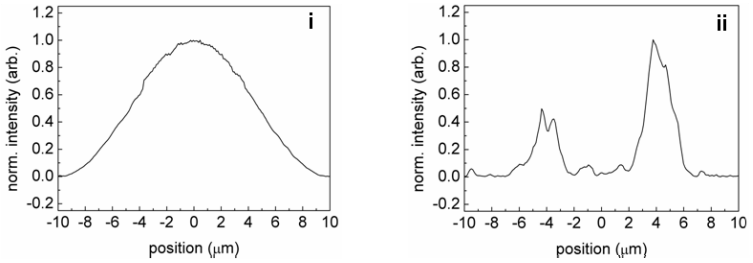

Fig. 5. Mode profiles obtained from the (i) 3 μm end and (ii) 0 μm end of the segmented Ti:LN waveguide. The positions where the modes were captured are marked as red in Fig. 4 (b).

The case of light propagation through a continuous Ti:LN tapered waveguide was simulated using the beam propagation method (BPM) in the commercially available RSoft Beamprop software, with the refractive index contrast values varying linearly from 0.0406 to 0.0322 throughout the length (~1 cm in this case) of the taper. The results depicted that the mode size increases from the higher index port of the taper to the lower index port, as expected for an adiabatic taper. The simulated mode profiles both for the higher and lower index ports are presented in Figs. 6 (a) and 6 (b) respectively. This confirms the dot-induced non-adiabatic refractive index structure observed for the segmented Ti:LN waveguides.

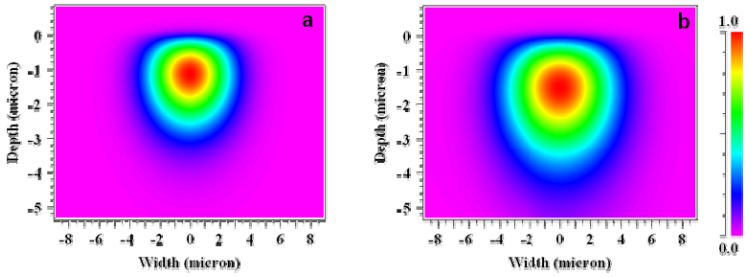

Fig. 6. Simulated near field intensity profiles obtained from (a) the high index and (b) the low index port of a continuous Ti:LN waveguide. The mode size increases as the refractive index contrast decreases along the length of the waveguide.

4. Conclusions

The control over the waveguide refractive index contrast obtained by adjusting the separation between adjacent segments of Ti which were LIFT-deposited and diffused into LN substrates has been used to fabricate a refractive index tapered waveguide device to be used as a mode filter. The propagation losses of the tapers were measured to be ~3.1 dB/cm at 1550 nm using the fibre mismatch technique. The mode profile pictures captured confirmed the mode filtering action performed by the index tapered waveguides. The corrugations introduced in the refractive index profile due to the segmented geometry of the deposits induce a non-adiabatic behavior in the tapers and this was confirmed by the theoretical modeling results.

Acknowledgement

Financial support from the Engineering and Physical Sciences Research Council (EPSRC), UK, (under Grant no. EP/C515668/1) and the European Community (under Grant no. 508581101, e-LIFT) are gratefully acknowledged.